



# Design and characterisation of a micro-flow cytometer with 3D hydrodynamic focusing

Stefano Chiavaroli

## Publication date

01-01-2011

## Licence

This work is made available under the [CC BY-NC-SA 1.0](#) licence and should only be used in accordance with that licence. For more information on the specific terms, consult the repository record for this item.

## Document Version

4

## Citation for this work (HarvardUL)

Chiavaroli, S. (2011) 'Design and characterisation of a micro-flow cytometer with 3D hydrodynamic focusing', available: <https://hdl.handle.net/10344/1679> [accessed 23 Jul 2022].

This work was downloaded from the University of Limerick research repository.

For more information on this work, the University of Limerick research repository or to report an issue, you can contact the repository administrators at [ir@ul.ie](mailto:ir@ul.ie). If you feel that this work breaches copyright, please provide details and we will remove access to the work immediately while we investigate your claim.

# DESIGN AND CHARACTERISATION OF A MICRO-FLOW CYTOMETER WITH 3D HYDRODYNAMIC FOCUSING



**Stefano Chiavaroli, MEng**

A thesis submitted for the degree of Doctor of Philosophy  
at the Faculty of Science and Engineering,  
University of Limerick, Ireland

Supervisor

**Dr. David Newport and Dr. Bernie Woulfe**

Stokes Institute

Department of Mechanical, Aeronautical and Biomedical Engineering  
University of Limerick

Submitted to the University of Limerick, April 2011

## **Declaration**

The substance of this thesis is the original work of the author, and due reference and acknowledgement has been made, where necessary, to the work of others. No part of this thesis has been submitted in candidature for any degree.

---

Stefano Chiavaroli (Candidate)

---

Dr. David Newport (Supervisor)

---

Dr. Bernie Woulfe (Supervisor)

This thesis was defended on the 28<sup>th</sup> of April, 2011.

## **Examination Committee**

Chairman	Prof. Tim McGloughlin	University of Limerick
Internal Examiner	Dr. Michael Walsh	University of Limerick
External Examiner	Dr. Juergen J. Brandner	Karlsruhe Institute of Technology

# Abstract

Recent advances in micro fabrication technology have resulted in proliferation of microscale mechanical devices, most of which are applied in the biomedical field and clinical diagnostics. One of the most promising technology platform is microflow cytometry, which requires biological cells to be focused in single file and presented in front of a detection system. The heart of a microflow cytometer is the generation of a sample stream with a diameter of the order of the particles to be measured. In order to be successfully analysed and to reduce measurement errors, particles should be focused in all three dimensions. Limitation in fabrication capability at reduced scales has resulted in adapting the macroscopic approach to a more simplified planar one. In recent years, a number of three dimensional flow focusing devices have been documented, but the "perfect" system still has to come.

The primary objective of this research thesis is to demonstrate that a microdevice for 3D hydrodynamic focusing can be fabricated at a dimension achievable from cost effective CNC manufacture. In order to do so, two devices of same design but different scale have been fabricated. CFD and confocal experiments demonstrated the ability of the proposed design to fully control size and dimension of the focused stream. The sample stream diameter were ten to twenty times smaller than the channel dimensions. Horizontal and vertical hydrodynamic focusing can be obtained independently and the flow remains stable until  $Re=30$ , which is six times higher than the appropriate operating condition of previously presented devices. The injection of microbeads proved that a stable cells/particles line-up can be achieved with 90% efficiency. The proposed device was also successfully employed with biological cells. A simple approximation of the theoretical model to predict the size of the focused stream is also presented.

An automated fluorescence-based optical counting technique was integrated with the system and evaluated using two different cell lines. This method compares favorably to the Trypan blue exclusion assay and to the visual count of the cells from the digital picture. In order to further improve the efficiency of the technique, the proposed device was employed to vertically focus the cells in a narrow region in the centre of the channel and therefore reduce fluorescence variability. Cell aggregation and sedimentation into the cell dispensing apparatus was reduced without reducing cell viability by developing a novel magnetic stirrer.

# Acknowledgements

At the end of this journey, it is time to look back and thank all of those who helped me reach this important goal.

First of all, I would like to express my gratitude and appreciation to Dr. David Newport for his guidance and support from the first day of this experience, and Dr. Bernie Woulfe, who tried to make a biologist out of this engineering mind. You both helped me considerably at every step of this journey. Also, a special thank to Prof. Morini, who should consider himself responsible for the insane decision to undertake this PhD :-)

I cannot imagine Stokes without Paddy, Fionnuala and David Jones: thanks for all your help and support. Also, the long days in the office would have not have been the same without the distractions of my "colleagues": Paul, Shiju, Dani, Jason, Fiachra, Kaayfe, Daithi, Mike, Ollie, Kev, Martin, Tom, Nick, Ger, Mark, Bubbles, TJ and all the people in Stokes. I will never forget all the jokes/spam emails/"Stables for one"/Mr Frosty, etc. BOOM!

Special thanks to all the full time and part time residents of 2, Dun An Oir: Alessio, Mike, Ned, Caro, Freddy and all the special guests who enjoyed dinner in our place. Life was easier with you! Not to mention my housemates at the penthouse: Mauro and Dave. What a wonderful time spent together! Thanks to my special "*little Italy*", you made me feel at home at any time: Francesco, Giorgio, Agata and Romina. To all my old time friends in Italy, for being so close from far away.

I would like to thank my family for being a continuous source of love and encouragement throughout my life. Without you I would never have been able to complete this work. Thanks for believing in me.

To Caterina, who has walked this road with me. Thanks for being by my side.

*Ai miei genitori, Giovanna e Nicola*

# Contents

<b>Abstract</b>	<b>iii</b>
<b>Acknowledgements</b>	<b>iv</b>
<b>List of Tables</b>	<b>x</b>
<b>List of Figures</b>	<b>xv</b>
<b>Nomenclature</b>	<b>xix</b>
<b>1 Introduction</b>	<b>1</b>
1.1 Flow focusing . . . . .	5
1.2 Hydrodynamic focusing . . . . .	6
1.2.1 2D-HF . . . . .	8
1.2.2 3D-HF . . . . .	9
1.3 Motivation for an automated optical cell-counting technique . . . . .	15
1.3.1 Motivation for a Biological Cell Dispenser . . . . .	18
1.4 Objective . . . . .	19

<b>2</b>	<b>Design &amp; Fabrication of microfluidic devices</b>	<b>21</b>
2.1	First prototype: Chang geometry . . . . .	22
2.1.1	Fabrication of the first prototype . . . . .	22
2.2	Second prototype: 3D-HFMD . . . . .	28
2.2.1	Design of the 3D-HFMD . . . . .	28
2.2.2	Fabrication of the second prototype . . . . .	30
2.3	Prototype validation . . . . .	33
2.3.1	Flow visualisation of dye . . . . .	34
2.3.2	Confocal analysis . . . . .	35
2.3.3	Testing with particles . . . . .	37
2.4	Selection of the materials . . . . .	38
2.5	Fabrication of the 3D-HMFD . . . . .	40
2.6	Magnetic stirrer assembly . . . . .	42
2.7	Summary . . . . .	45
<b>3</b>	<b>Biological Protocols, Methods and Experimentation</b>	<b>46</b>
3.1	Biological protocols . . . . .	47
3.1.1	Cell culture . . . . .	47
3.1.2	Cell staining . . . . .	52
3.2	Cell counting: Trypan Blue exclusion assay . . . . .	55
3.3	Flow visualisation . . . . .	58
3.3.1	Flow visualisation setup . . . . .	60
3.3.2	Selection of the dye . . . . .	62
3.3.3	Selection of the particles . . . . .	63
3.4	Confocal setup . . . . .	65
3.5	Summary . . . . .	68

<b>4</b>	<b>CFD simulations</b>	<b>69</b>
4.1	CFD simulations . . . . .	69
4.1.1	Meshing and analysis . . . . .	71
4.2	Summary . . . . .	75
<b>5</b>	<b>Hydrodynamic Focusing and Flow Cytometry</b>	<b>76</b>
5.1	2D focusing: flow visualisation of dye . . . . .	77
5.2	3D focusing: comparison of CFD and Confocal results . . . . .	80
5.2.1	Data extraction and analysis . . . . .	80
5.2.2	SSD . . . . .	84
5.2.3	LSD . . . . .	90
5.3	Particle focusing . . . . .	96
5.4	Cell focusing . . . . .	101
5.5	Theoretical model to predict the focused stream size . . . . .	106
5.5.1	Parabolic velocity profile of 3D merging streams . . . . .	113
5.5.2	Comparison between experimental results and theory . . . . .	116
5.6	Summary . . . . .	119
<b>6</b>	<b>Magnetic Stirrer and Optical counting technique for biological cells</b>	<b>120</b>
6.1	Magnetic stirrer . . . . .	120
6.2	Optical counting technique: principle . . . . .	124
6.3	Optical counting technique: results . . . . .	127
6.4	Summary . . . . .	134
<b>7</b>	<b>Conclusions &amp; Recommendations</b>	<b>135</b>
7.1	Conclusions . . . . .	135
7.2	Future works and Recommendations . . . . .	138

<b>References</b>	<b>140</b>
<b>A Biological materials</b>	<b>155</b>
<b>B Fabrication process of the 3D-HFMD</b>	<b>157</b>
B.0.1 Substrate preparation . . . . .	157
B.0.2 Photolithography . . . . .	158
B.0.3 Bonding . . . . .	159
B.0.4 Kapton releasing . . . . .	160
<b>C Videos</b>	<b>161</b>
<b>D PUBLISHED WORK</b>	<b>163</b>

# List of Tables

1.1	Literature review of 3D-HFMDs. . . . .	12
2.1	PMMA physical properties . . . . .	39
2.2	SU-8 physical properties . . . . .	40
3.1	Cell culture data of REH and L-929 cell lines. Source: DSMZ (2009) . . .	51
3.2	Flow rate ratios tested . . . . .	68
5.1	Sample sizes achieved on the 3D-HFMDs . . . . .	95
5.2	Particles VS biological cells. Right image: Lymphoblasts in a bone marrow smear from a 3-year-old male with acute lymphoblastic leukemia. Source: Soldin <i>et al.</i> [114] . . . . .	102

# List of Figures

1.1	(a) Principle of Flow cytometry. (b) Two-parameter histogram showing the blood profile of a healthy individual and one suffering from leukemia. . . .	2
1.2	Axisymmetric versus 2D planar devices. Adapted from Walsh <i>et al.</i> [123] .	7
1.3	Advantages of 3D-HF. . . . .	10
1.4	Cell trapped in the corner edges of the device of Lee <i>et al.</i> [63] . . . . .	11
1.5	The Coulter counter principle. Adapted from Hu <i>et al.</i> [46] . . . . .	17
2.1	3D-HF geometries published in literature. . . . .	23
2.2	Schematic of the device adapted from the geometry of Chang <i>et al.</i> [8]. . .	24
2.3	SEM images. Comparison between channels machined using air and liquid cooling. . . . .	26
2.4	Prototypes manufactured by CNC milling. Bonding between top and bottom layer is made using a) twelve M2.5 screws and b) 0.2mm thick double sided medical adhesive tape. €1 and €2 coins are shown for scale. . . . .	27
2.5	Schematic comparing the different geometries tested for hydrodynamic focusing. a) design presented by Chang <i>et al.</i> [8]; b) 3D-HFMD design. . . .	29
2.6	Schematic illustration of the 3D-HFMD. . . . .	30
2.7	Image of the second prototype manufactured by CNC milling on a single PMMA layer. Microfluidic nanoports and connectors are also visible. €2 coin is shown for scale. . . . .	31

2.8	Schematic illustration of the gasket assembly. The tubing is inserted through the gasket and halfway into the main substrate. . . . .	33
2.9	Test-piece positioned into the chip holder on the microscope stage. . . . .	34
2.10	Top views of a food colourant 2D hydrodynamic focused into the prototype. A reference to the measurement position is given. . . . .	35
2.11	Confocal images of Alexa Fluor 555 three-dimensionally focused into the prototype. a) 3D view; b) orthogonal image showing top, front and side views of the sample; c) magnification of the front view showing the 3D position of the sample into the channel. . . . .	36
2.12	Particles injected into the prototype. A small horizontal focusing effect is observed. Particles attached to the bottom surface are also visible as out of focus circles. . . . .	37
2.13	Image of the final chip. 1 cent coin is shown for scale. . . . .	42
2.14	Schematic of Stirrer Apparatus to rotate the magnetic field. . . . .	43
2.15	a) Close up of the magnetic bar rotating. b) Magnetic stirrer assembly connected to a syringe pump dispenser. . . . .	44
3.1	Cell culturing set up in the laminar flow hood. . . . .	48
3.2	A characteristic cell growth curve. . . . .	49
3.3	Fluorescent excitation and emission spectra of 5-chloromethylfluorescein, reagent of CMFDA. Adapted from [50] . . . . .	53
3.4	Standard curve of the CellTracker CMFDA with REH cells. Note that $x$ values are on a logarithmic scale. Values on the $y$ axis are arbitrary units. . .	54
3.5	An image of a haemocytometer. . . . .	56
3.6	Photograph of experimental set-up used for flow visualisation experiments. . .	59
3.7	Flow visualisation facility. . . . .	63
3.8	Excitation and emission spectra of the dextran-conjugated AlexaFluor 555. Adapted from [49] . . . . .	64

3.9	Excitation and emission spectra of 10 $\mu$ m FluoSpheres polystyrene microspheres. Adapted from [48]	65
3.10	Experimental set up used for confocal experiments.	66
4.1	Grid independence study carried out for SSD	72
4.2	Normalised sample concentration through the channel dimension.	74
5.1	Top views of the Alexa Fluor 555 hydrodynamic focused into LSD.	77
5.2	Flow visualisation frameset showing the stability of the flow into LSD.	79
5.3	Example of the data extracted from a typical confocal experiment on SSD. Flow rates used: $Q_B = 4\mu\text{l/min}$ , $\alpha_V = 4$ , $\alpha_H = 8.89$ , $\text{Re} = 30$ .	81
5.4	Example of the data extracted from a typical CFD experiment on SSD. Flow rates used: $Q_B = 1.5\mu\text{l/min}$ , $\alpha_V = 2$ , $\alpha_H = 4$ , $\text{Re} = 6.4$ .	82
5.5	Cross sectional confocal images showing three possible focusing configurations of the Alexa Fluor 555 into SSD.	85
5.6	Comparison of CFD simulations to confocal images for cross sections of SSD.	86
5.7	Cross sectional confocal images of SSD for constant flow rate ratios but different Re number.	87
5.8	Comparison of the size of the focused sample achieved on SSD for different flow rate ratios. a) vertical dimension; b) horizontal dimension.	89
5.9	3D views of the 3D focusing into LSD: (a) immediately downstream the intersection with D, (b) 11mm downstream E.	90
5.10	Comparison of CFD simulations to confocal images for cross sections of LSD.	91
5.11	Cross sectional confocal images of LSD for constant flow rate ratios but different Re number.	92

5.12	Comparison of the size of the focused sample achieved on LSD for different flow rate ratios. a) vertical dimension; b) horizontal dimension. . . . .	94
5.13	Hydrodynamic focusing of 10 $\mu$ m microbeads into SSD. . . . .	97
5.14	Hydrodynamic focusing of 10 $\mu$ m microbeads into LSD. . . . .	99
5.15	Human B-cell precursor leukaemia focused into LSD at two different focused values. a) single frame extracted from a video obtained for flow rates $\alpha_V = 0.5$ and $\alpha_H = 1$ ; b) single frame extracted from a video obtained for flow rates $\alpha_V = 1.5$ and $\alpha_H = 2$ . . . . .	103
5.16	Hydrodynamic focusing of Human B-cell precursor leukaemia into LSD. a) image obtained from a stack of 100 frames; b) image obtained from a stack of 200 frames. . . . .	105
5.17	Model developed by Knight <i>et al.</i> [57] using the electronic-hydraulic analogy. a) Hydrodynamic focusing on a T junction; b) correspondent resistive circuit. . . . .	106
5.18	Schematic representation of the theoretical model for a micro-flow cytometer with a inner and outer nozzle. Adapted from Lee <i>et al.</i> [61] . . . . .	108
5.19	Comparison of the normalised width of the focused sample as a function of the flow rate ratios for different channel aspect ratios $\epsilon$ . Adapted from Lee <i>et al.</i> [60] . . . . .	109
5.20	Schematic representation of the semi-empirical model to predict the size of the focused sample. . . . .	111
5.21	Schematic representation of the determination of the average velocity in the outlet channel. . . . .	112
5.22	Comparison between the theory of Lee <i>et al.</i> [60] and the proposed model for $\epsilon = 0.95$ . . . . .	113
5.23	Velocity profile of 3D merging streams. Velocity profiles of the two experiments are superimposed and compared to the theoretical solution. . . . .	115

5.24	Comparison of the focused sample sizes achieved on LSD and SSD against the theory of Lee <i>et al.</i> [60]. a) horizontal dimension; b) vertical dimension. Data extracted from the confocal experiments of Section 5.2. . . . .	117
6.1	Imaged flow of REH cells in the tubing with and without the stirrer assembly in operation. . . . .	121
6.2	Cell availability . . . . .	123
6.3	Schematic showing the optical counting technique facility. . . . .	125
6.4	Optical counting technique principle . . . . .	126
6.5	cell size over velocity . . . . .	128
6.6	Plot of cell availability with time. Test performed using the Trypan Blue exclusion assay and REH cell line. . . . .	129
6.7	The different intensity associated to the cells flowing into the microtube. Brightest cells are caused by overlapped cells in the flow. . . . .	130
6.8	Comparison between standard and automated counting techniques. Visual counting served as reference. . . . .	131
6.9	3D view of the vertical focusing into the microdevice: (a) CFD simulation, (b) Confocal image. Both images are acquired downstream of the intersection with channel D. . . . .	133
6.10	Cross sections of the vertical focused stream in channel E, downstream the intersection with channel D . . . . .	134
B.1	Fabrication process - physical run steps with wafer cross-section. . . . .	158

# Nomenclature

## Roman

$\beta$	ratio of side and sample pressures	-
$\chi$	ratio between maximum and average velocity	-
$\delta$	geometry of channel A	-
$\epsilon$	channel aspect ratio	-
$\gamma$	ratio of average velocities in the focused sample and the outlet channel	-
$A$	area	$m^2$
$\rho$	density	$\frac{kg}{m^3}$
$\sigma$	geometry of channel E	-
$f$	frequency	Hz
$h_f$	focused width	$\mu m$
$T_g$	glass transition temperature	$^{\circ}C$
$u_{avg}$	average velocity of channel E	m/s
$u_f$	average velocity in the focused sample	m/s
$u_{max}$	maximum velocity of channel E	m/s
$u_o$	average velocity in the outlet channel	m/s

$D$	channel diameter	$\mu\text{m}$
$H$	height	$\mu\text{m}$
$L$	length	$\mu\text{m}$
$n$	number of merging streams	-
$Q$	flow rate	$\mu\text{l}/\text{min}$
$W$	width	$\mu\text{m}$
$\alpha$	flow rate ratio	-

### Subscripts

$A$	channel A	-
$B$	channel B	-
$C$	channel C	-
$D$	channel D	-
$E$	channel E	-
$e$	experimental	-
$H$	horizontal	-
$max$	maximum	-
$s$	simulations	-
$V$	vertical	-

### Acronyms

3D-HFMD	Three Dimensional Hydrodynamic Focusing	-
ADC	Analog to Digital Converter	-

CFD	Computer Fluid Dynamic	-
CLSM	Confocal Laser Scanning Microscopy	-
CMFDA	5-chloromethylfluorescein diacetate	-
CNC	Computer Numerical Control	-
DEP	Dielectrophoretic	-
DI	distilled	-
DMSO	Dimethyl sulfoxide	-
DPBS	Dulbeccos Phosphate Buffered Saline	-
FACS	Fluorescence Activated Cell Sorter	-
HF	Hydrodynamic focusing	-
ID	Inner Diameter	-
IPA	Isopropyl Alcohol	-
LSD	Large Scale Device	-
MEMS	Micro Electro Mechanical System	-
OD	Outer Diameter	-
PGMEA	Propylene Glycol Methyl Ether Acetate	-
PIV	Particle Image Velocimetry	-
PMT	photo multiplier tube	-
RBC	Red Blood Cells	-
rpm	revolutions per minute	-
RT	room temperature	-

SEM	Scanning Electronic Microscope	-
SSD	Small Scale Device	-
SSD	Small Scale Device	-
UV	Ultra Violet	-

# Chapter 1

## Introduction

No more than twenty years ago, research on microfluidic phenomena and their application to the biomedical world was still non-existing. Nowadays, more than 2500 publications per year are produced on the topic and the attention is now moved to the nanofluidic field. Microfluidics is a multidisciplinary field which endeavours to integrate the disciplines of physics, chemistry, biology and engineering into efficient diagnosis technology for a wide range of practical applications. The advantages of microfluidic devices include low cost fabrication, short analysis times, low energy consumption, small sample and reagent volumes, minimal waste production and extremely sensitive detection. Microfluidic is having an increasing impact on biotechnology and life sciences and offers the great promise of fundamentally improving our way of life. A single device can integrate many steps that are currently performed in distinct, time-consuming steps in a laboratory. Indeed, Biomicrofluidics is centered on scaling laboratory processes into automated microfluidic devices, exploiting the enhanced mass and energy transport phenomena and smaller reagent and sample sizes required for analysis at the reduced scale. Much of the recent development in microscopic fluid dynamics is connected with the need to improve biomedical research and clinical diagnostics, such as cancer diagnostics [17]. In a recent critical review on microfluidic systems, Lenshof and Laurell stated that some of the most promising ruling technology platforms are the flow cytometry/fluorescence activated cell sorter (FACS) and the Coulter Counter [64].

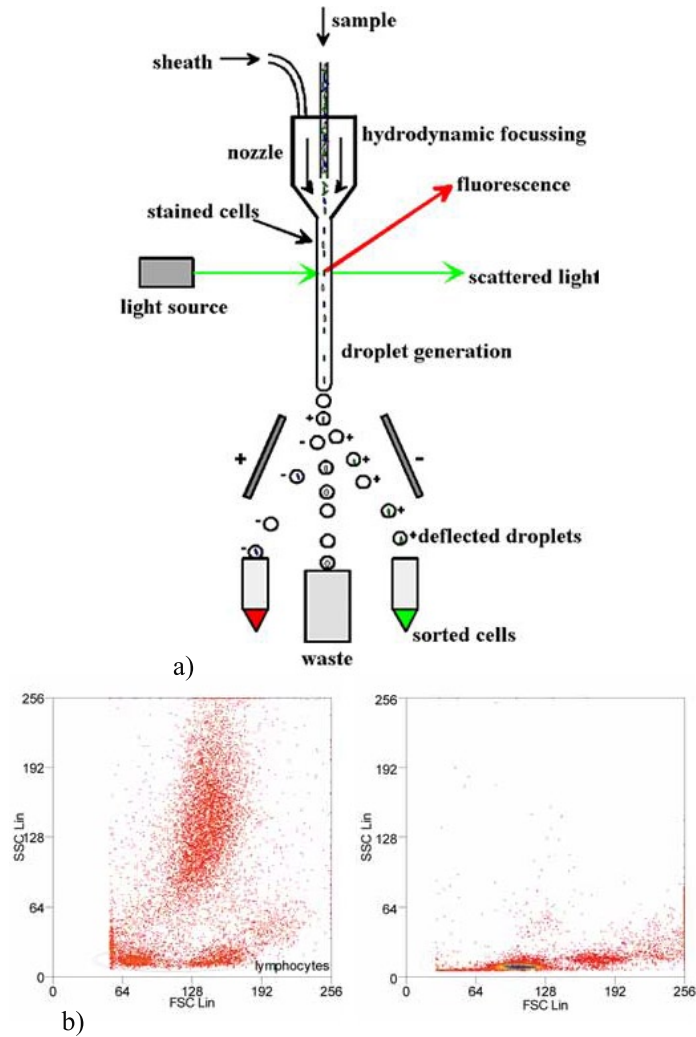


Figure 1.1: (a) Principle of Flow cytometry. (b) Two-parameter histogram showing the blood profile of a healthy individual and one suffering from leukemia. Forward Scatter (FSC) and Side Scatter (SSC) are plotted on the x- and y-axes, respectively, and cell count height on a density gradient. Adapted from Rahman [96]

Flow cytometry was first introduced by Crosland-Taylor [14] in 1955, and rapidly become a standard method in biology and medicine. The principle of flow cytometry is summarised in Figure 1.1 (a). Cells are first prepared in suspension and labeled with antibodies or stained with fluorescent dyes. Then, a sample of the cell population is slowly introduced into a fast flowing stream of fluid which surrounds the cells so that the cell suspension is coaxially laminated in the centre of the buffer flow. One or more laser lights are used to illuminate the sample and the fluorescence scattered by the particles is collected by a series of sensitive detectors, *e.g.* photo-multiplier tubes (PMT). The photo-detectors convert

the scattered and emitted light into electrical pulses. The signals are then amplified and processed by an Analog to Digital Converter (ADC), which allows for events to be plotted on a graphical scale. For instance, Figure 1.1 (b) depicts a two-parameter histogram measuring the differences between the blood profiles of a healthy individual and one suffering from leukemia. Cells can be discriminated based on size, density, viability, presence of a specific antibody or simply counted, and the method allows the simultaneous processing of a large number of samples in a very short time. Standard flow cytometry is nowadays used in a large number of scientific areas: pathology [13], *in vivo* flow cytometry [34], haematology, microbiology and marine biology, just to name a few. In the years, flow cytometers have begun to increase in complexity, employing a large number of lasers and detectors for multi-color fluorescence analysis [93]. Multiple molecules can be measured simultaneously at a rate of over 100,000 cells/s [121], allowing rare cell type with desirable properties to be isolated from a large number of cells. Current cytometers, however, are confined to laboratory settings due to dimensions, cost and power requirements [106]. The new challenge is to develop a flow cytometer which is small, cheap and easy to use. Nowadays, in the design of a new device, the choice is between a huge flexible device, with multiple lasers, high throughput and fast analysis, or a small simple device for a specific application. In this research thesis the latter is addressed.

In the last decade, several attempts have been performed to develop a flow cytometer on the microscale. The characteristic laminar flow regime of microfluidic systems, in fact, makes them suitable to flow cytometry. Miyake *et al.* [82] in 1997 reported the first flow chamber fabricated using micro-machining techniques. The flow behaviour was investigated into the 300 $\mu$ m squared microchannels with an analysis of the pressure losses. Gawad *et al.* [33] presented a micromachined impedance spectroscopy flow cytometer for cell analysis and particle sizing. Microelectrodes are integrated in the channels to allow simultaneous measurements at multiple frequencies. Numerous approaches to micro-flow cytometry have been reported for cell [53, 59, 67, 68] and particle [30, 42, 116] counting and sizing. Throughput is still one order of magnitude below that of the macro scale, but an astounding detection rate up to 17,000 particles/s have been reached [110]. An interesting approach is that combining microflow cytometry with the micro-Coulter counter

method [33, 43, 89, 100, 133]. Holmes *et al.* [43] performed a white blood cells differential count using impedance measurements. Microelectrodes are fabricated directly in the channel and both impedance and fluorescence signals are collected to identify cell phenotype or physiological state. While most authors have focused on technical advances in one specific area, a few emerge as a serious attempt to fabricate a device able to replicate the capabilities of benchtop instruments. Yang *et al.* [132] presented a complete device for cell counting and sorting with an integrated optical detection system and data analyser. Chang *et al.* [9] developed a PDMS microdevice integrated with pneumatic micropumps, embedded optical fibers for multi wavelength fluorescence detection and a microflow switching module.

In their review of microflow cytometry, Ateya *et al.* [4] asserted that recent efforts on the fields have focused on the development of a microflow cytometer which is simple to use (reduction of external components), inexpensive (low-cost manufacture) and portable (small dimension) [5]. Indeed, flow cytometry is technically already microscale, but the equipment takes up a room. The following engineering requirements must be addressed in the design of a system that will meet the needs discussed above:

- miniaturisation of the fluid-handling components (on-chip pumps and valves)
- miniaturisation of the optics (embedded optical fibers and lenses)
- integration of the device with the electronic components and
- focusing the cells.

As the heart of a microflow cytometer is the generation of a sample stream with a diameter of the order of the particles to be measured, among the different aspects, the attention of this work was mainly directed towards the flow focusing area. Focusing cells, indeed, is an essential step prior to detecting, counting and sorting. This research thesis addresses dispensing and focusing.

## 1.1 Flow focusing

In order to analyse a sample particle by particle, a microflow cytometer must introduce a single file stream of particles into an interrogation region. Few authors have fabricated sufficiently narrow channels so that particles are forced to flow in single file without the need for focusing [29, 33]. However, this is not very effective in the microscale as it increases the risk of channel clogging and surface fouling and the channel size is strictly related to the particle size used. Different methodologies can be employed to focus the sample into the channel, and these can be classified into two groups: sheath flow focusing and sheathless focusing [128]. The use of one or more sheath fluids to compress the sample is called Hydrodynamic Focusing (HF). Sheathless focusing methods include inertial, magnetic, acoustic and dielectrophoretic focusing. While HF involves the use of one or more sheath fluids, sheathless focusing rely on a force to control the stream flow and position. This force can be externally applied, also called active focusing (DEP, magnetic, acoustic), or internally induced by channel geometry, passive focusing (inertial) [128].

Dielectrophoretic (DEP) focusing uses an electric field gradient between patterned microelectrodes to polarise particles in the fluid, in order to move them relative to the fluid motion. Negative DEP [10, 42, 68, 84] is often used to focus particles vertically by pushing them away from the electrode surfaces. Cheng *et al.* [10] utilised DEP forces to focus, sort and trap bioparticles in a microchamber at a processing rate of 500 particles/sec. Lin and Lee [71] presented a microdevice capable of performing optically induced flow focusing of polystyrene microbeads using virtual electrodes. The device was also capable of counting and sorting particles based on the optically induced dielectrophoretic forces. The majority of the authors have combined hydrodynamic and DEP methods together [10, 42, 68]. While two side flows compress the sample on the horizontal dimension, DEP focusing is employed on the vertical. However, the force field is applied directly to the particles being injected and therefore it requires charged species. Moreover, it rapidly decreases away from the electrode surface and the focusing efficiency is therefore very sensitive to the particle location [128].

Electrokinetic focusing [31, 56, 130] utilises electroosmotic forces to spatially force the

sample into a small region. Differently from DEP, particles move along with the fluid. The technique allows fast focusing rates and great position and velocity control. Yang *et al.* [129] and Fu *et al.* [31] presented microflow cytometers using electokinetic forces generated by high voltage power supplies. The width of the focused stream is inversely proportional to the ratio of electric potentials applied at focus and sample channels. This approach presents many limitations. Then, the potential difference is not constant but it can vary over time reducing the reliability of the method. Also, the electric field can cause adverse effects to the physiology of biological cells.

Acoustic focusing is based on the creation of a standing acoustic wave into the microchannel to move the particles toward the acoustic pressure nodes or antinodes. Nilsson *et al.* [90] demonstrated particle separation in a silicon microchips using acoustic forces. Particles were successfully constrained in a single line in the centre of the channel. However, acoustic focusing is not very suitable for microfluidic devices due to its high costs. Also, it requires the transducer to be in close proximity to the microchannel, which complicates the fabrication procedure [128].

Inertial focusing rely on the passively positioning of microparticles by the cross-stream particles motion into the microchannel. This method was first investigated by Di Carlo *et al.* [16] and was demonstrated for both straight and curved microchannels. Without the need for external forces, self-ordering of particles and cells was observed at the centers of the channel faces. Oakey *et al.* [91] proposed a microflow cytometer using inertial focusing which matched the resolution provided by a commercial hydrodynamic focusing flow cytometer. Nevertheless, the particles behaviour is effected by inertial forces only when the  $Re$  number of the particle is much lower than that of the fluid.

## 1.2 Hydrodynamic focusing

Even though numerous techniques have been proposed in the years to reach flow focusing on the microscale, the majority of the authors employ hydrodynamic focusing. Hydrodynamic focusing (HF) is one of the most utilized techniques in microfluidics, applied not only in flow cytometry, but also in cell sorting [47, 66, 127], droplet emulsion [73, 86, 118],

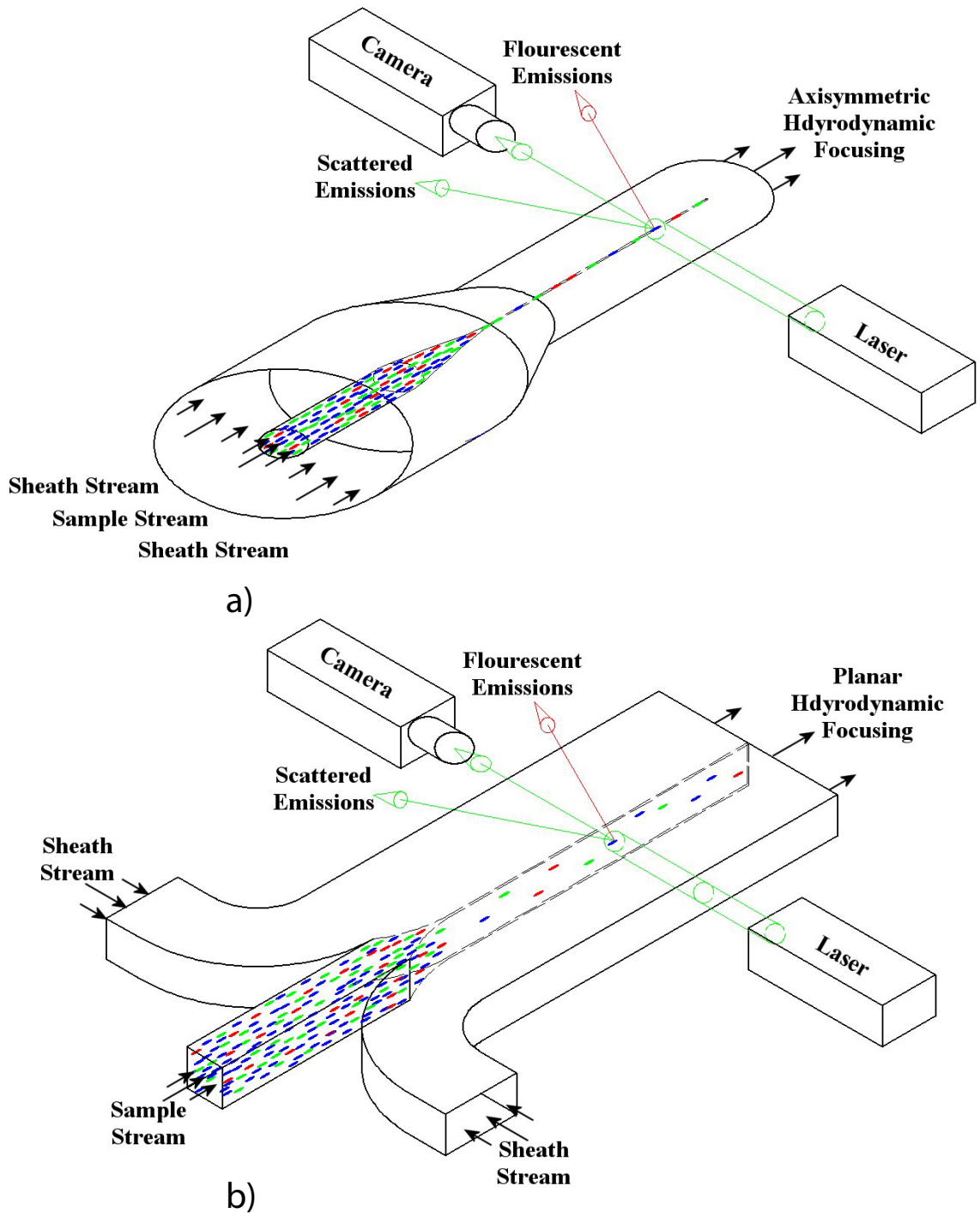


Figure 1.2: Axisymmetric versus 2D planar devices. Adapted from Walsh *et al.* [123]

mixing [57, 87], micro-PIV [18, 81] and many others. Also HF presents some disadvantages. The fluids are delivered by external pumps (*e.g.* syringe pumps) and their integration with miniaturised microdevices is still a challenge. Moreover, the use of more than two sheath fluids leads to an increase of hardware required. Despite these arguments, HF microfluidic devices are often preferable due to their fabrication simplicity, low costs and versatility.

The original design of macro flow cytometers was axisymmetric [14] where a high gauge blunt nozzle was placed concentrically within a glass capillary tube, Figure 1.2 (a). The particles were then injected through the needle so that the sheath flow hydrodynamically focused the sample in the capillary tube [124]. A round nozzle within a cylindrical sheath tube is very difficult to fabricate in a microfluidic system. Few attempts have been made to apply the axisymmetric approach to MEMS devices [73, 86], but the limitation in fabrication capability at reduced scales has resulted in more simplified planar devices [124]. In planar 2D micro-flow cytometers, the sample stream is focused in only one direction, usually horizontal, by two high-flow-rate sheath flows, as shown in Figure 1.2 (b).

### 1.2.1 2D-HF

Two Dimensional Hydrodynamic Focusing (2D-HF) has been employed on the macro and mini scale for many years, but the first application to the microscale was made by Knight *et al.* [57] in 1998, who fabricated a micromixer able to control the sample width from 10 $\mu$ m to 50nm. 2D-HF microfluidic devices introduced the great potential to control the horizontal position of the sample into the channel and to reduce sample dispersion. Stiles *et al.* [115] demonstrated a vacuum-pumped 2D-HF approach using a single suction pump, reducing sample consumption and hardware required. Lee G.B. *et al.* [60] investigated the parameters controlling the profile of the sample flow into a microchannel, showing that the size of the horizontal focused stream can be reduced to the same order of magnitude as that of 20 $\mu$ m micro beads. Howell *et al.* [45] reported two designs able to achieve 2D-HF using either a sequence of microstripes or a pair of chevrons fabricated on the channel surface. In both designs, sample and sheath fluids can be subsequently re-separated and re-employed.

However, 2D-HF presents many limitations. Most 2D-HF devices, in fact, only compress particles/cells in the horizontal, or in-plane, direction [61], therefore they do not provide the possibility of individual particle analysis. In 2D horizontal focusing the cells do not flow in the focused stream in single file, even though its width has the same order of magnitude as that of the cells size. This is because cells may be located at different depths in the microchannel. Gawad *et al.* [33] and Yang *et al.* [131], for instance, noticed discrepancies in the experimental results due to the wide vertical displacement of the sample into the channel. In order to solve this issue, Simonnet and Groisman [110] in 2005 have applied the HF technique to the vertical, or out-of-plane, dimension in a PDMS microdevice, squeezing the sample flow into a region equal to 10% of the channel height. Recently, Lin *et al.* [70] have numerically investigated two possible geometries to confine cells in a small vertical displacement. Many authors [36, 106, 120, 126] used vertical HF to push the sample to the bottom of the channel (non-coaxial sheath flow). This allows a close interaction with embedded electrodes, but this approach is limited to the Coulter counter or to applications where optical detection systems are placed on the channel surface. On the contrary, in most cases it is important to have full control of the sample position, *e.g.* flow splitting and switching. In literature, the need to compress cells on both vertical and horizontal directions simultaneously is commonly indicated as a possible improvement of the device being proposed [31, 125].

### **1.2.2 3D-HF**

The use of a 3D-HF technique instead of the 2D presents many advantages, some of which are outlined in Figure 1.3. First, cells can be located in the central controllable region of the microchannel and the interaction between sample and channel walls is minimised, an important aspect for biological applications where contamination is an issue. Second, as required in microflow cytometry, cells can be sorted in single file and presented in front of a detector for individual analysis. Also, 3D focusing leads to a more uniform velocity distribution and lower sample consumption, due to the artificial reduction in the channel dimensions. At the same time, the large physical dimensions of the channel reduce the risk

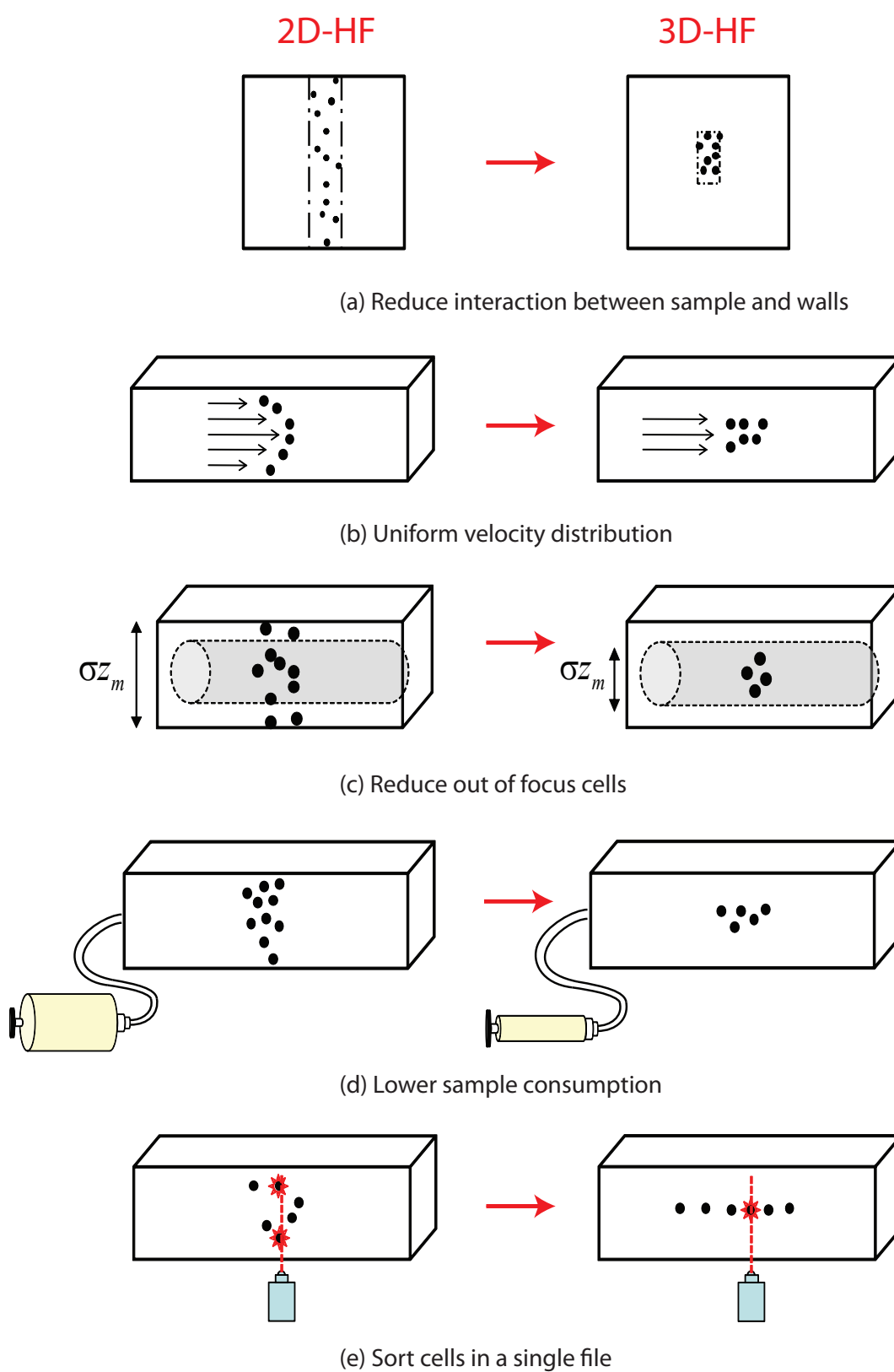


Figure 1.3: Advantages of 3D-HF.

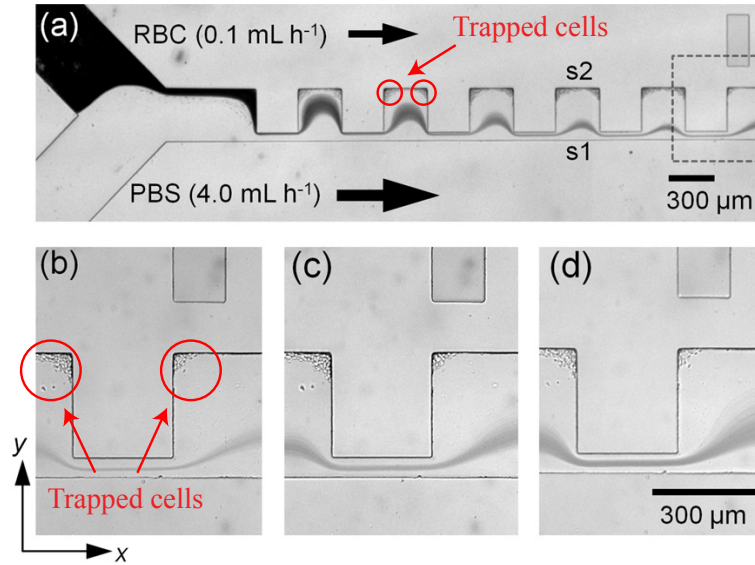


Figure 1.4: Cell trapped in the corner edges of the device of Lee *et al.* [63]

or channel clogging and air bubbles. Finally, with a micro fluorescing method, the whole volume of the flow is illuminated, which means all the cells are fluorescing, even the ones out of the measurement plane. Many detection devices are often unable to detect cells if their depth in the sample is out of the focal plane; those cells generate background noise and reduce the signal-to-noise ratio. 3D-HF solves this issue by forcing cells into the focal plane.

Several attempts have been made in the last few years to develop a planar Three Dimensional Hydrodynamic Focusing Microfluidic Device (3D-HFMD). Most of the so called 3D-HFMD, however, can only vertically constrain the flow on the bottom of the channel [36, 106, 120, 126], cannot control size and position of the sample profile [76, 129], or have complicated multilayer geometries [104, 117]. Table 1.1 represents all 3D-HF approaches available in literature relevant to this thesis. Different methodologies can be employed to force the sample in the centre of the channel. A single layer 3D-HFMD was proposed by Mao *et al.* [75, 76] using the principle of Dean flow, but it remains unclear whether this device can be used to control the vertical position of the stream, as underlined by Kennedy *et al.* [51]. The sample flow drifts to the centre of the microchannel by a centrifugal force which generates two counter-rotating vortices into a curved microchannel. The Dean flow approach has also been employed very recently by other groups [62, 63].

Table 1.1: Literature review of 3D-HFMDs.<sup>a</sup> Width x Height of the detection area; <sup>b</sup>No experimental verification.

Reference	Focusing method	Channel dimensions <sup>a</sup>	$Q_{sample}$ - $Re_{max}$	Focused % of channel dimension	Cells	Comments
Nieuwenhuis <i>et al.</i> (2003) [88]	4 sheath inlets	100x160 $\mu$ m	2 $\mu$ l/min	hor: 6.5% <sup>b</sup> - vert: 3% <sup>b</sup>	No	Full control of sample position. No confocal verification
Sundararajan <i>et al.</i> (2004) [117]	6 sheath inlets	100x50 $\mu$ m	10 $\mu$ l/min- $Re=5$	-	No	Four layers. CFD and confocal experiments
Chang <i>et al.</i> (2007) [8]	5 sheath inlets, 2 sample inlets	100x95 $\mu$ m	3.3 $\mu$ l/min- $Re \leq 5$	hor: 14% - vert: 23%	No	Two layers, easy manufacturing
Sato <i>et al.</i> (2007) [104]	Micro-grooves	100x100 $\mu$ m	1 $\mu$ l/min- $Re=28$	hor: $\approx 25\%$ - vert: $\approx 25\%$	No	Sample focused only for few $\mu$ m
Kennedy <i>et al.</i> (2009) [51]	4 sheath inlets	125x125 $\mu$ m	2 $\mu$ l/min- $Re=2.7$	vert: 15%	No	Analysis of center of mass
Hairer and Vellekoop (2009) [37]	4 sheath inlets	25x40 $\mu$ m	4 $\mu$ l/min- $Re=5$	hor: 6% - vert: 20%	No	Full control of sample position. CFD and confocal experiments
Lee M.G. <i>et al.</i> (2009) [63]	Dean flow	50x50 $\mu$ m	10 $\mu$ l/min- $Re \approx 85$	-	RBCs	No control of vertical position. Cells trapped in the corner edges
Kim <i>et al.</i> (2009) [56]	5 sheath inlets, 2 sample inlets	300x100 $\mu$ m	5 $\mu$ l/min- $Re=10$	hor: 43% - vert: 40%	No	Two layers. No confocal experiments
Golden <i>et al.</i> (2009) [35]	Microgrooves, 2 sheath inlets	390x130 $\mu$ m	5 $\mu$ l/min	hor: 5% - vert: 26%	<i>E.coli</i>	No control of vertical focusing
Mao <i>et al.</i> (2009) [75]	Dean flow, 3 sheath inlets	100x75 $\mu$ m curved $\mu$ channels	50 $\mu$ l/min- $Re=74$	-	No	No control of vertical focusing. Need for high velocity
Lee K.S. <i>et al.</i> (2010) [62]	Dean flow, 3 sheath inlets	curved $\mu$ channels	67 $\mu$ l/min- $Re=85$	-	No	No control of vertical focusing. Need for high velocity

Lee M.G. *et al.* [63] reported the first single layer 3D-HFMD with only one sheath flow using centrifugal forces generated by Dean flow. The lateral position of the sample can be controlled through a sequence of contraction and expansion regions, but the geometry could yield cells to be trapped in the corner edges of the channel, as observed in Figure 1.4. The Dean flow method is less applicable to cell applications because it only works at high  $Re$  number,  $Re \sim 85$ , which could cause apoptosis to the cells. An alternative methodology to perform 3D-HF is that using grooved microchannels. Golden *et al.* [35] developed a microflow cytometer with 3D-HF using only one sheath inlet for particles and *E.coli* counting. The flow was focused using microgrooves fabricated on the top and bottom of the microchannel, but the focused dimension is strictly dependent on the number of chevron-shaped grooves manufactured. The same device with integrated optical fibers has also been employed for bacteria detection [53]. In the grooved-based device proposed by Sato *et al.* [104], instead, the focused stream remains centered in the channel only for few microns, approximately  $30\mu\text{m}$ . Both approaches (Dean flow and grooved microchannels) require microchannels, curved or engraved, which would be difficult to fabricate without the use of sophisticated microtechniques (photolithography, micromolding, etc).

For this reason, the majority of the 3D-HFMD employ one or more pressure-driven sheath fluids to confine the flow into crossed rectangular microchannels. Nieuwenhuis *et al.* [88] presented a flow-cell for flow splitting and switching with full control of sample position using four sheath flows. However, no confocal experiments have been performed to confirm the CFD simulations. A complex four layers focusing geometry is that reported by Sundararajan *et al.* [117], which requires five inlets to achieve 3D-HF. However, in recent years, efforts have focused on fabrication simplicity and focus efficiency. A simple double-layer device proposed by Chang *et al.* [8] demonstrated the possibility to reduce the focused stream down to approximately 15% of the channel dimension for low Reynolds numbers. 3D focusing is carried out in three steps and size and position of the flow profile can be controlled by varying the flow rate ratios. This design has lately been modified by Kennedy *et al.* [51] to achieve 3D-HF in only two steps controlling the vertical position of the sample core. The flow was stable only until  $Re=2.7$ . A second attempt to improve this geometry has been made by Kim *et al.* [52], by locally increasing the aspect ratio of

top and bottom channels. The size of the focused core was only reduced down to 40% of the channel dimension. The 3D-HFMD presented by Hairer and Vellekoop [37], obtained sample stream diameters that were five to ten times smaller than the channel size. It is worth noting that none of the works described above has yet been successfully tested with biological cells.

It is also important to underline that accurately predicting the size of the focused stream is a key aspect of implementing HF schemes in microfluidic devices. To date various theoretical models, described in details in Section 5.5, have been proposed for both 2D [57,60,61,115] and 3D [8] hydrodynamic focusing. The electronic-hydraulic analogy [25] has been employed by Knight *et al.* [57] and Stiles *et al.* [115] to predict the focused width, but these models are limited by the ratio between the width of the channel and that of the focused stream and are only valid to channels with a low aspect ratio. An alternative approach has been proposed by the Lee group [60,61] using the mass conservation principle, but this is only applicable to channel with a high aspect ratio. The most accurate and general analytical expression to determine the width of the sample core for HF in rectangular microchannels has been introduced by Lee *et al.* [60]. This expression, however, involves considerable computational complexity and hardly results of practical use. CFD can also be used as a predictive tool, especially for laminar flows, but carries with it computational cost. Some of the analytical models are too computationally heavy and it is as easy to run a CFD simulation using commercial software, as it is to solve the equations provided. To conclude, various models to predict the dimension of the focused stream are available, but these are limited in the range of channel aspect ratios or use complicated formulas. No simple and accurate equation exists, and this would be beneficial to the HF community.

As suggested by Ateya *et al.* [4] and Lenshof and Laurell [64], the “perfect” flow focusing system still has to come. Literature has illustrated that flow conditions required to achieve a stable focusing are limited to a  $Re$  number either too high,  $Re \geq 80$  [62,63,75,76], or too low,  $Re \leq 5$  [8,37,51]. From the reviewed literature it was generally observed that few goals have to be accomplished:

- size and position of the focused stream should be fully controlled

- the size of the focused sample is meant to be of the same order of a cell size in order to sort particles in single file
- at the same time, however, the channel dimensions should be big enough to avoid clogging and to allow easy and cheap fabrication reproducibility.

A literature survey suggests that little progress has been made in this regard. Moreover, the majority of the previous 3D-HFMD cannot be reproduced without multi-step photolithography or etching methods, due to complicated multilayer geometries [51, 117], microflutings grooved in the channel surface [35, 104], or sequences of contraction and expansion regions [52, 63, 88]. These solutions could increase cost and complexity of the fabrication. Fabrication cost could also augment with the reduction of the channel dimensions and an effective cell line-up achieved in a larger size microchannel would therefore be preferred. With this in mind, in this research thesis the design of a cheap and simple geometry is pursued.

In addition to these requirements, a microflow cytometer should be able to quantify the cells being injected. On-chip integration of a cell counting system is therefore also recommended.

### **1.3 Motivation for an automated optical cell-counting technique**

In order to inject and count cells into a microflow cytometer, an in-depth understanding of cells behaviour at the microscale is required. A barrier in scaling laboratory processes into automated microfluidic devices has been the transfer of lab based assays: where engineering meets biological protocol. Biological cells often adhere, disintegrate, clump, coagulate and even mutate in a complex and unpredictable manner. Because of this, the ostensibly straight-forward task of dispensing a consistent and accurate number of cells is not trivial. Considerable temporal and spatial variability in the distribution of cells to inlet channels can be experienced, hindering the commercial development of bio-microfluidic platforms.

Moreover, in the past few years there has been a growing interest in developing alternative methods for animal testing; for any sort of cell toxicity tests, for instance, the need to accurately know the number of cells under investigation is a primary concern. In order to overcome these problems, an automation of the standard biological protocol that previously required manual operations, the Trypan Blue exclusion assay, is required. In the Trypan Blue assay, which is accurately described in Section 3.2, the percentage of cell suspension that is viable is calculated from a sample of the entire cell population [27], which exhibits a high degree of variability.

Various commercially available solutions for cell analysis and quantification have been proposed in recent years. ChemoMetec A/S, Axetris and Miltenyi Biotec., for instance, developed compact bench-top analysers for a wide range of applications, including viability measurement, cell count and cell discrimination. These systems, however, perform cell analysis using a destructive method. A sample is withdrawn from the cell population and injected into the device. The addition of chemical solutions into the sample causes lysis of the cell membranes and staining of the nuclei. Cell quantification is performed by counting the number of stained nuclei left in the suspension. Nuclei of non-viable cells do not fluoresce, and cell viability is deducted from a comparison between these two groups.

Several techniques and patents have also been established to address the counting problem, and most of them require the addition of chemical solutions into the suspension, or the use of sophisticated apparatus. In blood analysis systems, cell counting and differentiation is usually performed electrically using the Coulter method or optically using light scatter. The Coulter counter [12], developed in the '50s, is one of the most widely used apparatus for counting and sizing cells. Cell quantification is derived from the change in electric impedance of a small aperture when media containing cells passes through, as shown in Figure 1.5. The impedance change is monitored and correlated to an average diameter of the cell. Each impedance change over a set threshold is registered as a cell count, and very high throughput can be reached: modern systems can process samples at more than 100,000 cells/s.

This method has also been used for a wide range of applications. Simons [111] employed the Coulter counter principle to determine the volume of somatic cells; sodium

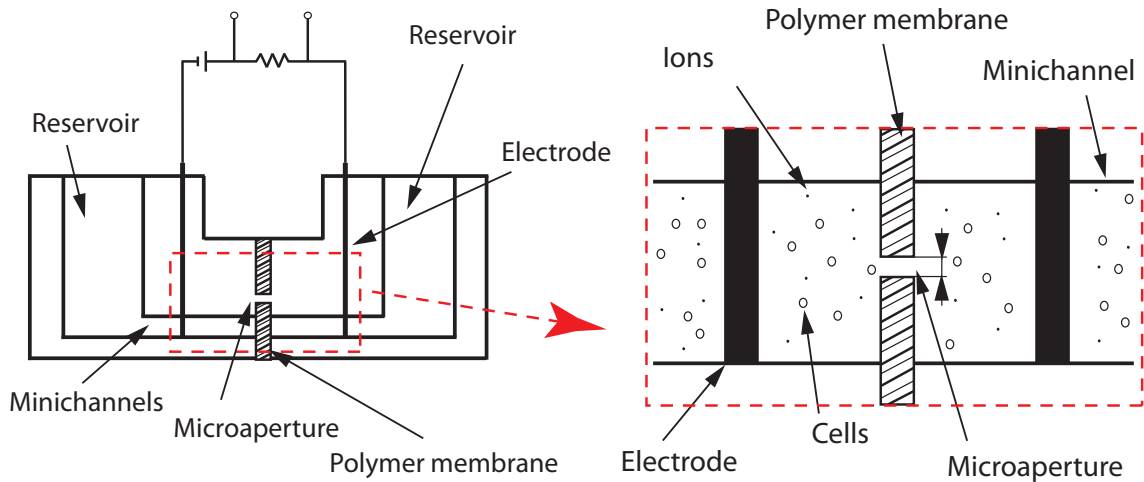


Figure 1.5: The Coulter counter principle. Adapted from Hu *et al.* [46]

citrate was also added to prevent cell clumping. Hoffman and Britt [41] developed a macro single cell analyser for simultaneous low and high frequency impedance examination using electrodes placed in a flow cell. Several attempts have been made to apply the Coulter counter principle to the micro scale. Gawad *et al.* [33] reported a microscale chip device for particle and cell sizing. Human erythrocyte and erythrocyte ghost cells were discriminated through electric impedance measurements. Counting and sizing of Juniper pollen have been carried out by Zhe *et al.* [133] using a micro Coulter counter with multiple sensing microchannels. The micro Coulter counter principle has also been employed by the Morgan group to demonstrate a microfluidic single cell impedance cytometer for leukocyte analysis and differentiation [42,43]. A key issue in Coulter counters has been clogging of the apertures, and because the operating range is less than 40% the aperture size, there is a need to modify the aperture size to extend the operating range. Nieuwenhuis *et al.* [89] developed a 2D liquid aperture controlled Coulter counter and achieved a 25% modulation in signal compared to 0.5% without the aperture control.

The importance of optically visualising the cells which are going to be tested, however, is becoming highly important, especially in morphological studies and long-term monitoring of cells [94], bacteria [10] and micro organisms [74]. Visually counting the cells is a tedious process, requiring tens of hours for several minutes of video. Automated approaches have been developed for detecting [19] and tracking [98] B-cells *in vivo* and *in*

*vitro* [2], but are computationally expensive, requiring many hours for one single video. Dong *et al.* [19] presented a method for identifying and counting rolling leukocytes within intravital microscopy, achieving 78% leukocyte detection accuracy with 13% false alarm rate. Both slow- and fast-rolling leukocytes can be tracked *in vivo* by Ray and Acton [97] using an active contour method. Recently, Boyer *et al.* [6] enhanced the tracking process using a CUDA-capable GPU, improving the process 200 fold. Phukpattaranont and Boonyaphiphat [95] developed a method to automatically count single images of breast cancer cells using a segmentation method. The image is first pre-processed, where the image colour is changed and an anisotropic diffusion is applied; then divided into single cells using watershed segmentation. Sizto and Dietz [112] patented a device which quantifies cells using a peak identification procedure. Cells are discriminated by a peak amplitude comparison with adjacent pixels. However, this method fails to distinguish overlapped cells and clusters of cells. To recapitulate, a simple, reliable and non destructive method to visually count the cells which are going to be tested into a microdevice is a commonly required analytical tool on the microfluidic field.

### **1.3.1 Motivation for a Biological Cell Dispenser**

To employ biological cells into a microdevice an important aspect has to be taken into account. As stated by Dietrich and Manz [17], aggregation of cells is a ongoing issue in bioengineering and this problem is reported very often in literature [28, 55, 72, 77, 111]. Cell clumping can lead to loss of cells and can affect cell function and phenotype. To date various biological and chemical solutions have been proposed and utilised ranging from the addition of DNase, proteases and/or buffered solutions containing anticoagulants and metal chelating agents [26]. None of the above are amenable to an automated microfluidic solution and, in a broader vision, with the advent of cellular-based therapy and the improved sensitivity of cellular-based assays, there is a need for purified cellular preparations free of residual levels of DNases, proteases, anticoagulants or heavy metal ions. Mechanical solutions have also been used, such as physical agitation using a vibration plate before delivery or pipetting up and down the sample before injection. However, the positive effect of this

artifices ends very quickly. The miniaturisation of a non-destructive mechanical method to keep cells agitated into a cell dispensing device, such a syringe, has not yet been proposed.

### 1.4 Objective

Literature has illustrated the characteristics required to a novel microflow cytometer. More in general, pros and cons of present 3D-HFMDs have been extensively described and the “way forward” has been clearly delineated. Also, as previously outlined, there is a necessity for automated techniques to perform cells counting and for engineering tools that are capable of extending the availability of biological cells into microfluidic devices.

With this in mind, the objectives of this research thesis are outlined as follows:

- To design and manufacture a low-cost and easily manufacturing 3D-HFMD able to fully control size and position of the focused sample.
- To prove that a device capable of focusing to the same order of magnitude of a cell size can be achieved from cost effective CNC manufacture.
- To establish a simple technique to predict the size of the focused stream.
- To propose a simple counting technique to automatically quantify cells being dispensed into a microfluidic device.
- To develop a microdevice in order to avoid cell aggregation and sedimentation into the syringe throughout the tests.

Chapter 2 discusses the design and fabrication of the microdevices developed for hydrodynamic focusing experimentation. The chapter details the design of each prototype and the final specimens separately and reviews the physical properties of the materials selected for the device fabrication. Chapter 3 outlines the biological protocols, methods and experimental apparatus employed during this research thesis. First, the cell lines adopted are presented and the cell culture and staining methods are also described. Following this, the experimental techniques and apparatuses used to validate the ability of the proposed device to perform hydrodynamic focusing are described. Chapter 4 describes the computational fluid dynamic simulations carried out during this research thesis. Chapter 5 provides critical analysis and discussion on the results obtained with the proposed device. Results are presented in 2D, 3D, particles and cell focusing sections. Finally, a simple model to predict the size of the sample stream is introduced. Chapter 6 presents the optical counting technique developed to accurately perform counting of biological cells. First, results obtained with the magnetic stirrer assembly are presented. Chapter 7 highlights the major conclusions drawn from this research study and possible improvements of the developed device.

## Chapter 2

# Design & Fabrication of microfluidic devices

As stated in the previous chapter, one of the main objectives of this research thesis is the design and fabrication of a simple and cheap microflow cytometer for focusing of cells/particles. Selection of the fabrication method, the dimension of the channels and the complexity of the geometry contribute enormously to increasing fabrication costs. Therefore, prior to fabrication and testing of the final specimens, a design achievable from cost effective CNC manufacture, chosen from the perspective of speed and economics, was pursued. In order to do so, a literature review on previous published geometries for 3D-HF was carried out and prototypes of the selected designs were manufactured by CNC milling in the workshop of the Stokes Institute.

This chapter outlines the development of the micro-fluidic specimens for 3D-HF experimentation. The first section describes the manufacture of the first prototype based on the geometry of Chang *et al.* [8]. Then, the design of the 3D-HFMD and the fabrication of the second prototype is presented. Following this, the material section reviews the physical properties of the materials selected for the device substrates. The fabrication steps of the final specimens are briefly presented. Finally, the magnetic stirrer assembly is described.

## 2.1 First prototype: Chang geometry

In the first chapter it was underlined that the majority of the previous microdevices are able to achieve 3D focusing using complicated multilayer geometries [51, 117], microflutings grooved in the channel surface [35, 104], or sequences of contraction and expansion regions [52, 63, 88], as depicted in Figure 2.1. The single layer designs proposed by Mao *et al.* [76] and Lee *et al.* [62], focus the sample fluid in a curved microchannel. None of these geometries can be reproduced without multi-step photolithography or etching methods, increasing cost and complexity of the fabrication. A simple double-layer device was reported by Chang *et al.* [8], which is a modified version of the design previously proposed by Simonnet and Groisman for 2D-HF [110]. The device was made of PDMS on two layers: two crossed rectangular microchannels on the top layer intersected with two rectangular microchannels on the bottom layer. The size of the microchannels of the top layer was 100 x 95  $\mu\text{m}$ , and that of bottom layer was 50 x 45  $\mu\text{m}$ . Hydrodynamic focusing was carried out in three steps, two for the vertical focusing and one for the horizontal focusing. The sample fluid is first squeezed on the vertical dimension by two sheath flows, then on the horizontal dimension by an additional horizontal sheath flow. Therefore, three sheath fluids are required, with seven inlets and one outlet. Size and position of the flow profile can be simply controlled by varying the flow rate ratios of sheath to sample fluid. Despite the drawbacks of the design (number of sheath fluids required and double layer geometry), preliminary investigations were carried out using this geometry due to its fabrication simplicity and reproducibility.

### 2.1.1 Fabrication of the first prototype

A first attempt was performed reproducing the design of Chang *et al.* [8] by standard CNC milling. An important consideration is required on the suitability of CNC machining for low cost manufacturing. CNC machining is an appropriate and cost effective method for the fabrication of single prototypes. Prior to the manufacture of the final specimens using a more accurate, but also expensive, technique it is advantageous to validate the proposed

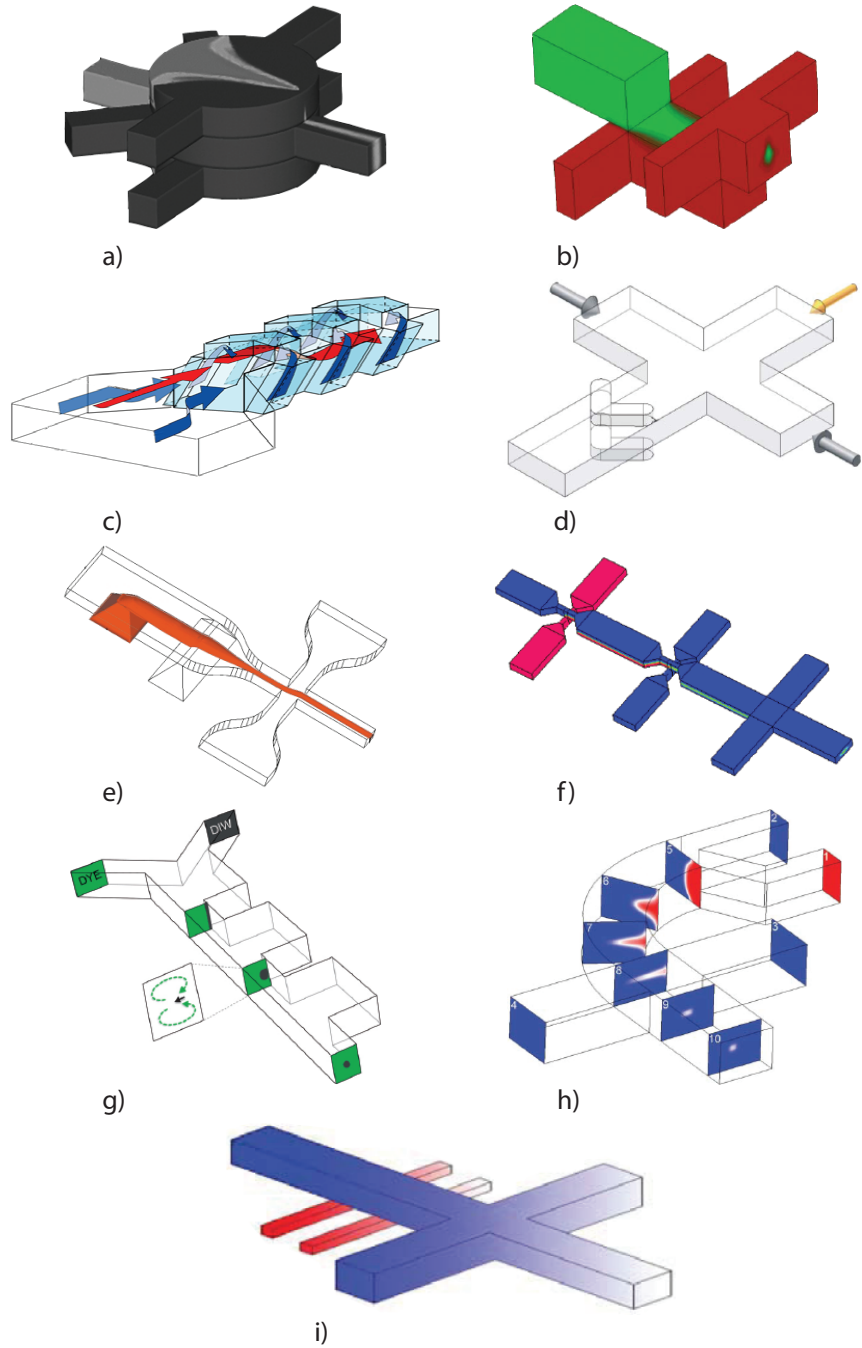


Figure 2.1: 3D-HF geometries published in literature. a) Sundararajan *et al.* [117]; b) Kennedy *et al.* [51]; c) Sato *et al.* [104]; d) Golden *et al.* [35]; e) Nieuwenhuis *et al.* [88]; f) Kim *et al.* [52]; g) Lee *et al.* [63]; h) Mao *et al.* [76]; i) Chang *et al.* [8].

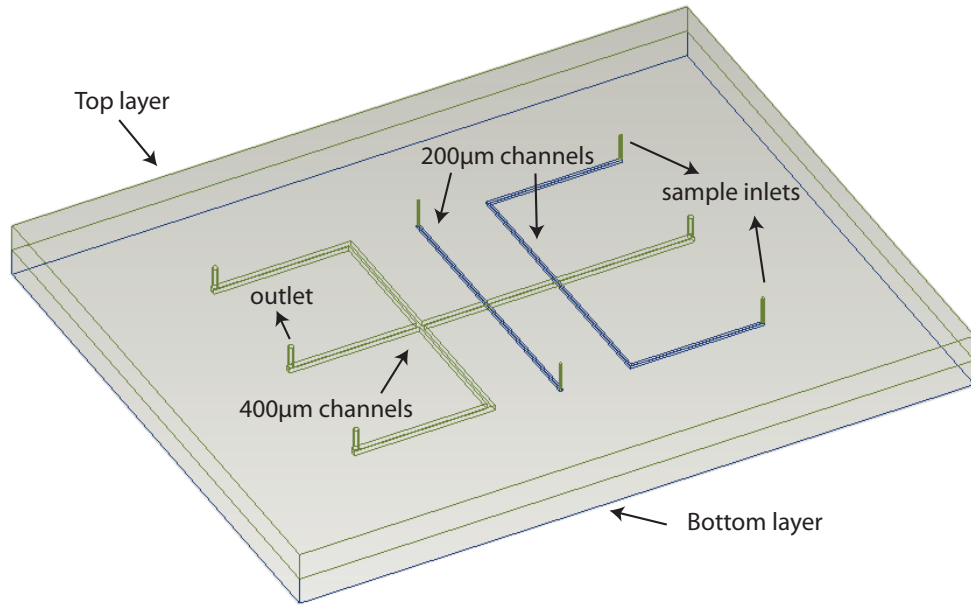


Figure 2.2: Schematic of the device adapted from the geometry of Chang *et al.* [8]. Channels on the top substrate are in blue while that on the bottom substrate are in green. Round holes are drilled from the top layer to reach the inlets of the channels on the bottom layer.

design by fabricating a single prototype using the facilities available in the workshop. However, for large scale production of disposable devices, generation of mould inserts by mechanical machining would be more effective and cheap. Moreover, other techniques like micro stereo lithography, glass etching or silicon technologies could provide better results for large-scale volume production from the perspective of speed and economics. For instance, hot embossing of more than hundreds devices can be achieved with a cost typically less than 1 cent per chip. However, CNC manufacture provided the most efficient and cheap method of fabricating the prototypes for the resources available in the workshop of Stokes Institute.

A number of practical constraints required consideration prior to the manufacture of the device. First, the channel dimension was limited to milling bits of 200μm in diameter. Then, due to the bio-related application of the micro flow cytometer, different materials for the substrates were investigated, as discussed in details in Section 2.4. Finally, the method employed to seal the bottom to the top layer required an additional consideration, as reported below.

A schematic of the design is depicted in Figure 2.2. A 2mm thick sheet of PMMA

(Engineering Steels Ltd., Ireland) was used for the top and bottom substrates. On both layers, 1mm of material was machined off with a 2.5mm milling bit at 0.01mm per step, prior to milling the channels, so that the final thickness of the device was 2mm. All surfaces were also finished and polished for two purposes: first, in order to reach a good alignment between the substrates in all points; second, to assure the same channel depth on along the full length of the device. Squared microchannels were machined, 200 x 200  $\mu\text{m}$  on the bottom layer, in blue in Figure 2.2, and 400 x 400  $\mu\text{m}$  on the top layer, in green. Tools used were two-flute 200 $\mu\text{m}$  and 400 $\mu\text{m}$  milling bits (Kildare Tooling Ltd., Ireland). In softer plastics, the material tends to plastically deform rather than cut during milling. The key to preventing plastics from rewelding is to use a cooling system to maintain the temperature down. Two methods have been employed and compared during this work: air and liquid cooling. The finish at the channels edges using the two methods was checked and the quality of the cuts was compared using SEM microscopy. Magnifications from x200 to x1000 were acquired for both 200 $\mu\text{m}$  and 400 $\mu\text{m}$  channels, as shown in Figure 2.3. Severe swarfs were observed in channels cooled with air, Figure 2.3(a). In some places, such as corners, burring covered 40% of the channel opening. On the other hand, a far superior cut was achieved in all channels by the use of a liquid cooler, as depicted in Figure 2.3(b). Thus, liquid rather than air cooling was employed throughout prototypes fabrication. However, plastic debris were still found in some locations, especially at the corners where the bit ends the run. These were removed with the aid of an air gun and a scalpel.

Two main problems were encountered during the manufacture of the first prototype. The first fabrication issue was observed in relation to the size of the channels. Once measured under the SEM, the width of the 200 $\mu\text{m}$  and 400 $\mu\text{m}$  microchannels was found to be bigger than expected. This was caused by an artificial increase of the tool diameter in CNC manufacturing due to plastic stuck on the cutter, despite the use of the cooling. The real channel dimensions were approximately 320 $\mu\text{m}$  and 480 $\mu\text{m}$  in width, respectively 160% and 120% of the channel size. It is important to underline that tolerances on CNC are not solely based on drill bit but on the system itself, *i.e.* CNC machine, material used and tool. Each CNC machine has different tolerances, which are directly related to the quality of the machine itself. Ultra precision machining can reach tolerances of  $\pm 1\mu\text{m}$ , however the

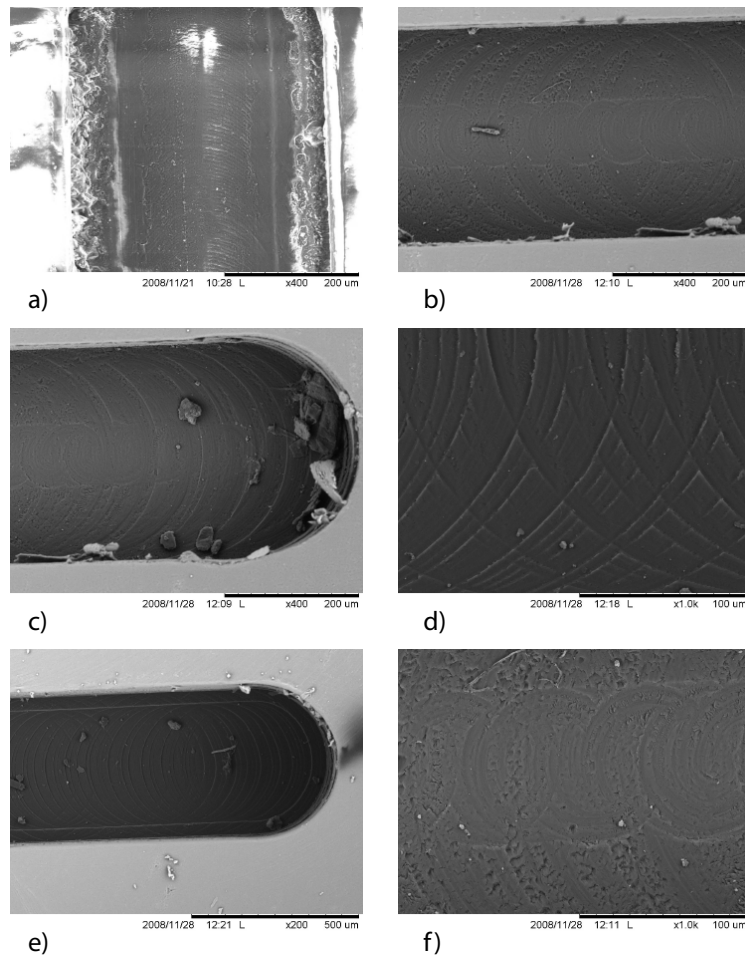


Figure 2.3: SEM images of the channels. Comparison between air and liquid cooling. a) air cooling. Sever burring is visible at the channel edge; b) liquid cooling. A cleaner cut is evident when compared to air cooling; c) x400 magnification of a 200µm channel; d) x1000 magnification of a 200µm channel; e) x200 magnification of a 400µm channel; f) x1000 magnification of a 400µm channel. A high quality channel finish is observed.

tighter the tolerance required, the more expensive the component will be to machine. Mechanical machining can be performed with reasonable costs for 200µm drill bit with fixed tolerances typically of  $\pm 10\mu\text{m}$  with metal (aluminum, brass and stainless steel) or glass being used. CNC performed in this research thesis has not been optimised for machining in plastic channels and this caused the first fabrication issue. The use of a more rigid material would also have improved surface quality and roughness.

The second problem encountered was the method to seal the two substrates. The risk to inadvertently fill the microchannels excluded the use of a liquid glue. A first attempt was made using M2.5 countersunk screws, wrench size equal to 5mm, as shown in Figure 2.4.

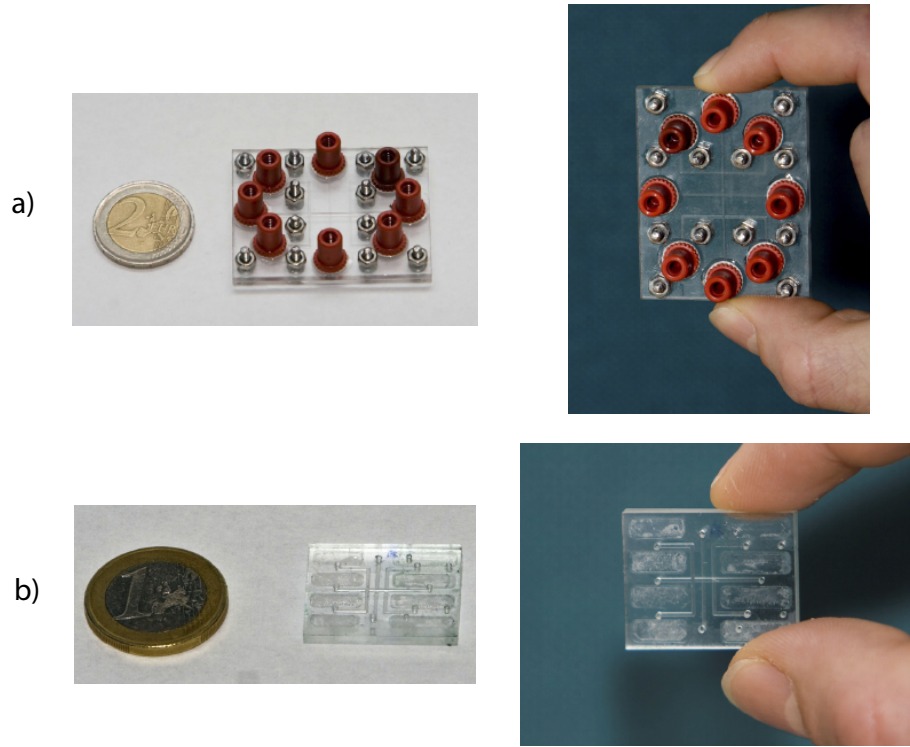


Figure 2.4: Prototypes manufactured by CNC milling. Bonding between top and bottom layer is made using a) twelve M2.5 screws and b) 0.2mm thick double sided medical adhesive tape. €1 and €2 coins are shown for scale.

A 50 x 40 mm chip was fabricated and twelve screws, tightened at the same pressure, were positioned at the chip corners and between the channels. A second attempt involved the use of an adhesive tape to bond the two layers. The absence of additional space required to lodge the screws led to fabricate a smaller chip, 25 x 20 mm. Eight pocket holes, measuring 3mm in width, 10mm long and 0.2mm deep, were machined at a distance of 0.2mm from the channels. A 0.2mm thick double sided medical adhesive tape (Adhesive Research, Ireland) was placed between the substrates, as observed in Figure 2.4. Both attempts failed because the pressure of the liquid within the channels was too high and in either case leaking of the sample fluid between the two layers was experienced. A third attempt was explored using thermal bonding of the two substrates. Zhu *et al.* [134] carried out a thorough study on thermal bonding between PMMA layers by hot embossing. The effect of bonding temperature and pressure on bond strength was investigated, and a range of optimum working values was given. The microchannel collapsed before reaching a proper bond. Because considerable bond strength and high quality of bonded microchannel

could not be reached without leaking of sample fluid between the two substrates, a different design was investigated.

## 2.2 Second prototype: 3D-HFMD

Due to limitation in fabrication capability, experiments on a double layer device could not be performed successfully, and a different geometry was therefore investigated. The design and fabrication of the second prototype is detailed in the following sections.

### 2.2.1 Design of the 3D-HFMD

This section describes the geometry of the second prototype. The design of the Three-Dimensional Hydrodynamic Focusing Microfluidic Device, 3D-HFMD, is a simplified geometry of that of Chang *et al.* [8]. As on the previous prototype, 3D-HF is carried out in three steps, two for the vertical focusing and one for the horizontal focusing. In fact, the sample fluid is injected from the inlet B and first vertically focused by channels A and C, then horizontally focused by an additional sheath fluid, as on the 2D counterpart. The two designs differ for the position and direction of the vertical focusing element, as highlighted in Figure 2.5. Channels B and C are placed vertically to the main channel A, rather than perpendicularly on a different plane parallel to it. Furthermore, in the new geometry there is only one channel for the vertical inlets, hence reducing possible pressure differences and/or presence of air bubbles.

As stated before, the device is made of two bottom cross channels, A and D, and two vertical channels, B and C, as depicted in Figure 2.5(b). Dimensions of the channels are defined as follows:

- $H$  = height of the cross channels A and D;
- $W$  = width of channels A, B and C and length of channel D;
- $L$  = length of the vertical channels B and C. It is worth noting that  $L = W/2$ .

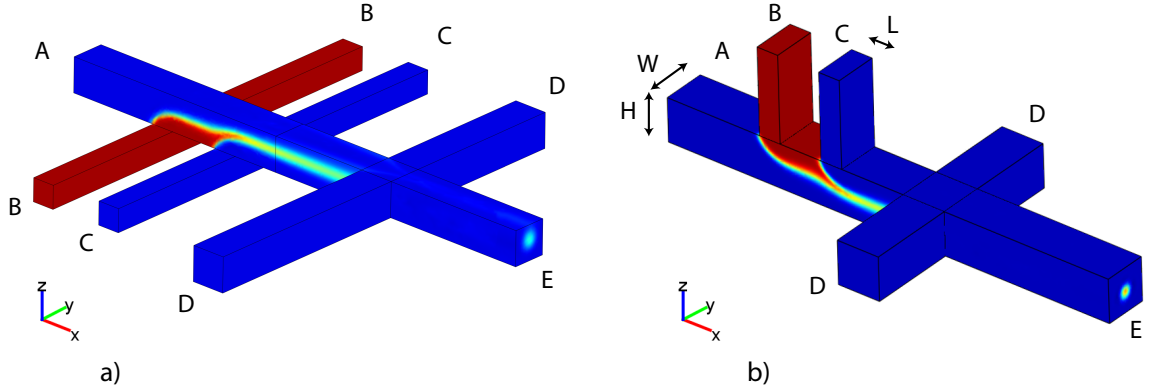


Figure 2.5: Schematic comparing the different geometries tested for hydrodynamic focusing. a) design presented by Chang *et al.* [8]; b) 3D-HFMD design. The different vertical focusing element is observed.

In the 3D-HFMD, the distance between the central point of B and C is  $1.5W$ , while C and D are  $2.5W$  apart. CFD simulations showed that the spacing between channels B and C and C and D had no significant influence.

To understand the operation of the device, the flow behavior is detailed in Figure 2.6. The device consists of one sample inlet, B, three sheath fluid inlets, A, C and D, and one outlet, E. The sample fluid B is forced to the top of the main channel by the sheath fluid A, and subsequently pushed down and centered in the vertical dimension by the inlet C, Figure 2.6(a). Finally, two additional side flows D focus the sample in the horizontal dimension, Figure 2.6(c), and the sample is then 3D focused for the remainder of the device, Figure 2.6(d). Vertical and horizontal focusing can also be obtained independently, as opposed to Chang's geometry. If only the vertical focusing element is activated, flow rate of the inlet  $D \approx 0$ , the 3D-HFMD can be utilised in applications where the sample must be constrained into the focal plane, as in the optical counting technique of Chapter 6. Whereas, if only horizontal focusing is used, the device operates as a standard 2D-HFMD. This design can be employed either with fluids, particles or biological cells.

By means of the electronic-hydraulic analogy [25], size, shape and position of the focused core can be controlled by varying the flow rates of sample and sheath fluids. The sample can be pushed to the top, bottom or side of the main channel. The flow rate ratio of vertical focusing is defined by eq. 2.1.

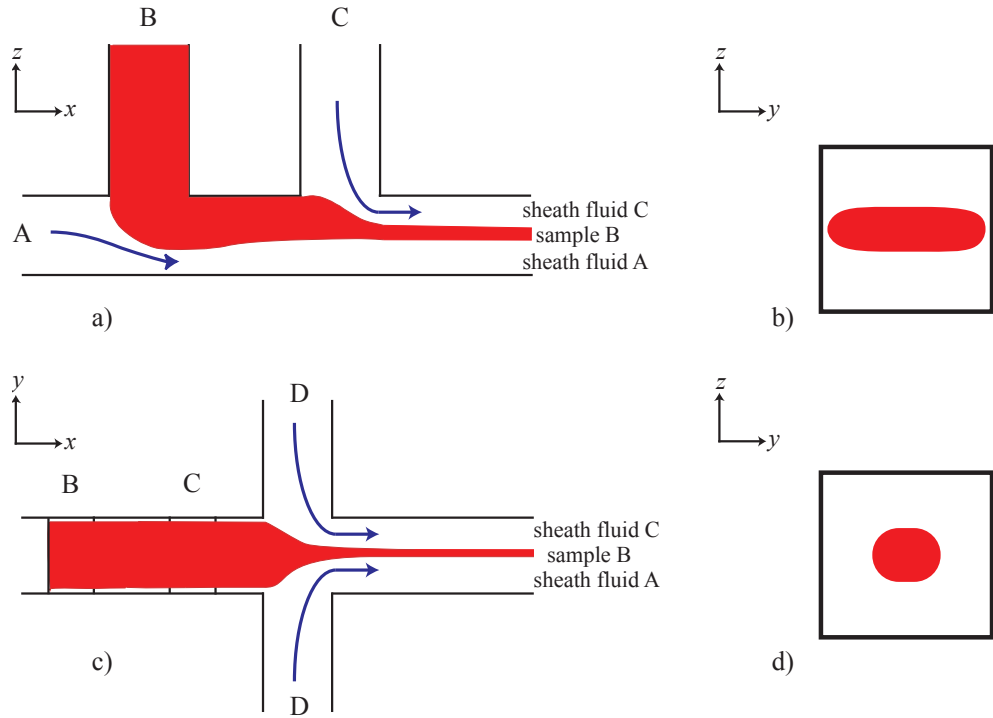


Figure 2.6: Schematic illustration of the 3D-HFMD. a) side view showing the vertical focusing element; b) front view before the intersection with channel D; c) top view showing the horizontal focusing element; d) front view after the intersection with channel D.

$$\alpha_v = \frac{Q_C}{Q_B} \quad (2.1)$$

where  $Q_B$  is the flow rate of the sample flow and  $Q_C$  is that of the vertical sheath fluid. It is worth noting that  $Q_A$  has been imposed equal to  $Q_C$  during the experiments of this study. The flow rate ratios of horizontal focusing is defined by eq. 2.2.

$$\alpha_H = \frac{Q_D}{(2Q_A + Q_B)} \quad (2.2)$$

where  $Q_D$  is the flow rate of the horizontal sheath fluid. Optimum working values of  $\alpha_v$  and  $\alpha_H$ , for 3D-HF, were found  $1 \leq \alpha \leq 6$  during the experiments of Chapter 5.

### 2.2.2 Fabrication of the second prototype

In this section, the fabrication process of the second prototype is presented. Machining and drilling of the channels were carried out on a CNC machine (Kosy Massive, Germany) at

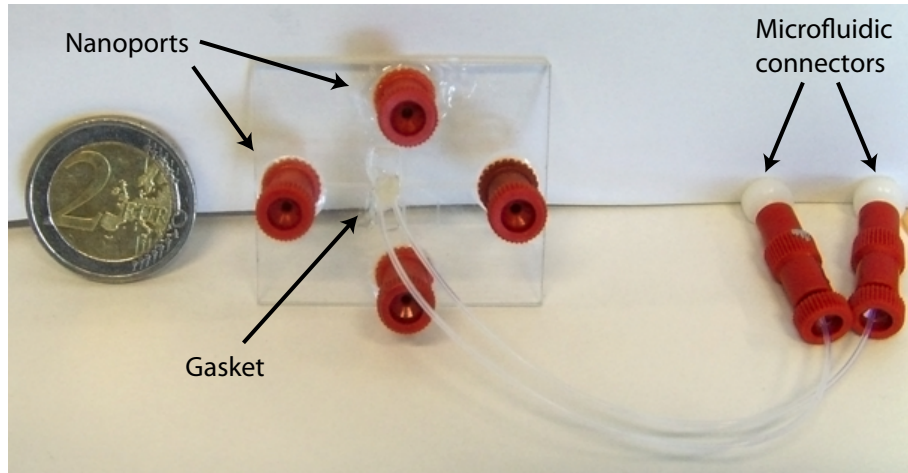


Figure 2.7: Image of the second prototype manufactured by CNC milling on a single PMMA layer. Microfluidic nanoports and connectors are also visible. €2 coin is shown for scale.

Stokes Institute. The device, depicted in Figure 2.7, was made of a 50 x 40 mm single piece of PMMA, cut from a 2mm thick substrate (Engineering Steels Ltd., Ireland). Top and bottom surfaces were finished with a 2.5mm milling bit prior to machining the channels. Milling was performed at 0.01mm per step at a speed feed of 20mm/s. On one side of the substrate, called bottom side for the remainder of this section, the two cross channels A and D were machined with a 400 $\mu$ m milling bit (Kildare Tooling Ltd., Ireland). As stated in Section 2.1.1, the real size of the channels was bigger than expected. Both channel A and D, which measured 3cm in length, were  $W = 480\mu\text{m}$  and  $H = 400\mu\text{m}$ . The fabrication was executed with the same settings utilised for the first prototype (liquid cooling, speed rate and depth per step), hence the quality of the channels can be assumed similar to that of Figure 2.3(e) and Figure 2.3(f). Since these microchannels were open, a 0.1mm thick single sided medical adhesive tape (Adhesive Research, Ireland) was employed to seal the bottom side of the chip. This avoided the need for a double layer device and allowed the channels to be kept clean at all time by replacing the thin adhesive film when required.

To connect the device with syringes and syringe-pumps, at the very end of channels A and D, 0.48mm holes were drilled from the bottom to the top side of the substrate using a 400 $\mu$ m drill bit (Kildare Tooling Ltd., Ireland). Microfluidic Nanoports (Upchurch Scientific, UK), were then bonded to the top side of the substrate using an adhesive ring and

epoxy glue. Glue was allowed to partially set and applied, once viscous enough, to the back and to the side of the nanoports. Care was taken to ensure that the holes were not covered with glue. The coned port, rubber gasket and adhesive ring were then clamped in position and placed in an oven at 100°C for 1 hour.

On a single layer device, the vertical rectangular microchannels could not be machined by CNC milling. Vertical round microducts were therefore drilled in place of the rectangular microchannels. However, in drilling channels on the micron scale, milling radius edge of order 1µm is achievable which can be considered rectangular in the context of a 200µm channel. Because the function of a prototype is to test the selected design prior to the final fabrication, this approximation was done with the assumption that, while the efficiency of the 3D focusing might vary, the efficacy of the design will not be compromised, since regions of major flow unsteadiness are channels A and E. Therefore, perpendicular to the main channel A, the two vertical ducts B and C were drilled, 0.7mm apart, using a 200µm drill bit (Kildare Tooling Ltd., Ireland). A center drill bit was used to provide the starting hole for the drill bit and drilling was started from the bottom side in order to avoid any possible damage to the channel surface. The diameter of the through holes was 0.32mm for a length of 1mm, then the hole was progressively enlarged to reach 0.8mm.

The connection between the vertical inlets and the syringes could not be done with the use of nanoports, because the outer diameter of the latter is larger than the distance between the ducts. In order to solve this problem, a 2 x 10 mm piece of PMMA, visible in Figure 2.7, was machined from the 2mm thick sheet of material and put as a gasket over the main substrate. In correspondence with the exit of the vertical inlets, two through holes were drilled on the gasket, with a diameter of 0.8mm. Two PFA micro medical tubing, 0.8mm OD, presented in Section 3.3.1, were forced into the gasket holes and stuck halfway through the vertical ducts in the main substrate, as illustrated in Figure 2.8. This was possible since the top side of the vertical ducts were 0.8mm in diameter. The use of the gasket enables the fluids to be injected into the inlets preserving optical access to the device. A small amount of epoxy glue was applied to the back and to the side of the gasket, and this was placed in position. Glue was also applied on the side of the tubing to fix it in place. Care was taken, once again, to ensure that the holes were not covered with glue. Since the tubing was

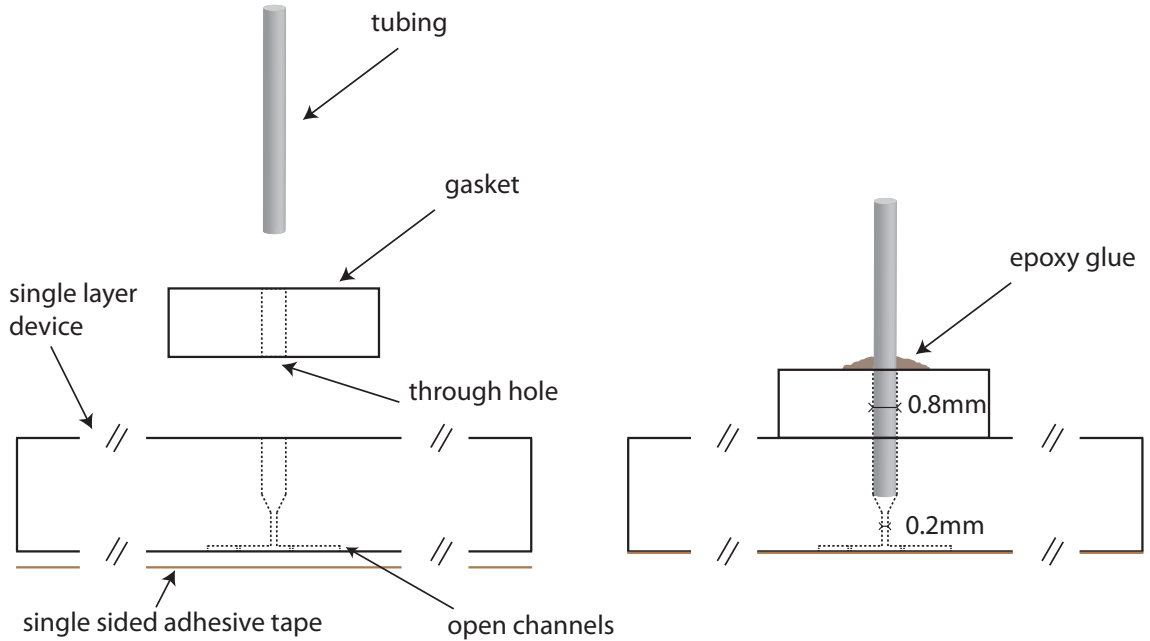


Figure 2.8: Schematic illustration of the gasket assembly. The tubing is inserted through the gasket and halfway into the main substrate.

lodged directly on the main substrate, no leaking was experienced between the gasket and the device. At the end of the tubing, a MicroTight® union assembly (Upchurch Scientific, UK) ensured connection with an additional tube attached to the syringe. Furthermore, since the gasket was placed before the intersection between channel A and D, transparency of PMMA ensured optical access for top or bottom views after this intersection.

A block of PMMA has been used as a chip holder to lodge the test-piece on the microscope stage of Section 3.3.1. The 2mm thick block was manufactured with a pocket hole in the center of the same size of the prototype described above. The rectangular shape of the chip holder fitted on to the microscope manual  $x$ - $y$  stage controller. The assembled test section and chip holder are shown in Figure 2.9.

## 2.3 Prototype validation

In order to investigate the efficacy of the proposed geometry as a flow cytometer, preliminary tests were carried out on the prototype prior to fabrication of the final specimens. First, 2D focusing was investigated using a food colourant. A preliminary confocal experiment

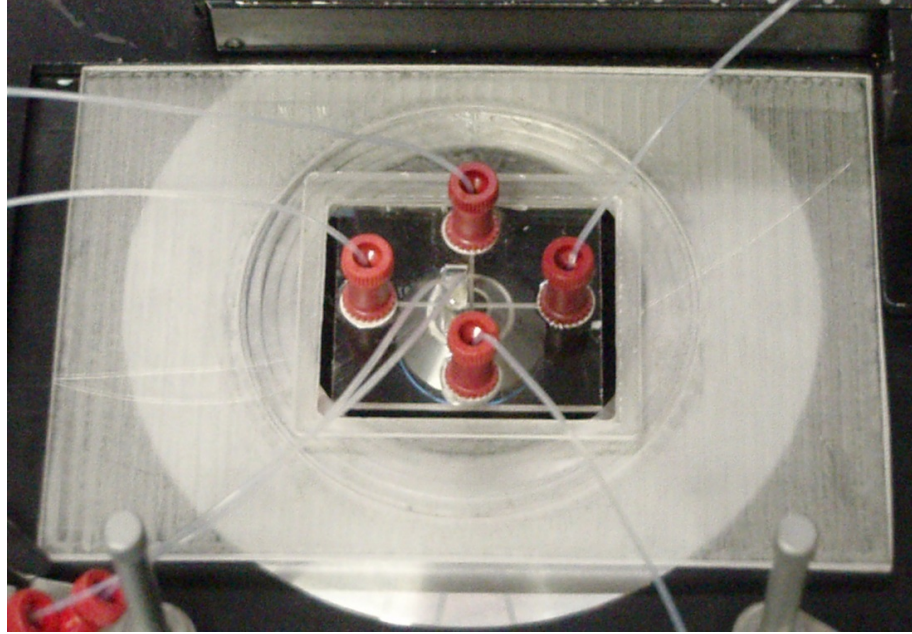


Figure 2.9: Test-piece positioned into the chip holder on the microscope stage.

was carried out to visualise the flow three dimensionally. Finally, particles were injected into the device.

### 2.3.1 Flow visualisation of dye

Figure 2.10 shows top views of a green food colourant hydrodynamically focused into the prototype described in Section 2.2.2. On the top of the image, a picture of the device is illustrated, with the channels and the fluid inlets clearly visible. On the bottom of the figure, three zoom in views of the dye flowing into the device are shown, and their correspondent position along the channel is indicated. On the first image, just after the intersection with channel D, the sample is horizontally focused into a region of approximately  $60\mu\text{m}$ , 15% of the channel width for flow rates  $Q_A = 1\mu\text{l/min}$ ,  $Q_B = 3\mu\text{l/min}$ ,  $Q_D = 10\mu\text{l/min}$ , with  $\alpha_V = 0.33$ ,  $\alpha_H = 2$  and  $Re = 0.64$ . Downstream the main channel, the sample remains focused, but the width occupied by the food colourant increases both on the second and third image, up to 50% of the channel size reaching the outlet E, which can be recognised from the shadow of the nanopore on the last image. This high value is also due to the mismatch between the density of the tracer and that of water. This simple investigation demonstrates the ability of

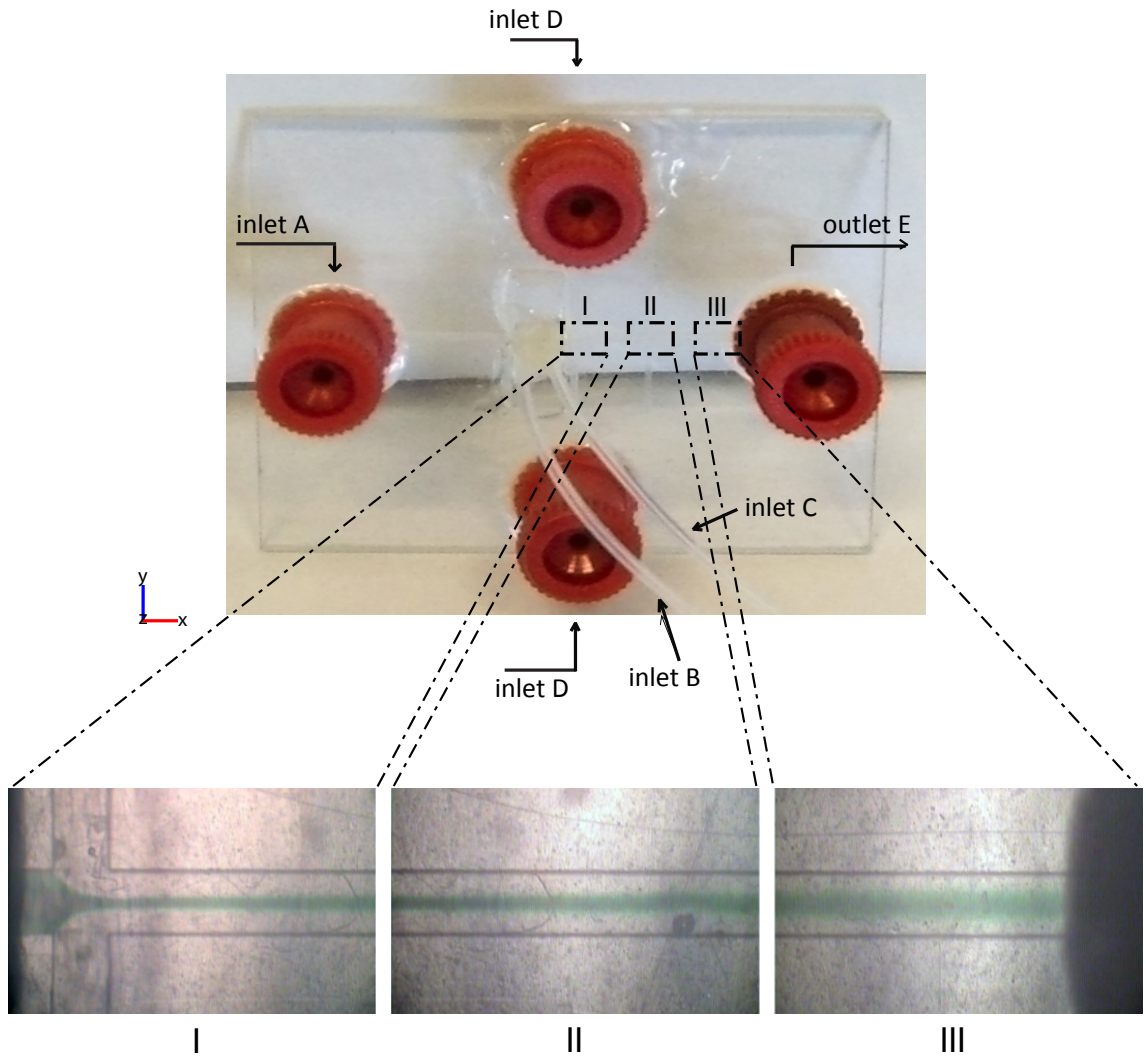


Figure 2.10: Top views of a food colourant 2D hydrodynamic focused into the prototype. A reference to the measurement position is given. Flow rates used:  $Q_A = 2\mu\text{l/min}$ ,  $Q_B = 5\mu\text{l/min}$ ,  $Q_D = 18\mu\text{l/min}$ , with  $\alpha_V = 0.4$ ,  $\alpha_H = 2$  and  $Re = 1.1$

the geometry to successfully focus the sample in 2D for a length of 20mm.

### 2.3.2 Confocal analysis

In order to visualise the 3D position of the sample into the prototype, a confocal experiment was carried out. Alexa Fluor 555, see Section 3.3.2 at a concentration of  $10\mu\text{M}$ , was injected into inlet B, whilst DI water was injected into any other inlets. Figure 2.11 represents the data extracted from the confocal result. Figure 2.11(a) depicts the 3D view of the dye, in red, at the intersection with channel D. A small amount of Alexa Fluor is

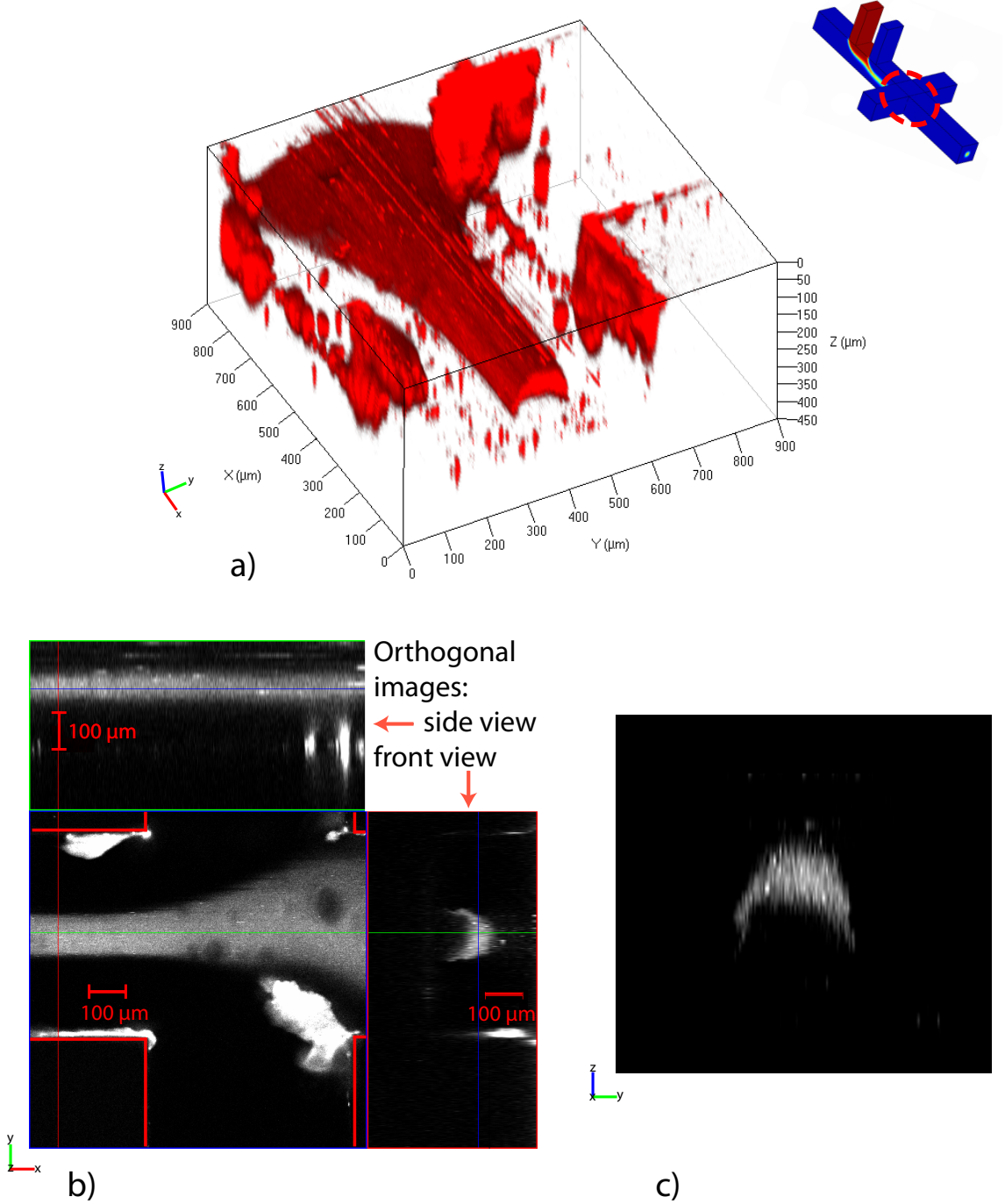


Figure 2.11: Confocal images of Alexa Fluor 555 three-dimensionally focused into the prototype at the intersection with channel D. a) 3D view; b) orthogonal image showing top, front and side views of the sample; c) magnification of the front view showing the 3D position of the sample into the channel. Flow rates  $Q_A = 5\mu\text{l/min}$ ,  $Q_B = 2\mu\text{l/min}$ ,  $Q_D = 20\mu\text{l/min}$ , with  $\alpha_V = 2.5$ ,  $\alpha_H = 1.6$  and  $\text{Re} = 1.3$

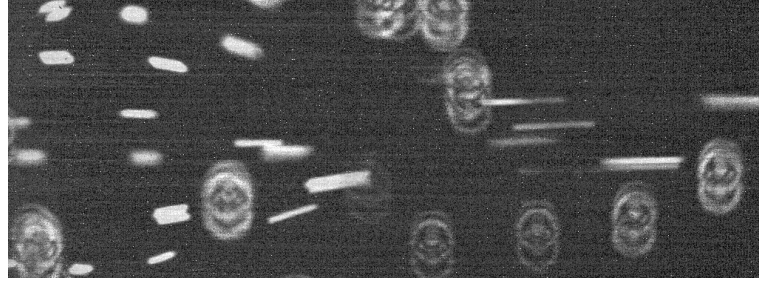


Figure 2.12: Particles injected into the prototype. A small horizontal focusing effect is observed. Particles attached to the bottom surface are also visible as out of focus circles.

attached to the wall (bottom right corner and left side) and this helps in positioning the flow with respect to the channels. A big clump of dye is also clearly visible on the top of the image. From this view, it is possible to visualise the bowed arrow shape of the sample. The orthogonal image, however, gives a better representation of the shape of the sample on the three dimensions. Figure 2.11(b), shows top, side and front views of the dye into the device. For the full visible length, the depth is constant at approximately  $74\mu\text{m}$ , 18% of the channel height (side view). From the top view it is possible to observe how the clump, stuck at the corner with channel D, is definitely effecting the flow, pushing the sample to the side. Despite this, after the intersection, the flow is still perfectly horizontally centered into the channel. Figure 2.11(c) is a rotated magnification of the front view. The dye presents a bowed shape on the bottom, which was also observed in a confocal result carried out on LSD, Section 5.2.3. Because the size of the Figure 2.11(c) is that of the channel, the sample is well centered and occupies an area of  $86\mu\text{m}$ , in the middle, and  $136\mu\text{m}$  on the side. This preliminary test confirmed the efficacy of the geometry to focus the flow in 3D.

### 2.3.3 Testing with particles

Polystyrene microspheres  $10\mu\text{m}$  sized, presented in Section 3.3.3, were injected into the inlet B at a flow rate  $Q_B = 2\mu\text{l/min}$ , with flow rates of the other inlets equal to  $Q_A = 5\mu\text{l/min}$  and  $Q_D = 24\mu\text{l/min}$ , with  $\alpha_V = 2.5$ ,  $\alpha_H = 2$  and  $\text{Re} = 1.55$ . Figure 2.12 shows the microbeads flowing from the left to the right side of the image and focused in the horizontal direction. At the intersection with channel D, right side of the image, particles appear streaking and

less bright, due to the increased velocity magnitude. Despite that before the main intersection particles occupy the full width of the channel, they are directed towards the centre. Because the prototype is sealed with an adhesive tape, microbeads can attach to this additional layer, and appear as out of focus circles in the picture. Once focused, the majority of the particles are constrained into a region equal to 20% of the channel dimension. Even though the microspheres are not sorted in single file, this experiment pointed out that this device can be used to focus particles.

After this set of preliminary tests, the final specimens were fabricated by photolithography on a more rigid material.

## 2.4 Selection of the materials

The rapid increase of engineering applications using biological cells had forced researchers to evaluate the “bio-compatibility” of materials used to fabricate microfluidic devices. Data on the toxicity of materials suitable for bio-fluidic applications are extremely limited, and standard tests are still to be defined [24, 40, 58]. A commonly used assay involves the effect of extracts of the material into the cell suspension [44]. A sample of the substance is immersed in the cell culture medium and the material is defined as “bio-compatible” when no decrease in cell viability is found. A more accurate definition for such materials should be “non-cytotoxic” [24], because no toxic compounds detach from the surface. However, this does not demonstrate its ability to kill cells placed directly on the surface. Even though 3D-HF reduces the contact between cells and device walls, it is important to select “bio-compatible” materials for the fabrication of the device.

Most of the previous 3D-HFMD were constructed from PDMS [8, 35, 51, 52, 62, 63, 76, 104, 117], which allows reproducibility at low cost and fabrication of channels of the same size of a human cell. Indeed, the rapid growth of biofluidic applications in the micro domain experienced in the last 10 years is due to the introduction of PDMS-based photolithographically fabricated devices [122]. However, PDMS deforms at high pressures, as experienced by Chang *et al.* [8] and the use of a more rigid material, such as glass, PMMA,

Table 2.1: PMMA physical properties

Properties	Unit	Value
Density	$\frac{kg}{m^3}$	1119
Water absorption ratio	%	0.3
Refractive index	—	1.49
Heat distortion temperature	$^{\circ}C$	99
Tensile strength	$MPa$	48-75
Transparency	—	clear
UV resistance	—	good
Fluorescence sensitivity (peak)	$nm$	inert

PC, silicon or metal, is suggested by many authors [4,8,64,122] and was pursued in this research thesis. The fabrication of the prototypes was performed using the facilities available in the workshop of the Stokes Institute. The biofluidic group of Stokes Institute commonly employs PMMA as a substrate for its low cost and physical properties, *e.g.* refractive index, transparency, inert to fluorescence, etc. PMMA is also bio-compatible, as reported by Ertel *et al.* [24], who had measured cell death on a PMMA surface using three different cell lines with a Trypan Blue exclusion assay. In their investigation, no toxic effect was experienced in cells seeded in serum-containing medium. It is important to underline that the use of a more rigid material, *i.e.* metal, leads to better fabrication tolerances and surface quality but lacks in transparency. Also machining on a glass substrate could improve the channel roughness. However, the selection of PMMA provided the most efficient fabrication method and channel quality, see Figure 2.3, for the resources available.

From these considerations, the prototypes of the 3D-HFMD manufactured by CNC milling were made using a single layer 2mm thick PMMA sheet (Engineering Steels Ltd., Ireland). Some of the most important physical properties of PMMA are summarised in Table 2.1.

The final specimens were composed of two layers, a base of PMMA and multiple depositions of SU-8 (Microchem Corporation). SU-8, an epoxy-based negative photoresist, has been utilised because it is photopatternable, mechanically reliable, bio-compatible and highly resistant to a wide variety of chemicals. Also, fabrication of nearly vertical side walls with an aspect ratios up to 25 has been demonstrated. SU-8 bio-compatibility has

been investigated by Hennemeyer *et al.* [40] and Kortzar *et al.* [58] showing cell proliferation for treated and untreated surfaces. SU-8 was shown to be non cytotoxic in either cases, with an increase of “bio-compatibility” if the surface was plasma activated. Furthermore SU-8 has excellent thermal stability and optically transparency, which is important for microscopy visualisations. SU-8 is sensitive to ultraviolet light with a maximum absorption wavelength of 365nm, thereby the spectra emission of fluorescent dyes has to be as far as possible from this value. SU-8 can also be diluted with other materials to modify its physical properties. Ruano *et al.* [102] have modified the fluorescence absorbance, while Helbo *et al.* [39] had changed its refractive index. Some of the most important physical properties of SU-8 are summarised in Table 2.2.

Table 2.2: SU-8 physical properties

Properties	Unit	Value
Density	$\frac{kg}{m^3}$	1120
Water absorption ratio	%	0.55
Refractive index	—	1.7
Glass transition temperature Tg	°C	200
Thermal conductivity	$\frac{W}{mK}$	0.2
Tensile strength	MPa	73
Fluorescence sensitivity (peak)	nm	365

## 2.5 Fabrication of the 3D-HMFD

The fabrication of the final specimens of the 3D-HFMD was carried out by microLIQUID s.l., Mondragón, Spain. Two devices with the same geometry were fabricated, a Small Scale Device and a Large Scale Device, called respectively “SSD” and “LSD” for the remainder of this research thesis. The size of the main channels was:  $W=100\mu m$ ,  $H=95\mu m$ ,  $L=50\mu m$  for SSD and  $W=400\mu m$ ,  $H=380\mu m$ ,  $L=200\mu m$  for LSD. The channel dimension on LSD is of the same order of magnitude of that of the prototypes manufactured by CNC milling. If 3D focusing will be reached on LSD, this demonstrates that 3D-HF focusing can be performed on a dimension achievable from cost effective CNC manufacturing. In this section, the appropriate fabrication program, which is the same for both SSD and LSD,

is only introduced. The detailed step by step fabrication process is described in Appendix B.

The 3D-HFMD was fabricated by SU-8 multilayer photolithography, using a technique described in details by Agirregabiria *et al.* [1] and Arroyo *et al.* [3]. This method has the advantage to photopattern the different layers before the bonding process, reducing fabrication costs and allowing repeatable volume reproduction. The fabrication process of the two 3D-HFMD consists of the reiteration of four steps:

1. substrates preparation.

In order to bond together different layers of SU-8, two substrates must be prepared: a bottom substrate on PMMA, and a temporary top substrate, Kapton on Pyrex. To reach a final thickness of few hundred microns two temporary top substrates were also required.

2. photolithography of two SU-8 layers.

Since the top and bottom substrates were prepared, two photolithography processes were carried out using photoplotter masks.

3. bonding of the two layers.

Once SU-8 was photopatterned on both substrates, top and bottom layers were placed into contact and bonded together in vacuum. After the bonding process the two SU-8 layers were irreversibly joined together.

4. final releasing step of the Kapton film.

The Pyrex layer was then removed by the use of a razor blade, and the Kapton film simply peeled off from the SU-8. Once the Kapton film was manually detached, the microfluidic inlets and outlets were open to the external world, which avoided drilling or etching procedures on the cover layer.

During the fabrication of the final specimens, a reference scale with a mark every 100 $\mu$ m was fabricated on the side of the main channel for a length of 14mm. A picture of the final chip, 25 x 15 mm in size, is shown in Figure 2.13.

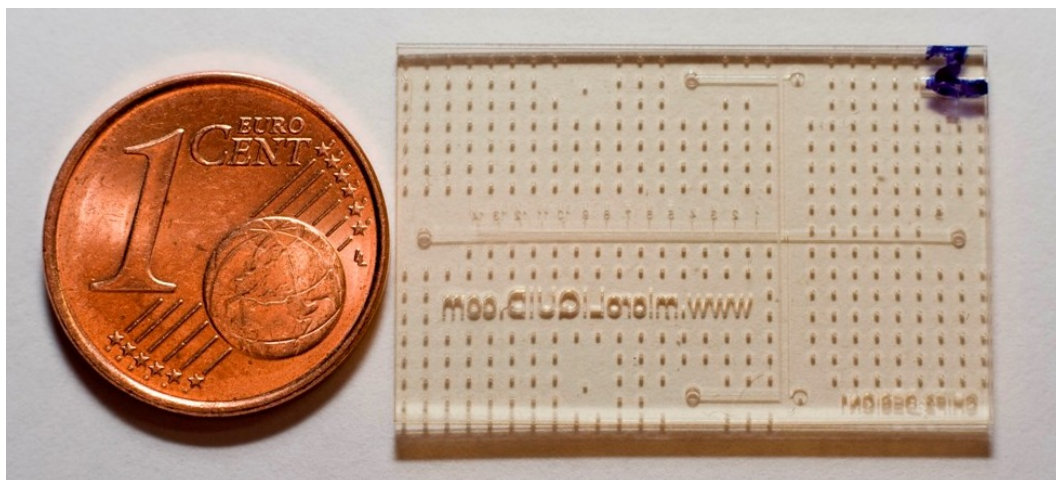


Figure 2.13: Image of the final chip. 1 cent coin is shown for scale.

## 2.6 Magnetic stirrer assembly

In this section, the concept and manufacture of a magnetic stirrer assembly is discussed. The stirrer assembly concept arose from initial experiments carried out injecting L-929 and B-lymphoid precursor cells stained with a fluorescent tag, Celltracker Green CMFDA, see Section 3.1.2, into a 0.15mm ID tubing (Upchurch Scientific, UK) immersed into an index matching fixture. Difficulty was experienced in dispensing a uniform distribution of biological cells into the microchannel. As stated by Kim *et al.* [54] culture media perfusion can be driven by gravity, external syringe pumps and on-chip peristaltic pumps. A Standard Infuse/Withdraw PHD 22/2000 syringe pump (Harvard Apparatus, UK) was employed during these experiments. Because the majority of the cells were sedimenting before leaving the syringe, the syringe pump was first placed vertically on a stand, to allow gravity push the sample through the syringe. However, all particles ended up being delivered within five minutes. Thus, a different approach was required. It was found that to prevent clumping and sedimentation, cells must be agitated throughout into the syringe.

In this research thesis, a mechanical method to prevent cell clumping and to deliver cells into a device at a constant rate without the concomitant introduction of additional substances into the cell suspension/preparation has been proposed. The concept is an extension of the commonly used laboratory benchtop magnetic stirrer used in conjunction with flasks and beakers [55]. A syringe pump is placed vertically over a stand which has a window

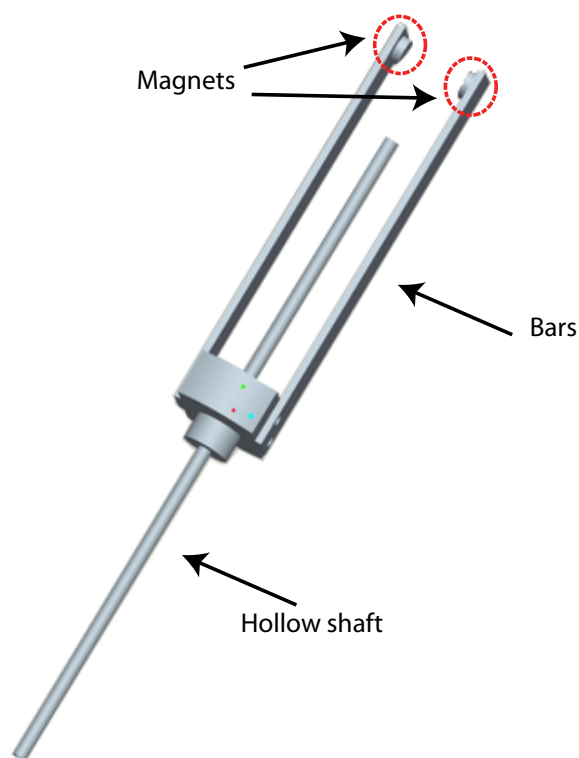


Figure 2.14: Schematic of Stirrer Apparatus to rotate the magnetic field.

aligned with the syringe lodgment, and a 2mm cylindrical magnetic bar (Fisher Scientific, Ireland) is placed in the standard syringe pump dispenser. The bar rotates through a rotating magnetic field using the apparatus illustrated in Figure 2.14. An electric motor, held by an arm, is used to provide the energy to spin the bar. The outlet of the syringe pump dispenser runs through the 15cm long central hollow shaft (Greenweld, UK) which turns about it. This causes the two magnets at the top of the apparatus to rotate, introducing a rotating magnetic field in the syringe pump dispenser. The stirrer inside the syringe pump dispenser then rotates, agitating the cell and media fluid mixture. Figure 2.15 shows the apparatus connected to a syringe pump, placed vertically on a stand, with a motor rotating the spinner. Figure 2.15(a) is a photograph taken of the device in operation, evident from the blurring of the spinner and magnetic bar caused by their rotation. Cells are kept in motion while the syringe pushes the flow into the tubing, avoiding aggregations and maintaining a uniform distribution of cells per unit of time. In Appendix C a video recording of the stirrer in action is available. Video I shows the stirrer while rotating and therefore keeping cells in motion into the syringe.

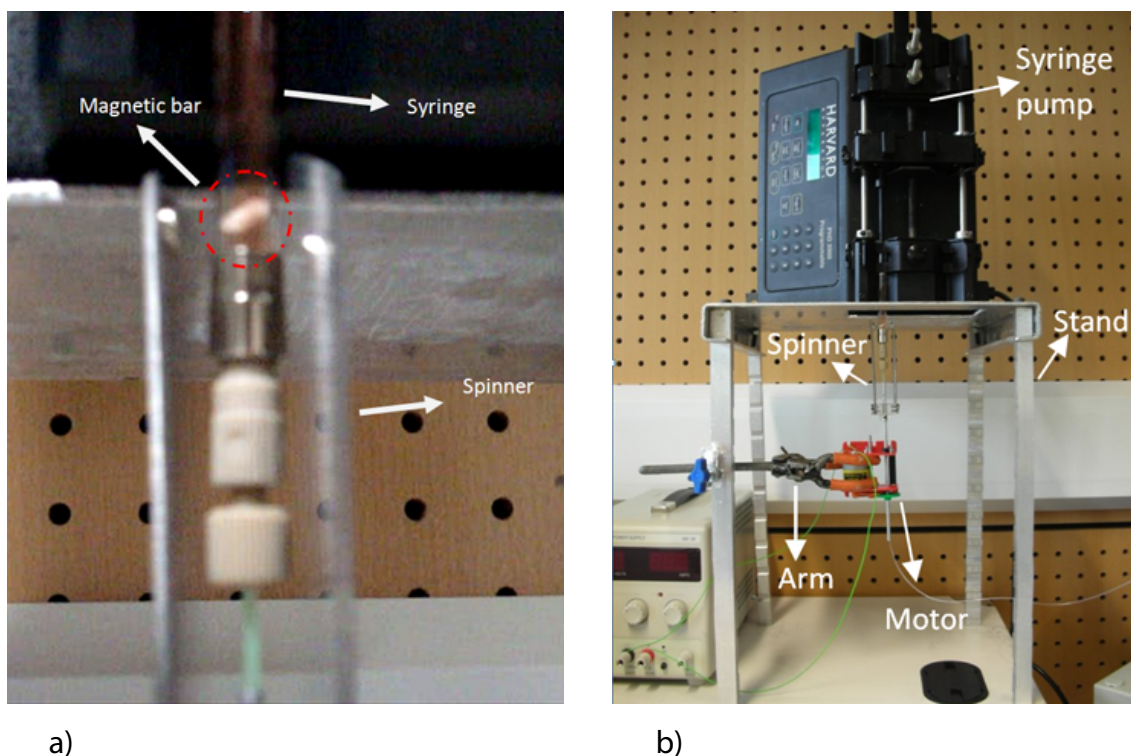


Figure 2.15: a) Close up of the magnetic bar rotating. b) Magnetic stirrer assembly connected to a syringe pump dispenser.

Having imaged the cells successfully using a fluorescent tag, it was noted that the images could be utilised to perform an accurate count of the cell population being dispensed. Incorporating CMOS camera technology to acquire the images and a Matlab algorithm to process them to detect and quantify the intensity peaks associated with the tagged cells, a cell count was carried out and compared with the Trypan Blue exclusion assay. Results performed with the magnetic stirrer assembly and the optical counting technique are presented in Chapter 6. This device has been used during cells and particles experiments throughout this thesis.

## **2.7 Summary**

This chapter outlined the conception of the two prototypes manufacture at Stokes Institute, the material selection and the fabrication technique of the 3D-HFMD. Next section will present the biological protocols, methods and experimental set ups utilised during this research thesis.

## **Chapter 3**

# **Biological Protocols, Methods and Experimentation**

In this chapter, details of the biological protocols, methods and experimental apparatus utilised during this work are presented. In the first part, the cell culture methods, the cell lines and the staining protocols adopted with the optical counting technique of Chapter 6 are examined in detail. After this, the experimental apparatus used within this research thesis are described. Because one of the the primary aims of this thesis is to validate the design of the 3D-HFMD, a number of experimental methods were employed. The flow visualisation technique was used in two variants: the ability of the proposed device to focus in the horizontal direction was investigated using dyed stream injections, the ability to focus particles in single file was investigated using selective seeding by microbeads. After validation of the 2D focusing, confocal microscopy experiments and computational fluid dynamic simulations were carried out and compared to establish the feasibility of the 3D hydrodynamic focusing. Each of the experimental techniques and methods considered are discussed in turn, firstly by considering a brief description of the technique, then by a description of the experimental apparatus used during testing.

## 3.1 Biological protocols

This section presents the cell culture techniques carried out during this work. All biological protocols were performed within the biological laboratory at the Stokes Institute. A more detailed description of the experiments performed with cells is explained in Chapter 6. A list of the cell dyes, chemicals and equipments used in this research thesis is detailed in Appendix A.

### 3.1.1 Cell culture

Since the beginning of the 19th century, researchers [7, 38] have been culturing cells in laboratories, or *in vitro*, in order to have a vast number of cells easily available for research purposes, without having to withdraw samples from an organism each time. Nowadays, most cell lines are sourced from cell culture banks, where cells originated from the first subculture of a primary culture, *i.e.* cell isolated directly from a tissue sample, are stored. Cells retrieved from the cell bank are then subcultured in the laboratory, also known as passaging or splitting, by transferring a small number of cells into a new vessel in a large volume of fresh medium and then grown at an appropriate temperature and gas mixture in a cell incubator. The major advantage of culturing *in vitro* is the consistency and reproducibility of results that can be obtained from using a batch of cells derived from a single parental cell, yielding a homogeneous genetically identical population. Cells cultured *in vitro*, either suspension or adherent cultures, are maintained in the growth medium, which contains all the nutrients required by the cell type of interest. Cell culture media may differ in pH, glucose concentration, growth factors, and the presence of other constituents. The growth factors used to supplement medium are often derived from animal blood, such as calf serum. Biological protocols and culturing techniques are described in detail by Freshney [27].

All cell culture techniques were carried out in a biological class II safety laminar flow hood, depicted in Figure 3.1. The cell culture medium, sterile pipettes, pipette controller and a T-175cm<sup>2</sup> culture flask used are indicated. Any item brought into the hood was first

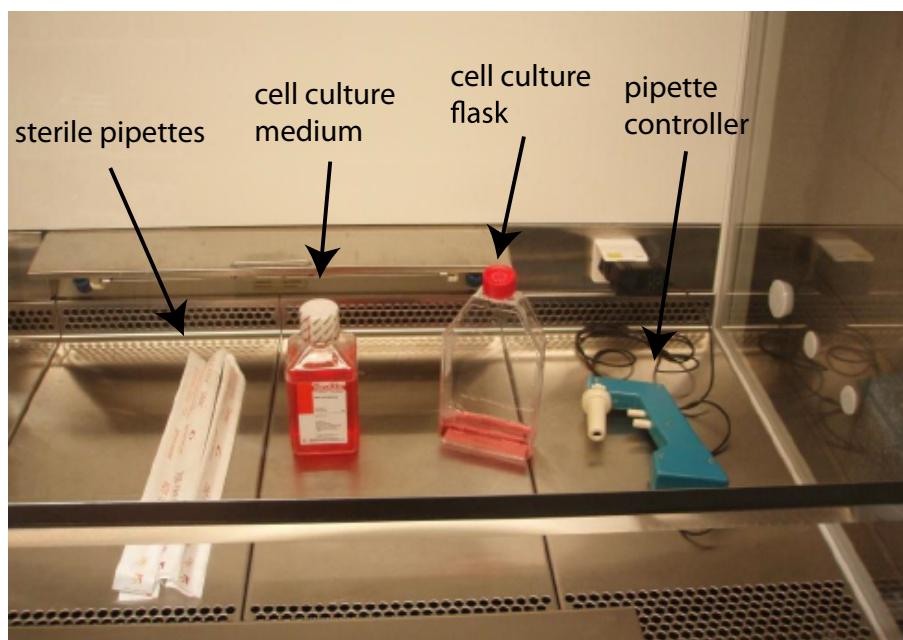


Figure 3.1: Cell culturing set up in the laminar flow hood.

sterilised by spraying with a 70% mixture of ethanol and DI water. The laminar flow hood was turned on 15 minutes before use, in order to purify the air. Also, before and after use, the UV light was also turned on into the hood to avoid any possible contamination.

The growth of cells *in vitro* follows a well known standard pattern, depicted in Figure 3.2. First, immediately after seeding, cells adapt to the new environment and enter into a lag phase of growth. After this, there is a period of exponential increase in cell number, called the log phase, due to the ample availability of nutrients. At the top of the log phase, when either the cell density (cells/cm<sup>2</sup> substrate) or the cell concentration (cell/ml medium) reaches the maximum level, cell growth is reduced and eventually stops. Therefore, a cell line must be subcultured before reaches its maximum saturation density, *i.e.* during the log phase of growth, otherwise it will die. Once cells are subcultured, the cell passage number increases and is recorded in a logbook. After a certain number of passages, cell characteristics can mutate and may become quite different from those found in the starting population. For this reason, it is important to perform experiments with cells at a low passage number. Accordingly, all experiments were carried out using cells below passage 12, as suggested by Freshney [27].

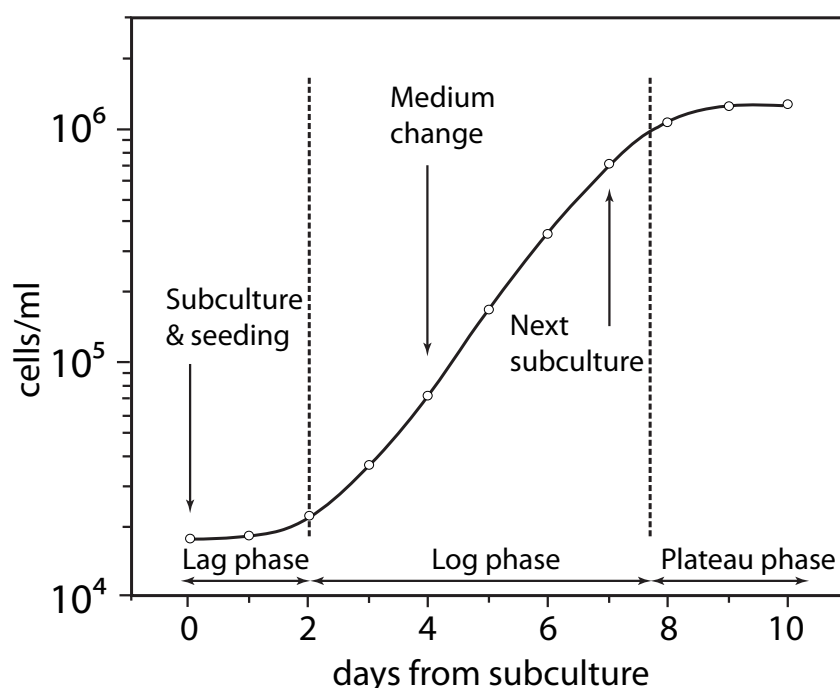


Figure 3.2: A characteristic cell growth curve. Time between subcultures might vary for different cell lines. Adapted from Freshney [27]

In subculturing new cell lines, care should be taken so that the cells are not diluted below their minimum density, defined by the specification sheet provided by the supplier. If seeding density is too low, cells will enter the lag phase of growth and the culture may exhibit extremely slow growth and possibly die. Daily monitoring and cell count is required when handling newly cultured cell lines. Cell cultures were routinely cultivated following the procedure outlined in cell culture techniques handbook (ECACC, 2005) [22]. On a daily basis, cells were examined under the microscope to monitor growth rate and viability. A cell count was performed, and the cells were subcultured if confluent, *i.e.* cells covering approximately 70% of the flask surface. Subculturing was performed by transferring a small proportion of cell culture, usually 5ml, into a new flask containing approximately 50ml of fresh prewarmed medium. The flask was then placed back in the incubator, allowing cells to enter again the log phase of growth. Cell lines, medium and growing conditions used during this work are described in the next section.

### Cell line selection

One of the main objectives of this research thesis is to study cancer cells, and in this research study, leukaemia cells in the microscale. Most previous researchers have used Red Blood Cells (RBCs) to validate the use of microdevices for hydrodynamic focusing [14, 63, 68, 129], or cell sorting [16, 127]. RBCs are designed to bend and get through micro-channels *in vivo*, *i.e.* capillaries, under conditions that regular cells would not survive. Testing micro-channels using RBCs is not a rigorous test as they are probably the most robust cell type to use in this way. In contrast Leukaemia cells are more representative of suspension cell lines and a cancer cell line and so the results obtained from same are more applicable in both the global sense and in relation to the particular focus of this thesis.

Leukaemia is a disease affecting white blood cells, which *in vivo* simply flow suspended in the blood. Therefore, *in vitro*, white blood cells grow in a suspension of cell nutrients with no need to anchor to a substrate. Suspension cell lines are easily passaged by diluting a small amount of culture containing a few cells into fresh medium. The leukaemic cells selected for use with the optical counting technique described in Chapter 6 was a REH cell line, human B-cell precursor leukaemia. Cells were routinely incubated at 37°C and 5%  $CO_2$  in RPMI-1640 medium, developed by Moore and Woods [83], supplemented with 10% foetal calf serum. They were subcultured twice weekly, since their doubling time is 50-70 hours, as depicted in Table 3.1. The standard medium for human leukaemia cell lines is RPMI-1640 medium. The media also contains phenol red which is used as a pH indicator, providing an additional information for the right timing for subculturing cells. The size of B-cells was investigated by Loiko *et al.* [72] using a specialised light microscopy method, who found an average value of 7.98 $\mu$ m from a population of 4,500 B-cells, as described and verified in Section 6.3.

In order to demonstrate the capacity of the stirrer, described in Section 2.6, to deliver a consistent distribution of a number of cell types, different cell lines were considered. With this in mind, a representative adherent endothelial cell line, L-929 mouse connective tissue fibroblast, was selected. REH and L-929 cell lines are robust and amenable to handling and

Table 3.1: Cell culture data of REH and L-929 cell lines. Source: DSMZ (2009)

	REH	L-929
morphology	small, round, single cells in suspension	adherent fibroblasts
doubling time	ca. 50-70 hours	ca. 21-24 hours
harvest	maximum density at ca. $3\text{-}5 \times 10^6$ cells/ml	ca. $4\text{-}8 \times 10^6$ cells/ $25\text{cm}^2$
medium	88% RPMI 1640 + 10% FBS + 1% PS + 1% LG	88% HEPES 199 + 10% FBS + 1% PS + 1% LG
incubation	at 37 °C with 5% $\text{CO}_2$	at 37 °C with 5% $\text{CO}_2$

are representative of adherent and suspension cells lines used by researchers. The main characteristics of the two cell types are summarised in Table 3.1.

Adherent cells, usually derived from mammalian solid tissues, require a rigid surface to attach, such as plastic flasks, Petri dish or microcarriers, which may be coated with extra-cellular matrix components to increase adhesion properties. Subculture is performed first by detaching cells from the growing surface, commonly done with a mixture of Trypsin-EDTA. Cells are subsequently washed with Dulbecco's Phosphate Buffered Saline (DPBS), which is a balanced salt solution used for the handling and culturing of mammalian cells. DPBS is used to irrigate, wash, and dilute mammalian cells whilst maintaining the pH in the physiological range. DPBS also facilitates cell binding and clumping. The use of Trypsin-EDTA makes cell maintenance both slower and more traumatic for adherent cell lines. L-929 cells were incubated at 37°C and 5%  $\text{CO}_2$  in 199 Modified HEPES medium, developed by Morgan *et al.* [85]. Each cell line has a specific doubling time which effects the time between consecutive subcultures. Average doubling time for L-929 cells is shorter than that of REH cell, 21-24 hours, therefore L-929 cells had to be subcultured more often.

Both RPMI-1640 and 199 HEPES modified medium were supplemented with 10% fetal bovine serum (FBS), 1% 200mM L-glutamine and 1% 1mM penicillin-streptomycin. Serum is an important component of the medium since it contains growth and adhesion factors to promote cell proliferation and attachment to the flask surface. L-glutamine is used to compensate the lack of amino acids, required for cell growth, and penicillin-streptomycin is used as a source for antibiotics, essential in the medium to inhibit growth of bacterial.

REH and L-929 batches were sourced from the Deutsche Sammlung von Mikroorganismen und Zellkulturen GmbH, DSMZ, the German resource centre for biological material. The specification sheet for both cell lines can be found online on the DSMZ website [20]. All information about organic components, media, serum, L-glutamine and penicillin-streptomycin are acquired from the Sigma Aldrich website [109]. A detailed description of the chemicals used during this study can be found in Appendix A.

### 3.1.2 Cell staining

The optical counting technique presented in Chapter 6 is based on a measure of the fluorescent intensity from leukaemic cells. Prior to testing, REH cells were stained with a fluorescent probe, Celltracker Green CMFDA dye, supplied by Invitrogen (Ireland). This particular dye was chosen because it is inherited by daughter cells after cell fusion and is not transferred to adjacent cells in a population. CMFDA is also colorless and nonfluorescent until the acetate groups are cleaved by intracellular esterases [50]. In other words, only living cells emit a fluorescent signal resulting in minimal background noise. Once inside the cell, the probe reacts with intracellular components to produce cells that are both fluorescent and viable for at least 24 hours after loading. The reagent of CMFDA is the green-fluorescent chloromethyl derivatives of fluorescein diacetate, which excites at a peak wavelength of 492nm (blue-green) and emits at a peak wavelength of 517nm (green), as depicted in Figure 3.3.

REH cells were stained with the sequence of steps described below, following the procedure suggested by the product information sheet provided by the supplier [50].

1. First, the CellTracker, in a lyophilised form, was dissolved in  $\geq 99.7\%$  pure, sterile-filtered DMSO (Sigma-Aldrich, Ireland), to a final concentration of 10mM. Single use aliquots were stored at  $-20^{\circ}\text{C}$ , desiccated and protected from light. At the suggested conditions, the prepared stock solutions were stable for at least 6 months. Before use, the stock solution was diluted in serum-free medium to a final working concentration of 5 $\mu\text{M}$ , determined by standard curve depicted in Figure 3.4.

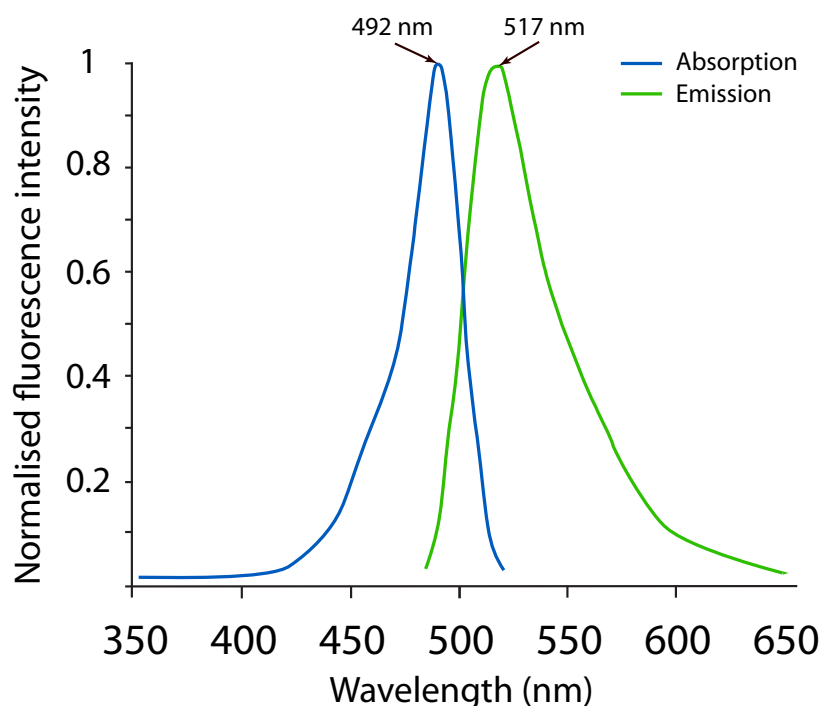


Figure 3.3: Fluorescent excitation and emission spectra of 5-chloromethylfluorescein, reagent of CMFDA. Adapted from [50]

2. REH cells were withdrawn from the incubator and centrifuged at 700 rpm for 8 minutes at 4°C to isolate the cell pellet and aspirate the supernatant which contains the cell culture medium.
3. Cells were subsequently resuspended in prewarmed working solution containing dye and incubated for 45 min at 37°C and 5%  $CO_2$ .
4. A second centrifuging was carried out at 700 rpm for 8 minutes at 4°C to remove the dye working solution.
5. Cells were again resuspended in fresh, prewarmed, culture medium and incubated for another 30 min. During this time, the chloromethyl and acetate groups of the dye either undergo modification or are secreted from the cell.
6. REH are now fluorescing and ready for testing.

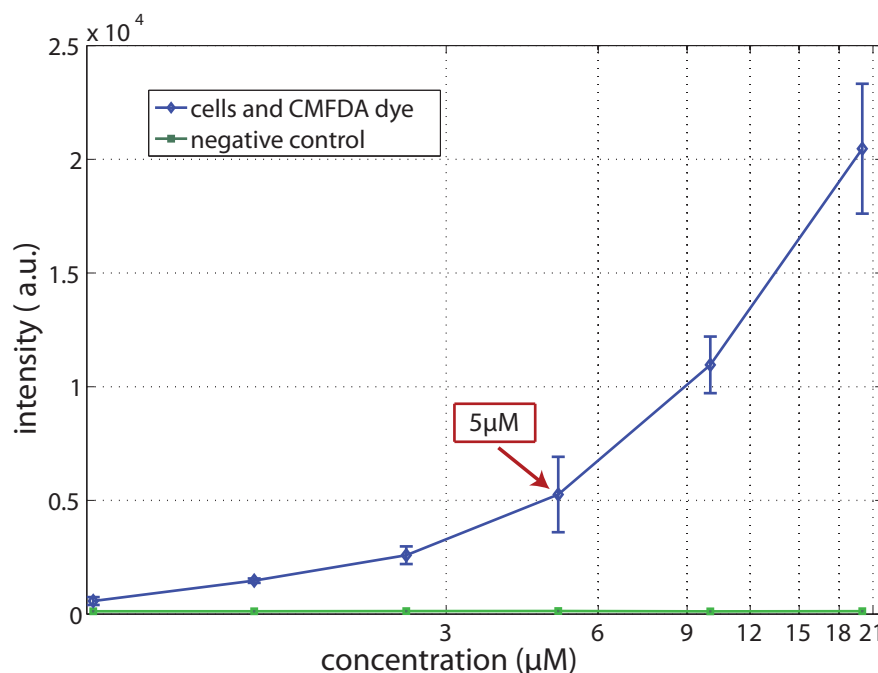


Figure 3.4: Standard curve of the CellTracker CMFDA with REH cells. Note that  $x$  values are on a logarithmic scale. Values on the  $y$  axis are arbitrary units.

### Dye concentration

The final working concentration of the CellTracker CMFDA was obtained from the standard curve of the dye calculated using a Tecan spectrophotometer GENios™ 96-well plate reader, in tandem with the dedicated software Magellan. Standard curves are used in biology to determine the concentration of substances, such as proteins, DNA or dyes, by measuring the response, usually fluorescence, optical density, luminescence or absorbance, at various known concentrations. The product information sheet of CMFDA [50] suggested ranges of working concentration equal to 5-25μM for long-term staining (up to about three days) and 0.5-5μM for short time experiments. Serial dilutions of the dye were performed to find out the best trade-off between higher concentration, more fluorescent intensity, and lower concentration, less dye consumption. Furthermore, the concentration should be maintained as low as possible in order to retain normal cellular physiology and activity. Triplicate measurements were tested for the following range of concentrations: 0.6, 1.25, 2.5, 5, 10, 20μM. The fluorescent intensity of the dye was then measured and plotted over the range of concentrations on a logarithmic scale, as depicted in Figure 3.4.

The first column of a 96-well plate, already containing a pellet of REH cells left from a 100 $\mu$ l culture previously centrifuged, was filled with 100 $\mu$ l of CellTracker CMFDA at a concentration of 40 $\mu$ M in order to reach a final volume of 200 $\mu$ l at 20 $\mu$ M. Serial dilutions were performed on the rows of the triplicate samples in order to achieve the desired concentrations. The solution containing cells and dye was then prepared following the protocol described in Section 3.1.2 and a fluorescence intensity test was carried out in the 96-well plate reader. An equal volume of cells without dye was used as a negative control. The results obtained are shown in Figure 3.4. The negative control confirms negligible intensity values, while the solution of cells and dye presents an exponential trend increasing with the concentration. The best compromise was found at 5 $\mu$ M, which shows more than 25% of the maximum relative intensity and allowing four times the number of aliquots. REH cells stained at 5 $\mu$ M were also fluorescing for one to two days.

### **3.2 Cell counting: Trypan Blue exclusion assay**

In cell culture, cell quantification is executed on a daily basis and for a number of different reasons. Firstly, a cell count is routinely performed to estimate if the cells are nearing their maximum saturation density and hence need to be subcultured, as outlined in Section 3.1.1. Secondly, an estimate of the cell number is required prior to freezing the cells. This is done in order that, upon recovery, cells are above the maximum seeding density ensuring successful initiation of the cell culture again. Finally, a cell count is conducted to ensure that there is an adequate number of cells present in the sample during testing.

The standard method for cell quantification is the Trypan Blue exclusion assay, which involves the use of a haemocytometer and Trypan blue solution. A haemocytometer is a thick glass microscope slide with a rectangular grid engraved on its surface. The number of cells present in the culture flask can be estimated from the count of the number of cells in the grid. An image and a close up view of the haemocytometer counting grid is shown in Figure 3.5. As observed in the image, the main divisions separate the grid into 9 large squares and each square has a surface area of one square mm.

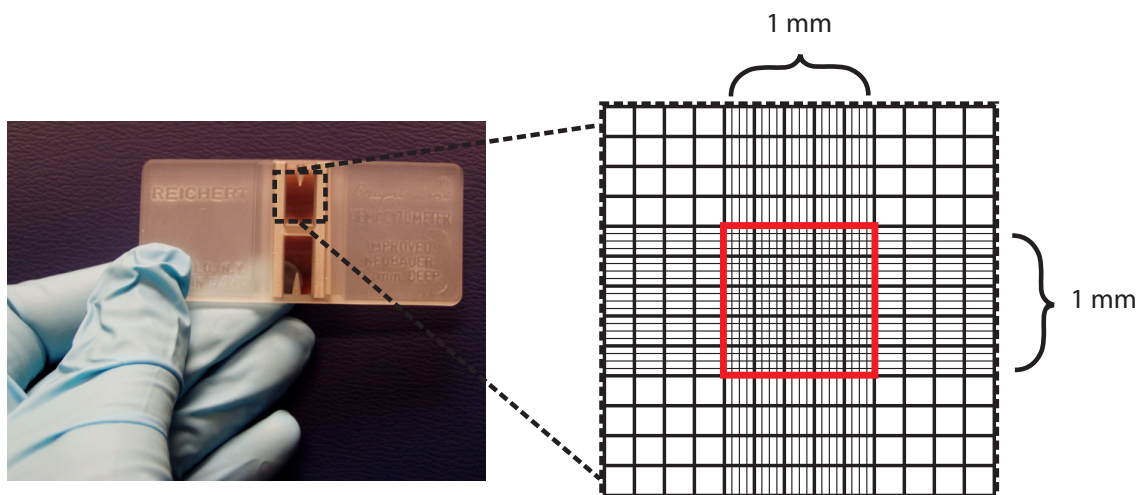


Figure 3.5: On the left of this figure an image of a haemocytometer is shown. A close up view of the counting grid is indicated. In red, the central 25 squares ( $1\text{mm}^2$  area) area used for counting the cells is illustrated.

The Trypan Blue exclusion assay protocol is outlined in the ECACC cell culture handbook [22]. Briefly, the protocol is described. Prior to use, the haemocytometer and the cover slide are cleaned with a 70% mixture of ethanol and DI water. Once dry, the moist glass cover slide is slid over the chambers, back and forth until the Newton's refraction rings appear. This ensures that the cover slide remains in position and an accurate cell count can be obtained. Coverslips for counting chambers must be heavy enough to overcome the surface tension of a drop of liquid. Cell suspensions should be dilute enough so that the cells do not overlap each other on the grid, and should be uniformly distributed. To ensure an accurate cell count, a pipette is used to break up any clumps that may be present in the cell suspension. Following this, 10ml of cell suspension are transferred from the culture flask to a 125ml sterile polypropylene container and again the cell suspension is vigorously mixed using a pipette or a vortex. Using a micro pipette,  $20\mu\text{l}$  of the cell suspension is removed from the container and placed in a sterile tube. An equal amount of Trypan blue solution is added and then mixed by pipetting, giving a dilution factor equal to 2. The molecular weight of Trypan blue excludes it from crossing the membrane of healthy living cells, therefore these viable cells appear bright when examined. On the other hand, due to their disrupted cell wall, dead cells in the culture will take up the stain and therefore appear blue under the microscope.

Using a pipette, 10 $\mu$ l of the Trypan blue cell suspension is placed into each V-shaped well of the clean haemocytometer. Capillary action draws the cell solution under the cover slip and fills the chambers. The haemocytometer is then positioned on the microscope stage and the central 25 squares (1mm<sup>2</sup> area) counting grid is brought into focus and viewed under a light microscope using x10 magnification. The number of viable (bright cells) and non viable cells (blue stained) are counted in the 1mm<sup>2</sup> area, in each chamber and then averaged. For a statistically significant count, the total count in each chamber should be 100 cells per square or so.

The concentration of viable cells  $C$ , in cells/ml, can be calculated from eq.3.1:

$$C = N_V \times D_F \times C_F \quad (3.1)$$

where  $N_V$  is the average number of viable cells counted in the red square of Figure 3.5,  $D_F$  is the dilution factor based on the volume of Trypan blue added, usually 2, and  $C_F$  is the correction factor which takes into account the depth and area of the chamber viewed.  $C_F$  can be calculated as follows: the chamber depth is 0.1mm, so when the cells are counted in the central 25 squares (each of area 0.04mm<sup>2</sup>), this yields a total volume of 0.04 x 0.1 x 25 = 0.1mm<sup>3</sup> or 10<sup>-4</sup>ml. Therefore, the correction factor  $C_F$  is 10<sup>4</sup>. To obtain the total number of viable cells in the flask,  $C$  is multiplied by the volume of media in the flask.

On the other hand, the concentration of non-viable cells  $C_N$ , in cells/ml, can be calculated using the following equation:

$$C_N = N_N \times D_F \times C_F \quad (3.2)$$

where  $N_N$  is the average number of non-viable cells counted in the red square of Figure 3.5. Accordingly,  $N_V + N_N$  gives the total number of cells. The percentage viability,  $P$ , is given by eq. 3.3:

$$P = \frac{N_V \times 100}{N_V + N_N} \quad (3.3)$$

### 3.3 Flow visualisation

The flow visualisation experiments served the following purposes:

- to predict the horizontal focusing effect into the microdevice.
- to investigate the design ability to focus particles/cells in single file.

A fluorescent dye, described in section 3.3.2, was used to study the diffusion on along the y axis for the 2D focusing. Microbeads, presented in section 3.3.3, were employed to validate the ability to focus in single file. It is important to underline that the diffusion coefficient of the fluid tracer is in the order of  $10^{-9}$ - $10^{-10}$  m<sup>2</sup>/s, while that of cells or particles of 10µm in size, calculated from the Stokes-Einstein equation, eq. 4.4, is around  $10^{-14}$  m<sup>2</sup>/s. The analysis of the dye diffusion, as a result, is a conservative estimation of the cells/particles behavior.

Flow visualisation is a widely used scientific tool for understanding fluid mechanics phenomena. The different variants of the technique, described in details by Smits and Lim [113], involve the injection of dyes, particles or smoke into the fluid flow and the examination of their motion with a camera or naked eye. Due to its simplicity, it was the first technique employed by researchers to analyse diffusion of species, fluid velocities and boundary layers. In recent years, the method has become a standard criteria in the preliminary investigation of the efficiency of 2D-HF microfluidic devices [57, 60, 61, 124]. The horizontal, or in-plane, focusing effect can be simply evaluated from the diffusion of the sample along the length of the channel. In micro-flow cytometers or cell sorters, the diffusion of the sample is a fundamental aspect of the device operation. In a given amount of time, dyes, cells or particles are affected by diffusion along the concentration gradient, and by convection which carries the molecules along with the fluid. The ratio between convection and diffusion is given by the Péclet number,  $Pe$ , a non-dimensional parameter that determines the relative contribution of the two phenomena. The Péclet number is defined by the product of the Reynolds number and the Schmidt number, formulated in eq. 3.4.

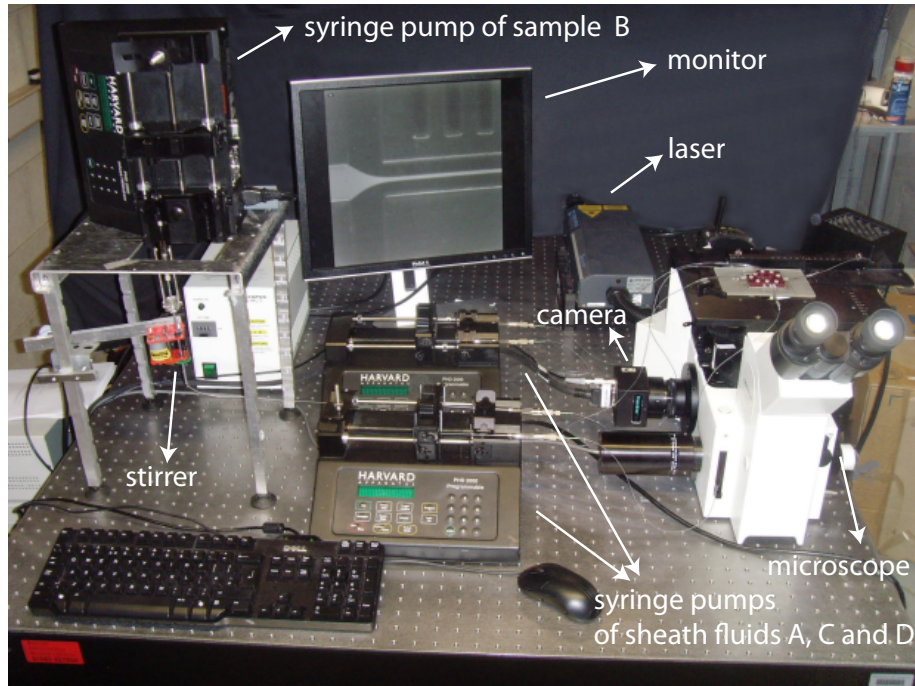


Figure 3.6: Photograph of experimental set-up used for flow visualisation experiments.

$$Pe = Re \times Sch = \frac{UL}{D} \quad (3.4)$$

where  $U$  is the main velocity of the fluid,  $L$  the characteristic length and  $D$  the diffusion coefficient, described in Section ???. The Reynolds number,  $Re = \rho LU/\mu$ , is a dimensionless parameter that gives a measure of the ratio of inertial forces to viscous forces.  $Re$  is used to determine the nature of a flow, whether it is laminar, transitional or turbulent. All experiments carried out within this work were performed at a  $Re$  number below 30, in laminar regime. The Schmidt number,  $Sch = \mu/\rho D$ , however, defines the ratio of viscous momentum diffusivity to mass diffusivity. A high Péclet number means that convection prevails whereas low values indicate that diffusive mixing will be dominant. For liquid-liquid diffusion, where  $D$  is approximately  $10^{-9} \text{ m}^2/\text{s}$ ,  $Pe$  is on the order of  $10^4$ . This high value suggests that mass diffusion should be negligible in the micro-scale experiments of this research thesis and the dominant mixing mode will be by convective mixing.

### 3.3.1 Flow visualisation setup

Flow visualisation tests were implemented with the experimental instrumentation depicted in Figure 3.6. The specimens tested, whose design is detailed in Chapter 2, were inserted into the chip holder and placed on the top of the microscope stage, described below. Microfluidic interconnections (Upchurch Scientific, UK) were used to connect all fluid ports, five inlets and one outlet, to the external PFA micro medical tubing, 380 $\mu$ m ID x 800 $\mu$ m OD (Scientific Commodities Inc., USA). All fluid streams were injected using 1ml GASTIGHT glass syringes (Hamilton, USA) in order to minimise flow disturbances caused by plastic or larger syringes. Waste from the outlet E was then collected into a beaker. Three Standard Infuse/Withdraw PHD 22/2000 syringe pumps (Harvard Apparatus, UK) were required for reaching a fully 3D-HF. Previous work at the Stokes Institute [123] estimated the accuracy of the pumps for flow rates in the range of microliters per minutes. The actual volume displaced was compared with that reported on the pump display and the two values were found to agree to within 0.4%. In preliminary tests using particles the sample settled at the bottom of the syringe and considerable difficulty was experienced in dispensing the particles at a constant rate. Moreover, aggregation of particles, but also of cells as shown in Chapter 6, was a regular issue. In order to overcome these problems, the syringe pump used for the sample fluid B was placed vertically on a stand, to allow gravity push the sample through the syringe. However, all particles ended up being delivered within five minutes. A stirrer dispenser assembly, described in details in section 2.6, was therefore used to avoid particles/cells aggregation and to inject a uniform number of particles/cells per unit of time. The results on the efficacy of the stirrer with biological cells are presented in Chapter 6.

All equipments used in this study are described below. The set up was mounted on an high performance laminar flow isolator, I-2000 Series (Newport, USA), to minimise vibration and interference with the flow fields. An Olympus IX50 inverted stage microscope, equipped with fluorescent attachments and a camera side-port, was used to image the microfluidic flows within the device. An inverted stage microscope presents two main advantages:

1. it gives no limitation to the size and shape of the test pieces.
2. it allows microfluidic connections, tubing and detector to be placed anywhere on the side of the device.

Two different fluorescence filter cubes were mounted in the microscope. The Olympus U-MWG2 was composed of three filters: a band-pass (excitation) filter that transmits green light in the range 510-550nm, a dichromatic mirror that reflects below 570nm and transmits above 570nm and a barrier (emission) filter that transmits above orange light from 590nm. The Olympus U-MWIB2 was composed of a band-pass (excitation) filter that transmits blue light in the range 460-490nm, a dichromatic mirror that reflects below 500nm and transmits above 500nm and a barrier (emission) filter that transmits above green light from 520nm. The dye and particles described respectively in Section 3.3.2 and Section 3.3.3 were selected to match the above wavelengths.

Two cameras were used, a MV-D1024E-160-CL-12 CMOS camera (Photonfocus, Switzerland) and a TSI POWERVIEW™ Plus 11MP CCD camera (TSI Incorporated, USA). The CMOS camera was selected due to its linear-logarithmic response curve which allows recording extremely high contrast images at a high frame rate, up to 150 Hz. The sensor characteristic presents both advantages of CCD and CMOS sensors: linear response at low intensities and logarithmic compression for high intensities, reducing the risk of pixel saturation. The camera has a 1" monochrome CMOS image sensor and provides a high dynamic range of up to 120 dB. The maximum resolution is 1024 x 1024 pixels with pixel size of 10.6 x 10.6  $\mu\text{m}$ . The CCD camera was selected for its high resolution, 4008 x 2672 pixels with a pixel size of 7.4 x 7.4  $\mu\text{m}$ , ideal for global flow measurements. The camera provides a 12-bit output with 50% quantum efficiency and 340-900 nm spectral range. However, it only works at 15 frames per second. Both cameras were connected to the PC with a CameraLink cable.

The illumination sources used throughout this work were a mercury burner and double pulsed Nd:YAG lasers. The 100W mercury burner, a continuous illumination source emitting light across a bandwidth of 250-600nm, was employed for dye experiments and with particle experiments at long exposure. The 50mJ laser, running at 532nm with pulse

duration of 6ns and frequency of 15Hz, was utilised to acquire the stroboscopic images of Chapter 5 and the PIV experiments of Section 5.5.1. Recorded images were acquired using the software IC Capture 2.0 and saved in a PC.

An existing PIV system was integrated with the microscope described above to complete a  $\mu$ PIV system and record the images of microscale flows depicted in Section 5.5.1. The measurement apparatus used in this study consisted of the Insight 3G processor and the TSI laser pulse synchroniser (Model 610035), combined with a timing function in the software program to ensure the correct synchronised timing of the laser pulses and the camera exposures. TSI's Insight 3G software program was used for the computational analyses of the particle displacements between the image pairs and the corresponding velocity vector field generation. The software also controlled the laser and camera synchronisation and enabled post processing of the image pairs.

A schematic of the experimental facility employed for flow visualisation studies is shown in Fig 3.7. The next two subsections describe the dye and the particles used within this research thesis.

### 3.3.2 Selection of the dye

A commercially available fluorescent dye, dextran-conjugated Alexa Fluor 555, supplied by Invitrogen (Ireland) was employed as a tracing fluid for both the flow visualisation tests and the confocal experiments described in Section 3.4. Dextran-hydrophilic polysaccharides have a good water solubility, low toxicity and are relatively inert, as stated in the product information sheet [49]. Once conjugated with the Alexa Fluor series, which is brighter and more stable than standard dyes [92], *e.g.* fluorescein or rhodamine, dextrans are suitable water-soluble carriers for fluid tracers. Fluorescent dextrans have also been used in blood flow studies by Rovainen *et al.* [101]. Velocities in blood vessels have been investigated *in vivo* by injecting a given percentage of the tracer in newborn and adult mice. The dextran-conjugated Alexa Fluor 555 was selected for its excitation and emission spectra: far enough from the ultraviolet light, at which SU-8 is sensitive, but compatible with the filter cube installed in the microscope. The peak excitation wavelength is at 555nm, green

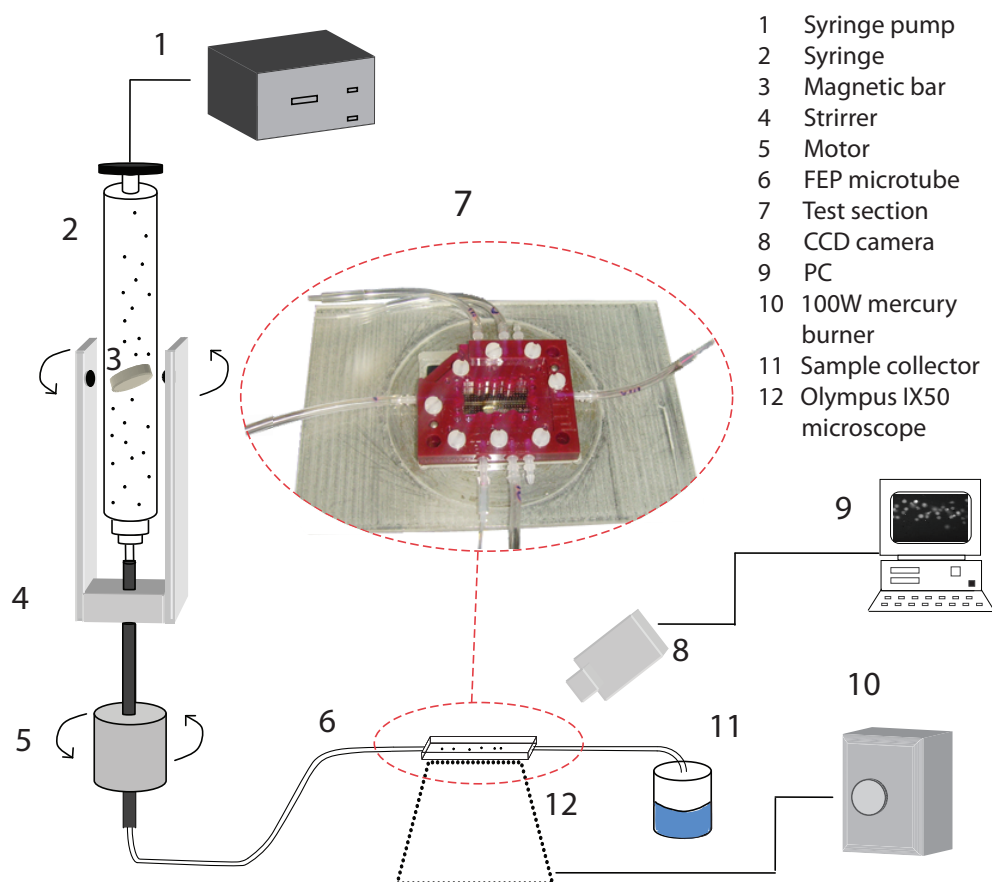


Figure 3.7: Flow visualisation facility.

light, whereas the peak emission is at 565nm, green-yellow light, as depicted in Figure 3.8. The dye, with a nominal molecular weight of 10,000 MW, was supplied in powder form into a vial of 5 mg and was stored in a desiccator at -20 °C. Prior to use, the vial was immersed in a sonic bath for 5 min and then diluted into DI water, previously degassed for 30 min to reduce presence of bubbles, to a final working concentration of 10 $\mu$ M. Flow visualisation tests were carried out using the U-MWG2 fluorescence filter cube.

### 3.3.3 Selection of the particles

Selection of the right particles for flow seeding is crucial for the flow visualisation experiments. Durst *et al.* [21] described the properties that microbeads, whose motion is used to represent a fluid continuum, should have: capacity to follow the flow faithfully, good light scatter, cheap, chemically inactive and non-toxic. Furthermore, in order to avoid the

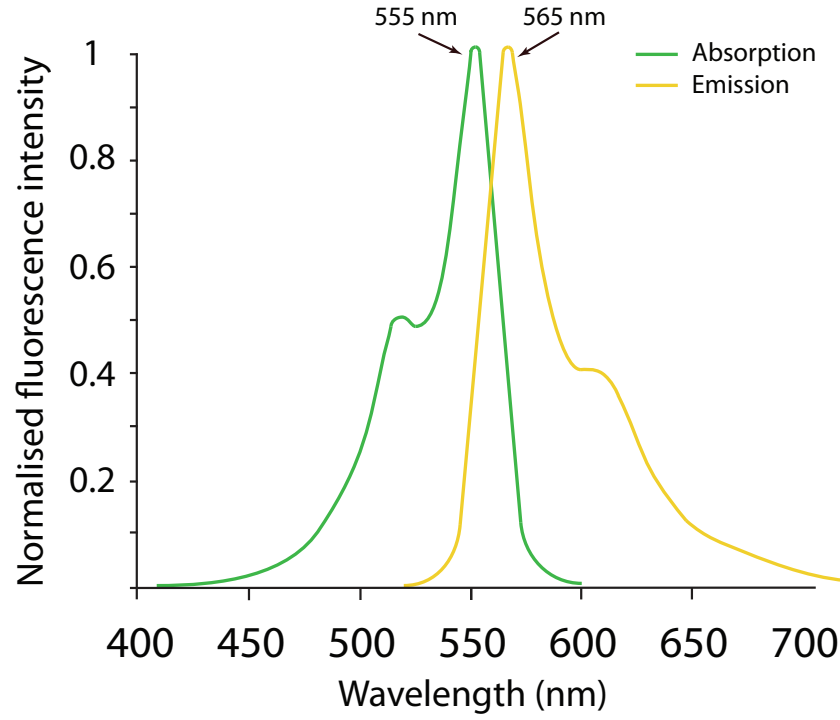


Figure 3.8: Excitation and emission spectra of the dextran-conjugated AlexaFluor 555. Adapted from [49]

sedimentation of the particles, their density should match that of the solution. The settling velocity of a spherical particle in a solution is mainly a function of the particle size and the mismatch between the two densities, eq. 3.5:

$$u_g = d_p^2 \frac{(\rho_p - \rho)}{18\mu} g \quad (3.5)$$

where  $d_p$  is the particles diameter,  $g$  the acceleration due to gravity,  $\mu$  the dynamic viscosity and  $\rho_p$  and  $\rho$  are respectively the density of the particle and of the fluid. In the present study, particles are used as a benchmark for B-lymphoid leukaemia cells, which are sized approximately  $8\mu\text{m}$  but ranging from  $5$  to  $12\mu\text{m}$  [72]. Since cells consist mostly of water, the selected beads must be similar in size with B-cells and match the density of DI water. The peak wavelength must match the fluorescent attachments spectra of the microscope. The particles employed for this study were red fluorescent  $10\mu\text{m}$  FluoSpheres® polystyrene microspheres (Invitrogen, Ireland) with a density of  $1.05 \text{ g/ml}$ , specific for blood flow determination [48]. These particles are internally labelled with a fluorescent

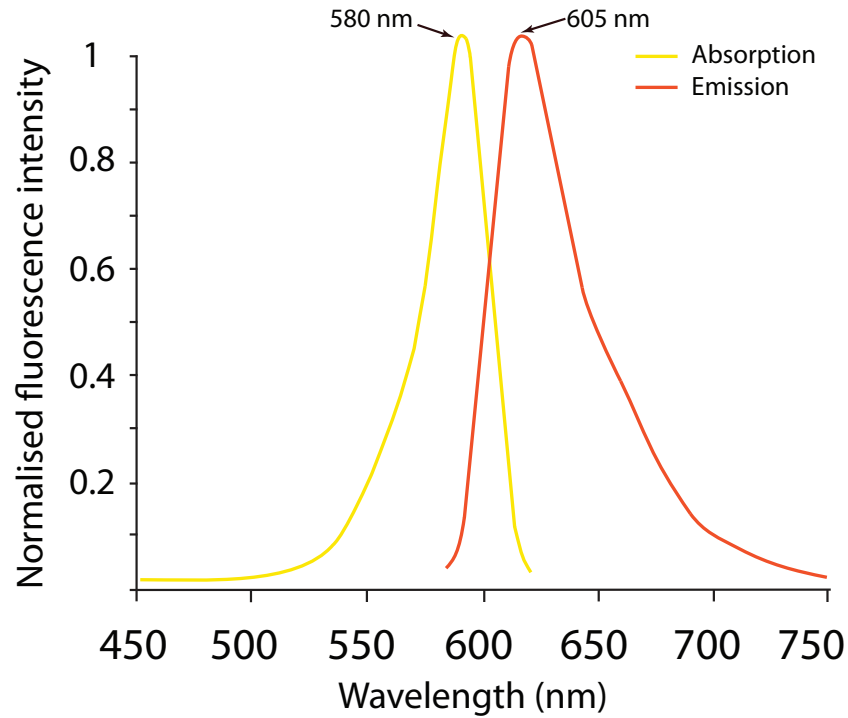


Figure 3.9: Excitation and emission spectra of 10µm FluoSpheres polystyrene microspheres. Adapted from [48]

dye which excites at 580nm (yellow) and emits at 605nm (red), as shown in Figure 3.9, suited for use with the U-MWG2 filter cube. The sedimentation velocity for the selected particles was calculated equal to 1.17µm/s. Particles were supplied as suspensions in 10ml of 0.15M NaCl with 0.05% Tween 20 at a concentration of  $3.6 \times 10^6$  beads/ml. The final working solution of the sample fluid was prepared by diluting 30µl of particles into 1ml DI water. It is worth noting that the dimension of the microbeads, whose actual size is 9.7µm, is sufficiently large not to be influenced by Brownian motion.

### 3.4 Confocal setup

Various techniques, such as 3D Ultrasound, Optical Coherence Tomography, Confocal Microscopy and Photoacoustic Tomography allow the optical resolution of three-dimensional structures in the sample depth direction. However, Confocal Microscopy is the most employed technique to predict the 3D-HF effect in a sample. Even though some authors

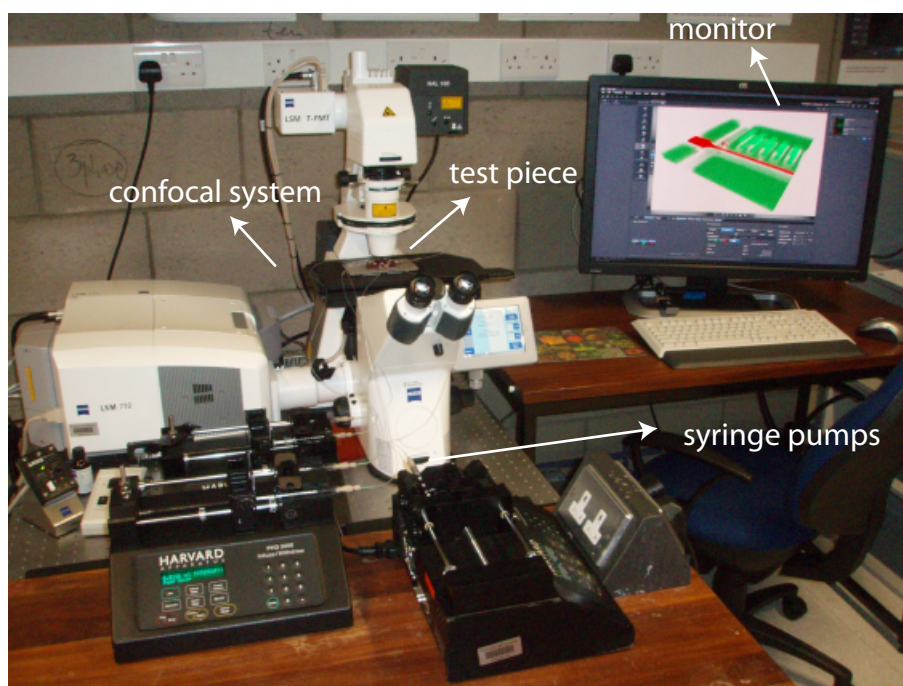


Figure 3.10: Experimental set up used for confocal experiments.

measure the 3D-HF from the variation in fluorescent intensity [36, 52, 88, 106], the simple investigation of the sample diffusion using a conventional fluorescence microscope can only accurately demonstrate the efficiency of the horizontal focusing, as in the 2D technique. A more precise investigation is required for 3D-HF experiments [8, 51, 63, 76, 104]. In this work, confocal images of the fluid flowing into the microdevice were compared with CFD simulations at the same position in the channel.

Confocal Laser Scanning Microscopy, CLSM is a technique for obtaining sharp images of a selected depth of a specimen which would otherwise appear blurred when viewed with a conventional microscope [107]. A laser beam passes through a spatial pinhole employed to eliminate light out of the focal plane. Point by point acquisition of the specimen is acquired and the the full image can be reconstructed.

In the present experiments, cross sectional images of SSD and LSD were recorded with a LSM710 microscope (Zeiss, Germany), coupled with a dedicated ZEN 2008 software. The CLSM, depicted in Figure 3.4, was equipped with the following instrumentation: a motorized  $xy$ -scanning stage, a digital microscope camera AxioCam, two individually driven galvanometric scanners performing up to 5 frames/sec and an EC Plan Neofluar 10x Ph1

(NA=0.3) objective lens. Two laser modules were employed during experiments of this research thesis: a 25mW Argon laser, emitting blue light at 488nm, and a 1mW Helium Neon laser, emitting green light at 543nm. The first excitation source was used to visualise the walls of the microdevice made of SU-8, the second excitation source was used to visualise the position of the dye into the channels.

The microdevice was placed on top of the microscope and sample and sheath fluids were injected using the same microfluidic interconnections, tubing and syringes employed for flow visualisation studies, Section 3.3.1. Images of the microdevices were acquired with the 10x objective lens at a resolution of 1024x1024 pixels with a resultant field of view of 849.36 x 849.36  $\mu\text{m}$  on the *xy* plane. SSD was scanned for 160 $\mu\text{m}$  at 3  $\mu\text{m}$  per z-sectioning step while 410 $\mu\text{m}$  were scanned at 4 $\mu\text{m}$  per step for LSD. In both chips the acquisition speed was set to 5. The fluid tracer, Alexa Fluor 555 described in Section 3.3.2, diluted into DI water was injected into channel B while DI water was employed as the sheath fluid and loaded into inlets A, C and D. During all experiments flow rate ratios of the sheath fluids A and C were imposed of equal magnitude, therefore three syringe pumps were required: one syringe pump for the inlets A and C, one for the sample fluid B and one for the two inlets of the sheath fluid D. Confocal experiments have been carried out at different flow rate ratios and Re number, summarised in Table 3.2.

Table 3.2: Flow rate ratios tested

SSD		LSD	
$\alpha_v = 0.3$	Re = 11.4	$\alpha_v = 0.25$	Re = 2
$\alpha_h = 3.13$		$\alpha_h = 7$	
$\alpha_v = 1$	Re = 12.9	$\alpha_v = 1$	Re = 1.3
$\alpha_h = 4$		$\alpha_h = 1$	Re = 10.3
$\alpha_v = 1.5$	Re = 7.9	$\alpha_v = 4$	Re = 1.9
$\alpha_h = 0.15$		$\alpha_h = 4$	
$\alpha_v = 2$	Re = 6.4	$\alpha_v = 6$	Re = 1.9
$\alpha_h = 4$	Re = 30	$\alpha_h = 6$	Re = 9.8
$\alpha_v = 3$	Re = 30.2	$\alpha_v = 7$	Re = 0.9
$\alpha_h = 4$		$\alpha_h = 0.4$	
$\alpha_v = 3.75$	Re = 30	$\alpha_v = 10$	Re = 4
$\alpha_h = 4.12$		$\alpha_h = 10$	
$\alpha_v = 4$	Re = 7.6	$\alpha_v = 12$	Re = 7.5
$\alpha_h = 8.89$	Re = 30	$\alpha_h = 6$	

### 3.5 Summary

In this chapter, the biological protocols and the experimental apparatus were described. In the next chapter, the computational fluid dynamic simulations are presented.

# Chapter 4

## CFD simulations

In this chapter, details of the computational fluid dynamic simulations are presented. The governing equations, the simulations method and the model employed are detailed. The grid independence analysis carried out to validate the accuracy of the CFD simulations and to determine the correct number of cells in the system is also described.

### 4.1 CFD simulations

Computational fluid dynamics (CFD) simulations enable the performance characteristics of microfluidic devices to be extensively explored over a wide range of system parameters. The optimal device design can be established before committing to the time and expense of fabricating actual physical models. In the current study, the flow field and the diffusion of the dye along the length of the microchannels were investigated and compared with results obtained from confocal experiments. In modelling flow into microchannels, two dimensional simulations are used with the assumption that the depth, or z-direction, of the channel geometry is infinite or that the flow takes place at a low Reynolds number. Three dimensional numerical models should be employed when sudden expansions are present in the channel geometry, causing possible flow separation vortexes in the corner edges [119], or in the case of intrinsically three dimensional flow behaviour. Due to the position and number of inlets and the 3D nature of the focusing effect, a three dimensional CFD model

was required to accurately predict the hydrodynamic focusing effect of the proposed device.

Commercial software COMSOL Multiphysics version 3.4 was used to generate the CFD model to represent the focusing efficiency of both SSD and LSD. COMSOL includes all modules required for the simulation, modeling, mesh generation, analysis and post-processing, into a single software package. To simplify calculations, the real geometry of the chips, shown in Chapter 2, was reduced to a 3D model with two bottom cross channels and two vertical channels, as illustrated in the schematic of SSD in Figure 4.1(a). Individual channels were modelled as subdomains connected to the next channel through a boundary, in order to conserve mass flow through boundaries. The finite element analysis was carried out using the incompressible Navier-Stokes and convection and diffusion equations. The governing mass, momentum and species equations are written respectively in eq. 4.1, eq. 4.2 and eq. 4.3:

$$\frac{\partial U_j}{\partial x_j} = 0 \quad (4.1)$$

$$U_j \frac{\partial U_i}{\partial x_j} = -\frac{1}{\rho} \frac{\partial p}{\partial x_i} + \frac{\partial}{\partial x_j} \left( \nu \frac{\partial U_i}{\partial x_j} \right) \quad (4.2)$$

$$U_j \frac{\partial C}{\partial x_j} = D \frac{\partial}{\partial x_j} \left( \frac{\partial C}{\partial x_j} \right) \quad (4.3)$$

where  $U_j$  is the  $x_j$  component of the fluid velocity,  $\rho$  the density of the fluid,  $p$  the pressure,  $\nu$  the kinematic viscosity,  $D$  the diffusion coefficient of the dye and  $C$  the concentration of dye injected into DI water.

The diffusion coefficient is a property of a compound which depends on molecular weight, size and the intermolecular forces of attraction between the molecules in the mixture. The diffusion of a particle through a liquid, regarded as the measure of the viscous resistance to its motion through the liquid [80], is given by the *Stokes-Einstein equation*, eq. 4.4, for molecules of molecular weight over 1000:

$$D = \frac{k_B T}{6\pi\mu R_d} \quad (4.4)$$

where  $k_B$  is the Boltzmann constant,  $T$  the temperature of the liquid (in Kelvin),  $\mu$  the dynamic viscosity and  $R_d$  the radius of the diffusive molecule. The dimensions of  $D$  are  $\text{m}^2/\text{s}$ , measured as the area occupied by the diffused molecules in a second. In case of liquid *in liquid* diffusion,  $D$  is in the order of magnitude of  $10^{-8} - 10^{-12} \text{ m}^2/\text{s}$ . Alexa Fluor 555, described in Section 3.3.2, was employed as a tracing fluid for the confocal experiments of Chapter 5 and its diffusion coefficient was determined from the product information sheet [49] and imposed equal to  $D = 5e^{-10} \text{ m}^2/\text{s}$ . In the simulations the dye was applied to the inlet B and DI water was applied to the sheath fluids. The values of  $\rho$  and  $\mu$  are specified as  $1000 \text{ kg/m}^3$  and  $0.001 \text{ Pa}\cdot\text{s}$  for both DI water and Alexa Fluor 555 and the temperature of the liquid was measured. The concentration of dye injected into water was imposed to  $10\mu\text{M}$ . The analysis was carried out with the assumption that the flow was laminar, incompressible and isothermal. Flow in the inlets was specified to be fully developed with a velocity assumed to have a uniform profile in both water and dye boundaries. A pressure outlet boundary condition is imposed at the downstream boundary of channel E. Finally, no slip conditions with zero flux of the species concentration are applied at all the solid walls within the device.

#### 4.1.1 Meshing and analysis

In CFD an acceptable mesh is important in reaching a correctly converged solution in order to simulate the hydrodynamic focusing of the dye. In meshing the 3D model with COMSOL, the computational power required for each simulation was a concern because solution time did not scale linearly with mesh size. For instance, a model with 100,000 elements required 19 minutes to solve but a model with 200,000 elements (100% increase) required 75 minutes (294% increase) to solve. Furthermore, the number of cells in the system was limited by the processor used, since too many nodes lead the software to run out of available memory and the simulation fails. For these reasons, a mesh fine enough to accurately capture the appropriate details of the fluid flow and diffusion, but coarse enough

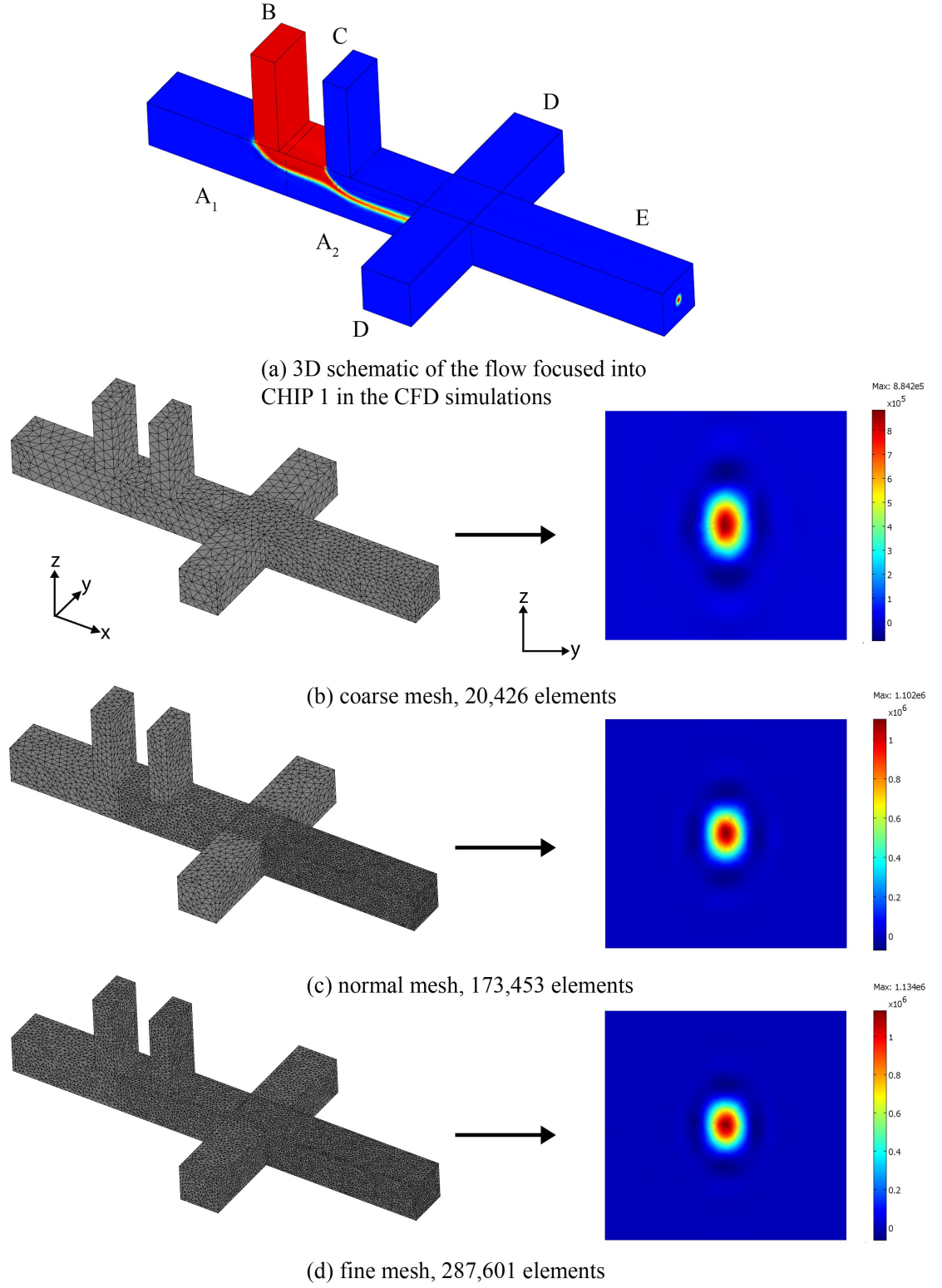


Figure 4.1: Grid independence study carried out for SSD. (a) coarse mesh with 20,426 elements; (b) normal mesh with 173,453 elements, (c) fine mesh with 287,601 elements. The correspondent focused size 500 $\mu$ m downstream channel E is shown on the right. Flow rate ratios are  $\alpha_v = 2$ ,  $\alpha_h = 4$  and  $Re = 6.4$ .

not to be overly computationally expensive is desired. This can be achieved by producing a detailed mesh in regions of high fluid and concentration gradients, with lower resolution mesh density elsewhere.

In order to validate the accuracy of the CFD simulations and to determine the correct number of cells in the system, a grid independence study was carried out. Three mesh densities, coarse, normal and fine, were compared in terms of focused size of the dye [52, 69] in the same geometry location, 500 $\mu\text{m}$  and 900 $\mu\text{m}$  downstream channel E respectively for SSD and LSD. The 3D model was first meshed to the COMSOL autogenerated density using tetrahedral element patterns. The initial default mesh was already automatically refined nearby boundaries or corners but was also uniformly distributed along the channels. Since the focusing of the Alexa Fluor 555 into water occurs after the intersection between channels  $A_1$  and B, Figure 4.1(a), and mainly along the  $x$  direction, the mesh density was further refined in section  $A_2$ , in channel E and at the edges of the junctions. In regions where simple parallel flow was expected coarser elements were meshed, such as channels  $A_1$ , B, C and D. The coarse grid, Figure 4.1(b), was then made of element edge lengths of between 12 $\mu\text{m}$  to 25 $\mu\text{m}$  for SSD and 50 $\mu\text{m}$  to 85 $\mu\text{m}$  for LSD to reach approximately 20,426 cells. This primary mesh density was refined until a total number of cells of 173,453 for SSD and 212,285 for LSD, with element edge lengths respectively of between 8.5 $\mu\text{m}$  to 15 $\mu\text{m}$  and 28 $\mu\text{m}$  to 60 $\mu\text{m}$ , as illustrated in Figure 4.1(c). A 4.6 % variation in the diameter of the focused sample with respect to the coarse grid was found. Regions of flow unsteadiness, channels  $A_2$ , E and all the boundaries, where further refined for the fine grid, shown in Figure 4.1(d), until a minimum element size of 7.5 $\mu\text{m}$  for SSD and 23 $\mu\text{m}$  for LSD with a total number of cells respectively of 287,601 and 334,718. A 65% increase in mesh density only leads to 1.2% improvement in focused size. Therefore, the normal cell density has been selected for the simulation since the fine grid increases the computational resources and time without providing additional resolution. Figure 4.1 illustrates the different mesh densities applied to the subdomains of SSD and the relative focused size. Flow rate ratios are  $\alpha_v = 2$ ,  $\alpha_h = 4$  and  $\text{Re} = 6.4$ . Fig. 4.2 shows normalised concentrations of the sample for each of the 3 meshes.

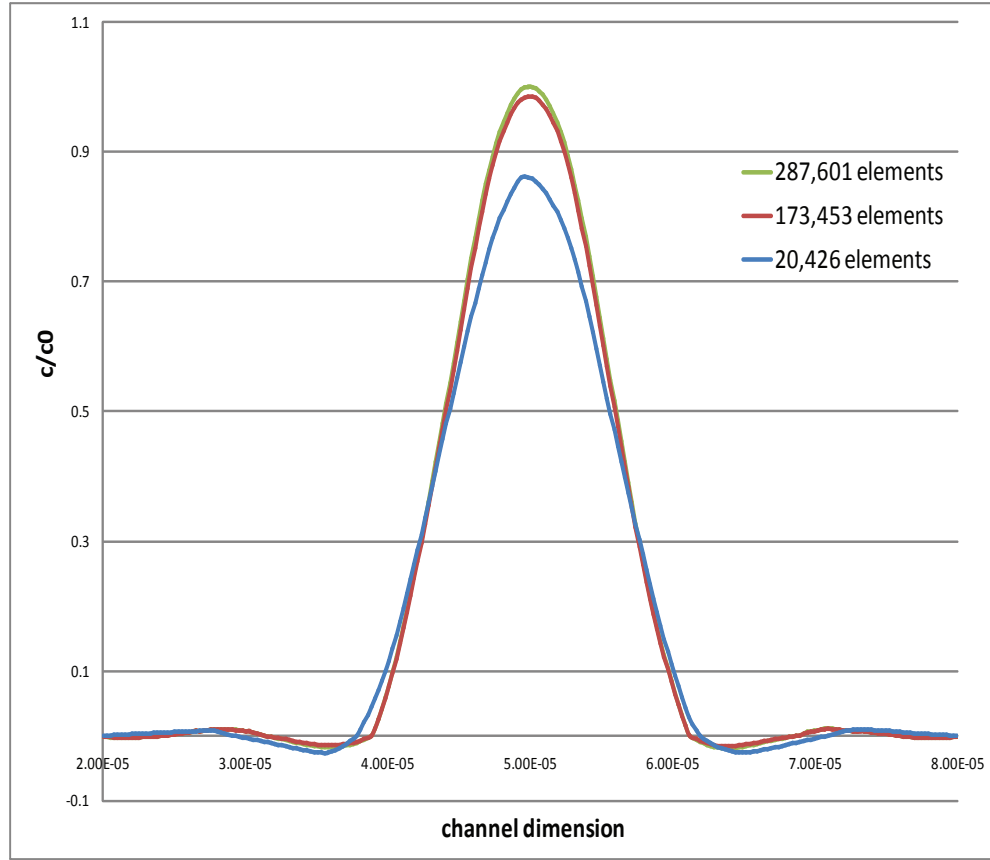


Figure 4.2: Normalised sample concentration through the channel dimension.

Following the drawing of the model and the definition of the governing equations and mesh, the 3D model was solved using the stationary UMFPACK direct solver. In order to reduce computational time, variables from the incompressible Navier-Stokes equation were solved first. The outcome from this analysis, velocity components  $u$ ,  $v$  and  $w$ , was stored and used as initial value to determine the variable for convection and diffusion,  $c$ . This provided the most efficient method of solution for the time and processing resources available. A cross-section plot showing the concentration of the dye into the device was extracted from the result files. Every cross-section was acquired on the  $y$ - $z$  plane of the main channel E, 600 $\mu\text{m}$  downstream the intersection with channel D. Simulations of the fluid flowing into the microdevice were then compared with confocal experiments, as documented in Chapter 5.

## **4.2 Summary**

In this chapter, the computational fluid dynamic simulations were described. In the next chapter, the results of the numerical modelling and experimental investigations of the 3D-HFMD are presented and discussed.

## **Chapter 5**

# **Hydrodynamic Focusing and Flow Cytometry**

In this chapter the experimental results obtained with the 3D-HFMD are presented in 2D, 3D, particle and cell focusing sections. A flow visualisation method is first reported to establish the 2D hydrodynamic focusing effect into the microdevice and to demonstrate the stability of the flow. Confocal results and CFD simulations are then correlated in order to verify the ability of the geometry to achieve a fully 3D hydrodynamic focusing configuration and to prove the potential to control size and position of the focused stream. Following this, images of the micro particles focused in single file into the channels served to confirm the capability of the 3D-HFMD to perform as a flow cytometer. An application of the device with biological cells is also reported. Finally, a simplified model of the theoretical expression to predict the size of the focused sample stream is introduced.

In the next section, top views of LSD are shown first in order to investigate the stability of the sample for the full length of the device. After this, results for SSD and LSD are presented separately for either confocal, CFD, particle and cell studies.

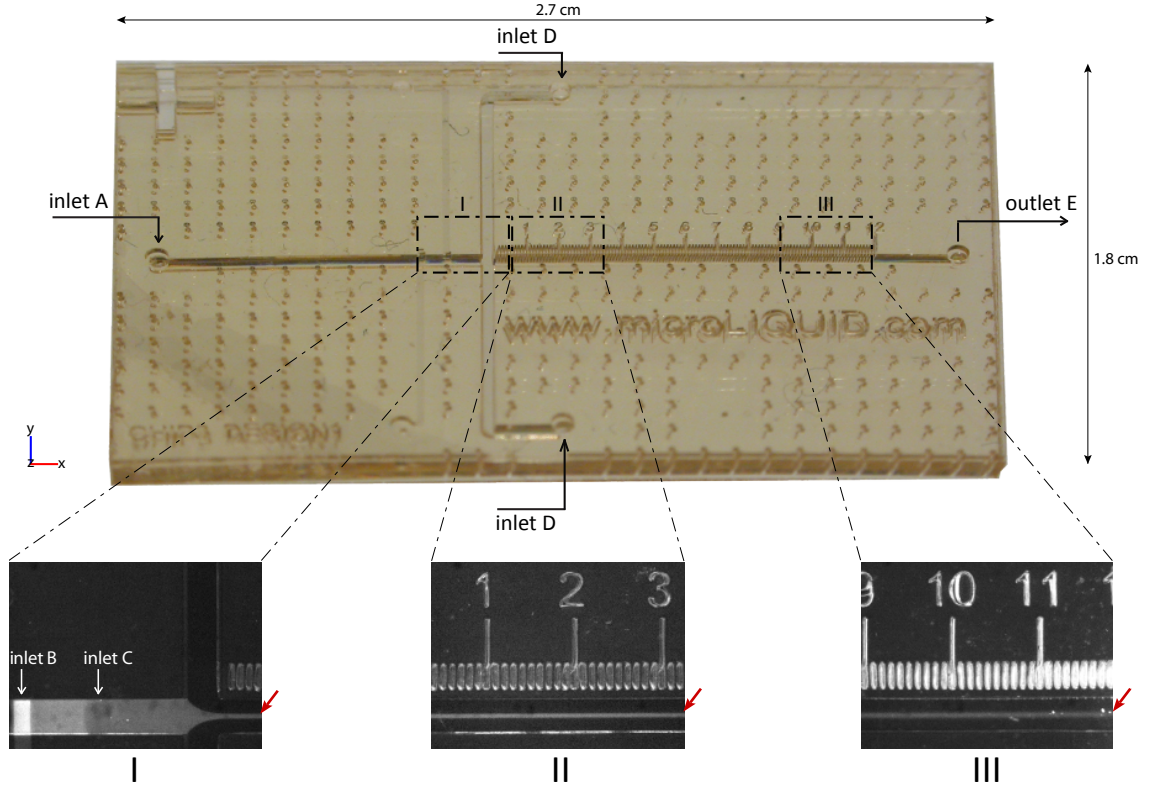


Figure 5.1: Top views of the Alexa Fluor 555 hydrodynamically focused into LSD. A reference to the measurement position is given. The dye is focused in 3D in a width of circa  $50\mu\text{m}$ , indicated by the red arrows. Flow rates used:  $Q_A = 2\mu\text{l/min}$ ,  $Q_B = 5\mu\text{l/min}$ ,  $Q_D = 18\mu\text{l/min}$ , with  $\alpha_V = 0.4$ ,  $\alpha_H = 2$  and  $\text{Re} = 1.1$

## 5.1 2D focusing: flow visualisation of dye

The diffusion of the fluid into the microchannel is a fundamental aspect of the device operation. As described in Section 3.3, the ratio between convection and diffusion is given by the Péclet number, eq. 3.4 and a high Péclet number means that convection dominates. For low Reynolds numbers, the diffusion of molecules through liquid is given by the Stokes-Einstein equation [23], eq. 4.4. The diffusion coefficient of the Alexa Fluor 555 is in the order of  $10^{-10} \text{ m}^2/\text{s}$ , while that of cells or particles of  $10\mu\text{m}$  in size is around  $10^{-14} \text{ m}^2/\text{s}$ . The analysis of the dye diffusion, as a result, is a conservative estimation of the cells/particles behaviour.

Figure 5.1 represents top views of the Alexa Fluor 555, indicated by the red arrows, 3D hydrodynamically focused into LSD. On the top of the image, a picture of the device is

illustrated, with the two cross channels A and D clearly visible. On the bottom of the figure, three zoom in views of the dye flowing into the device are shown, and their correspondent position along the channel is indicated. On the first magnification, upstream the T-junction with channel D, the intensity fades out as the dye flows along the device. The highest fluorescence intensity is noticed at the vertical channel B, where the sample is injected. Immediately downstream the intensity reduces because the sample is pushed to the top of the channel, following the scheme shown in Figure 2.6. A second intensity reduction is noted at the intersection with channel C, where the dye is moved down to the centre of the channel and it is finally vertically constrained for the remainder of the device. The focusing effect is shown for a length equal to 12mm, indicated by the reference scale at the side of the main channel. The sample is forced to flow in the central region of the microchannel in a width of approximately 13% of the channel dimension, for flow rates:  $Q_A = 2\mu\text{l/min}$ ,  $Q_B = 5\mu\text{l/min}$ ,  $Q_D = 18\mu\text{l/min}$ , with  $\alpha_V = 0.4$ ,  $\alpha_H = 2$  and  $Re = 1.1$ . No significant variation in the size of the focused region is caused by diffusion for the full length of the device, ensuring the focusing reliability of the geometry and a large test area. The fluorescent intensity of the dye, however, slightly reduces, but no quantifiable data about the vertical displacement of the sample can be estimated from this analysis. Even though some authors measure the 3D-HF from the variation in fluorescent intensity [36,52,88,106], this method can only accurately demonstrate the efficiency of the horizontal focusing, as in the 2D technique, but a more precise investigation is required for 3D-HF experiments. Similar results are obtained for SSD, where the sample width is equal to  $9.5\mu\text{m}$ , for flow rates:  $Q_A = 2.5\mu\text{l/min}$ ,  $Q_B = 1.25\mu\text{l/min}$ ,  $Q_D = 12.5\mu\text{l/min}$ . A video recording of the dye hydrodynamically focused into the 3D-HFMD is available in Appendix C. Video II and Video III show the size of the focused stream for the full length of SSD and LSD respectively.

The flow visualisation technique was also employed to investigate the behaviour of the flow under shock stimuli. Figure 5.2 lists a sequence of frames of the dye in motion extracted from a video recorded at 30Hz with a CCD camera. A sudden shock was induced to the stage of the microscope, and the response of the fluid was observed. The arrow-like shape of the flow remained unchanged through the frameset but a wave effect was

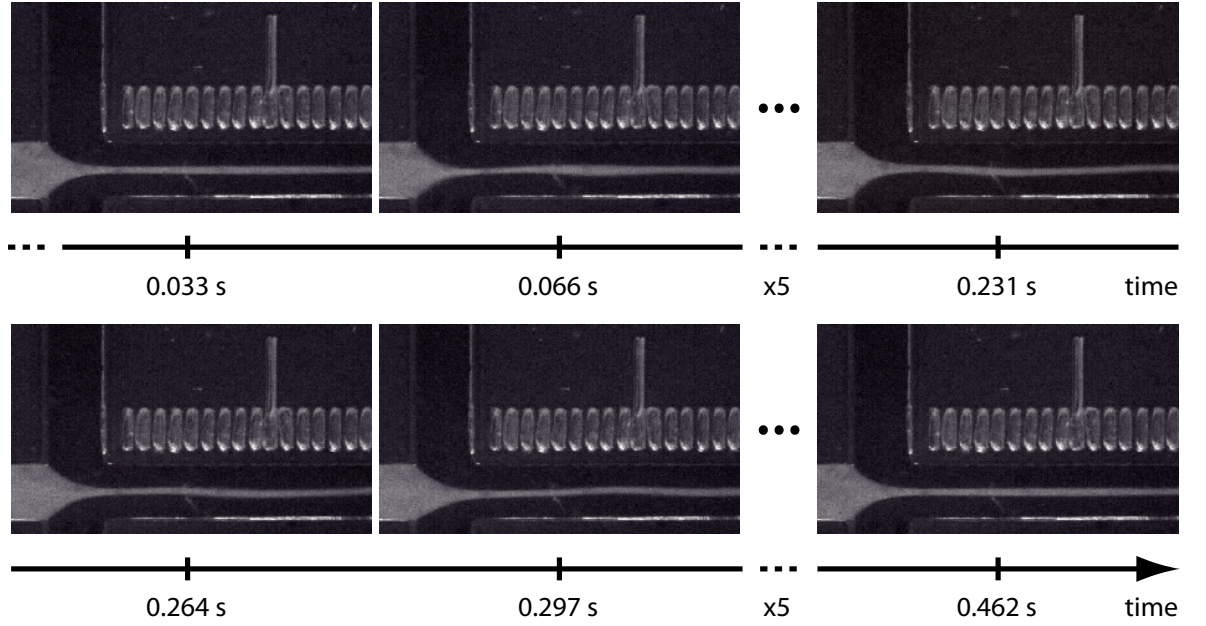


Figure 5.2: Flow visualisation frameset showing the stability of the flow into LSD.

propagated to the fluid. Because the time between each frame is known, equal to 0.033s, it was possible to calculate the time required by the flow to revert to its original stage. In less than half of a second, the effect of the induced shock disappeared. The same test was repeated 12mm downstream channel E with similar results. The same effect was observed when a flow rate 50 times higher than the value currently tested was set and immediately stopped on inlet B. In less than one second the flow returned to normal. These simple tests verified the stability of the flow in the device under the influence of exterior disturbances. Videos of the stability of the flow on LSD are available in Appendix C. Videos IV and V show the flow behaviour under shock and under the influence of an extremely high flow rate at the intersection with channel D . Video VI shows the flow behaviour under shock at the outlet E.

While the singularities presented in this section mainly arose from undesired and self-caused events, they proved invaluable in identifying erroneous datasets and providing insight into the behaviour of the flow under accidental conditions.

## 5.2 3D focusing: comparison of CFD and Confocal results

In order to demonstrate the ability of the proposed device to focus the sample in 3D, confocal images showing the displacement of the Alexa Fluor 555 into the microdevices are acquired and compared to CFD simulations at different flow rate ratios. The settings used during the confocal experiments and CFD simulation are described respectively in Section 3.4 and Section 4.1. In the next sections, examples of data extracted from the experiments and the equations established to analyse the results are first presented. Following this, results for SSD and LSD are presented separately.

### 5.2.1 Data extraction and analysis

Several flow rate ratios were analysed both in experiment and simulation in order to investigate the 3D nature of the flow. The set of flow rate ratios and Reynolds numbers tested were previously summarised in Table 3.2. The data presented in this section are from single measurements, and for each experiment data concerning height, width and position of the sample core were extracted. The aggregated data and the analogy between experiments and simulations are presented in the next section.

Figure 5.3 shows an example of the data derived from a typical confocal result obtained for SSD. Figure 5.3(a) is a 3D view of the reconstructed  $x$ - $y$  scans of the device with an indication of the orientation and the size of the field of view. The Alexa Fluor 555, in red, and the walls of the channel, in green, are both clearly visible. Even though the height of the channel is  $95\mu\text{m}$ , scanning was performed for a depth of  $190\mu\text{m}$  in order to ensure that the channel was included in the field of view. Figure 5.3(b) illustrates the top view of the device at the intersection with channel D. In each test, the sample is confined to the central region of the main channel for the full visible length,  $600\mu\text{m}$ , as indicated by the graduation marks etched during the fabrication process  $100\mu\text{m}$  apart over channel E. No change in the sample width is noticed for a distance  $6W$  downstream E. The three dimensional shape of the dye, however, is only visible from the front views of the confocal experiments. Figure 5.3(c) depicts the depth coding image, where a different colour is given to each depth of the

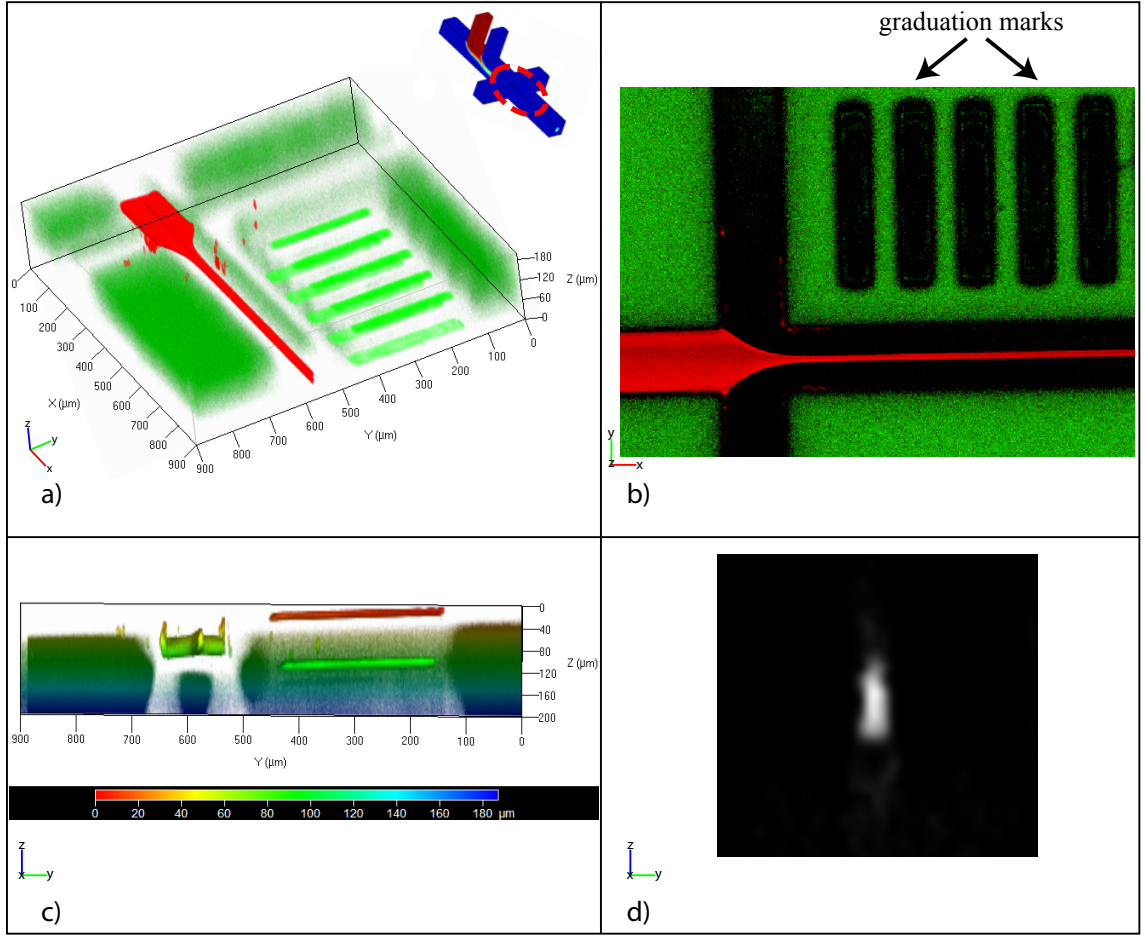


Figure 5.3: Example of the data extracted from a typical confocal experiment on SSD. Flow rates used:  $Q_B = 4 \mu\text{l}/\text{min}$ ,  $\alpha_V = 4$ ,  $\alpha_H = 8.89$ ,  $\text{Re} = 30$ .

channel. This view documents the vertical position of the sample core with respect to the channel edges. The legend on the bottom of the figure is a guide to the scale used for the colours. The graduation marks, fabricated on the top and on the bottom surfaces of the chip, are used as a visible reference for the upper and lower walls of the channel. Finally, the analogy with the CFD analysis was performed using Figure 5.3(d). A cross-section of the  $y$ - $z$  plane is converted in grayscale to represent size, shape and position of the sample core into the channel. Height and width of the image are that of channel E, therefore the sample is shown in its real position in the surrounding fluid. The measurement tool in the ZEN 2008 software allows the precise quantification of the focused size in the three dimensions in all points. These values were then compared to that acquired from the CFD simulations. It is important to underline that the same datasets were also extracted for LSD.

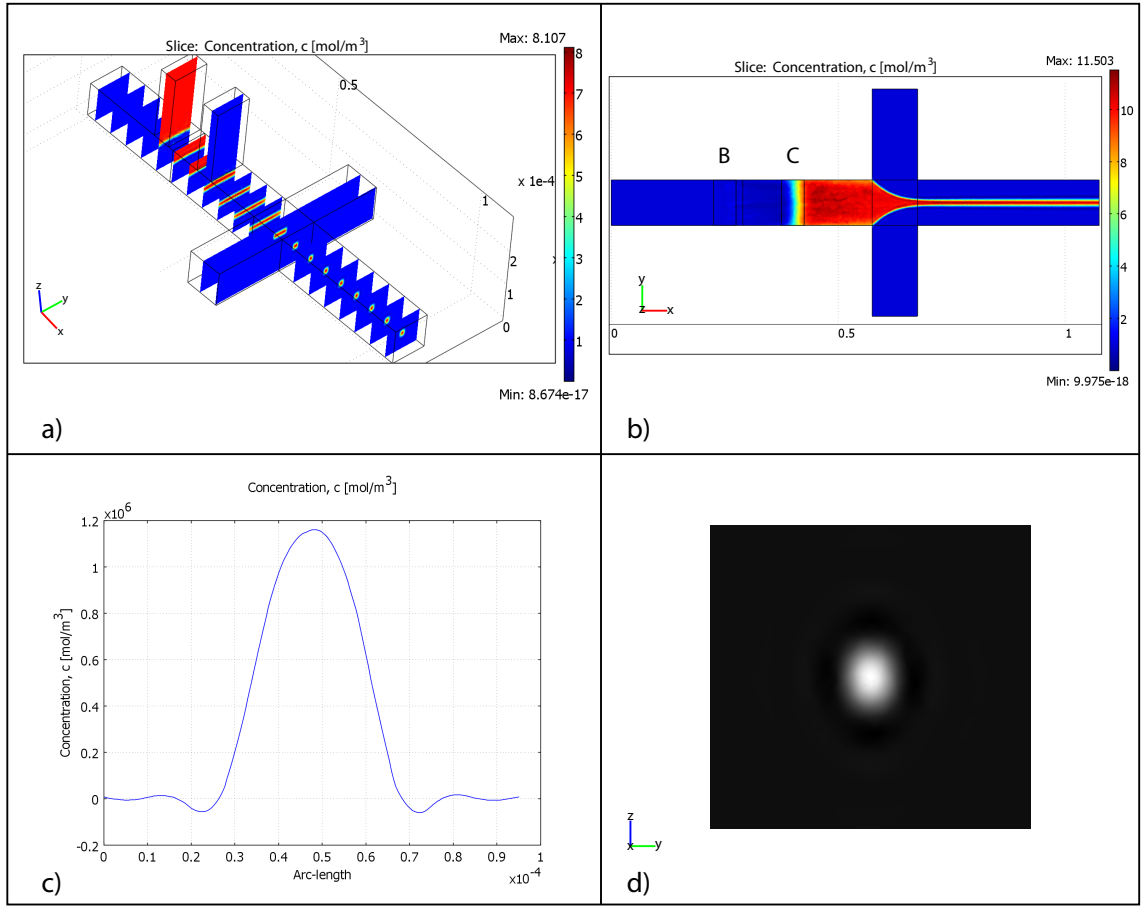


Figure 5.4: Example of the data extracted from a typical CFD experiment on SSD. Flow rates used:  $Q_B = 1.5 \mu\text{l/min}$ ,  $\alpha_V = 2$ ,  $\alpha_H = 4$ ,  $\text{Re} = 6.4$ .

Figure 5.4 shows an example of a typical CFD simulation performed on SSD. In order to compare the simulations with the experiments, the same data were extrapolated from the CFD. Thus, as for the confocal experiments, Figure 5.4(a) represents the 3D view of the CFD. In the post-processing phase, the 3D model was partitioned into 20 cross-sections plotting the dye concentration on the  $z$ - $y$  plane, in order to track the area occupied by the sample throughout the device. The behaviour of the flow followed the expected path detailed in Figure 2.6. A top view of the model is outlined in Figure 5.4(b), showing the device at the intersection with channel D. Because the slice of the  $x$ - $y$  plane is cut halfway through the channel height, the sample is visible only after the junction with channel C, where it is confined into the central region of the channel. The size of the sample core is then derived from the 2D plots of concentration over the channel dimensions, as documented in Figure 5.4(c) for the channel width, and it is considered

the distance between intensity values at 1/5 of the maximum concentration. Figure 5.4(d), instead, serves to visualise the shape of the sample as a direct analogy with Figure 5.3(d) of the associated experiment. Both Figure 5.4(d) and Figure 5.3(d) are acquired on the same position of the main channel E, 600 $\mu$ m downstream the intersection with channel D for either SSD and LSD. For the rest of this work, values and description of the size and shape of the flow are obtained at this specific geometry location.

In order to compare experiments with simulations, the following parameters need to be defined. The percentage vertical focusing of the dye over the channel height on the experimental results is defined as:

$$\%v_e = \frac{v_e}{H} \times 100 \quad (5.1)$$

where  $v_e$  is the vertical focusing size on the confocal image. The percentage vertical focusing of the dye over the channel height on the simulations is defined as:

$$\%v_s = \frac{v_s}{H} \times 100 \quad (5.2)$$

where  $v_s$  is the vertical focusing dimension on the CFD image. The difference between  $\%v_e$  and  $\%v_s$  gives an indication of the percentage mismatch between CFD simulations and confocal results over the channel height for the vertical focusing:

$$\Delta v = | \%v_e - \%v_s | \quad (5.3)$$

$\Delta h$ ,  $\%h_e$ ,  $\%h_s$ ,  $h_e$ ,  $h_s$  are the equivalents of  $\Delta v$ ,  $\%v_e$ ,  $\%v_s$ ,  $v_e$ ,  $v_s$  for the horizontal direction.

### 5.2.2 SSD

First, confocal results of SSD are shown to prove that the position of the central core of the sample can be fully controlled. Three possible flow configurations, corresponding to three different possible applications of the 3D-HFMD, are shown in Figure 5.5. On the left of the image the 3D scans are illustrated for a quick representation of the shape of the flow and the associated cross sections are presented on the right side. Although the geometry was designed for 3D-HF, it is also possible to achieve only 2D focusing, either horizontal or vertical, independently. In Figure 5.5(a), the fluid is confined to the vertical dimension (horizontal focusing) by applying low flow rates to the inlets A and C. This is the 2D focusing mode mostly employed in the last twenty years both in the macro and micro scale. For  $\alpha_V = 0.3$  and  $\alpha_H = 3.13$ , the sample flow is constrained into a region equal to  $h_e = 14.94\mu\text{m}$  and  $v_e = 70\mu\text{m}$  with  $\%h_e = 15\%$  and  $\%v_e = 74\%$ . Figure 5.5(b) shows the 2D focusing mode when applied to the vertical dimension. This is a more interesting feature of the 3D-HFMD which can be used in many optical applications where it is important to keep the sample into the focal plane. As discussed in Section 6.3, many detection devices are unable to identify out of focus cells/particle, leading to a loss of information. Moreover, the sample out of the focal plane generates background noise and reduces the signal-to-noise ratio. The vertical focusing mode of Figure 5.5(b) confined the sample into an area equal to  $h_e = 66.42\mu\text{m}$  and  $v_e = 21.3\mu\text{m}$ , with  $\%h_e = 66\%$  and  $\%v_e = 22\%$ , for flow rate ratios  $\alpha_V = 1.5$  and  $\alpha_H = 0.15$ . A small horizontal focusing effect was applied to avoid contact between the dye and the channel walls. This configuration was employed with the optical counting technique of Chapter 6. It is interesting to observe that the sample can also be successfully pushed to the bottom by applying a non-coaxial sheath flow,  $Q_C > Q_A$  (or to the top if  $Q_C < Q_A$ ). This is useful in applications where cells/particles are desired to flow in close proximity to a photodetector deposited on the channel floor for increased signal-to-noise ratio. In Figure 5.5(c) the dye was forced to flow into a region  $h_e = 20\mu\text{m}$  and  $v_e = 28\mu\text{m}$  with  $\%h_e = 20\%$  and  $\%v_e = 29\%$ . If the two side sheath fluids  $Q_D$  have different magnitude, the sample can also be positioned on the right or on the left of the channel. However, due to a limitation in the geometry design, a minimum of three syringe pumps is already required for a doubly symmetric test (sample focused in 3D). Because each flow rate value requires

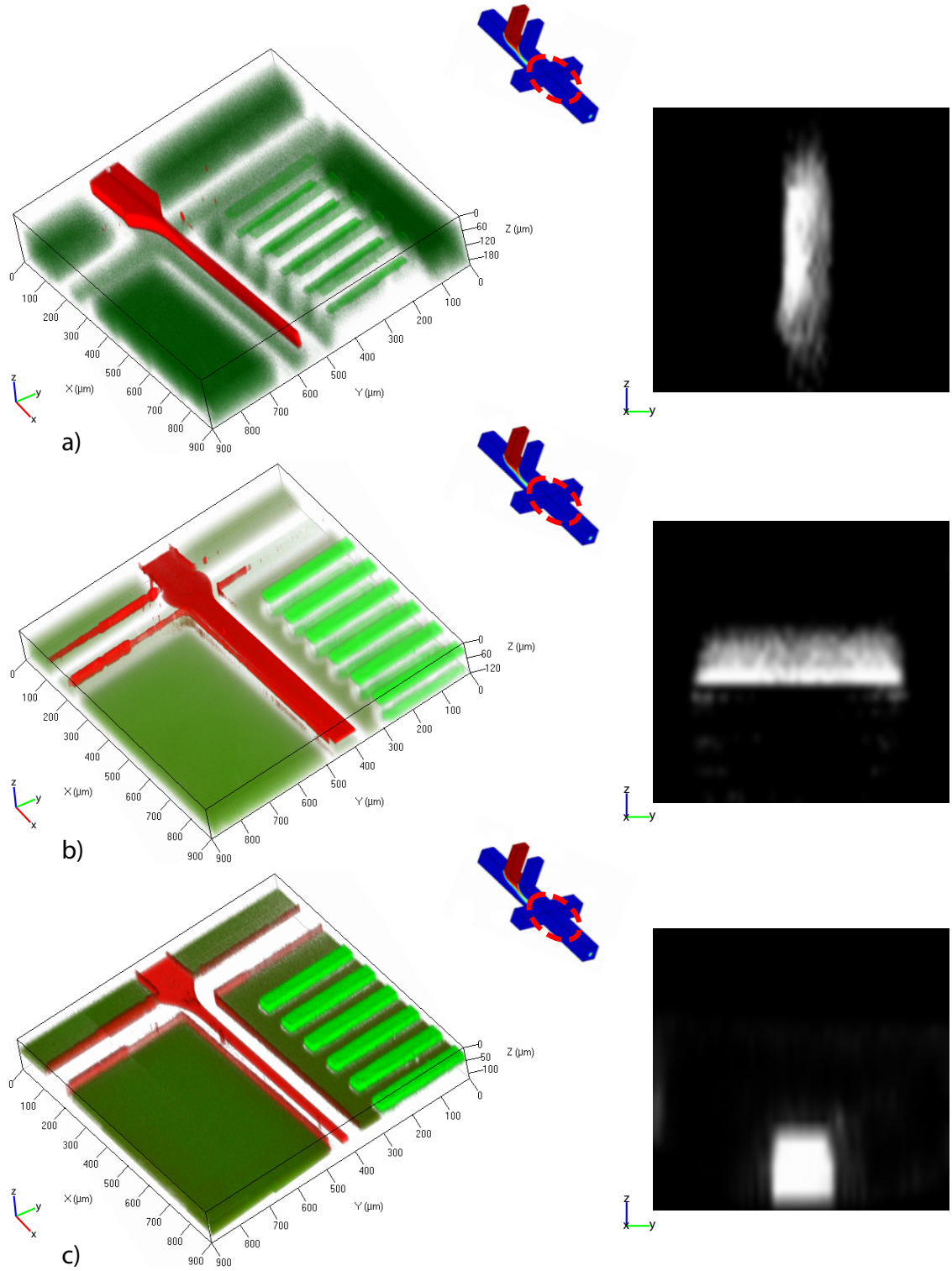


Figure 5.5: Cross sectional confocal images showing three possible focusing configurations of the Alexa Fluor 555 into SSD: (a) horizontal focusing in a region  $15 \times 70 \mu\text{m}$ ; (b) vertical focusing ( $66.42 \times 21.3 \mu\text{m}$ ); (c) bottom focusing ( $20 \times 28 \mu\text{m}$ )

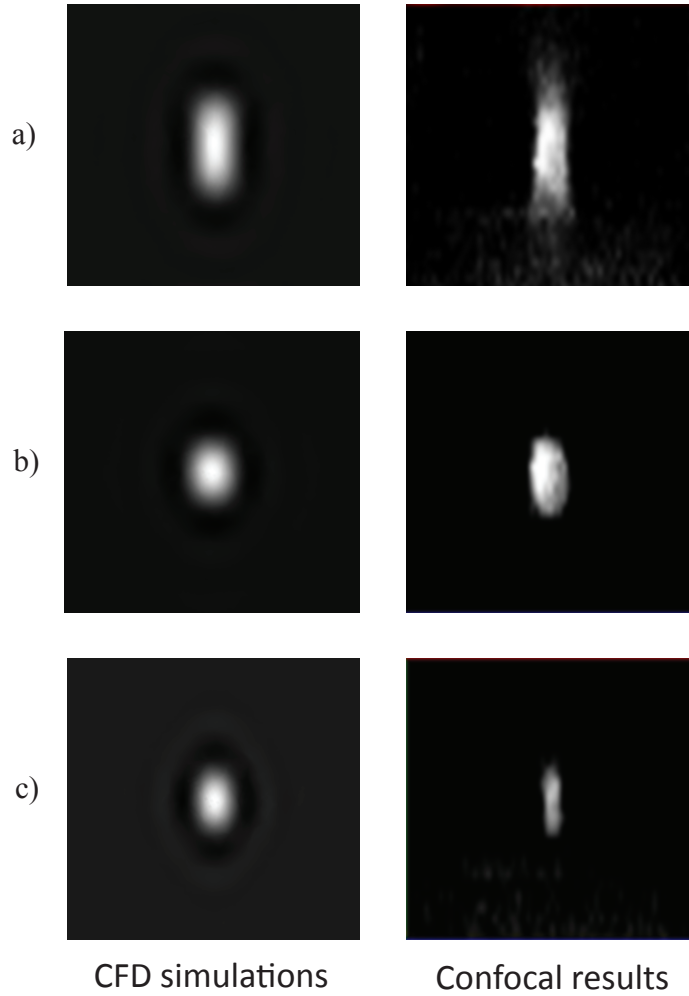


Figure 5.6: Comparison of CFD simulations to confocal images for cross sections of SSD. (a)  $Q_B = 5 \mu\text{l/min}$ ,  $\alpha_V = 1$ ,  $\alpha_H = 4$ ,  $\text{Re} = 12.9$ , (b)  $Q_B = 1.5 \mu\text{l/min}$ ,  $\alpha_V = 2$ ,  $\alpha_H = 4$ ,  $\text{Re} = 6.4$ , (c)  $Q_B = 0.5 \mu\text{l/min}$ ,  $\alpha_V = 4$ ,  $\alpha_H = 8.89$ ,  $\text{Re} = 7.6$

a dedicated syringe pump, an additional pump or a variable geometry is required for the asymmetric configurations of Figure 5.5(c) or if different flow rates are injected into the inlets D. The same focusing modes can also be achieved on LSD.

After presenting the possible flow geometries which could be performed with the 3D-HFMD, the analysis of the different sizes and shapes of the sample achieved on SSD are shown in the following figures. Figure 5.6 compares CFD simulations to confocal experiments for three different flow rate ratios. While the focused stream is always positioned in the centre of the channel, its dimension can be controlled by varying the flow rate ratios of sample to sheath fluids,  $\alpha_V$  and  $\alpha_H$ .

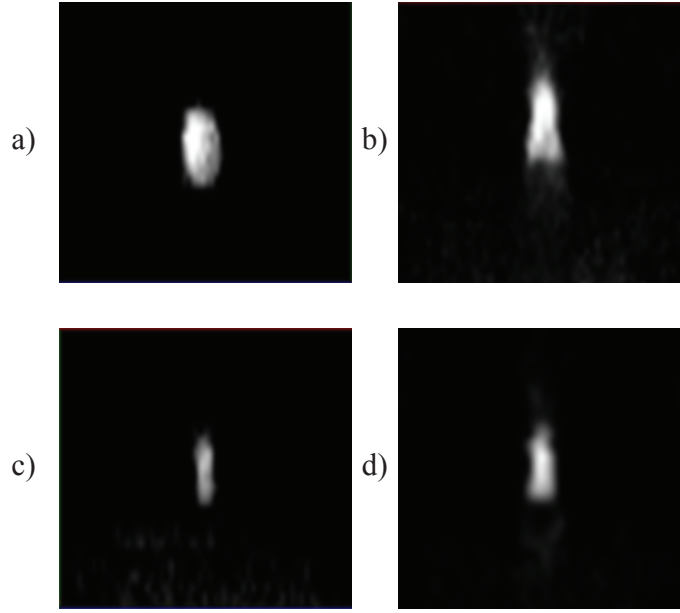


Figure 5.7: Cross sectional confocal images of SSD for constant flow rate ratios but different  $Re$  number: (a)  $Q_B = 1.5 \mu\text{l/min}$ ,  $\alpha_V = 2$ ,  $\alpha_H = 4$ ,  $Re = 6.4$ ; (b)  $Q_B = 5 \mu\text{l/min}$ ,  $\alpha_V = 2$ ,  $\alpha_H = 4$ ,  $Re = 30$ ; (c)  $Q_B = 0.5 \mu\text{l/min}$ ,  $\alpha_V = 4$ ,  $\alpha_H = 8.89$ ,  $Re = 7.6$ ; (d)  $Q_B = 4 \mu\text{l/min}$ ,  $\alpha_V = 4$ ,  $\alpha_H = 8.89$ ,  $Re = 30$ .

For  $\alpha_V = 1$  and  $\alpha_H = 4$  the shape of the sample is almost rectangular,  $h_e$  and  $v_e$  match  $h_s$  and  $v_s$  with  $\Delta h = 0.54\%$  and  $\Delta v = 1.2\%$ , Figure 5.6(a). When  $\alpha_V = 2$  without varying  $\alpha_H$ , the sample assumes an elliptic form, more similar to the simulation, and the difference in height increases to  $\Delta v = 4.7\%$ , Figure 5.6(b). According to the CFD,  $v_e$  reduces as  $\alpha_V$  increases up to  $\alpha_V = 3$ . Above this value,  $v_e$  reaches its minimum at  $20.11 \mu\text{m}$ ,  $21.16\%$  of the channel height. On the other hand,  $h_e$  follows  $h_s$  only until  $\alpha_H = 4$ , where  $h_e = 10 \mu\text{m}$ , Figure 5.6(b). For values above, as for  $\alpha_V = 4$  and  $\alpha_H = 8.89$ , however,  $h_e$  is smaller than predicted, with  $\Delta h = 2.52\%$ , as shown in Figure 5.6(c). Higher values of  $\alpha_V$  and  $\alpha_H$  will require an elevated velocity and Reynolds number, which can cause disruption of the cells membrane and lysis of cells. The smallest horizontal dimension achieved on SSD with these parameters,  $h_e = 6.64 \mu\text{m} = 6.64\%$  of the channel width, is of the same order of magnitude of an average B-cell,  $8 \mu\text{m}$  [72], which makes the device suitable for leukaemia studies, one of the higher level objectives of this research thesis. Due to cell-cell interaction, a configuration similar to Figure 5.6(c),  $v_e = 21 \mu\text{m}$  and  $h_e = 6.64 \mu\text{m}$ , should ensure that cells will flow into the device in single file.

The same flow rate ratio can be achieved at a different Reynolds number. Figure 5.7 depicts how size and shape of the focused sample can be influenced by this parameter. Images of Figure 5.7(a) and Figure 5.7(b) are both acquired at  $\alpha_V = 2$  and  $\alpha_H = 4$ , but with  $Re = 6.64$  ( $Q_B = 1.5\mu\text{l/min}$ ) and  $Re = 30$  ( $Q_B = 5\mu\text{l/min}$ ), respectively. While for  $Re = 6.64$  the sample presents the same shape as the CFD simulation, Figure 5.6(b), the typical parabolic flow structure of the laminar regime is observed on the side of the sample stream for  $Re = 30$ . The bow shaped profile, previously described by Walsh *et al.* [124], is less evident on the top and bottom of the sample. This is because, in order to have  $\alpha_H = 4$ ,  $Q_D$  has to be 10 times higher than  $Q_A$  and 20 times higher than  $Q_B$ . This was also observed by Hairer and Vellekoop [37]. For higher values of  $\alpha_V$  and  $\alpha_H$ , however, the bow profile is less evident, due to the small size of the focused core, Figure 5.7(b). The proposed geometry proved to be stable until  $Re = 30$ , which is 6 times the appropriate operating conditions of the device of Chang *et al.* [8].

Figure 5.8 plots the experimental and simulated vertical (a) and horizontal (b) focused sizes achieved on SSD for different flow rate ratios. The trend, in both dimensions, gradually reduces with the increase of  $\alpha_H$  and  $\alpha_V$ . This is less evident on the vertical focusing due to an odd value obtained for  $\alpha_V=2$ . Beside this value, the trends of  $v_e$  and  $v_s$  are in relative good agreement with an average scatter equal to  $\Delta v=2.6\%$ . The smallest focused height, equal to  $20.11\mu\text{m}$ , is reached for  $\alpha_V=3$ , but in the range  $1.5<\alpha_V\leq 4$  no significant variation is noticed on  $v_e$ , as predicted by the simulations. On the contrary, on the horizontal dimension  $h_e$  constantly reduces until  $6.64\mu\text{m}$ , Figure 5.8(b). This is probably related to the design of the 3D-HFMD which has the horizontal focusing element downstream the vertical. This means that, while the value of  $\alpha_V$  is exactly the ratio between  $Q_A$  and  $Q_B$ , in order to impose  $\alpha_H=4$ , for instance, the magnitude of  $Q_D$  must be four times  $2Q_A+Q_B$ , as explained before. Therefore, the horizontal focusing is probably more effective than the vertical. Figure 5.8(b) plots the horizontal focused size,  $h_e$ , against the flow rate ratio of vertical focusing,  $\alpha_H$ . Throughout the values,  $h_e$  follows  $h_s$  in trend and  $\Delta h$  is almost constant. Beside at  $\alpha_H=0.15$ , simulations overestimate the confocal results. The horizontal focused size varies from  $66.4\mu\text{m}$  to  $6.64\mu\text{m}$ . It is interesting to observe that when very little flow is imposed to inlets D,  $\alpha_H=0.15$ , the sample is already confined into 66% of the width.

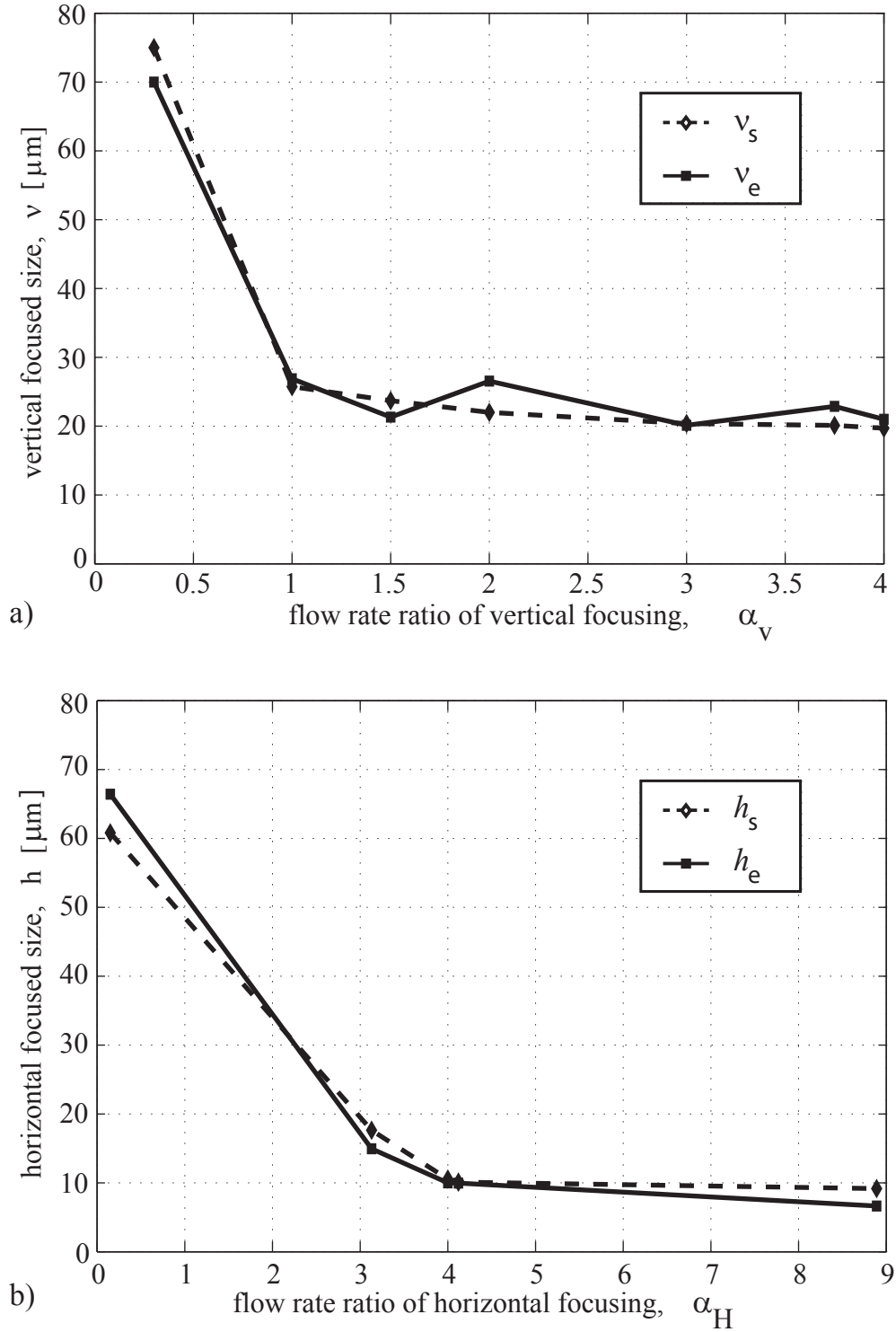


Figure 5.8: Comparison of the size of the focused sample achieved on SSD for different flow rate ratios. a) vertical dimension; b) horizontal dimension.

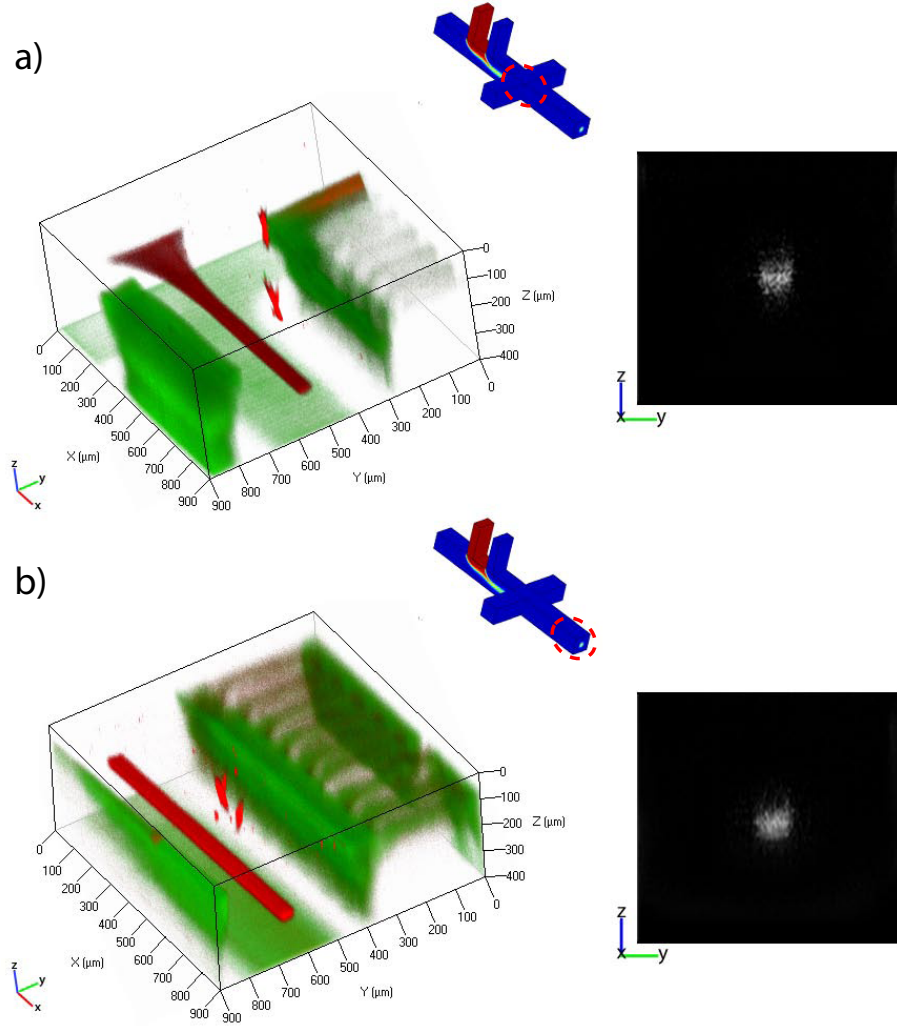


Figure 5.9: 3D views of the 3D focusing into LSD: (a) immediately downstream the intersection with D, (b) 11mm downstream E. Correspondent cross sections are shown on the right.  $Q_A = 4\mu\text{l/min}$ ,  $Q_B = 1\mu\text{l/min}$ ,  $Q_D = 36\mu\text{l/min}$ ,  $\alpha_V = 4$ ,  $\alpha_H = 4$ ,  $\text{Re}=1.9$  in either case.

### 5.2.3 LSD

The LSD was fabricated with channels of the same dimension of the prototype achieved from CNC manufacturing. On the SSD the 10x lens of the confocal microscope can visualise at a distance  $6W$  downstream E. Due to the larger size of the channels of LSD, images could only be acquired at a length  $1.25W$ , thus two distinct measurements were required:

1. Figure 5.9(a): just after the intersection with channel D;
2. Figure 5.9(b): 11mm downstream channel E in the position depicted on image III of Figure 5.1.

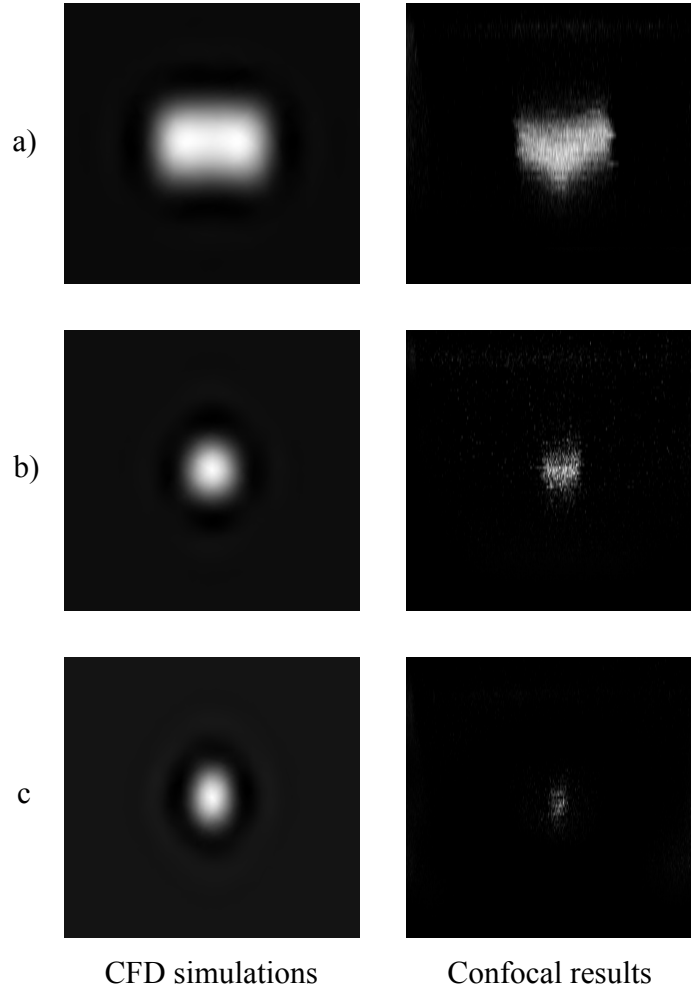


Figure 5.10: Comparison of CFD simulations to confocal images for cross sections of LSD. (a)  $Q_B = 5\mu\text{l/min}$ ,  $\alpha_V = \alpha_H = 1$ ,  $\text{Re} = 1.3$ , (b)  $Q_B = 1\mu\text{l/min}$ ,  $\alpha_V = \alpha_H = 4$ ,  $\text{Re} = 1.9$ , (c)  $Q_B = 0.4\mu\text{l/min}$ ,  $\alpha_V = \alpha_H = 10$ ,  $\text{Re} = 3.9$

An analogy between the two pictures of Figure 5.9 once again shows the stability of the device. The size of the sample core is almost unaltered for 11mm, equal to 27.5W, with  $h_e$  increasing 9.3% from 44 to 48.1 $\mu\text{m}$  and  $v_e$  varying 3.8% from 44.9 to 46.7 $\mu\text{m}$ . Therefore, for the remainder of the paper only measurements acquired immediately after the intersection with channel D will be considered.

In Figure 5.10 confocal results are compared to CFD simulations for three different flow rate ratios. The sample stream is always forced to flow in the centre of the channel, but at different focused dimensions. For  $\alpha_V = \alpha_H = 1$ , Figure 5.10(a), the sample stream matches the size of the simulation with an error margin of  $\Delta h = 1.45\%$  and  $\Delta v = 0.21\%$

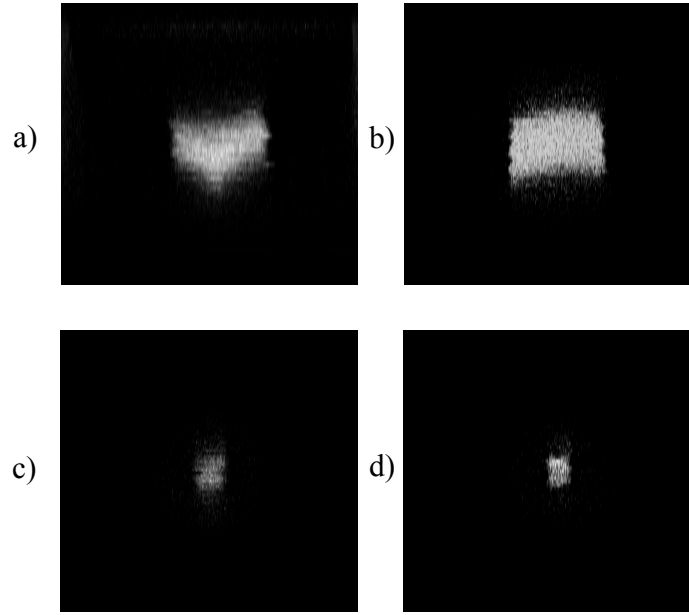


Figure 5.11: Cross sectional confocal images of LSD for constant flow rate ratios but different  $Re$  number: (a)  $Q_B = 5\mu\text{l/min}$ ,  $\alpha_V = \alpha_H = 1$ ,  $Re = 1.3$ ; (b)  $Q_B = 40\mu\text{l/min}$ ,  $\alpha_V = \alpha_H = 1$ ,  $Re = 10.3$ ; (c)  $Q_B = 0.5\mu\text{l/min}$ ,  $\alpha_V = \alpha_H = 6$ ,  $Re = 1.9$ ; (d)  $Q_B = 2.5\mu\text{l/min}$ ,  $\alpha_V = \alpha_H = 6$ ,  $Re = 9.8$ .

in the middle and  $\Delta v = 1.72\%$  on the side, but differs in shape, where two bow profiles are clearly visible on the bottom side. As  $\alpha_H$  and  $\alpha_V$  increase, a reduction in size of  $h_e$  and  $v_e$  is noticed and the simulations overestimate the experimental results. For  $\alpha_V = \alpha_H = 4$ , the focused stream assumes a more regular shape and its size is  $h_e = 48.16\mu\text{m}$  and  $v_e = 41.2\mu\text{m}$  with  $\Delta h = 3.71\%$  and  $\Delta v = 1.94\%$ , Figure 5.10(b). The smaller dimension is achieved for  $\alpha_V = \alpha_H = 10$ , where the sample is constrained in a region smaller than predicted,  $\Delta h = 5.48\%$  and  $\Delta v = 1.72\%$ , which is only 4.5% of the channel width and 8.33% of the channel height, Figure 5.10(c). The parameters of Figure 5.10(c), indeed, allow focusing on a very narrow region,  $h_e = 18\mu\text{m}$  and  $v_e = 33\mu\text{m}$ , with a main velocity on channel E equal to  $5.53 \times 10^{-3} \text{m/s}$  with  $Re = 3.9$ , which is a velocity suitable for cells [10, 59].

As for SSD, in Figure 5.11 the comparison between images achieved at the same flow rate ratios but different  $Re$  number is shown. Figure 5.11(a) and Figure 5.11(b) are both acquired at  $\alpha_V = \alpha_H = 1$  but at  $Re = 1.3$  ( $Q_B = 5\mu\text{l/min}$ ) and  $Re = 10.3$  ( $Q_B = 40\mu\text{l/min}$ ) respectively. The two images are very similar in size, 0.6% variation in  $h_e$  and 3.6% in  $v_e$  in the central region, but differ in shape. The result shown on the right presents a more

rectangular-like shape, according to the simulation of Figure 5.10(a), with a small bow effect on the bottom. For higher values of  $\alpha_V$  and  $\alpha_H$ , however, the two profiles are comparable in either dimension and form, Figure 5.11(c).

An accurate evaluation of the results shown in Figure 5.10 and Figure 5.11 depicts how the size of the focused sample reduces on LSD as the flow rate ratios increase from  $\alpha_V = \alpha_H = 1$  to  $\alpha_V = \alpha_H = 10$ . All the experimental and simulated vertical (a) and horizontal (b) focused sizes achieved on LSD for different flow rate ratios are plotted in Figure 5.12. Differently from SSD, the focusing effect is very effective on the sample sizes. On the horizontal dimension, in particular, the size can be controlled from  $184\mu\text{m}$  to  $18\mu\text{m}$ , which enables the device to be employed in a wide range of applications. Figure 5.12(a) shows the resultant vertical focused dimension against  $\alpha_V$ . The size can be controlled from  $173\mu\text{m}$  to  $32\mu\text{m}$  and the trends of  $v_e$  and  $v_s$  are very similar. In the range  $4 < \alpha_V \leq 12$ , the improvement in focused height is insubstantial, and  $v_e$  only varies by 2.6% from  $41.2\mu\text{m}$  to  $36.5\mu\text{m}$  according to the CFD data. This finding demonstrates that a high value of  $\alpha_V$  is not necessary, leading to a lower velocity imposed to the sample. Figure 5.12(b) illustrates the resultant horizontal focused size against  $\alpha_H$ . As previously mentioned,  $h_e$  can be controlled more efficiently, showing that the horizontal focusing is more influencing than the vertical for the reasons outlined in the discussion of Figure 5.8. In both vertical and horizontal dimensions, experiments and simulations are very similar in trend and the simulations overestimate the confocal results.

$\alpha_H$  and  $\alpha_V$  can be combined together in order to reach the desired focusing for any particular application. While a combination of  $\alpha_H = 0.4$  and  $\alpha_V = 4$  can be used when only vertical focusing is required, such as the optical counting technique of Section 6.2 or for  $\mu$ -PIV studies, on the contrary flow rate ratios  $\alpha_H = 7$  and  $\alpha_V = 1$  represent the 2D focusing technique mostly employed in the last 30 years. The small values of  $h_e$  and  $v_e$  reached in Figure 5.10(c),  $h_e = 18\mu\text{m}$  and  $v_e = 33\mu\text{m}$ , are ten to twenty times smaller than the channel dimensions and prove that a flow cytometer can be fabricated at a dimension achievable using CNC technology. All the sample sizes accomplished on both SSD and LSD at the different flow configurations and their comparison with CFD simulation are summarised in Table 5.1.

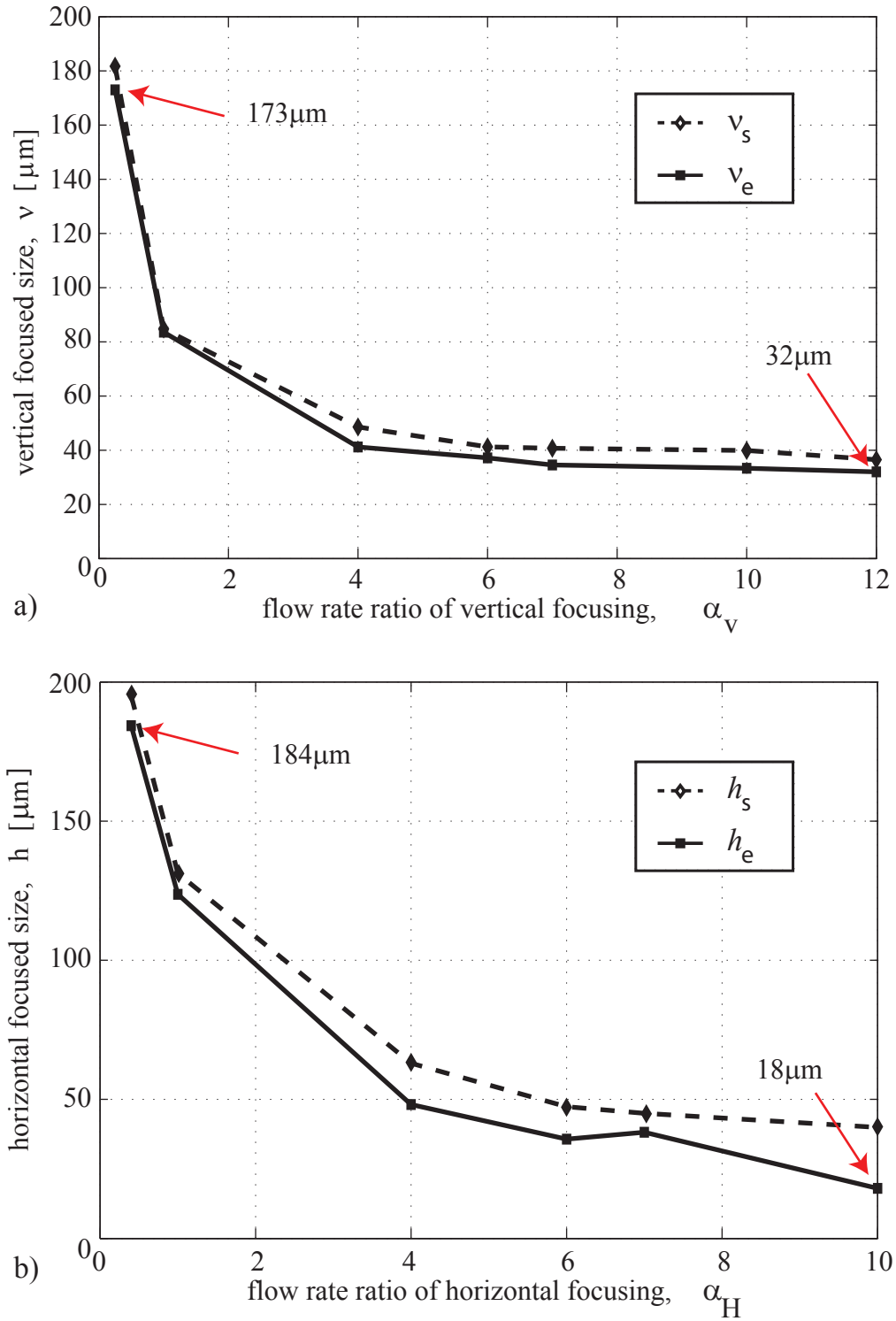


Figure 5.12: Comparison of the size of the focused sample achieved on LSD for different flow rate ratios. a) vertical dimension; b) horizontal dimension.

Table 5.1: Sample sizes achieved on the 3D-HFMDs

		$h_e$	$h_s$	$\Delta h$	$v_e$	$v_s$	$\Delta v$
SSD	$\alpha_V = 0.3$ $\alpha_H = 3.13$	14.94 $\mu\text{m}$	17.63 $\mu\text{m}$	2.69%	70 $\mu\text{m}$	75 $\mu\text{m}$	5.26%
	$\alpha_V = 1$ $\alpha_H = 4$	10 $\mu\text{m}$	10.54 $\mu\text{m}$	0.54%	26.88 $\mu\text{m}$	25.73 $\mu\text{m}$	1.2%
	$\alpha_V = 1.5$ $\alpha_H = 0.15$	66.42 $\mu\text{m}$	60.8 $\mu\text{m}$	5.62%	21.3 $\mu\text{m}$	23.69 $\mu\text{m}$	2.51%
	$\alpha_V = 2$ $\alpha_H = 4$	10 $\mu\text{m}$	10.59 $\mu\text{m}$	0.59%	26.54 $\mu\text{m}$	22 $\mu\text{m}$	4.7%
	$\alpha_V = 3$ $\alpha_H = 4$	9.96 $\mu\text{m}$	10.64 $\mu\text{m}$	0.68%	20.11 $\mu\text{m}$	20.37 $\mu\text{m}$	0.27%
	$\alpha_V = 3.75$ $\alpha_H = 4.12$	9.96 $\mu\text{m}$	10.1 $\mu\text{m}$	0.05%	22.87 $\mu\text{m}$	20.1 $\mu\text{m}$	2.91%
	$\alpha_V = 4$ $\alpha_H = 8.89$	6.64 $\mu\text{m}$	9.16 $\mu\text{m}$	2.52%	21 $\mu\text{m}$	19.7 $\mu\text{m}$	1.37%
LSD	$\alpha_V = 0.25$ $\alpha_H = 7$	38.19 $\mu\text{m}$	44.98 $\mu\text{m}$	1.69%	173 $\mu\text{m}$	181.7 $\mu\text{m}$	2.29%
	$\alpha_V = 1$ $\alpha_H = 1$	125.4 $\mu\text{m}$	131.2 $\mu\text{m}$	1.45%	83.59 <sup>a</sup> $\mu\text{m}$	84.39 $\mu\text{m}$	0.21% <sup>a</sup>
	$\alpha_V = 4$ $\alpha_H = 4$	48.16 $\mu\text{m}$	63 $\mu\text{m}$	3.71%	41.2 $\mu\text{m}$	48.59 $\mu\text{m}$	1.94%
	$\alpha_V = 6$ $\alpha_H = 6$	28.23 $\mu\text{m}$	48.53 $\mu\text{m}$	5%	37.15 $\mu\text{m}$	41.23 $\mu\text{m}$	1.07%
	$\alpha_V = 7$ $\alpha_H = 0.4$	184.3 $\mu\text{m}$	195 $\mu\text{m}$	2.67%	34.56 $\mu\text{m}$	40.71 $\mu\text{m}$	1.61%
	$\alpha_V = 10$ $\alpha_H = 10$	18 $\mu\text{m}$	39.92 $\mu\text{m}$	5.48%	33.35 $\mu\text{m}$	39.92 $\mu\text{m}$	1.72%
	$\alpha_V = 12$ $\alpha_H = 6$	30.72 $\mu\text{m}$	49.7 $\mu\text{m}$	4.75%	32 $\mu\text{m}$	36.5 $\mu\text{m}$	1.18%

<sup>a</sup>the maximum vertical focusing size is considered.

### 5.3 Particle focusing

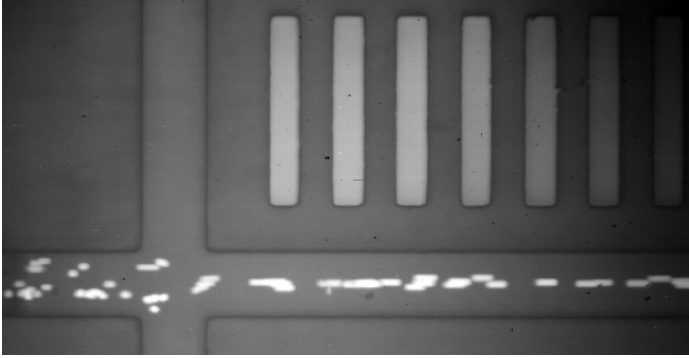
In order to test the efficiency of the proposed device, a very systematic approach was employed. First, the dye, easily checked against CFD, was used to test the diffusion of the liquid. Then, particles, more representative but not quite cells, were injected into the device. Finally, real cells were employed. While in the previous section it was stated that the device is capable to focus the sample into a region of the same order of magnitude of cells/particles of  $10\mu\text{m}$  in size; in this section, the ability of the 3D-HFMD to focus in single file will be demonstrated.

As reported in Section 3.3.3, red fluorescent  $10\mu\text{m}$  FluoSpheres® polystyrene microspheres were injected into inlet B in both SSD and LSD at different flow rates. Images of particles flowing into the device were then recorded and the path followed by the particles was tracked. The following figures are obtained applying a standard deviation to a stack of images, acquired at the same flow rates in a given time interval, and then superimposed the result on the illuminated background. This is done to give a special representation of the particle trajectory to the geometry, as the standard deviation will hide the stationary background in the stack images. The final result shows the area of the channel occupied by all the particles in the given experiment, rather than a frozen frame at a given instant.

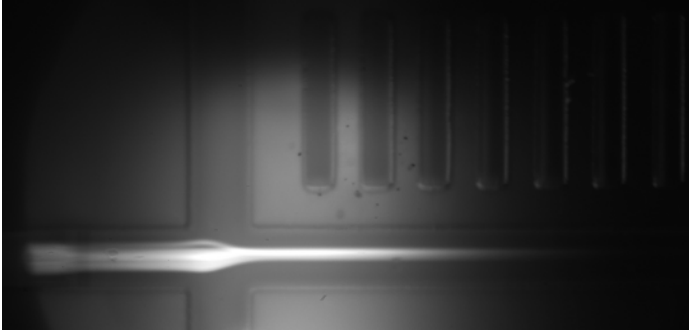
#### SSD

Figure 5.13(a) depicts particles focused in single file into SSD. A sequence of 50 frames are acquired at  $86\text{Hz}$  for  $\alpha_V = \alpha_H = 1.5$ . Whilst before the main intersection particles are distributed on along the width of the channel, after channel D the device is able to focus 85% of the particles into a region of approximately  $15.7\mu\text{m}$ , whereas the totality of them are constrained into  $24.8\mu\text{m}$ . Note that most of the non-aligned beads are clusters of particles stuck together. Since the velocity increases after the intersection with D, round microspheres appear streaking in channel E.

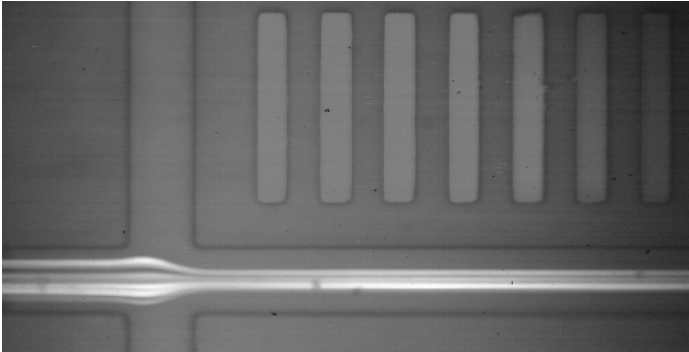
The same focusing result can be achieved at a higher  $Re$  number by acquiring frames with the 11Mp camera at a long exposure, Figure 5.13(b). In this situation a single particle



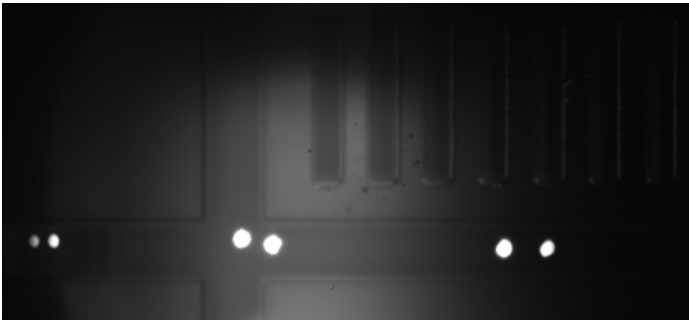
a) Image acquired at 86Hz.  $Q_A=0.3\mu\text{l/min}$ ,  $Q_B=0.2\mu\text{l/min}$ ,  $Q_D=1.2\mu\text{l/min}$ ,  $\alpha_V=\alpha_H=1.5$ ,  $Re=0.34$



b) Image acquired at 15Hz with a 11Mpixel camera at a long exposure.  
 $Q_A=7.5\mu\text{l/min}$ ,  $Q_B=5\mu\text{l/min}$ ,  $Q_D=30\mu\text{l/min}$ ,  $\alpha_V=\alpha_H=1.5$ ,  $Re=8.6$



c) Image acquired at 7Hz.  $Q_A=5\mu\text{l/min}$ ,  $Q_B=5\mu\text{l/min}$ ,  $Q_D=15\mu\text{l/min}$ ,  $\alpha_V=\alpha_H=1$ ,  $Re=5.31$



d) Stroboscopic image acquired with a dual Nd:YAG 15Hz pulsed laser.  
 $Q_A=7.5\mu\text{l/min}$ ,  $Q_B=5\mu\text{l/min}$ ,  $Q_D=30\mu\text{l/min}$ ,  $\alpha_V=\alpha_H=1.5$ ,  $Re=8.6$

Figure 5.13: Hydrodynamic focusing of 10µm microbeads into SSD.

is illuminated for the full length of the field of view and the streak shows the trajectory travelled by the particle. By applying the standard deviation to a stack of 20 images, as described before, the total width covered by the streaks is shown equal to  $21.5\mu\text{m}$  for  $\alpha_V = \alpha_H = 1.5$ . No evident information is deduced about the vertical displacement from the intensity of the traces.

For low flow rate ratios, as expected, the particles' trajectories occupy a larger region on the horizontal direction. Figure 5.13(c), depicts a stack of 20 images recorded at 7Hz in which the streaks fill 33% of the channel width for  $\alpha_V = \alpha_H = 1$ . Due to the relative small size of the channels and to particle-particles interaction while flowing into the fluid,  $33\mu\text{m}$  was the largest focused area occupied by the particles achieved during testing on SSD.

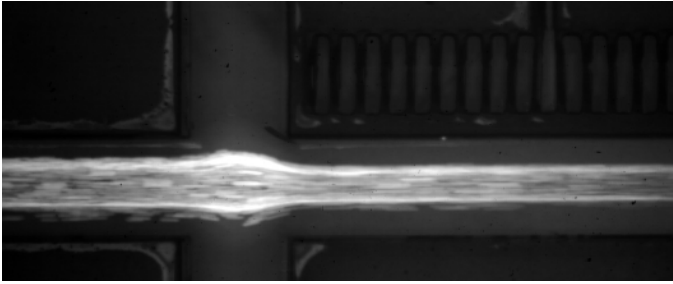
A singular way of visualising the trajectory is illustrated in Figure 5.13(d). This is a single stroboscopic frame acquired illuminating the test-piece with a 15Hz dual Nd:YAG pulsed laser. With the exposure of the camera set to a high value, 0.22s, the dual laser was flashing three times during this interval, with a very brief  $\Delta t$  between the two flashes of the same pulse. In this way, in each frame the same particle is impressed six times, and its trajectory while moving into the device can be easily followed. In Figure 5.13(d) the same bead is observed while approaching the main intersection, then directing towards the center of channel E and finally centrally focused.

These tests proved that particles of  $10\mu\text{m}$  in size can be successfully focused in single file into SSD.

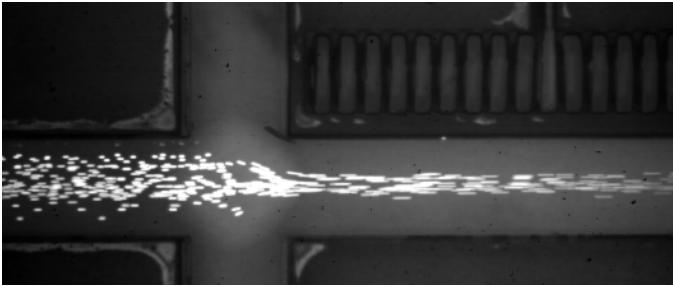
## LSD

The same focusing result can also be performed on LSD, where the size of the channels is  $400 \times 380\mu\text{m}$ . Due to the channel dimensions, higher flow rates can be imposed without significantly increasing the particle velocity. The dataset of Figure 5.14, recorded using a CMOS camera at different frame rates and a 4x objective lens, show the different focusing size achieved during testing on LSD.

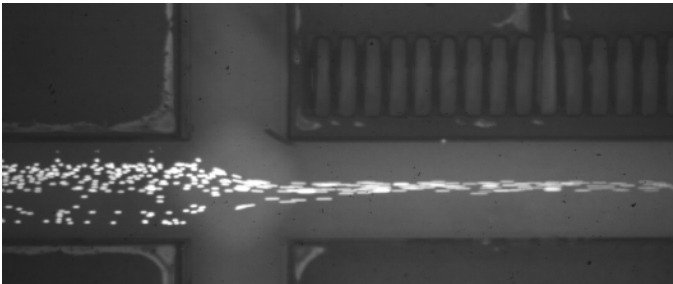
When minimal focusing is imposed, beads occupy the full dimension of the channel. Figure 5.14(a) is an image deriving from a stack of 100 consecutive frames recorded at



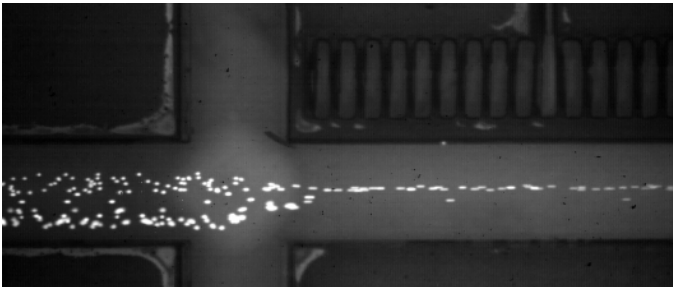
a) Image acquired at 60Hz,  $\alpha_v=0.13$ ,  $\alpha_H=0.32$ .  $Q_A=5\mu\text{l/min}$ ,  $Q_B=40\mu\text{l/min}$ ,  $Q_D=16\mu\text{l/min}$ ,  $Re=2.8$



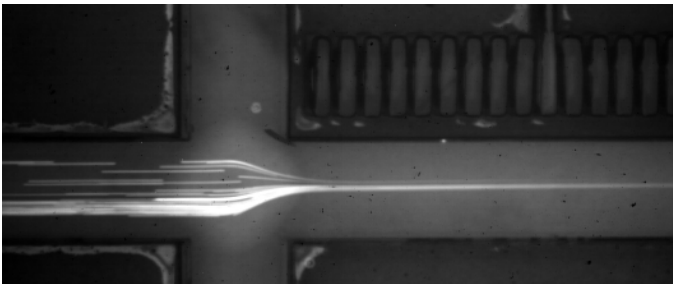
b) Image acquired at 60Hz,  $\alpha_v=1.67$ ,  $\alpha_H=1.23$ .  $Q_A=5\mu\text{l/min}$ ,  $Q_B=3\mu\text{l/min}$ ,  $Q_D=16\mu\text{l/min}$ ,  $Re=1.2$



c) Image acquired at 60Hz,  $\alpha_v=1.33$ ,  $\alpha_H=1.36$ .  $Q_A=4\mu\text{l/min}$ ,  $Q_B=3\mu\text{l/min}$ ,  $Q_D=15\mu\text{l/min}$ ,  $Re=1.12$



d) Image acquired at 86Hz,  $\alpha_v=4$ ,  $\alpha_H=2$ .  $Q_A=4\mu\text{l/min}$ ,  $Q_B=1\mu\text{l/min}$ ,  $Q_D=18\mu\text{l/min}$ ,  $Re=1.16$



e) Image acquired at 20Hz,  $\alpha_v=2$ ,  $\alpha_H=4$ .  $Q_A=20\mu\text{l/min}$ ,  $Q_B=10\mu\text{l/min}$ ,  $Q_D=200\mu\text{l/min}$ ,  $Re=10.7$

Figure 5.14: Hydrodynamic focusing of 10 $\mu\text{m}$  microbeads into LSD.

60Hz for  $\alpha_V = 0.13$  and  $\alpha_H = 0.32$ . Due to the high flow rate imposed to inlet B,  $Q_B = 40\mu\text{l/min}$ , the traces appear streaking in the image. This is the largest focused width which was possible to reach on LSD, equal to  $200\mu\text{m}$  and 50% of the channel size.

The flow rate ratios can be adjusted depending on the application required. By increasing the values for  $\alpha_V$  and  $\alpha_H$  the focusing improves and the throughput reduces. Figure 5.14(b) is achieved from a 125 frameset acquired at 60Hz for  $\alpha_V = 1.67$  and  $\alpha_H = 1.23$ . The area covered by the microbeads is approximately  $100\mu\text{m}$ , 25% of the channel width. Even if the frame rate was unchanged from the previous test, the particle shape is more recognisable due to the lower value of  $Q_B$ .

Between Figure 5.14(b) and (c), the horizontal focusing effect was intensified,  $\alpha_H = 1.36$ , while the vertical process was reduced to  $\alpha_V = 1.33$ . As expected, the focused width was further reduced to  $61\mu\text{m}$ , 15% of the channel dimension, for the full visible length, 1.5mm equal to 3.75W. In each frame the image is slightly darker on the right side, but this is due to the illumination source and no visible information is deduced for the vertical displacement of the particles. This image is the result of 125 frames recorded at 60Hz.

Figure 5.14(d) is obtained from a stack of 176 consecutive frames with  $\alpha_V = 4$  and  $\alpha_H = 2$ . A  $28.3\mu\text{m}$  focusing width, 7% of the channel dimension, is achieved for 95% of the beads.  $10\mu\text{m}$  particles are shown to be successfully lined up for a length of 1.5 mm. Only two over forty four particles would have been missed by a single-cell detection method in this particular test. The frame rate was also brought to 86Hz without increasing the main velocity. For this reason, round microspheres appear less streaking on the image. In all the results reported before,  $Re$  was always below 2.8.

Figure 5.14(e) shows the smallest focusing size obtained on LSD, reached for flow rate ratios  $\alpha_V = 2$  and  $\alpha_H = 4$ . Figure 5.14(e) is derived from a stack of 108 frames acquired at 20Hz. Flow rates were considerably increased,  $Q_B = 10\mu\text{l/min}$  and  $Q_D = 200\mu\text{l/min}$  with  $Re = 10.7$ , and the particles appear as long streaks in the image. The focused size, approximately  $22.8\mu\text{m}$ , is 50% of the width achieved by the confocal experiments at the same flow configurations, which confirms the assumption made in the flow visualisation section. These results indicate that the organisation of particles is primarily a function of the particle

diffusion coefficient rather than interactions between the particles and the flow or geometric arrangement of the device, *e.g.* Saffman effects etc.

In this research thesis particles are shown to be focused in single file in both SSD and LSD on a device able to fully control position and size of the focused stream. This allows the integration of the 3D-HFMD upstream a detection system and will add the potential to present cells/particles to a sensing area for individual analysis. The device also demonstrated to be stable until  $Re = 30$ , which is six times higher than the appropriate operating condition of the device of Chang *et al.* [8]. Videos of particles focused into the two devices are available in Appendix C. Videos VII and VIII, respectively, show the particles and the streaks highlighting the trajectory of the particles focused in single file into SSD. Video IX is the video from which the 125 frames of Figure 5.14(b) were mounted. Finally, Videos X and XI correspond to the frames of Figure 5.14(c) and (d).

In the next section, the application of the 3D-HFMD to biological cells is presented.

## 5.4 Cell focusing

Working with living organisms involves a series of complications which are not present in fluorescent particles studies. As underlined by Messner [79]: “... cells are a whole different beast because they are very small and they are very complicated. If you think about a cell as a machine, you have on the order of 100 million proteins or parts. They are far more complicated than even the largest engineered system, than the Space Shuttle”. Even if in most studies cells are modelled as uniform spheres [28, 33], the differences are many. As summarised in Table 5.2, while particles are made of a solid and rigid material, biological cells can deform and disintegrate in response to certain stimulations and forces. The microscopic structure of a cell contains nuclear and cytoplasmic material of aqueous consistency, enclosed by a semipermeable membrane. Due to the different physical response of the membrane under shear stress, the cell shape can differ from steady state to motion. Also, in the case of the lymphocytes studied in this research thesis, their size varies considerably up to 50% of the average value [72]. Cells behaviour is also influenced by their

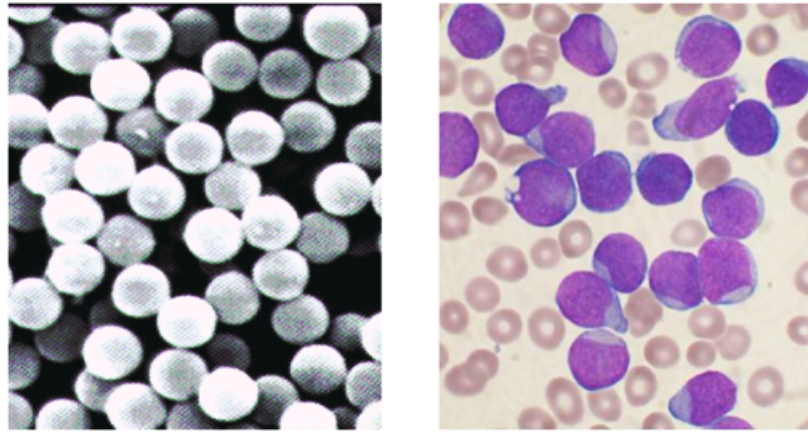


Table 5.2: Particles VS biological cells. Right image: Lymphoblasts in a bone marrow smear from a 3-year-old male with acute lymphoblastic leukemia. Source: Soldin *et al.* [114]

	Particles	B-Cells
Size	$10\mu\text{m} \pm 1\mu\text{m}$ [48]	4.8-12 $\mu\text{m}$ [72]
Shape	Homogeneous	Non Homogeneous
Solidity	Solid	Deform and Disintegrate

stage into the cells cycle. Samples belonging to the same population behave in a different manner when affected by the same stimuli. In their doubling phase, for instance, if the daughter cells are not fully detached from the parental cells, they often result as two cells attached to each other, see the red circle of Figure 5.15(b). Also, biological cells may experience additional hydrodynamic forces than particles in the flow field [16]. Finally, changes in the external environment, such as temperature drop or rise, contamination of the working ambient, use of a new cell batch, can also affect the cell response. In order to optically visualise the cells, their velocity should be maintained within a given range. In the experiments carried out during this work, in velocities above 5 cm/s the shear stress generated to the cells shrank and modified their original round shape or even caused lysis of the membrane, as documented in Section 6.3.

The framesets in Figure 5.15 show human lymphocytes, B-cell precursor leukaemia, focused into LSD, recorded with the 11Mp CCD camera and a 40X lens. The images are acquired 900 $\mu\text{m}$  downstream the intersection with channel D halfway through the channel height. The use of a lens with a bigger magnification reduces the size of the field of view, thus the channel walls are not visible. However, this was required in order to detect the low

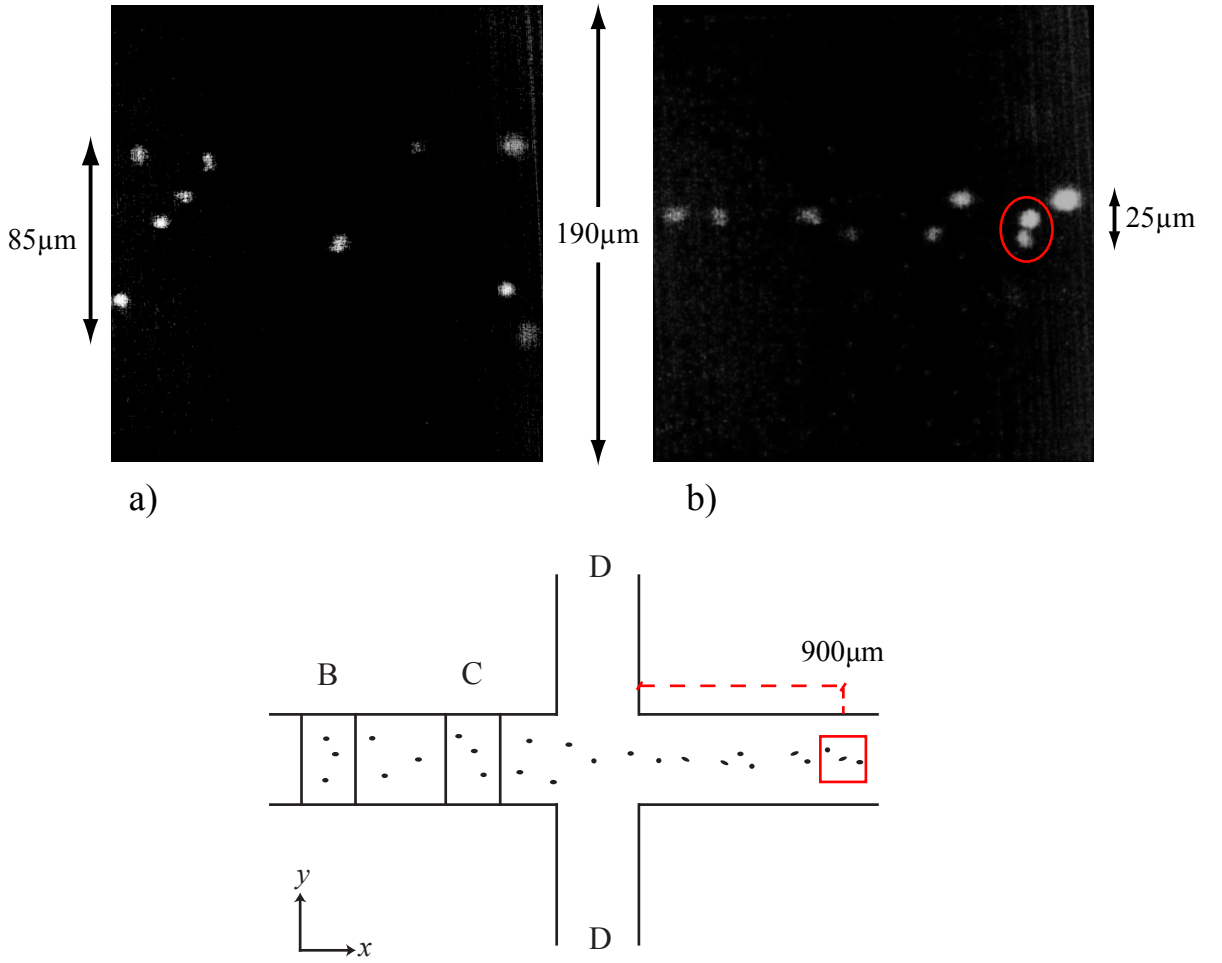


Figure 5.15: Human B-cell precursor leukaemia focused into LSD at two different focused values. a) single frame extracted from a video obtained for flow rates  $\alpha_V = 0.5$  and  $\alpha_H = 1$ ; b) single frame extracted from a video obtained for flow rates  $\alpha_V = 1.5$  and  $\alpha_H = 2$ .

signal emitted by the cells. The fluorescent intensity scattered by the cells, in fact, is lower than the intensity emitted by the particles. Moreover SU-8, with which the 3D-HFMD is fabricated, has its own low fluorescent emission in the range 380-500nm which contributes in increasing the background noise. An undesired fluorescence contribution is also added by the cells surrounding environment, the RPMI-1640 medium. For these reasons, the images are not as clear as those presented in Chapter 6.

In Figure 5.15, the size of the focused area is compared for two flow rate ratios. The fluorescence intensity of the cells is not constant within the same image. This is due to a combination of reasons: first, cells may be located at different depths in the microchannel and the intensity is proportional to their distance from the focal plane, as documented in

Section 6.2. Second, if the size distribution of the cells is wide, bigger cells emit a greater scatter. Finally, as a result of an intrinsic difference in their behaviour due to the stage they occupy on the cell cycle. Figure 5.15(a) depicts a single frame extracted from a video of B-cells, attached in Appendix C, flowing into the channel at a focusing ratio of  $\alpha_V = 0.5$  and  $\alpha_H = 1$ . The width occupied by the lymphocytes is approximately  $85\mu\text{m}$ , which is 21% of the channel size, for a main velocity of  $1.75\text{ mm/s}$ . From the video is it possible to observe the different velocity at which cells flow into the channel, due to the vertical position occupied in the channel. Some cells also appear blurring in the video. Those out-of-focus cells are outside the measurement depth and would not contribute significantly to the detection.

Figure 5.15(b) is the superposition of two frames extracted from a video of the lymphocytes flowing into the LSD at  $\alpha_V = 1.5$  and  $\alpha_H = 2$ . This is the smallest focused area accomplished on the 3D-HFMD with cells. In these specific frames the cells are confined into  $25\mu\text{m}$ , approximately 6% of the channel width. With the exception of the two cells highlighted in the red circle, the majority of them pass the detection region in single file even if the focused area is wider than an average cell size. This is because, as simulated by Fu *et al.* [30] using particles, when two cells approach and then enter the focusing region, they are gradually segregated in the vertical dimension. Thus, after the main intersection, cells retain their vertical spacing and remain focused in the  $x$ - $z$  plane. This does not happen to the cells attached to each other into the red circle. From an analysis of Video XII it is interesting to observe that even if the attached cells flow together, they have two distinct spin axes.

Engineers commonly look at the relationship between time and response. In biology, however, that time relationship is not well characterized because it is hard to isolate and look at living systems over time [79]. The investigation of an extremely large number of consecutive images of cells in motion can add information about the cells behaviour over time. In this work, a standard deviation was applied to a stack of images acquired at the same flow rates, as previously performed in the particles section, in order to follow the path travelled by each cell into the channel in a given time interval. Due to the low velocity of cells, in the time  $\Delta T$  between each frame the cells only travel a short distance  $\Delta s$  and their

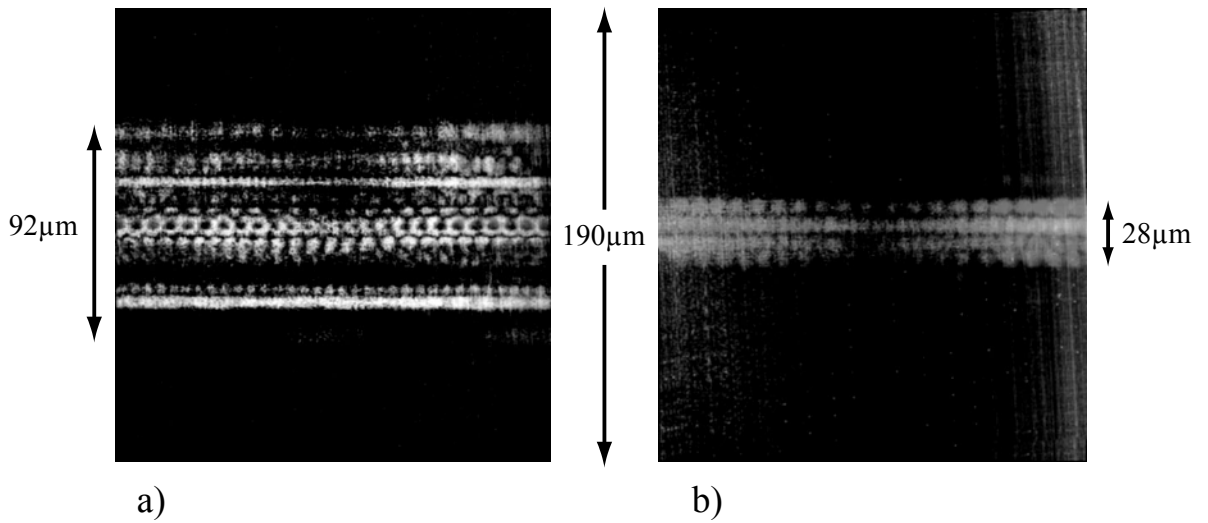


Figure 5.16: Hydrodynamic focusing of Human B-cell precursor leukaemia into LSD. a) image obtained from a stack of 100 frames; b) image obtained from a stack of 200 frames.

trajectory can be easily followed. Figure 5.16 shows both a global information about the test, the space occupied by all cells into the channel, and a local information, the trajectory covered by each lymphocytes. In both frames cells are less visible in the centre of the field of view, in correspondence to the illumination source. At this point the light emitted by the mercury lamp covers the scatter of the cells which is therefore neglected. On the analysis of over 200 frames, the totality of them are confined into a region of  $92\mu\text{m}$ , Figure 5.16(a), and  $28\mu\text{m}$ , Figure 5.16(b), for  $\alpha_V = 0.5$  and  $\alpha_H = 1$  or  $\alpha_V = 1.5$  and  $\alpha_H = 2$ , respectively. Even if cells are spinning along their rotational axis, as observed in Video XIII, the trajectory is a straight line.

3D focusing is not fully accomplished as in the particle studies because some cells are noticed moving faster than the others. However, considering the difficulties involved in optically visualising the cells in motion, a visual investigation showed that only 10% of the cells were not flowing at the same velocity (with the assumption that same velocity=same position into the channel). To the knowledge of the author, this is the first example showing biological cells 3D hydrodynamic focused into a device of the same dimension of the prototype readily fabricated by CNC manufacturing. A video recording of cells flowing into LSD is available in Appendix C. Video XII shows the focusing obtained in Figure 5.16(a). Video XIII shows the smallest focused area achieved with cells in the device.

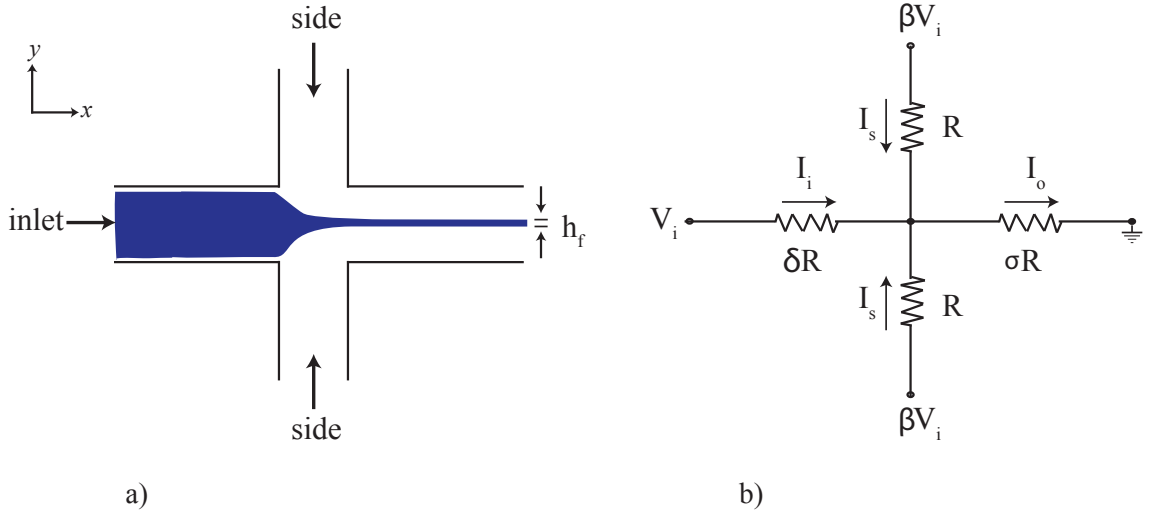


Figure 5.17: Model developed by Knight *et al.* [57] using the electronic-hydraulic analogy. a) Hydrodynamic focusing on a T junction; b) correspondent resistive circuit.

## 5.5 Theoretical model to predict the focused stream size

Accurately predicting the size of the focused stream is crucial in various applications, including micro-flow cytometry and diffusion-based mixing. As shown in the previous sections, the dimension of the sample core can be controlled by adjusting the flow rates of sheath and sample fluids and varied from the size of a cell, for single cell analysis, to that of the channel, for high throughput applications. For example, the throughput of the optical counting technique of Chapter 6 can be predicted by achieving a precise control of the focused sample height. Also in diffusion-based mixers, the diffusion characteristic length, which determines the mixing time, depends on the width of the focused stream. In general, the diffusion time increases as the size of the focused stream reduces. As outlined by Lee *et al.* [60], developing suitable techniques to control the dimension and position of the center stream is a key aspect of implementing HF schemes in microfluidic devices. To date various theoretical models have been proposed for both 2D [57,60,61,115] and 3D [8] hydrodynamic focusing, but these are limited in the range of channel aspect ratios or use complicated formulas.

Knight *et al.* [57] employed the electronic-hydraulic analogy [25] to develop an expression to describe the width of the focused inlet stream against  $\beta$ , the ratio of the side port

pressures to that of the sample port. The fluid flow on a T junction, Figure 5.17, is simplified to a circuit model with a network of resistors having resistance of the side, inlet and outlet arms equal to  $R$ ,  $\delta R$  and  $\sigma R$ , with the assumption that the flow is laminar and the width of the intersection negligible compared to the length of the channels. The parameters  $\delta$  and  $\sigma$  indicate dissimilarities in channel geometry. Consequently, in a rectangular microchannel the focusing ratio is described in eq. 5.4:

$$\frac{h_f}{W} = G \frac{(1 + 2\sigma - 2\sigma\beta)}{(1 + 2\sigma\delta\beta)} \quad (5.4)$$

where  $h_f$  is the focused width,  $W$  is the width of the outlet channel,  $\beta = P_s/P_i$  is the ratio of the side and sample pressures and  $G$  is a constant of order 1 dependent on channel geometry. However, this equation is only valid in the limit of  $h_f/W \ll 1$  and is not capable of directly predicting the value of  $h_f$ .

An expression to describe the focused stream width using an analogous circuit has also been derived by Stiles *et al.* [115]. For mechanically pumped systems the focused width is determined by eq. 5.5:

$$\frac{h_f}{W} = \frac{Q_i}{Q_i + 2Q_f} \quad (5.5)$$

where  $Q_i$  and  $Q_f$  denote the inlet and sheath flow rates respectively. However, this model is limited to geometries in the Hele-Shaw limit, with a high channel width to channel height (*i.e.* a low aspect ratio  $\epsilon = H/W$ ).

A different approach is that of the Lee group, using the mass conservation principle to derive equations to predict the width of the centre stream. In Lee *et al.* [61], the focused stream width of the cytometer depicted in Figure 5.18, made of a single channel with an inner and outer nozzle, is related to the velocity ratio between inlet and side flows using eq. 5.6:

$$h_f = \frac{\rho_a W}{1.5(\rho_1 \frac{u_1}{u_2} \frac{D_1}{D_2} + \rho_2 + \rho_3 \frac{u_3}{u_2} \frac{D_3}{D_2})} \quad (5.6)$$

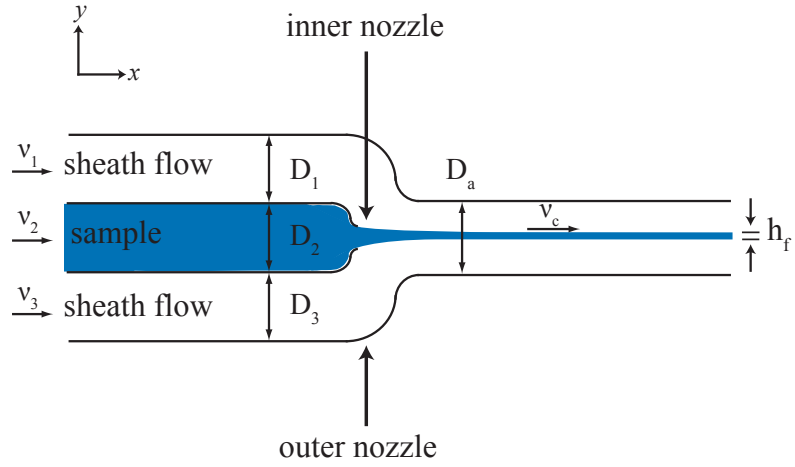


Figure 5.18: Schematic representation of the theoretical model for a micro-flow cytometer with a inner and outer nozzle. Adapted from Lee *et al.* [61]

where the subscripts  $a$ ,  $1$ ,  $2$  and  $3$  indicate the outlet and the different sections of the channel,  $\rho$  is the density of the fluid,  $D$  is the width of the different sections and  $u$  the velocity. The width of the focused stream is therefore directly proportional to the volumetric flow rate of the sample and inversely proportional to the relative sheath and sample flow rates. However, this model is limited to channels with a high aspect ratio and is again valid only for  $h_f / W \ll 1$ .

More recently, Lee *et al.* [60] proposed a more general expression to determine the width of the sample core for both symmetric and asymmetric hydrodynamic focusing in rectangular microchannels using the mass conservation principle. With the assumption that the flow is laminar, fluids are Newtonian and have the same density and channels are of the same height, the relationship between the focused stream width and the volumetric flow rates in the symmetric case of Figure 5.17(a) is described in the following equation:

$$\frac{h_f}{W} = \frac{Q_i}{\gamma(Q_i + 2Q_s)} \quad (5.7)$$

where  $Q_i$  and  $Q_s$  are the flow rates of sample and sheath fluids and  $\gamma$ , the ratio between the average velocities in the focused sample ( $u_f$ ) and outlet channel ( $u_0$ ), is given by eq. 5.8:

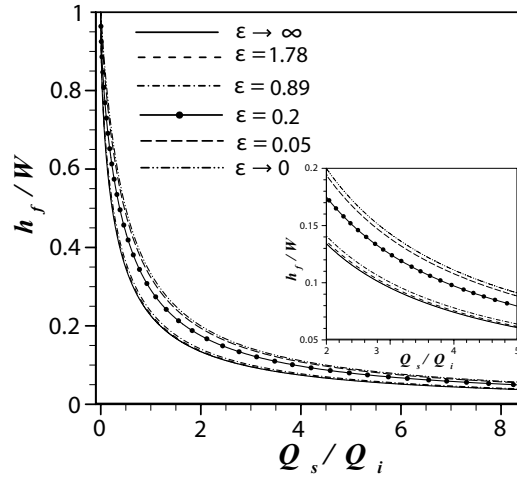


Figure 5.19: Comparison of the normalised width of the focused sample as a function of the flow rate ratios for different channel aspect ratios  $\epsilon$ . Adapted from Lee *et al.* [60]

$$\gamma = \frac{u_f}{u_o} = \frac{\left\{ 1 - \left( \frac{192H}{\pi^5 h_f} \right) \sum_{n=0}^{\infty} \frac{1}{(2n+1)^5} \frac{\sinh\left[(2n+1)\pi \frac{h_f}{2H}\right]}{\cosh\left[(2n+1)\pi \frac{W}{2H}\right]} \right\}}{\left\{ 1 - \left( \frac{192H}{\pi^5 W} \right) \sum_{n=0}^{\infty} \frac{1}{(2n+1)^5} \frac{\tanh\left[(2n+1)\pi \frac{W}{2H}\right]}{(2n+1)^5} \right\}} \quad (5.8)$$

where  $H$  is the height of the channel. This velocity ratio is therefore dependent on the channel aspect ratio,  $\epsilon = H/W$ , and the focused stream dimension,  $h_f$ . In the particular case of a rectangular microchannel with a low aspect ratio [115], *i.e.*  $\epsilon \rightarrow 0$ , the velocity profile is parabolic across the channel height and  $\gamma = 1$ , see eq. 5.5. On the contrary, in the case of a microchannel with a high aspect ratio [61], *i.e.*  $\epsilon \rightarrow \infty$ , the velocity profile is parabolic across the channel width and  $\gamma = 1.5$ . This model imposes no limitation on the value of  $\epsilon$  or to the ratio  $h_f/W$ . Moreover, this approach is also valid for 3D-HF, as shown by the same group in Chang *et al.* [8].

Eq. 5.7 is the most accurate model developed for rectangular microchannels. However, since  $\gamma$  involves considerable computational complexity, because  $\gamma$  and  $h_f$ , which show a nonlinear relationship, are mutually dependent [60], a CFD simulation is as easily done. For a given value of  $\epsilon$ , the relationship between the focused width and the flow rate ratios can therefore be expressed by first solving  $\gamma$  in eq. 5.8, and then substituting the result into eq. 5.7. The trend of this relationship for different values of  $\epsilon$  is depicted in Figure 5.19. As

expected, the focused stream width is larger for low flow rate ratios, defined as  $\alpha = Q_s/Q_i$  for the 2D focusing, and reduces when  $\alpha$  increases.

In this research thesis, a simple approximation of this theory, based on a semi-empirical investigation, is presented for rectangular microchannels. In the proposed model, the size of the focused sample is derived from the ratio between the volumetric flow rate of the sample and that of the total fluid in the outlet channel.

First, an assumption is made. In the particular case of high flow rate ratios (*i.e.* the focused width is small relative to the overall channel) the average velocity of the sample core can be approximated to the maximum velocity of the overall fluid, as seen in Fig. 5.20. Thus, the flow rate ratio of the sample fluid can be explicated as in eq. 5.9:

$$Q_i = u_{max} h_f W \quad (5.9)$$

where  $u_{max}$  is the maximum velocity in the outlet channel and  $h_f$  is the size of the focused sample. The flow ratio ratio of sample and overall fluid can therefore be explicated as in eq 5.10:

$$\frac{Q_i}{Q_t} = \frac{u_{max} h_f H}{u_{avg} W H} = \frac{u_{max} h_f}{u_{avg} W} \quad (5.10)$$

where  $u_{avg}$  is the average velocity in the outlet channel. From this equation it can be easily noticed that, in order to find  $h_f$ , the other terms of the equation are easily determined.  $Q_i$  is the flow rate of the sample imposed to the syringe pump,  $Q_t$  is the flow rate of sample and sheath fluids and  $W$  is the channel dimension. Thus, the ratio between focused width and channel size,  $h_f/W$ , only depends on two terms: the first is related to the settings imposed to the test (flow rate ratios); the second is connected to the geometry of the device (velocity ratios), eq. 5.11:

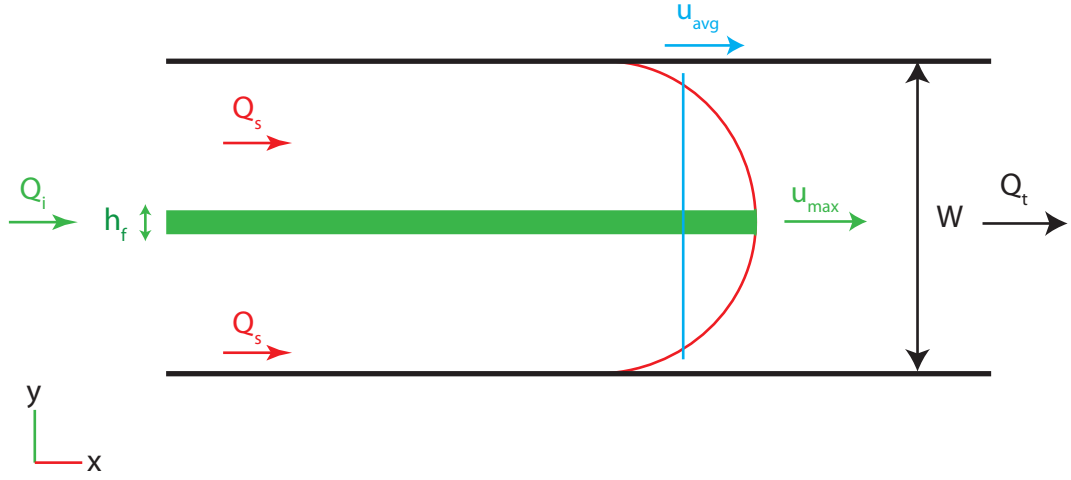


Figure 5.20: Schematic representation of the semi-empirical model to predict the size of the focused sample.

$$\frac{h_f}{W} = \frac{Q_i}{Q_t} \frac{u_{avg}}{u_{max}} \quad (5.11)$$

For fully developed laminar flows, the maximum velocity  $u_{max}$ , which is achieved in the centre of the channel width, can be calculated by multiplying the average velocity in the outlet channel,  $u_{avg}$ , by a constant,  $\chi$ , which depends on the channel aspect ratio  $\epsilon$ . Once  $\epsilon$  is fixed,  $\chi$  can be easily found in any fluid dynamics book, such as Shah and London [108], and varies from 1.5 for  $\epsilon = 0$ , to 2.0962 in squared microchannels,  $\epsilon = 1$ . The average velocity in the outlet channel,  $u_{avg}$ , is simply obtained from the total flow rate,  $Q_t = Q_i + nQ_s$ , where  $n$  is the number of merging streams, divided by the area occupied by the overall fluid, *i.e.* sample and sheath fluids,  $A = W * H$ . This is possible because the flow in the outlet channel is assumed fully developed, as shown in Section 5.5.1, and the combination of sample and sheath fluids form a parabolic velocity profile along the  $y$  axis, as depicted in Fig. 5.21. In the particular case of a squared microchannel, similar to the design of the 3D-HFMD,  $u_{max}$  is twice  $u_{avg}$  and the model is further simplified to eq. 5.12:

$$\frac{h_f}{W} = \frac{Q_i}{2Q_t} \quad (5.12)$$

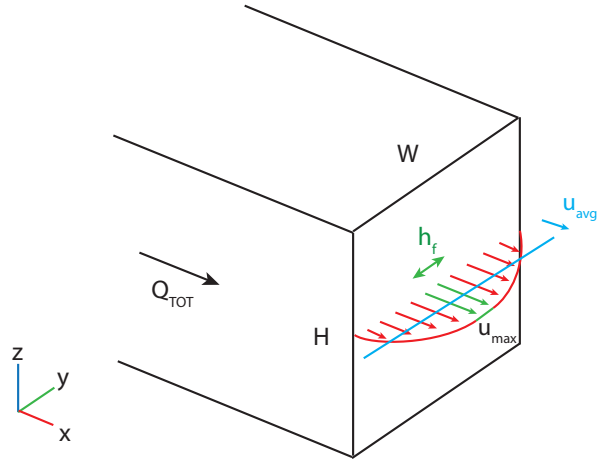


Figure 5.21: Schematic representation of the determination of the average velocity in the outlet channel.

This means that, once the geometry of the device is established, a given flow rate ratio can be imposed to the syringe pump in order to predict in advance the size of the sample core expected in that particular experiment. This would save precious experimental time and cost. It is important to underline that this technique can be applied to any rectangular microchannel with a minimum of one sheath fluid, but only works for high flow rate ratios and if the focused flow is centrally located.

The proposed model is validated against the theory of Lee *et al.* [60] in Figure 5.22 for the specific aspect ratio of the 3D-HFMD,  $\epsilon = 0.95$ . The theoretical curve is simplified to a sequence of segments which follows the theory in trend, as shown by the red line of Figure 5.22. The mismatch between the two curves is relatively high for low values of  $\alpha$ , but progressively reduces with the increase of the flow rate ratio until the simplified model perfectly matches the theory. While at  $\alpha = Q_s/Q_i = 0.15$  the percentage error is approximately 32%, in the region  $\alpha > 4$  the values are getting closer with a maximum mismatch below 11% and are almost identical for  $\alpha > 9$ . However, the scatter is higher in geometries with a low aspect ratio. The larger percentage error, equal to 38%, is found at  $\alpha = 2$  for  $\epsilon \rightarrow 0$ . To summarise, the simple model can be employed when the flow rate ratios are reasonably high. This is not a real limitation because in practice, that is why focusing is done: there is no need to do focusing at low flow rate ratios as nothing is really achieved.

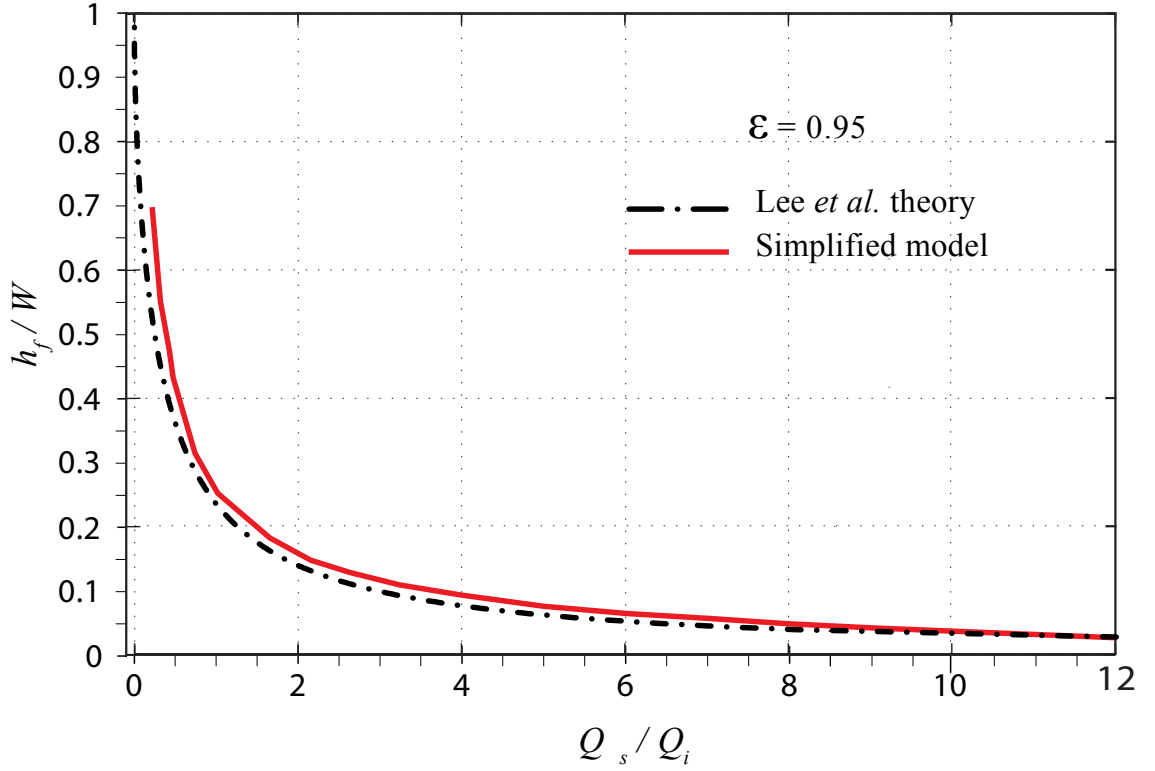


Figure 5.22: Comparison between the theory of Lee *et al.* [60] and the proposed model for  $\epsilon = 0.95$ .

Engineers often look at the trade-off between complexity and accuracy of the instruments available. A very simple and easy-to-use tool is often preferable to a labyrinthine but more accurate one. Due to the simplicity of eq. 5.11, the proposed expression to predict the focused sample size could be considered a valid alternative to the accurate analytical model for geometries with a aspect ratio above  $\epsilon = 0.5$  in the region  $\alpha \geq 4$ , where the percentage error is constantly below 11%.

### 5.5.1 Parabolic velocity profile of 3D merging streams

The assumption that the flow is fully developed was investigated experimentally in two separate experiments using the LSD. In the first test, a solution containing  $1\mu\text{m}$  fluorescent microbeads (Invitrogen) was injected into inlets A, C and D while DI water was injected into inlet B. Due to the 3D nature of the flow, the flow pattern in the centre of the channel height is that depicted in Figure 5.23(a): before the intersection with channel D particles

appear out-of-focus in the image because they are confined in the top and bottom region of the channel by the sample fluid (water); after the main intersection, instead, the small volume of water is confined in the centre of the channel while particles coming from the side inlets are visible in focus. On the contrary, in the second test microbeads were injected into inlet B while DI water was injected in the remaining inlets. This is the standard 3D focusing application where particles are surrounded by water in the vertical and horizontal dimensions and appear on focus in the centre of the channel height, as shown in Figure 5.23(b). It is worth noting that the two particle image fields are complementary to each other. The solution containing particles was prepared diluting 25 $\mu$ l of particles into 1.2ml of DI water. The flow rates imposed to the inlets were  $Q_A = Q_C = 0.25$   $\mu$ l/min,  $Q_B = 0.25$   $\mu$ l/min and  $Q_D = 1.5$   $\mu$ l/min in both experiments, with  $\alpha_V = 1$  and  $\alpha_H = 2$ . The Reynolds number based on the average velocity in channel E is 0.097, which is clearly in the creeping flow range.

The velocity profiles in the two cases were determined using a micro-PIV technique with the system described in Section 3.3.1. Figure 5.23(c) and Figure 5.23(d) show the ensemble average of 30 vector fields correspondent to the first and second experiments, respectively. The particle concentration in the near-wall region is quite low, which is due to hydrodynamic interactions between the particles and the wall, as noted by Meinhart *et al.* [78]. Also, the area occupied by out-of-focus particles has a little contribution to generate vector fields. Higher velocity vectors are achieved on the side of channel E in Figure 5.23(c) and in the center in Figure 5.23(d). In order to demonstrate that vector fields of the two figures are complementary, the velocity profiles were extracted 200 $\mu$ m downstream the intersection with channel D and the data obtained from the separate experiments were then merged to give a complete vector field across the width of the channel.

The resultant velocity profile shown in Figure 5.23(e) clearly illustrates a developed flow with a peak velocity at the center of the channel, approaching zero near the wall. Blue and red squares represent experimental data from the first and second experiment, respectively, and are compared to the theoretical velocity profile of fully developed flows in rectangular ducts [108]. The combination of the two data points follows the theory in trend. Reasonable agreement is noticed between the experimental and theoretical data

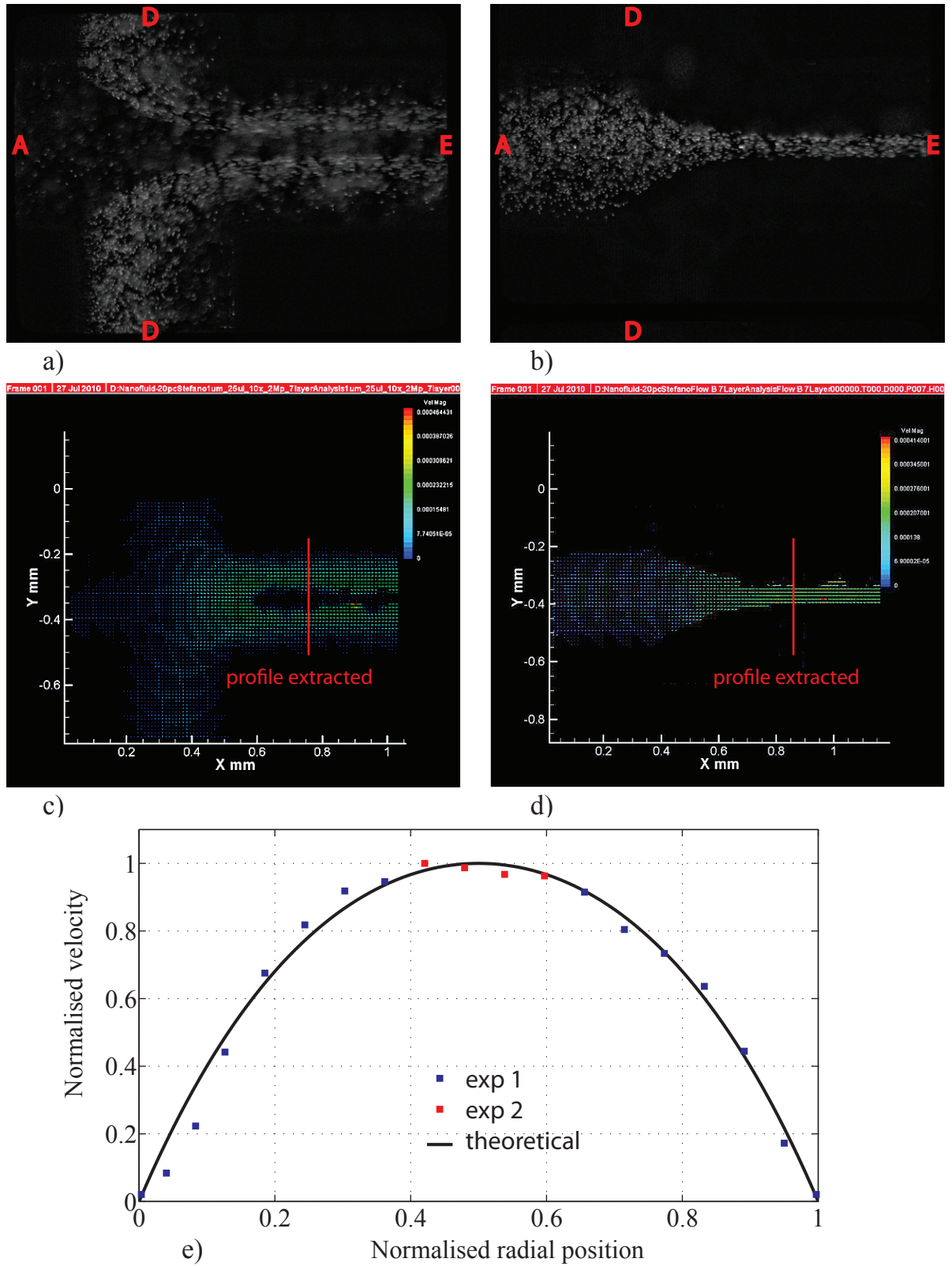


Figure 5.23: Velocity profile of 3D merging streams. Still images of particles in exp 1 (a) and exp 2 (b); ensemble-averaged  $\mu$ PIV vector fields of exp 1 (c) and exp 2 (d); (e) Normalised velocity profile of the merging streams. Velocity profiles of the two experiments are superimposed and compared to the theoretical solution. Flow direction is from left to right.

with a mean velocity deviation equal to 7.8%. The slight change in data trend is probably due to the influence that the vertical hydrodynamic focusing effect has on the horizontal effect. Less agreement is observed in the region close to the left wall (following the flow direction). This graph shows that the velocity profile in the outlet channel develops into a parabolic shape within a short distance from the main intersection. This agrees with the findings of Walsh *et al.* [124], in that the developed velocity profile of merging streams is parabolic, and with the findings of Curtin *et al.* [15] in that the entrance length of the channel is usually in the order of microns for creeping flows,  $Re \simeq 1$ . A well accepted correlation reported by Schlichting [105] predicts the entrance length for laminar flows to be  $EL \approx 0.06 * Re$ .

### 5.5.2 Comparison between experimental results and theory

Figure 5.24 compares the experimental results presented in Section 5.2 to the theoretical model of Lee *et al.* [60] for both LSD and SSD. The data are normalised with respect to the channel dimension. The focused sample width, Figure 5.24(a), is in relative good agreement with the theory for both LSD and SSD. This is more evident for low values of flow rate ratios of horizontal focusing,  $\alpha_H < 1$ . In the majority of the cases, however, the experimental results overestimate the analytical values. Less agreement is found for the vertical hydrodynamic focusing, Figure 5.24(b). The normalised focused sample height is in good agreement with the theory only for low values of the flow rate ratios of vertical focusing,  $\alpha_V < 2$ , while a larger scatter is found for higher values of  $\alpha_V$ . This is noticed for both LSD and SSD. A restriction in the vertical focused dimension is also observed in LSD for values above  $\alpha_V = 6$ ; the normalised focused height does not reduce with the increase of  $\alpha_V$  but shows instead an inferior limit of  $v_e/H = 0.08$ . The experimental results for the vertical dimension in the SSD do not match the theory above  $\alpha_V = 2$ . This confirms the difficulties found during confocal experiments to achieve a vertical focused stream smaller than  $20\mu\text{m}$ .

During the discussion of these results, three aspects should be underlined. First, even-though the 3D-HFMD is able to achieve vertical or horizontal focusing independently, the

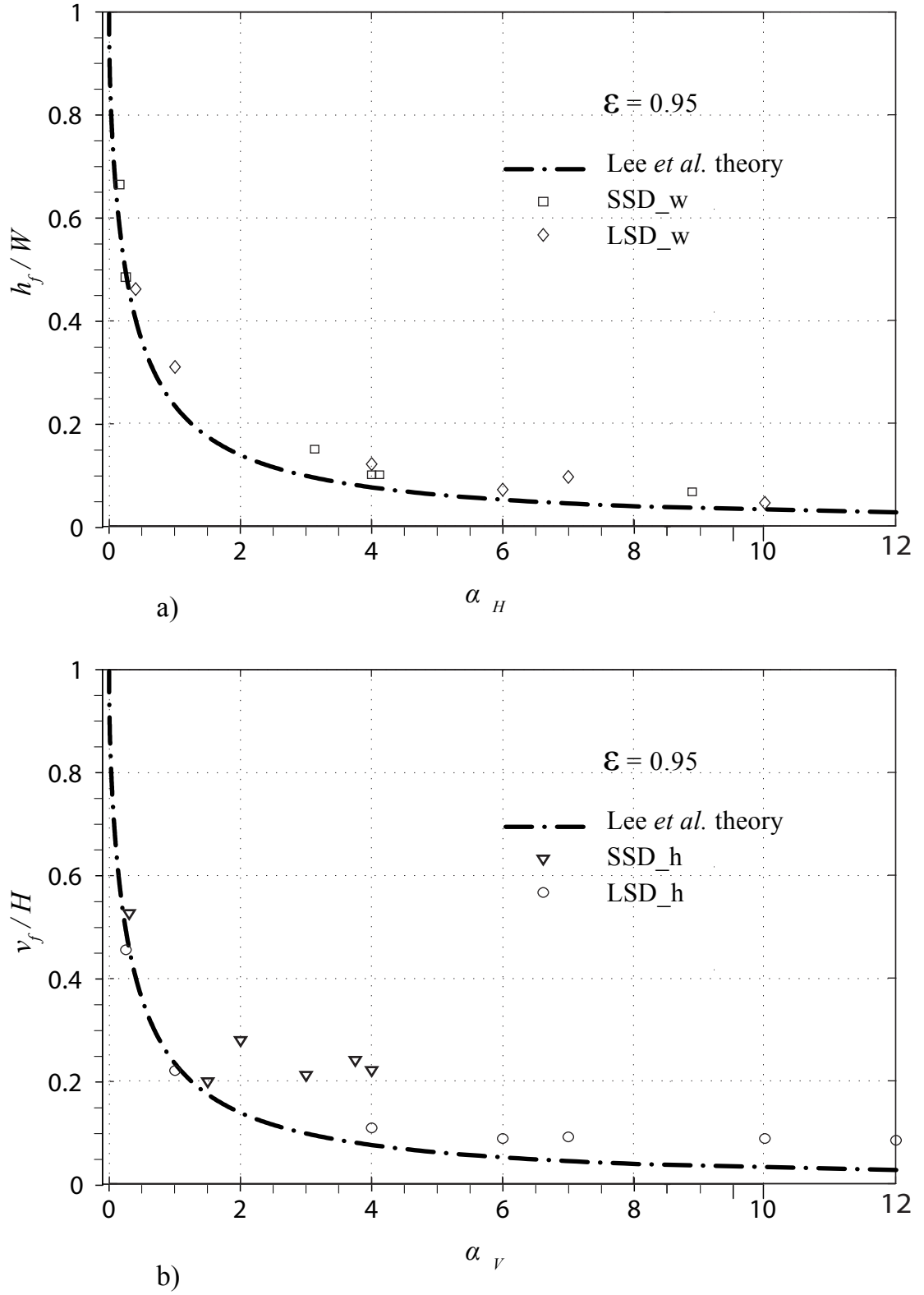


Figure 5.24: Comparison of the focused sample sizes achieved on LSD and SSD against the theory of Lee *et al.* [60]. a) horizontal dimension; b) vertical dimension. Data extracted from the confocal experiments of Section 5.2.

device has been designed to perform 3D hydrodynamic focusing. Consequently, the analysis on the performance of the horizontal focusing should also take into account the effect that the vertical focusing element has on the focused width, and vice-versa. The lateral compression to the flow, for instance, could force the sample to spread to the vertical dimension. This was observed also by Hairer and Vellekoop [37] and is visible from a comparison of the values of Table 5.1. When the same flow rate ratio of horizontal focusing,  $\alpha_H = 6$ , but different vertical focusing,  $\alpha_V = 6$  and  $\alpha_V = 12$ , was set on LSD, two different focused widths were achieved. The discrepancy between experimental data and theory due to the 3D nature of the flow was also investigated by Lee G.B. *et al.* [61] with numerical simulations. Second, the horizontal focusing effect is generally more efficient than the vertical in both LSD and SSD. This is because, in the design of the 3D-HFMD, the horizontal focusing element is positioned downstream the vertical. In other words,  $Q_B$  is compressed by a side flow which is much greater than its magnitude and the focused width is therefore more affected. The last aspect which is interesting to observe is that the scatter associated to the normalised results of SSD is generally larger than that of LSD and this is due to the smaller size of the channels of SSD, 100 $\mu\text{m}$  against 400 $\mu\text{m}$ . Since the data are normalised to the channel dimensions, a small difference in the focused size on SSD leads to a higher variation of the normalised focused stream dimension. A change in  $v_e$  of five microns in SSD, for instance, leads to a variation of  $v_e/H$  more than four times bigger than in LSD, equal to 0.053 and 0.013 respectively.

## 5.6 Summary

In this chapter, results achieved with the SSD and LSD have been presented. A flow visualisation method was used to initially characterise the efficiency and stability of the 2D hydrodynamic focusing effect into the microchannels. The sample was found to be stable for the full length of the main channel. Then, confocal experiments and CFD simulations have been compared in order to establish the ability of the geometry to focus in 3D. By altering the flow rate ratios it was possible to adjust the sample size in both vertical and horizontal dimensions and to compress the sample into a region of the same size of biological cells in both SSD and LSD. The sample stream diameters were ten to twenty times smaller than the channel dimensions. The proposed geometry proved to be stable until  $Re = 30$ , which is 6 times the appropriate operating conditions of the device of Chang et al. [8]. The injection of microbeads and biological cells proved that a stable cells/particles line-up can be achieved, allowing the 3D-HFMD to be employed as a micro-flow cytometer for cell analysis. Finally, a simplified expression has been proposed as an alternative to the accurate theoretical model to predict the size of the sample stream.

In the following chapter, the optical counting technique developed to accurately quantify biological cells dispensed into a microfluidic device will be presented.

## **Chapter 6**

# **Magnetic Stirrer and Optical counting technique for biological cells**

This chapter outlines the automated optical counting technique developed to efficiently quantify B-lymphoid precursor leukaemia cells. First, results obtained with the magnetic stirrer assembly are presented. Following an accurate description of both the manual approach and the proposed technique, results are presented and compared to both the standard manual approach and to the visual count of the cells from the digital picture. The application of the vertical hydrodynamic focusing effect using the 3D-HFMD to improve the automated technique is also reported.

### **6.1 Magnetic stirrer**

The stirrer assembly concept, whose manufacture is detailed in Section 2.6, arose from a need established during preliminary tests for biological cells to be dispensed into a microchannel and their response to the localised shear gradients experienced in microchannels examined. Considerable difficulty was experienced in dispensing a uniform distribution of both adherent and suspension cells lines and accurately quantifying viability using the Trypan Blue assay and a haemocytometer, see Section 3.2.

During preliminary tests, L-929 and B-lymphoid precursor cells were stained with a

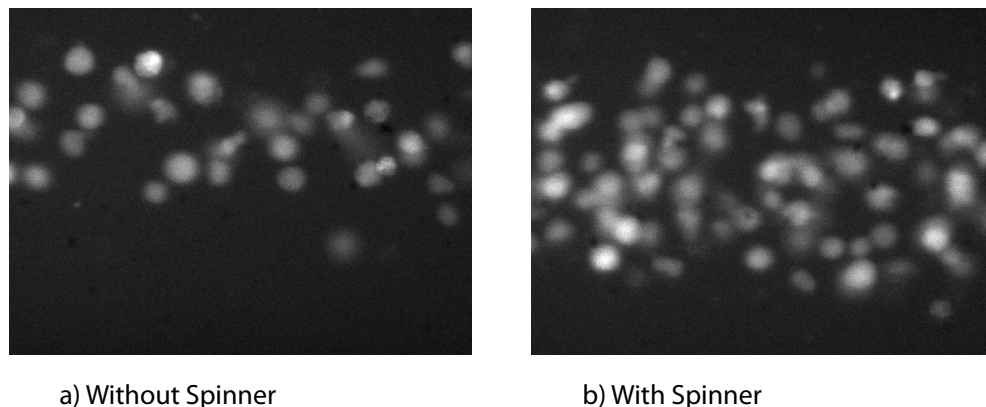


Figure 6.1: Imaged flow of REH cells in the tubing with and without the stirrer assembly in operation. The image has been edited so that the tubing walls are located at the top and bottom of the image. Index matching was performed to image without refraction into the tube.

fluorescent tag, CellTracker Green CMFDA, see Section 3.1.2 and injected into a 0.15mm ID tubing, immersed into an index matching fixture. Before injection the suspension was agitated for few seconds to dis-aggregate clusters of cells using a vortex (Scientific Instruments, USA). However, this effect ended very quickly and during testing it was found that cells must be agitated throughout into the syringe in order to lengthen the positive effect of agitation. Two main problems were experienced during the injection concerning concentration and distribution of cells into the tubing. The first problem was caused by clusters of cells formed into the syringe and observed under the microscope. This reduced the number of individual cells available for experimentation and influenced the result. Second, cells were noticed settling on the bottom of the syringe and considerable difficulty was experienced in injecting them into the tubing and reaching a constant and uniform distribution. Thus, the use of the magnetic stirrer was required.

Figure 6.1 shows the change in REH cell distribution with and without the device in operation. The image on the left shows bias to the top, and strong temporal variation was observed. The image on the right maintained uniform distribution of cells across the tube and in time over a period of three hours. Moreover, no cell aggregates were observed in the image. This agrees with the findings of Mc Limans *et al.* [77] in the first application of the stirrer culture, who observed that the agitation induced by the spinner appeared sufficient to break up cell clumps into individual units within several hours, with viability above 95%.

## CHAPTER 6. MAGNETIC STIRRER AND OPTICAL COUNTING TECHNIQUE FOR BIOLOGICAL CELLS

---

Very few cells were still observed as clusters, and limited to groups of 2-4 cells.

The efficacy of the magnetic stirrer was checked against both L-929 and REH cell lines in two separate experiments, as shown in Figure 6.2. Cells were injected into the microtube at a velocity of 0.0264 cm/s, and every 20min, for more than two hours, one sample was collected at the outlet and counted in triplicate using a haemocytometer. The experiment was performed with and without the use of the stirrer and the values obtained were plotted against time. In order to compare data acquired during different tests, the values were normalised with respect to the initial concentration of cells before injection. It is worth noting that it could happen that the concentration of cells measured after two hours was found higher than that before the injection. This was experienced in the experiment of Figure 6.2(a) and it is due to the high variability associated to the Trypan Blue assay.

The data accomplish with and REH(a) L-929(b) cells are similar in trend with some discrepancies. In either case, when the spinner was turned off, the number of cells collected after 20min was higher than the initial value, meaning that the majority of cells pass through the tube immediately. After this period, the concentration gradually reduces, and the majority of cells are expected to be sedimented on the bottom of the syringe. With the spinner on, instead, the trend is more regular and cells are still available at a high concentration after few hours. At the first sample withdraw, however, a reduction was observed in almost all experiments. This was probably due to the action of the magnetic bar which does not allow the cells to go through the syringe in the first few minutes by holding them in suspension. This test was repeated more times, obtaining different values but similar trends.

In experiments of this research thesis, the small vortex produced by the agitation did not compromise viability of cells, and the static magnetic field measured by a gaussmeter into the syringe, was below 10mT. Moreover, as outlined by Furlani [32] in separating white blood cells (WBC) from red blood cells (RBC), WBC behave as diamagnetic microparticles and are not effected by magnetic forces.

It was proved that the mechanical method presented in this research thesis allows to

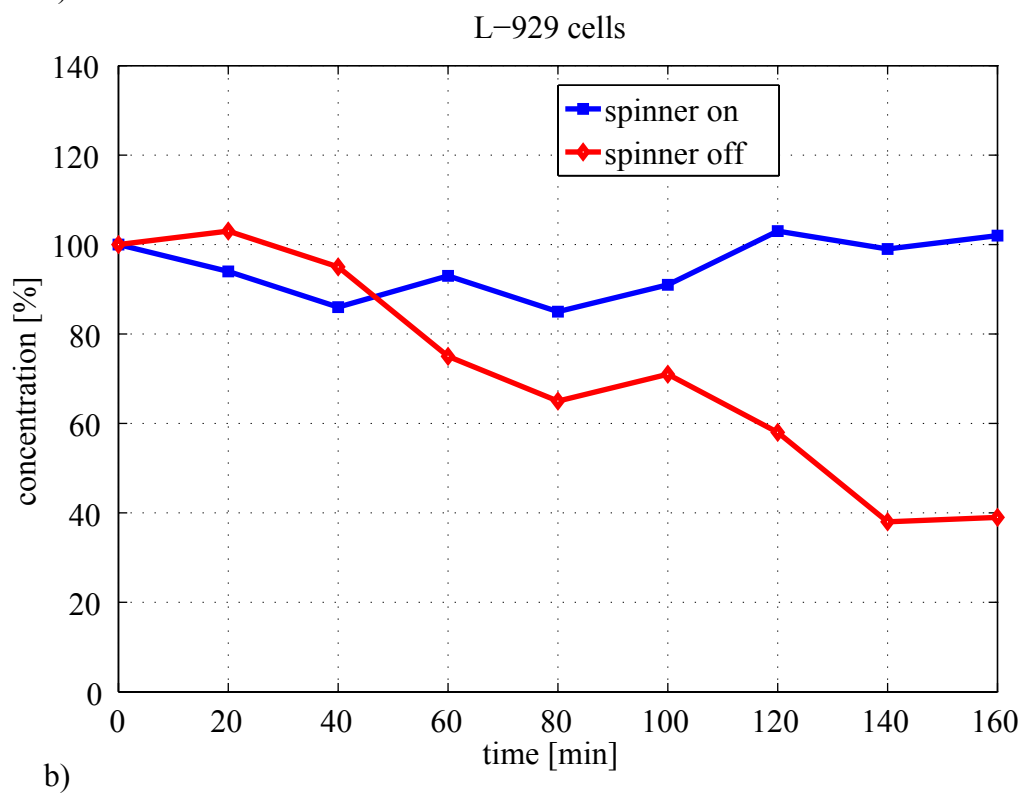
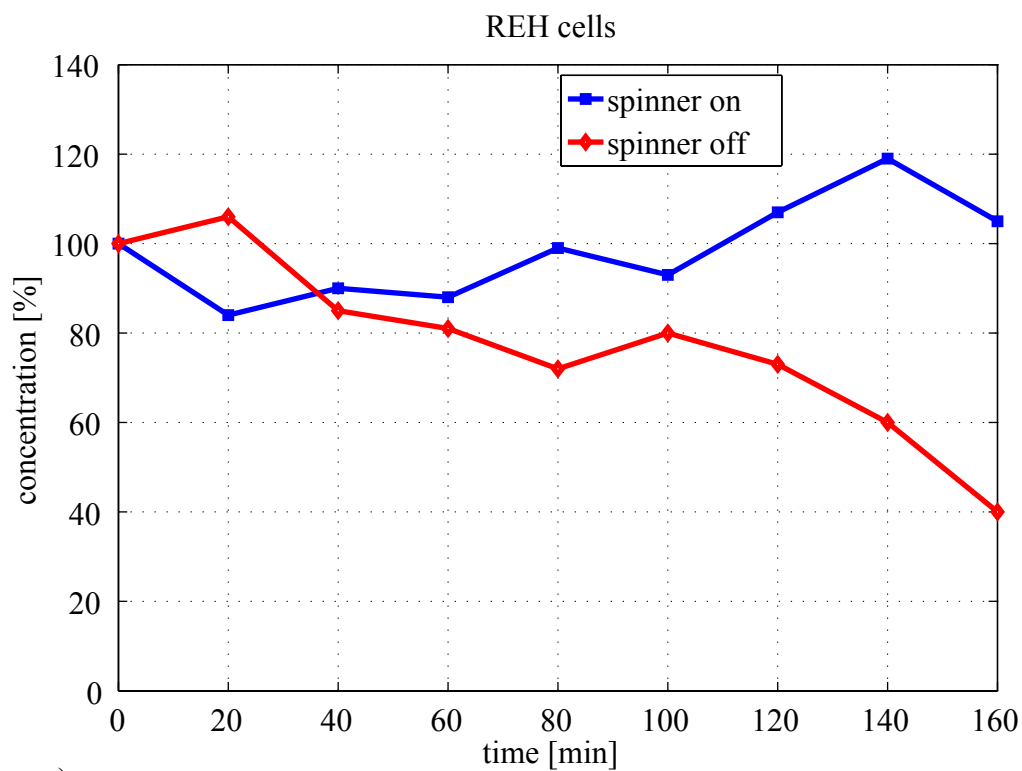


Figure 6.2: Cell availability

prevent cell clumping and to deliver cells into a device at a constant rate without the concomitant introduction of additional substances into the cell suspension. The magnetic stirrer assembly demonstrated to be a valid aid for engineering application involving the use of biological cells, thus, it was used during both cells and particles experiments throughout this thesis. However, using the Trypan Blue exclusion assay, a high variability was found between the triplicate measurements belonging to the same sample. A different technique to count cells was therefore developed. In the next sections, the alternate optical counting technique is presented.

### 6.2 Optical counting technique: principle

In this section, the optical cell counting method is described. Experiments were performed with two different cell types, a suspension cell line (REH) and an adherent cell line (L-929), successfully cultured and stained using standard biological protocols, as discussed in Section 3.1.1. Preliminary investigations have been carried out using a 200 $\mu$ m ID Teflon FEP microtube (Upchurch Scientific) which was introduced into a microchamber, as shown in Figure 6.3. To facilitate imaging, the chamber and outer surface was filled with an index matching liquid (mixture of DI water and glycerin). The cell culture media containing cells was utilised as the working fluid and the flow was controlled by a syringe pump. Because high velocity values can cause disruption of the cell membrane and lysis of the cell [99], the flow rate used was 0.5 $\mu$ l/min, which provides an average velocity of 0.0264cm/s and a Reynolds number of 0.05, indicating laminar flow. The instrumentation used during testing, described in Section 3.3.1, is depicted in Figure 6.3. The microchamber was placed on the top of the Olympus microscope, and the illumination beam was produced by the 100W Mercury Burner. Images of the cell flow were recorded using a CCD camera and analysed with a Matlab script, R2008a. The stirrer dispenser assembly of Section 2.6 was used to avoid cell aggregation and to inject a uniform number of cells per unit of time.

Differently from the manual approach, on the method proposed cell quantification is derived from an intensity count of the image using a simple script. The different steps required to obtain the cell quantification are shown in Figure 6.4, where (a) and (b) are the

## CHAPTER 6. MAGNETIC STIRRER AND OPTICAL COUNTING TECHNIQUE FOR BIOLOGICAL CELLS

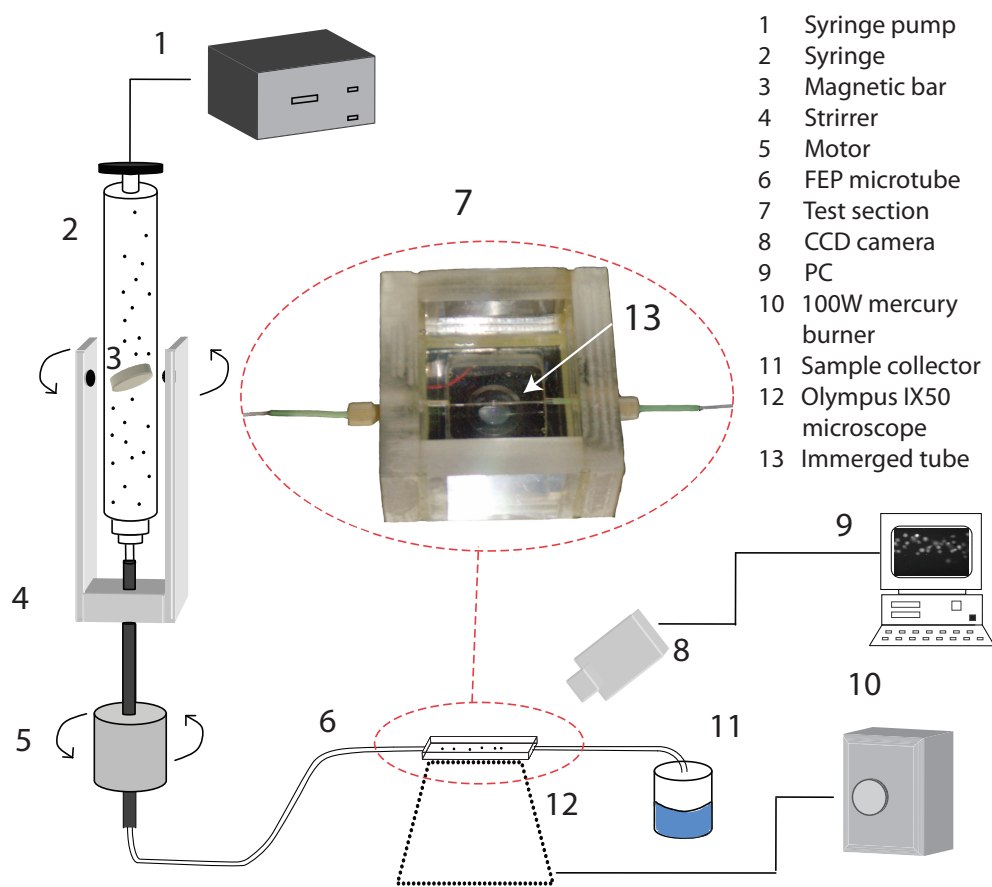


Figure 6.3: Schematic showing the optical counting technique facility.

original images taken by the camera and (c) and (d) are the pixel intensity of (a) and (b). A load of cells at a concentration of approximately  $2 \times 10^6$  cells/ml was injected into the tube. A sequence of frames was recorded using a CCD camera at a sampling frequency of 30Hz and exposure time of  $33,333 \mu\text{s}$ . The image resolution is  $640 \times 480$  pixels, corresponding to  $364 \times 300 \mu\text{m}$  with a 10x objective lens. To perform the counting, the original image is converted into a pixel intensity image, and a threshold is applied to remove background noise and irregularities. The total fluorescent intensity of the image is calculated by summing the intensity of every pixel in the image. The total fluorescent intensity value is then divided by the average intensity of a single cell to give the number of cells in that particular image. The average fluorescent intensity of a single cell is found by converting an original image of a cell, Figure 6.4(b) into a pixel intensity image, Figure 6.4(d). Due to the variability in size and shape of cells in motion, as described in Section 6.3, this count is repeated three times, considering cells of different dimensions, and the mean value is taken.

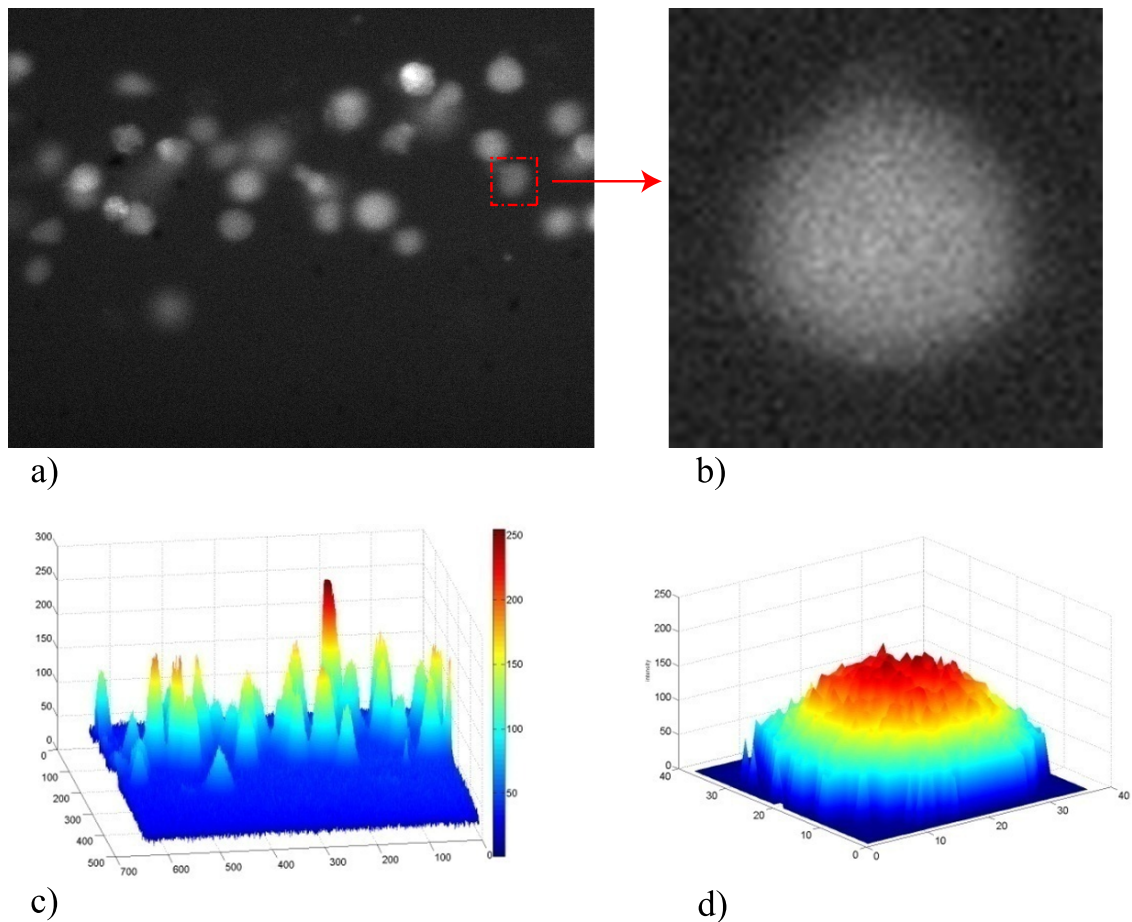


Figure 6.4: Optical counting technique principle: a) fluorescent image of the flowing cells b) zoom on a single cell of the same image c) pixel intensity image d) intensity of a single cell.

This technique allows the number of cells in the field of view of the camera to be determined at regular time intervals. This can be done because the average velocity with which the cells travel through the field of view is known. On average it takes 1.5 seconds for the cells to pass through the field of view. By taking 45 frames at a frame rate of 30 Hz (*i.e.* 1.5 seconds), the average number of cells passing through the field of view can be found for this time interval by taking the average number of cells in each of the 45 frames. This approach takes into consideration both the size and the intensity of the cell.

In a laminar regime, due to the parabolic velocity distribution, cells at different  $z$  position in the tube have different velocity magnitude; hence two cells can be overlapped within the flow, resulting as a single cell twice brighter than the others. The method, considering

both pixels and intensities, is able to count the two separated cells even if they are overlapped, as shown from the comparison of Figure 6.4(a) and Figure 6.4(c). Figure 6.4(c) also shows the wide range of pixels intensity associated to the cells, due to their different vertical position in the channel. If the distribution of pixel intensity of the different cells is too broad, the linear superposition of individual cell intensity is invalidated; this is because the intensity is proportional to their distance from the focal plane. The error associated with this system is mainly caused by this variability in intensity distribution. To achieve a uniform cell intensity, hydrodynamic focusing can be applied. A review on vertical hydrodynamic focusing applications is given in Chapter 1. In classic 2D hydrodynamic focusing microdevices [60] cells are only compressed on the horizontal dimension, therefore they may not pass the focused stream in single file, even though its width has the same order of magnitude as that of the cells size, due to the wide vertical distribution of the cells. To overcome these problems, the hydrodynamic focusing technique can be applied to the vertical dimension. By reducing the  $z$  distribution of the cells activating only the vertical focusing of the 3D-HFMD, the measurement accuracy should improve.

### 6.3 Optical counting technique: results

In most studies cells are simplified as spherical particles [28, 33], but their shape and size can change due to different reasons, such as the cell cycle phase or the flow rate imposed. Loiko *et al.* [72] gave a statistical distribution of the B-cells size using a flow cytometric technique. On the analysis of over 3000 lymphocytes (B cells and T cells), the size varied in the range from  $4.8\mu\text{m}$  to  $12.0\mu\text{m}$ . The mean value was found to be  $7.8\mu\text{m}$ , with a standard deviation of  $0.7\mu\text{m}$ . A pixel count of the acquired images confirmed similar values: B-cells size ranging from 12 to 26 pixels, equal to  $6.5\text{-}14\mu\text{m}$ .

From steady state to motion the cell size also differs and the shape can deform from round to elliptical. A simple experiment was first performed to measure the cell size against the velocity imposed to the cell solution into the tubing, Figure 6.5. A given velocity was imposed for 1 min to the suspension and three frames were then recorded with a CCD camera. Immediately downstream the detection, a sample of the suspension was collected

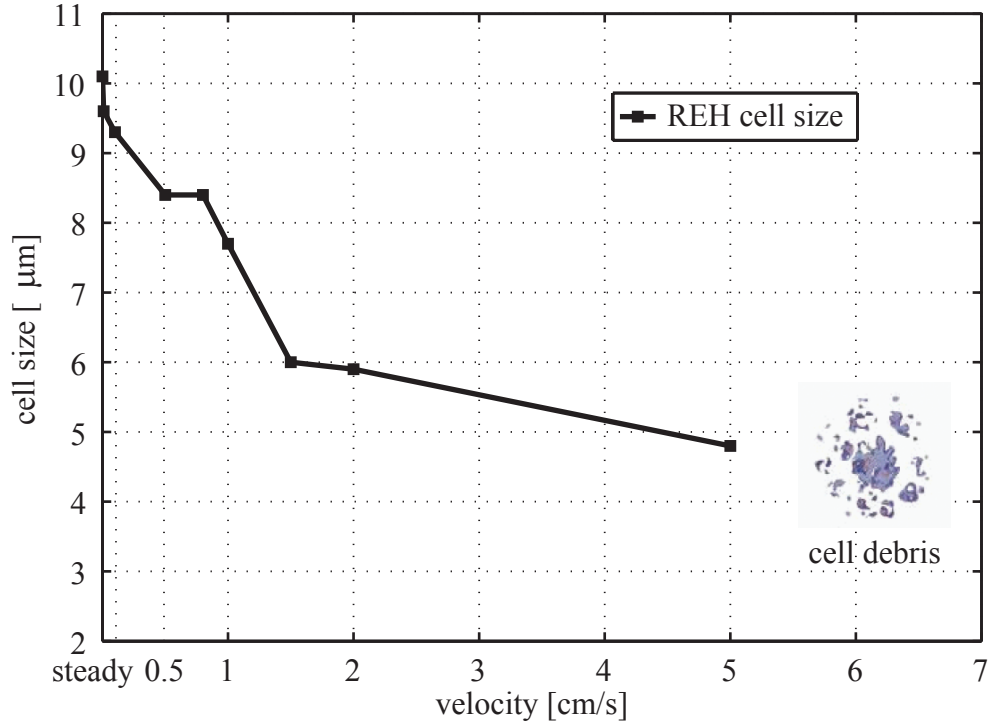


Figure 6.5: cell size over velocity

and a viability test was performed using the Trypan Blue assay, Section 3.2. The average dimension of the two axis for each cell in the field of view was calculated from a pixel count of the digital image. The average cells size in the three frames was then plotted against the correspondent velocity. First, a steady measurement was performed. Then, velocities margin of 0.01 to 7 cm/s were imposed to the flow. Between 0.01 and 0.1cm/s the cells retained their original dimension, with little discrepancies which are in good agreement with the standard deviation of Loiko *et al.* [72]. A first noticeable size reduction is observed at 0.5 cm/s. However, cell viability is not compromised. A second reduction, up to 50% of the measurement performed at steady state, occurs over 1.5 cm/s and a greater disparity between the length of the two axis was found. Few cell debris also appeared in the image. Above 5 cm/s, a consistent number of cell debris were found in the cell suspension and the number of viable cells reduced considerably. This suggested that velocity over 1 cm/s were not employed in this study. The Reynolds number at which apoptosis occurred, *i.e.* velocity of 5 cm/s into a 200μm microtube, is equal to  $Re = 10$ . Even if some authors performed cell studies at higher values of Reynolds [10, 63], these were accomplished using more robust

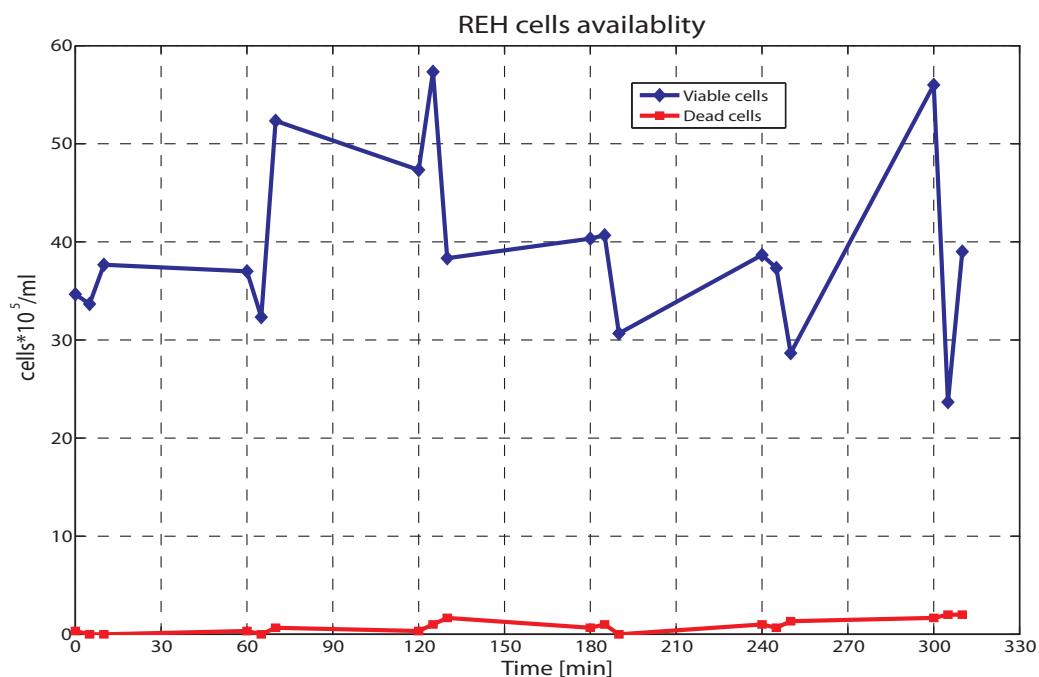


Figure 6.6: Plot of cell availability with time. Test performed using the Trypan Blue exclusion assay. REH cells are collected at the outlet of a microtube and quantified in triplicate every hour. Variability from 15% to 50% is obtained at every time step. On the x axis the exact time when the samples were collected is indicated. Similar results were obtained using L-929 cell line.

cell types (RBCs, E-coli). Apoptosis of RBCs, in fact, occurs over a specific hemolytic threshold value which is greater than that of White Blood Cells [103]. This is because RBCs flow through capillaries under conditions, *i.e.* shear stress, that WBCs would not survive. Lysis of the cell membrane differs greatly depending on which cell species is being disrupted, *e.g.* a plant cell is significantly stronger than a mammalian cell [65]. Thus, the results presented in Figure 6.5 are specific for the cell line and flow conditions analysed and cannot be extended to any cell type or experiment.

In Figure 6.6 the validation of the Trypan Blue exclusion assay is discussed. As detailed in Section 3.2, the cell concentration is calculated from a manual count on the cell population. REH cells were injected into a 200 $\mu$ m ID microtube at 0.5 $\mu$ l/min, and every 60min, for five hours, one sample was collected at the outlet and counted in triplicate using a haemocytometer. Variability of approximately 50% was found from the triplicate measurements belonging to the same sample. Even if the mean value was relatively constant,

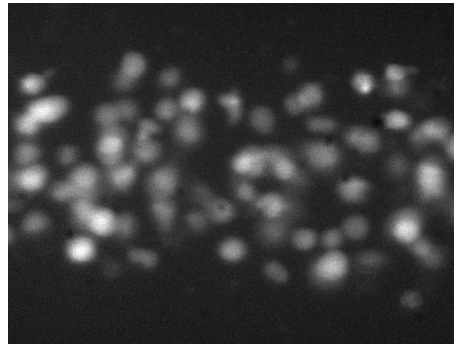


Figure 6.7: The different intensity associated to the cells flowing into the microtube. Brightest cells are caused by overlapped cells in the flow.

the fluctuation was significant. Moreover, the exact concentration of cells cannot be quantified. Results also show that viability is not an issue, as the concentration of dead cells, *i.e.* not fluorescing cells, is negligible. This confirms that the shear force exerted by the flow on the cells is insufficient to cause lysis. For these reasons, availability of cells, rather than viability is an issue, and in the following, viability will not be considered. The results only give a rough approximation of the number of cells present in the sample taken from the cell preparation, before or after the injection. This indicates that a different methodology should be used to quantify the number of cells under test. Similar results were obtained using the L-929 cell line.

The approach proposed, as opposed to the manual technique, is based on the analysis of recorded images of cells in motion. Figure 6.7 shows a typical fluorescent image of the moving cells. The fluorescent intensity of the cells is not constant, which is attributed to two factors:

- Cells can be sited at different vertical positions in the tube, and their intensity varies with the location.
- The intensity of overlapped cells is the linear superposition of their individual intensity.

The cell count obtained using the automated technique is compared to both the manual approach and to the visual count of the cells from the digital picture, and the results are shown in Figure 6.8. Results from the manual technique are again acquired every 20min

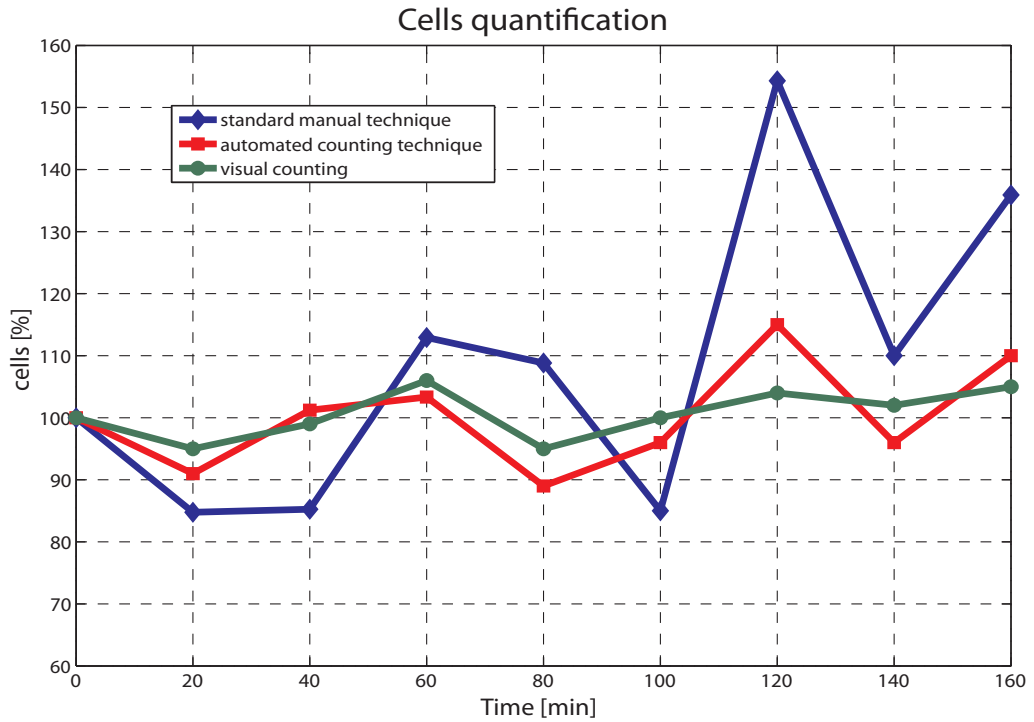


Figure 6.8: Comparison between standard and automated counting techniques. Visual counting served as reference.

for three hours, and the average of the three values is plotted against time. Visual manual counting is considered most accurate owing to the “unbeatable combination of the human eye and brain” [11], but is time consuming and not practical. To compare together the different results obtained from different tests, all the experimental profiles were normalized with respect to the initial concentration at time zero, before injection.

The method proposed shows an average error of 4.7%, with a maximum value equal to 11% obtained after two hours. Moreover, for the first hour, the scatter is lower than 3%, giving sufficient time for a test to be run on the cells. On the other hand, the average error associated to the manual technique is  $\approx 18.7\%$ , with a maximum value approximately 51%. The automated and the manual techniques also vary in trend, where the automated approach follows the trend of the visual counting, as opposed to the manual which varies significantly. After the first hour size and shape of the cells introduce an additional effect on the measurements. Due to the continuous stress applied by the syringe pump and the time spent out of the ideal growing conditions, size and shape distribution change much more, hence influencing the cell detection. Moreover, due to the physical properties of the

cells, their distribution along the tube is not constant with time. As previously mentioned, the intensity of overlapped cells is the linear superposition of their individual intensity. However, if more than three cells overlap, saturation of the pixel occurs. The fluorescent intensity of four cells overlapped, for instance, is the same of that of three cells. The use of a sensor with a different response may overcome this problem. In addition, the distribution of B-lymphoid cells along the full height of the microtube increases the range of fluorescent intensities, as seen in Figure 6.4(c). Out of focus cells, up to 100 $\mu\text{m}$  from the centre of the tube, reduce the reliability of the automated method and increase the measurement error, hence should be avoided. The fluorescent intensity of in-focus cells can be two times greater than the fluorescent intensity of cells in the top, or bottom, of the tube. To solve both issues, the width of focus of the stream of cells can be reduced. The application of vertical hydrodynamic focusing, using the 3D-HFMD, to the automated counting technique should reduce the error associated to the method. In the classical 2D focusing cells are often compressed horizontally, therefore they can overlap on the vertical dimension and result in a wide range of cell intensity. In order to reach a high throughput and the best performance, it is important to maximize the number of cells per image within the smallest z displacement, thereby vertical focusing is an ideal solution. Confocal experiments have been carried out to validate the use of the 3D-HFMD with the optical counting technique, and results are in good agreement with the CFD simulations. Size and position of the focused profile downstream the intersection with channel D are shown in Figure 6.9, where the 3D view of CFD (a) and confocal (b) images are compared. In green, the walls of the microchannel are shown.

The size of the focused stream after the vertical focusing process is approximately 68 $\mu\text{m}$ , 18% of the entire channel height, Figure 6.10. The cross sectional profiles in Figure 6.10(a) and (b) differ for the position of the centre of the focused stream, which was shifted down the vertical axis in (b). Flow rates used for both simulations and experiments were:  $Q_A = Q_C = 7 \mu\text{l/min}$ ,  $Q_B = 1 \mu\text{l/min}$ ,  $Q_D = 2 \mu\text{l/min}$ , with a velocity in the main channel E of 0.186 cm/s, which is a velocity achieved in most micro-flow cytometers [10, 59]. By varying the flow rate ratios of sample and sheath fluids, the size of the focused profile can be controlled and therefore the throughput of the optical counting technique. An optimum

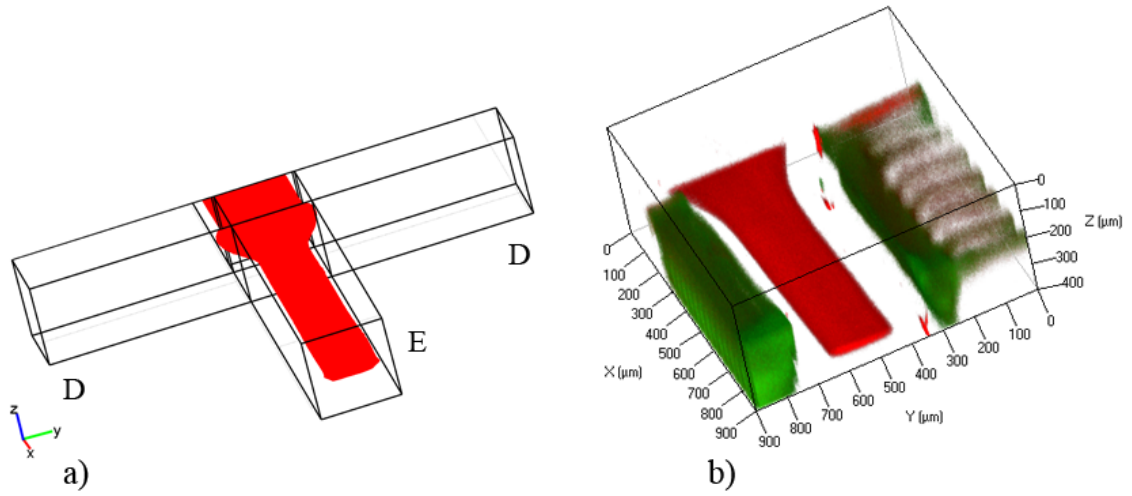


Figure 6.9: 3D view of the vertical focusing into the microdevice: (a) CFD simulation, (b) Confocal image. Both images are acquired downstream of the intersection with channel D.

can be found for a specific application between less focusing/more cells and more focusing/less error associated with the method. The throughput of micro-devices is always lower than their macroscopic counterpart. Halving the diameter of the stream entails a quadruplet flow velocity to maintain the same volume throughput [4], and this is difficult to achieve, as shown in Figure 6.5. For the values used within these experiments the throughput would be around 100-200 cells/s, based on the delivered flow rate from the dispenser and the cell density determined over the measurement volume (*i.e.* from a cell count per unit volume). The density of cells being delivered is higher than expected based on the cell dilution in the dispenser and is caused by cell sedimentation in the dispenser device. The range is consistent with the operating of Nieuwenhuis *et al.* [89] who used hydrodynamic focusing in a microfluidic Coulter counter. Their upper flow rate limit was 10  $\mu\text{l/s}$  at which stage unstable flow occurred. The present device is similarly restricted, but can operate at lower flow rates than the minimum 0.5  $\mu\text{l/s}$  limit in the equivalent Coulter device. This is because the technique is not influenced by ion diffusion. The throughput is lower than dielectrophoretic devices, such as Cheng *et al.* [10] who achieved a throughput of approximately 500 cells/s in sorting a mixture of three bacterial strains. The present device however, has been demonstrated to count only two cell types, but this is achieved with a less complex manufacture, negating the need for embedded electrodes, and using a readily implemented optical setup to interface with the device.

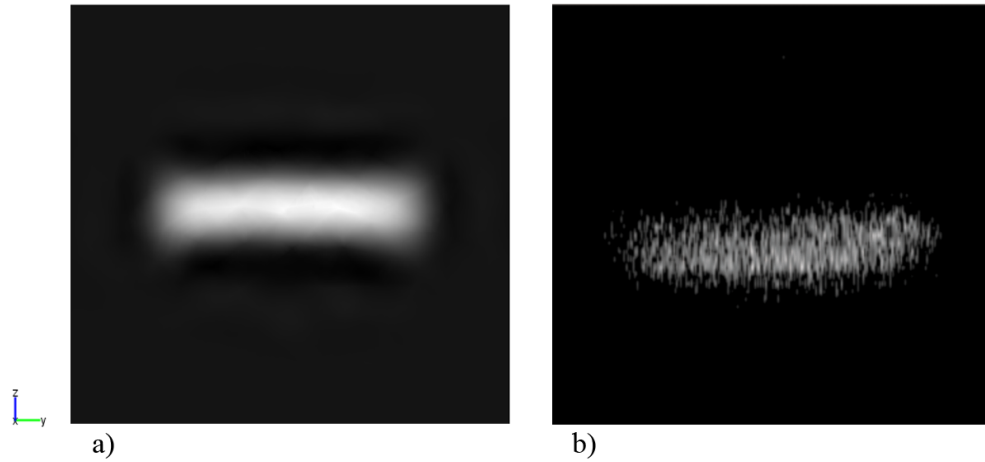


Figure 6.10: Cross sections of the vertical focused stream in channel E, downstream the intersection with channel D for  $Q_A = Q_C = 7 \mu\text{l/min}$ ,  $Q_B = 1 \mu\text{l/min}$ ,  $Q_D = 2 \mu\text{l/min}$ : (a) CFD simulation, (b) confocal image. A small horizontal focusing effect is applied. Size of the focused sample is  $68\mu\text{m}$  in height and  $300\mu\text{m}$  in width.

## 6.4 Summary

This chapter describes the automated optical counting technique for biological cells. The method has been tested using adherent and suspension cell lines providing similar results. Both cell lines were successfully cultured and stained using standard biological protocols. The optical approach was compared with both the Trypan Blue exclusion assay and to the visual count of the cells from the digital picture. The effect of velocity on cell viability was also investigated using two different cell lines providing comparable results. The application of the 3D-HFMD to vertically focus the cells in a narrow region in the centre of the channel is made to further improve the efficiency of the technique.

# Chapter 7

## Conclusions & Recommendations

In this chapter, the conclusions drawn from this thesis are first documented in the context of the objectives presented in Chapter 1. Some key recommendations for further investigation are also presented.

### 7.1 Conclusions

*To design and manufacture a low-cost and easily manufacturing 3D-HFMD able to fully control size and position of the focused sample.*

- A low-cost 3D-HFMD prototype was manufactured in a single PMMA substrate using conventional CNC milling. Preliminary tests were performed on the prototype to validate the geometry proposed. A 2D investigation and confocal experiments have shown that the design is able to focus in the three dimensions. 10 $\mu$ m particles were injected and successfully focused into the prototype. These preliminary tests confirmed the efficacy of the proposed geometry.
- Two devices of different size were fabricated by standard photolithography. A flow visualisation investigation using a dye confirmed that 2D focusing was achieved for the full length of the channels. CFD simulations and confocal experiments were compared and proved that size and position of the focused sample can be fully controlled

in both devices. Vertical and horizontal focusing were also obtained independently. The smallest sample sizes achieved on the larger device were  $18\mu\text{m}$  on the horizontal dimension and  $32\mu\text{m}$  on the vertical dimension, which are 4.5% and 8.4% of the channel sizes, respectively. Both LSD and SSD proved to be able to focus the sample in 3D.

- Previous works have illustrated that flow conditions required to achieve a stable 3D focusing are limited to a  $Re$  number either too high,  $Re \geq 80$  or too low,  $Re \leq 5$ . In this research thesis, the flow was shown to be stable in the range from  $Re = 0.1$  until  $Re = 30$ , which is six times higher than the appropriate operating condition of the device of Chang *et al.* [8].

*To prove that a device capable of focusing to the same order of magnitude of a cell size can be achieved from cost effective CNC manufacture.*

- Microbeads were injected into both devices and framesets of particles in motion demonstrated that microparticles can be sorted in single file. The dimension of the large scale device,  $400 \times 380\mu\text{m}$ , proved that a microflow cytometer can be achieved from cost effective CNC manufacture. This is the first example showing particles lined-up using 3D-HF in a channel larger than  $200\mu\text{m}$  in size.
- B-cells were injected into the large scale device and sorted in single file with 90% efficiency. To the knowledge of the authors, this is the first example showing biological cells 3D hydrodynamic focused into a device of the same dimension of a prototype easily fabricated by CNC manufacturing. These findings proved that the 3D-HFMD could be used in front of a detection system in order to analyse and count biological cells.

*To establish a simple technique to predict the size of the focused stream.*

- A simplified expression of the accurate analytical model proposed by Lee *et al.* [60] to predict the size of the focused stream was presented. This expression, based on the ratio between sample and total flow rates, could be considered a valid alternative

for geometries with a aspect ratio above  $\epsilon = 0.5$  in the region  $\alpha \geq 4$ . In this model, the ratio between the focused sample size and the channel width depends on two terms: the flow rate ratio and a parameter which depends on the channel geometry. The mismatch between the two equations gradually reduces from 32% to 11%. By fixing the flow rates imposed to the syringe pumps, it is possible to predict in advance the size of the focused sample expected in that particular experiment.

*To propose a simple counting technique to automatically quantify cells being dispensed into a microfluidic device.*

- An automated optical counting technique for biological cells was developed. Two different cell lines were employed providing similar results. The method compares favorably to the Trypan blue exclusion assay and to the visual count of the cells from the digital picture. The method proposed shows an average error of 4.7%, with a maximum value equal to 11% obtained after two hours. Moreover, for the first hour, the scatter is lower than 3%, giving sufficient time for a test to be run on the cells.
- The application of the 3D-HFMD to vertically focus the cells in a narrow region in the centre of the channel was shown as a possibility to further improve the efficiency of the technique.

*To develop a microdevice in order to avoid cell aggregation and sedimentation into the syringe throughout the tests.*

- A magnetic stirrer was successfully developed to keep cells in suspension into the syringe and to deliver a uniform number of cells per unit of time. The stirrer was employed with two different cell lines. No influence on cell viability was observed throughout the experiments due to the low magnetic field generated by the small vortex, 10mT.

## 7.2 Future works and Recommendations

- Experiments proved that the proposed device works as a microflow cytometer with 90% efficiency. However, in the conception of a new device, more numerical models could be evaluated in order to improve the design geometry prior to committing to the fabrication of the final specimens. CFD simulations allow to implement new designs reducing the time and operation cost compared to experiments setup and prototyping.
- The main dis-advantage of the proposed geometry is the need for three external syringe pumps to achieve fully 3D-HFMD. In the design of a new device, the same flow configurations should be accomplished in a single layer device and with the reduction of the number of fluidic inlets. This would further reduce the number of external pumps, sample consumption and the risk of pressure differences between channels.
- The characteristic of lab-on-chips is the complete independence from external hardware and the possibility to “*bring the device to the sample, rather than the sample to the lab*”. One possibility is to employ on-chip optic fibers, embedded on the channel surface, to allow real time detection, improved sensitivity and provide data of the same quality as laboratory systems.
- The easy-to-use model for the calculation of the focused width in rectangular microchannels, proposed in eq. 5.11, is a very handy tool for pre-calculation of hydrodynamic focusing in fluid handling devices. Once the design geometry is fixed, researchers can simply set a flow rate ratio on the syringe pump and therefore predict the size of the sample core expected for that particular experiment.
- The improvement of the optical counting technique with the application of vertical hydrodynamic focusing was demonstrated using CFD and confocal experiments. Given that different cell lines behave in a different manner, this result should be validated also using different biological cell lines.
- The magnetic stirrer assembly proved to deliver a constant and uniform distribution of cells into the tubing. However, for future developments this concept should be miniaturised in order to be integrated into the microdevice.

- Image quality is strictly dependent of the equipment used in terms of cameras and illuminations source. The use of a sensor with a different response, such as a complementary metal-oxide-semiconductor CMOS sensor with a LinLog curve and a dedicated illumination source should also be employed to minimise exposure times and improve image contrast for quantitative extraction.

## References

- [1] M. Agirregabiria, F. J. Blanco, J. Berganzo, M. T. Arroyo, A. Fullaondo, K. Mayora, and J. M. Ruano-Lopez. Fabrication of su-8 multilayer microstructures based on successive cmos compatible adhesive bonding and releasing steps. *Lab On A Chip*, 5(5):545–552, 2005. 2.5
- [2] C. Anderson, G. Georgiou, I. Morrison, G. Stevenson, and R. Cherry. Tracking of cell-surface receptors by fluorescence digital imaging microscopy using a charge-coupled device camera - low-density-lipoprotein and influenza-virus receptor mobility at 4-degrees-c. *Journal of Cell Science*, 101:415–425, Feb. 1992. 1.3
- [3] M. T. Arroyo, L. J. Fernandez, M. Agirregabiria, N. Ibanez, J. Aurrekoetxea, and F. J. Blanco. Novel all-polymer microfluidic devices monolithically integrated within metallic electrodes for sds-cge of proteins. *Journal of Micromechanics and Micro-engineering*, 17(7):1289–1298, July 2007. 2.5
- [4] D. A. Ateya, J. S. Erickson, P. B. H. Jr, L. R. Hilliard, J. P. Golden, and F. S. Ligler. The good, the bad, and the tiny: a review of microflow cytometry. *Anal Bioanal Chem*, 391:1485–1498, 2008. 1, 1.2.2, 2.4, 6.3
- [5] G. Blankenstein and U. D. Larsen. Modular concept of a laboratory on a chip for chemical and biochemical analysis. *Biosensors and Bioelectronics*, 13(3-4):427–438, 1998. 1
- [6] M. Boyer, D. Tarjan, S. T. Acton, and K. Skadron. Accelerating leukocyte tracking using cuda: A case study in leveraging manycore coprocessors. *23rd International Parallel and Distributed Processing Symposium*, pages 1–12, 2009. 1.3

## REFERENCES

---

- [7] A. Carrel. On the permanent life of tissues outside the organism. *J. Exp. Med.*, 15(5):516–528, 1912. 3.1.1
- [8] C. C. Chang, Z. X. Huang, and R. J. Yang. Three-dimensional hydrodynamic focusing in two-layer polydimethylsiloxane (pdms) microchannels. *Journal of Micromechanics and Microengineering*, 17(8):1479–86, 2007. (document), 1.1, 1.2.2, 2, 2.1, 2.1.1, 2.1, 2.2, 2.2.1, 2.5, 2.4, 3.4, 5.2.2, 5.3, 5.5, 5.5, 5.6, 7.1
- [9] C.-M. Chang, S.-K. Hsiung, and G.-B. Lee. Micro flow cytometer chip integrated with micro-pumps/micro-valves for multi-wavelength cell counting and sorting. *Japanese Journal of Applied Physics*, 46(5A):3126–3134, 2007. 1
- [10] I.-F. Cheng, H.-C. Chang, D. Hou, and H.-C. Chang. An integrated dielectrophoretic chip for continuous bioparticle filtering, focusing, sorting, trapping, and detecting. *Biomicrofluidics*, 1(2):021503, 2007. 1.1, 1.3, 5.2.3, 6.3, 6.3
- [11] G. Cloud. *Optical Methods of Engineering Analysis*. Cambridge University Press, 1995 first edn. 6.3
- [12] W. Coulter. Means for counting particles suspended in a fluid, us patent, 1953. 1.3
- [13] E. Coustan-Smith, R. C. Ribeiro, P. Stow, Y. M. Zhou, C. H. Pui, G. K. Rivera, F. Pedrosa, and D. Campana. A simplified flow cytometric assay identifies children with acute lymphoblastic leukemia who have a superior clinical outcome. *Blood*, 108(1):97–102, July 2006. 1
- [14] P. J. Crosland-Taylor. A device for counting small particles suspended in a fluid through a tube. *Nature*, 171(4340):37–38, 1953. 1, 1.2, 3.1.1
- [15] D. Curtin, D. Newport, and M. Davies. A comparison of micro-piv experiments in a mini-channel to numerical and analytical solutions. *Thermal Science and Engineering*, 11 (6):35–42, 2003. 5.5.1
- [16] D. Di Carlo, D. Irimia, R. G. Tompkins, and M. Toner. Continuous inertial focusing, ordering, and separation of particles in microchannels. *Proc Natl Acad Sci U S A*, 104(48):18892–7, 2007. 1.1, 3.1.1, 5.4

## REFERENCES

---

- [17] P. S. Dittrich and A. Manz. Lab-on-a-chip: microfluidics in drug discovery. *Nat Rev Drug Discov*, 5(3):210–218, 2006. 1474-177610.1038/nrd198510.1038/nrd1985. 1, 1.3.1
- [18] P. M. Domagalski, M. M. Mielnik, I. Lunde, and L. R. Sætran. Characteristics of hydrodynamically focused streams for use in microscale particle image velocimetry (micro-piv). *Heat Transfer Engineering*, 28:680–687, 2007. [1][2][3][3]doi:10.1080/01457630701326316. 1.2
- [19] G. Dong, N. Ray, and S. T. Acton. Intravital leukocyte detection using the gradient inverse coefficient of variation. *Ieee Transactions On Medical Imaging*, 24(7):910–924, July 2005. 1.3
- [20] DSMZ. Human and animal cell lines, cell line index, germany, April 2010. 3.1.1
- [21] F. Durst, A. Melling, and J. H. Whitelaw. *Principles and practice of laser-Doppler anemometry*. 1981. 3.3.3
- [22] ECACC. Fundamental techniques in cell culture: A laboratory handbook, sigma-aldrich, 2005. 3.1.1, 3.2
- [23] A. Einstein. *On the movement of small particles suspended in a stationary liquid demanded by the molecular-kinetic theory of heat. In: Theory of the Brownian Movement*. Dover Publications, Inc, New York, 1905. 5.1
- [24] S. Ertel, B. Ratner, A. Kaul, M. Schway, and T. Horbett. In vitro study of the intrinsic toxicity of synthetic surfaces to cells. *Journal of Biomedical Materials Research*, 28(6):667 – 675, 1994. 2.4, 2.4
- [25] A. Esposito. A simplified method for analyzing hydraulic circuits by analogy. *Machine Design*, 41(24):173–177, 1969. 1.2.2, 2.2.1, 5.5
- [26] O. S. Frankfurt. Assessment of cell viability by flow cytometric analysis using dnase exclusion. *Experimental Cell Research*, 144(2):478 – 482, 1983. 1.3.1

## REFERENCES

---

- [27] R. I. Freshney. Culture of animal cells: A manual of basic technique. page 496. New York, 4th edn. edition, 2005. 1.3, 3.1.1, 3.1.1, 3.2
- [28] N. Frische, P. Datta, and J. Goetttert. Development of a biological detection platform utilizing a modular microfluidic stack. *Microsystem Technologies*, 16:1553–1561, 2010. 10.1007/s00542-010-1066-0. 1.3.1, 5.4, 6.3
- [29] A. Y. Fu, C. Spence, A. Scherer, F. H. Arnold, and S. R. Quake. A microfabricated fluorescence-activated cell sorter. *Nat Biotech*, 17(11):1109–1111, 1999. 1087-015610.1038/1509510.1038/15095. 1.1
- [30] L.-M. Fu, C.-H. Tsai, and C.-H. Lin. A high-discernment microflow cytometer with microweir structure. *Electrophoresis*, 29(9):1874–1880, 2008. 10.1002/elps.200700630. 1, 5.4
- [31] L.-M. Fu, R.-J. Yang, C.-H. Lin, Y.-J. Pan, and G.-B. Lee. Electrokinetically driven micro flow cytometers with integrated fiber optics for on-line cell/particle detection. *Analytica Chimica Acta*, 507(1):163–169, 2004. 0003-2670doi: DOI: 10.1016/j.aca.2003.10.028. 1.1, 1.2.1
- [32] E. Furlani. Magnetophoretic separation of blood cells at the microscale. *J. Phys. D: Appl. Phys.*, 40:1313–1319, 2007. 6.1
- [33] S. Gawad, L. Schildb, and P. Renauda. Micromachined impedance spectroscopy flow cytometer for cell analysis and particle sizing. *Lab on a Chip*, 1:76–82, 2001. 1, 1.1, 1.2.1, 1.3, 5.4, 6.3
- [34] I. Georgakoudi, N. Solban, J. Novak, W. L. Rice, X. B. Wei, T. Hasan, and C. P. Lin. In vivo flow cytometry: A new method for enumerating circulating cancer cells. *Cancer Research*, 64(15):5044–5047, Aug. 2004. 1
- [35] J. P. Golden, J. S. Kim, J. S. Erickson, L. R. Hilliard, P. B. Howell, G. P. Anderson, M. Nasir, and F. S. Ligler. Multi-wavelength microflow cytometer using groove-generated sheath flow. *Lab on a Chip*, 9(13):1942–1950, 2009. 10.1039/b822442k. 1.1, 1.2.2, 2.1, 2.1, 2.4

## REFERENCES

---

- [36] G. Hairer, G. Pärre, P. Svasek, A. Jachimowicz, and M. Vellekoop. Investigations of micrometer sample stream profiles in a three-dimensional hydrodynamic focusing device. *Sensors and Actuators B: Chemical*, 132(2):518 – 524, 2008. Transducers '07/Eurosensors XXI, The 14th International Conference on Solid-State Sensors, Actuators and Microsystems and the 21st European Conference on Solid-State Transducers. 1.2.1, 1.2.2, 3.4, 5.1
- [37] G. Hairer and M. Vellekoop. An integrated flow-cell for full sample stream control. *Microfluidics and Nanofluidics*, 7(5):647–658, 2009. 1.1, 1.2.2, 5.2.2, 5.5.2
- [38] R. G. Harrison. Observations on the living developing nerve fiber. *Anat. Rec.*, 1:116–118., 1907. 3.1.1
- [39] B. Helbo, S. Kragh, B. G. Kjeldsen, J. L. Reimers, and A. Kristensen. Investigation of the dye concentration influence on the lasing wavelength and threshold for a micro-fluidic dye laser, Mar. 2004. 2.4
- [40] M. Hennemeyer, F. Walther, S. Kerstan, K. Schurzinger, A. M. Gigler, and R. W. Stark. Cell proliferation assays on plasma activated su-8, May 2008. 2.4, 2.4
- [41] R. A. Hoffman and W. B. Britt. Flow-system measurement of cell impedance properties. *Journal of Histochemistry & Cytochemistry*, 27(1):234–240, 1979. 1.3
- [42] D. Holmes, H. Morgan, and N. G. Green. High throughput particle analysis: Combining dielectrophoretic particle focussing with confocal optical detection. *Biosensors and Bioelectronics*, 21(8):1621 – 1630, 2006. 1, 1.1, 1.3
- [43] D. Holmes, D. Pettigrew, C. H. Reccius, J. D. Gwyer, C. van Berkel, J. Holloway, D. E. Davies, and H. Morgan. Leukocyte analysis and differentiation using high speed microfluidic single cell impedance cytometry. *Lab on a Chip*, 9:2881–2889, 2009. 1, 1.3
- [44] C. A. Homsy. Bio-compatibility in selection of materials for implantation. *Journal of Biomedical Materials Research*, 4(3):341–356, 1970. 2.4

## REFERENCES

---

- [45] P. B. Howell Jr, J. P. Golden, L. R. Hilliard, J. S. Erickson, D. R. Mott, and F. S. Ligler. Two simple and rugged designs for creating microfluidic sheath flow. *Lab on a Chip*, 8(7):1097–1103, 2008. 10.1039/b719381e. 1.2.1
- [46] Hu. Coulter counter having a plurality of channels, us patent, 2008. (document), 1.5
- [47] S. F. Ibrahim and G. van den Engh. High-speed cell sorting: fundamentals and recent advances. *Current Opinion in Biotechnology*, 14(1):5–12, 2003. 1.2
- [48] Invitrogen. *FluoSpheres Fluorescent Microspheres for Blood Flow Determination*. Molecular probes, January 2002. (document), 3.3.3, 3.9, 5.2
- [49] Invitrogen. *Dextran Conjugates*. Molecular probes, April 2006. (document), 3.3.2, 3.8, 4.1
- [50] Invitrogen. *CellTracker Probes for Long-Term Tracing of Living Cells*. Molecular probes, February 2008. (document), 3.1.2, 3.1.2, 3.3, 3.1.2
- [51] M. Kennedy, S. Stelick, S. Perkins, L. Cao, and C. Batt. Hydrodynamic focusing with a microlithographic manifold: controlling the vertical position of a focused sample. *Microfluidics and Nanofluidics*, 7(4):569–578, Oct. 2009. 1.2.2, 1.1, 2.1, 2.1, 2.4, 3.4
- [52] D. S. Kim, D. S. Kim, K. Han, and W. Yang. An efficient 3-dimensional hydrodynamic focusing microfluidic device by means of locally increased aspect ratio. *Microelectronic Engineering*, 86(4-6):1343–1346, Apr. 2009. 1.2.2, 2.1, 2.1, 2.4, 3.4, 4.1.1, 5.1
- [53] J. S. Kim, G. P. Anderson, J. S. Erickson, J. P. Golden, M. Nasir, and F. S. Ligler. Multiplexed detection of bacteria and toxins using a microflow cytometer. *Analytical Chemistry*, 81(13):5426–5432, 2009. 1, 1.2.2
- [54] L. Kim, Y. C. Toh, J. Voldman, and H. Yu. A practical guide to microfluidic perfusion culture of adherent mammalian cells. *Lab on a Chip*, 7(6):681–694, June 2007. 2.6

## REFERENCES

---

- [55] S. S. Kim, C. A. Sundback, S. Kaihara, M. S. Benvenuto, B. S. Kim, D. J. Mooney, and J. P. Vacanti. Dynamic seeding and in vitro culture of hepatocytes in a flow perfusion system. *Tissue Engineering*, 6(1):39–44, Feb. 2000. 1.3.1, 2.6
- [56] Y. W. Kim and J. Y. Yoo. Three-dimensional focusing of red blood cells in microchannel flows for bio-sensing applications. *Biosensors and Bioelectronics*, 24(12):3677 – 3682, 2009. 1.1, 1.1
- [57] J. B. Knight, A. Vishwanath, J. P. Brody, and R. H. Austin. Hydrodynamic focusing on a silicon chip: Mixing nanoliters in microseconds. *Physical Review Letters*, 80(17):3863, 1998. Copyright (C) 2008 The American Physical Society Please report any problems to prola@aps.org PRL. (document), 1.2, 1.2.1, 1.2.2, 3.3, 5.17, 5.5, 5.5
- [58] G. Kotzar, M. Freas, P. Abel, A. Fleischman, S. Roy, C. Zorman, J. M. Moran, and J. Melzak. Evaluation of mems materials of construction for implantable medical devices. *Biomaterials*, 23(13):2737–2750, July 2002. 2.4, 2.4
- [59] G. Lee, C. Lin, and S. Chang. Micromachine-based multi-channel flow cytometers for cell/particle counting and sorting. *Journal of Micromech and Microeng*, 15:447–454, 2005. 1, 5.2.3, 6.3
- [60] G.-B. Lee, C.-C. Chang, S.-B. Huang, and R.-J. Yang. The hydrodynamic focusing effect inside rectangular microchannels. *Journal of Micromechanics and Microengineering*, (5):1024, 2006. (document), 1.2.1, 1.2.2, 3.3, 5.5, 5.5, 5.19, 5.5, 5.5, 5.22, 5.5.2, 5.24, 6.2, 7.1
- [61] G.-B. Lee, I. H. Chen, K. Bin-Jo, H. Guan-Ruey, H. Bao-Herng, and L. Hui-Fang. Hydrodynamic focusing for a micromachined flow cytometer. *Journal of Fluids Engineering*, 123(3):672–679, 2001. (document), 1.2.1, 1.2.2, 3.3, 5.5, 5.5, 5.18, 5.5, 5.5.2
- [62] K. S. Lee, S. B. Kim, K. H. Lee, H. J. Sung, and S. S. Kim. Three-dimensional microfluidic liquid-core/liquid-cladding waveguide. *Applied Physics Letters*, 97(2):021109, July 2010. 1.2.2, 1.1, 2.1, 2.4

## REFERENCES

---

- [63] M. G. Lee, S. Choi, and J. K. Park. Three-dimensional hydrodynamic focusing with a single sheath flow in a single-layer microfluidic device. *Lab On A Chip*, 9(21):3155–3160, 2009. (document), 1.4, 1.2.2, 1.1, 2.1, 2.1, 2.4, 3.1.1, 3.4, 6.3
- [64] A. Lenshof and T. Laurell. Continuous separation of cells and particles in microfluidic systems. *Chemical Society Reviews*, 39:1203–1217, 2010. 1, 1.2.2, 2.4
- [65] F. L. Liao, D. Han, and J. Cao. Endothelial cell, shear stress and biomechanopharmacology. *Acta Pharmacologica Sinica*, 27:432–432, July 2006. 6.3
- [66] C.-H. Lin, C.-Y. Lee, C.-H. Tsai, and L.-M. Fu. Novel continuous particle sorting in microfluidic chip utilizing cascaded squeeze effect. *Microfluidics and Nanofluidics*, 7(4):499–508, Oct. 2009. 1.2
- [67] C.-H. Lin and G.-B. Lee. Micromachined flow cytometers with embedded etched optic fibers for optical detection. *Journal of Micromechanics and Microengineering*, 13(3):447–453, 2003. 1
- [68] C. H. Lin, G. B. Lee, L. M. Fu, and B. H. Hwey. Vertical focusing device utilizing dielectrophoretic force and its application on microflow cytometer. *Microelectromechanical Systems, Journal of*, 13(6):923–932, 2004. 1057-7157. 1, 1.1, 3.1.1
- [69] T. A. Lin. *Vertical Hydrodynamic Focusing in an Isotropically Etched Glass Microfluidic Device*. PhD thesis, Massachusetts Institute of Technology (MIT), 2007. 4.1.1
- [70] T. A. Lin, A. E. Hosoi, and J. E. Daniel. Vertical hydrodynamic focusing in glass microchannels. *Biomicrofluidics*, 3(1):014101, 2009. 1.2.1
- [71] Y.-H. Lin and G.-B. Lee. Optically induced flow cytometry for continuous microparticle counting and sorting. *Biosensors and Bioelectronics*, 24(4):572–578, 2008. 1.1
- [72] V. A. Loiko, G. I. Ruban, O. A. Gritsai, A. D. Gruzdev, S. M. Kosmacheva, N. V. Goncharova, and A. A. Miskevich. Morphometric model of lymphocyte as applied to scanning flow cytometry. *Journal of Quantitative Spectroscopy and Radiative Transfer*, 102(1):73–84, 2006. 1.3.1, 3.1.1, 3.3.3, 5.2.2, 5.4, 5.2, 6.3, 6.3

## REFERENCES

---

- [73] A. Luque, F. Perdigones, J. Esteve, J. Montserrat, A. Ganan-Calvo, and J. Quero. Silicon microdevice for emulsion production using three-dimensional flow focusing. *Microelectromechanical Systems, Journal of*, 16(5):1201–1208, Oct. 2007. 1.2
- [74] H. Ma, L. Jiang, W. Shi, J. Qin, and B. Lin. A programmable microvalve-based microfluidic array for characterization of neurotoxin-induced responses of individual *c. elegans*. *Biomicrofluidics*, 3(4):044114, 2009. 1.3
- [75] X. Mao, S.-C. Lin, C. Dong, and T. Huang. Single-layer planar on-chip flow cytometer using microfluidic drifting based three-dimensional (3d) hydrodynamic focusing. *Lab on a Chip*, 9(11):1583 –9, 2009. 1.2.2, 1.1
- [76] X. Mao, J. R. Waldeisen, and T. J. Huang. ”microfluidic drifting”-implementing three-dimensional hydrodynamic focusing with a single-layer planar microfluidic device. *Lab on a Chip*, 7(10):1260–1262, 2007. 1.2.2, 2.1, 2.1, 2.4, 3.4
- [77] W. F. McLimans, E. V. Davis, F. L. Glover, and G. W. Rake. The submerged culture of mammalian cells; the spinner culture. *J Immunol*, 79(5):428–33, 1957. 1.3.1, 6.1
- [78] C. D. Meinhart, S. T. Wereley, and J. G. Santiago. A piv algorithm for estimating time-averaged velocity fields. In *Proc. of Optical Methods and Image Processing in Fluid Flow, 3rd ASME/JSME Fluids Engineering Conference, San Francisco, CA.*, 1999. 5.5.1
- [79] W. Messner. Give it time. *Mechanical Engineering Magazine*, 129:31, November 2007. 5.4, 5.4
- [80] S. Middleman. *An Introduction to Mass and Heat Transfer: Principles of Analysis and Design*. Wiley, 1998. 4.1
- [81] M. Mielnik and L. Saeiran. Selective seeding for micro-piv. *Experiments in Fluids*, 41(2):155–159, 2006. 10.1007/s00348-005-0103-8. 1.2
- [82] R. Miyake, H. Ohki, I. Yamazaki, and T. Takagi. Investigation of sheath flow chambers for flow cytometers : Micro machined flow chamber with low pressure loss.

## REFERENCES

---

- JSME international journal. Series B, Fluids and thermal engineering*, 40(1):106–113, 1997. 1
- [83] G. E. Moore and L. K. Woods. Culture media for human cells:rpmi 1603, rpmi 1634, rpmi 1640 and gem 1717. *Methods in Cell Science*, 3(1):503–509, Mar. 1977. 3.1.1
- [84] H. Morgan, D. Holmes, and N. G. Green. 3d focusing of nanoparticles in microfluidic channels. *Nanobiotechnology, IEE Proceedings -*, 150(2):76–81, 2003. 1478–1581. 1.1
- [85] J. F. Morgan, H. J. Morton, and R. C. Parker. The nutrition of animal cells in tissue culture; initial studies on a synthetic medium. *Proc. Soc. Exp. Biol. Med.*, 73:1–8, 1950. 3.1.1
- [86] Y. Morimoto, W.-H. Tan, and S. Takeuchi. Three-dimensional axisymmetric flow-focusing device using stereolithography. *Biomedical Microdevices*, 11(2):369–377, Apr. 2009. 1.2
- [87] N.-T. Nguyen and Z. Wu. Micromixers - a review. *Journal of Micromechanics and Microengineering*, 15(2):R1–R16, 2005. 1.2
- [88] J. Nieuwenhuis, J. Bastemeijer, P. Sarro, and M. Vellekoop. Integrated flow-cells for novel adjustable sheath flows. *Lab Chip*, 3(2):56–61, 2003. 1.1, 1.2.2, 2.1, 2.1, 3.4, 5.1
- [89] J. H. Nieuwenhuis, F. Kohl, J. Bastemeijer, P. M. Sarro, and M. J. Vellekoop. Integrated coulter counter based on 2-dimensional liquid aperture control. *Sensors and Actuators B: Chemical*, 102(1):44 – 50, 2004. Selected papers from Transducers 03. 1, 1.3, 6.3
- [90] A. Nilsson, F. Petersson, H. Jonsson, and T. Laurell. Acoustic control of suspended particles in micro fluidic chips. *Lab Chip*, 4(2):131–135, 2004. 1.1
- [91] J. Oakey, R. W. Applegate, E. Arellano, D. D. Carlo, S. W. Graves, and M. Toner. Particle focusing in staged inertial microfluidic devices for flow cytometry. *Analytical Chemistry*, 82(9):3862–3867, 2010. 1.1

## REFERENCES

---

- [92] N. Panchuk-Voloshina, R. P. Haugland, J. Bishop-Stewart, M. K. Bhalgat, P. J. Millard, F. Mao, W. Y. Leung, and R. P. Haugland. Alexa dyes, a series of new fluorescent dyes that yield exceptionally bright, photostable conjugates. *The Journal Of Histochemistry And Cytochemistry: Official Journal Of The Histochemistry Society*, 47(9):1179 – 1188, 1999. 3.3.2
- [93] S. P. Perfetto, P. K. Chattopadhyay, and M. Roederer. Innovation - seventeen-colour flow cytometry: unravelling the immune system. *Nature Reviews Immunology*, 4(8):648–U5, Aug. 2004. 1
- [94] P. Phukpattaranont and P. Boonyaphiphat. An automatic cell counting method for a microscopic tissue image from breast cancer, 2007. 1.3
- [95] P. Phukpattaranont and P. Boonyaphiphat. Color based segmentation of nuclear stained breast cancer cell images. *ECTI Trans. on Electrical Eng., Electronics and Communication*,, 5(2):158–164, 2007. 1.3
- [96] M. Rahman. *Introduction to Flow Cytometry*. Abd serotec, 2007. 1.1
- [97] N. Ray and S. T. Acton. Motion gradient vector flow: An external force for tracking rolling leukocytes with shape and size constrained active contours. *Ieee Transactions On Medical Imaging*, 23(12):1466–1478, Dec. 2004. 1.3
- [98] N. Ray, S. T. Acton, and K. Ley. Tracking leukocytes in vivo with shape and size constrained active contours. *Ieee Transactions On Medical Imaging*, 21(10):1222–1235, Oct. 2002. 1.3
- [99] D. Recktenwald and A. Radbruch. *Cell separation methods and applications*. Marcel Dekker, Inc., New York, 1997. 6.2
- [100] R. Rodriguez-Trujillo, C. Mills, J. Samitier, and G. Gomila. Low cost micro-coulter counter with hydrodynamic focusing. *Microfluidics and Nanofluidics*, 3(2):171–176, 2007. Hydrodynamic focusing;Micro-Coulter counter;. 1

## REFERENCES

---

- [101] C. M. Rovainen, A. B. Wang, and T. A. Woolsey. Strobe epi-illumination of fluorescent beads indicates similar velocities and wall shear rates in brain arterioles of newborn and adult mice. *Microvascular Research*, 43:235–239, 1992. 3.3.2
- [102] J. M. Ruano, M. Aguirregabiria, M. Tijero, M. Arroyo, J. Garcia, J. Berganzo, I. Aramburu, F. J. Blanco, and K. Mayora. Monolithic integration of microfluidic channels and optical waveguides using a photodefinable epoxy. In *17th IEEE International Conference on Micro Electro Mechanical Systems*, pages 121–124, Maastricht, NETHERLANDS, 2004. Ieee. 2.4
- [103] A. M. Sallam and N. H. Hwang. Human red blood cell hemolysis in a turbulent shear flow: contribution of reynolds shear stresses. *Biorheology*, 21 (6):783–797, 1984. 6.3
- [104] H. Sato, Y. Sasamoto, D. Yagyu, T. Sekiguchi, and S. Shoji. 3d sheath flow using hydrodynamic position control of the sample flow. *Journal of Micromechanics and Microengineering*, (11):2211, 2007. 1.2.2, 1.1, 2.1, 2.1, 2.4, 3.4
- [105] H. Schlichting. *Boundary Layer Theory*. McGraw-Hill, Inc., New York., seventh ed. edition, 1979. 5.5.1
- [106] R. Scott, P. Sethu, and C. K. Harnett. Three-dimensional hydrodynamic focusing in a microfluidic coulter counter. *Review of Scientific Instruments*, 79(4):046104, 2008. 1, 1.2.1, 1.2.2, 3.4, 5.1
- [107] D. Semwogerere and E. R. Weeks. Confocal microscopy. *Encyclopedia of Biomaterials and Biomedical Engineering*, Taylor and Francis, 2005. 3.4
- [108] R. K. Shah and A. L. London. *Laminar flow forced convection in ducts*. Academic Press, New York, 1978. 5.5, 5.5.1
- [109] Sigma-Aldrich. Product directory home, April 2010. 3.1.1
- [110] C. Simonnet and A. Groisman. Two-dimensional hydrodynamic focusing in a simple microfluidic device. *Applied Physics Letters*, 87(11):114104–3, 2005. 1, 1.2.1, 2.1

## REFERENCES

---

- [111] J. W. I. M. Simons. Characterization of somatic cells by determination of their volumes with a coulter counter. *Journal of Cell Biology*, 46(3):610–612, 1970. 1.3, 1.3.1
- [112] N. Sizto and L. Dietz. Method and apparatus for cell counting and cell classification, us patent, 1996. 1.3
- [113] A. J. Smith and T. T. Lim. *Flow visualization: techniques and examples*. Imperial College Press, 2000. 3.3
- [114] O. P. Soldin, H. Nsouly-Maktabi, J. M. Genkinger, C. A. Loffredo, J. A. Ortega-Garcia, D. Colantino, D. B. Barr, N. L. Luban, A. T. Shad, and D. Nelson. Pediatric acute lymphoblastic leukemia and exposure to pesticides. *Therapeutic Drug Monitoring*, 31(4):495–501, 2009. (document), 5.2
- [115] T. Stiles, R. Fallon, T. Vestad, J. Oakey, D. W. M. Marr, J. Squier, and R. Jimenez. Hydrodynamic focusing for vacuum-pumped microfluidics. *Microfluidics and Nanofluidics*, 1(3):280–283, Jul 2005. 1.2.1, 1.2.2, 5.5, 5.5, 5.5
- [116] T. Sun, D. Holmes, S. Gawad, N. G. Green, and H. Morgan. High speed multi-frequency impedance analysis of single particles in a microfluidic cytometer using maximum length sequences. *Lab on a Chip*, 7:1034–1040, 2007. 1
- [117] N. Sundararajan, M. S. Pio, L. P. Lee, and A. A. Berlin. Three-dimensional hydrodynamic focusing in polydimethylsiloxane (pdms) microchannels. *Journal of Microelectromechanical Systems*, 13(4):559–567, 2004. 1.2.2, 1.1, 2.1, 2.1, 2.4
- [118] S. Takeuchi, P. Garstecki, D. B. Weibel, and G. M. Whitesides. An axisymmetric flow-focusing microfluidic device. *Advanced Materials*, 17(8):1067–1072, Apr. 2005. 1.2
- [119] C.-H. Tsai, H.-T. Chen, Y.-N. Wang, C.-H. Lin, and L.-M. Fu. Capabilities and limitations of 2-dimensional and 3-dimensional numerical methods in modeling the fluid flow in sudden expansion microchannels. *Microfluidics and Nanofluidics*, 3(1):13–18, Feb. 2007. 4.1

## REFERENCES

---

- [120] C.-H. Tsai, H.-H. Hou, and L.-M. Fu. An optimal three-dimensional focusing technique for micro-flow cytometers. *Microfluidics and Nanofluidics*, 2008. 10.1007/s10404-008-0284-6. 1.2.1, 1.2.2
- [121] G. Vacca, M. R. Junnarkar, N. R. Goldblatt, M. W. Yee, B. M. V. Slyke, and T. C. Briesse. Laser rastering flow cytometry: fast cell counting and identification. volume 7182, page 71821T. SPIE, 2009. 1
- [122] A. van den Berg, H. G. Craigheadb, and P. Yang. From microfluidic applications to nanofluidic phenomena. *Chemical Society Reviews*, 39:1203–1217, 2010. 2.4
- [123] P. Walsh. *Optical field measurements in microscale flow focusing*. PhD thesis, University of Limerick, 2006. (document), 1.2, 3.3.1
- [124] P. A. Walsh, E. J. Walsh, and M. R. D. Davies. On the out-of-plane divergence of streamtubes in planar mini-scale flow focusing devices. *International Journal of Heat and Fluid Flow*, 28(1):44–53, 2007. 1.2, 3.3, 5.2.2, 5.5.1
- [125] J.-H. Wang, C.-H. Wang, C.-C. Lin, H.-Y. Lei, and G.-B. Lee. An integrated microfluidic system for counting of cd4+/cd8+ t lymphocytes. *Microfluidics and Nanofluidics*, pages 1–11, 2010. 10.1007/s10404-010-0687-z. 1.2.1
- [126] N. Watkins, B. M. Venkatesan, M. Toner, W. Rodriguez, and R. Bashir. A robust electrical microcytometer with 3-dimensional hydrofocusing. *Lab Chip*, 9(22):3177–3184, 2009. 1.2.1, 1.2.2
- [127] A. Wolff, I. R. Perch-Nielsen, U. D. Larsen, P. Friis, G. Goranovic, C. R. Poulsen, J. P. Kutter, and P. Telleman. Integrating advanced functionality in a microfabricated high-throughput fluorescent-activated cell sorter. *Lab on a Chip*, 3(1):22–27, 2003. 1.2, 3.1.1
- [128] X. Xuan, J. Zhu, and C. Church. Particle focusing in microfluidic devices. *Microfluidics and Nanofluidics*, 9:1–16, 2010. 10.1007/s10404-010-0602-7. 1.1

## REFERENCES

---

- [129] R. Yang, D. L. Feedback, and W. Wang. Microfabrication and test of a three-dimensional polymer hydro-focusing unit for flow cytometry applications. *Sensors and Actuators A: Physical*, 118(2):259–267, 2005. 1.1, 1.2.2, 3.1.1
- [130] R.-J. Yang, C. Chih-Chang, H. Sung-Bin, and L. Gwo-Bin. A new focusing model and switching approach for electrokinetic flow inside microchannels. *Journal of Micromechanics and Microengineering*, (11):2141, 2005. 1.1
- [131] S. Yang, A. Undar, and J. D. Zahn. Continuous cytometric bead processing within a microfluidic device for bead based sensing platforms. *Lab Chip*, 7(5):588–595, 2007. 1.2.1
- [132] S.-Y. Yang, S.-K. Hsiung, Y.-C. Hung, C.-M. Chang, T.-L. Liao, and G.-B. Lee. A cell counting/sorting system incorporated with a microfabricated flow cytometer chip. *Measurement Science and Technology*, 17(7):2001, 2006. 1
- [133] J. Zhe, A. Jagtiani, P. Dutta, JunHu, and J. Carletta. A micromachined high throughput coulter counter for bioparticle detection and counting. *Journal of Micromechanics and Microengineering*, 17:304–313, 2007. 1, 1.3
- [134] X. Zhu, G. Liu, Y. Guo, and Y. Tian. Study of pmma thermal bonding. *Microsystem Technologies*, 13(3):403–407, 2007. 10.1007/s00542-006-0224-x. 2.1.1

# **Appendix A**

## **Biological materials**

### **Cell culture equipment**

- Laminar flow hood (Holten Safe 2010 Class II BioSafety Cabinet, Thermo Electron Corporation, Bio-Sciences, Dublin, Ireland)
- Incubator (Forma series II, water jacketed CO<sub>2</sub> incubator, Thermo Electron Corporation, Bio-Sciences, Dublin, Ireland)
- Olynous CKX31 inverted light microscope (Mason Technology, Dublin, Ireland)
- Centrifuge (Sorvall® Legend RT Centrifuge, DJB labcare, Buckinghamshire, UK)
- Haemocytometer (Bright-line haemocytometer, Sigma®, Dublin, Ireland)
- Freezing container (Nalgene™ Mr. Forsty, Sigma®, Dublin, Ireland)
- Liquid nitrogen storage dewar (Taylor-Wharton®, Bio-Sciences, Dublin, Ireland)
- 96-well plate reader (Tecan spectrophotometer GENios™, Tecan Group Ltd., Männedorf, Switzerland)

### **Cell culture media and supplements**

- RMPI-1640 media (Sigma® , Dublin, Ireland)

## APPENDIX A. BIOLOGICAL MATERIALS

---

- Fetal Bovine Serum (FBS) (Sigma® , Dublin, Ireland)
- L-Glutamine Solution (Sigma® , Dublin, Ireland)
- Penicillin-Streptomycin (Sigma® , Dublin, Ireland)

### **Chemicals**

- Trypan blue stain (Sigma® , Dublin, Ireland)
- Dimethyl sulfoxide (DMSO, Sigma® , Dublin, Ireland)
- Isopropanol (Sigma® , Dublin, Ireland)
- Ethanol (Sigma® , Dublin, Ireland)

# Appendix B

## Fabrication process of the 3D-HFMD

In this appendix, the steps required for the fabrication of the two 3D-HFMD are described. The fabrication process consists of the reiteration of four steps, summarised in Fig. B.1:

1. substrates preparation
2. photolithography of two SU-8 layers
3. bonding of the two layers
4. final releasing step of the Kapton film

In the following sections the four steps are described in details.

### B.0.1 Substrate preparation

In order to bond together different layers of SU-8, two substrates must be prepared: a bottom substrate on PMMA, and a temporary top substrate, Kapton on Pyrex. To reach a final thickness of few hundred microns two temporary top substrates were required.

**Bottom substrate:** The 1mm thick sheet of PMMA used for the bottom substrate was first immersed into methanol in ultrasonic bath for 5min, then rinsed into deionised water for 5min and finally dry spinned.

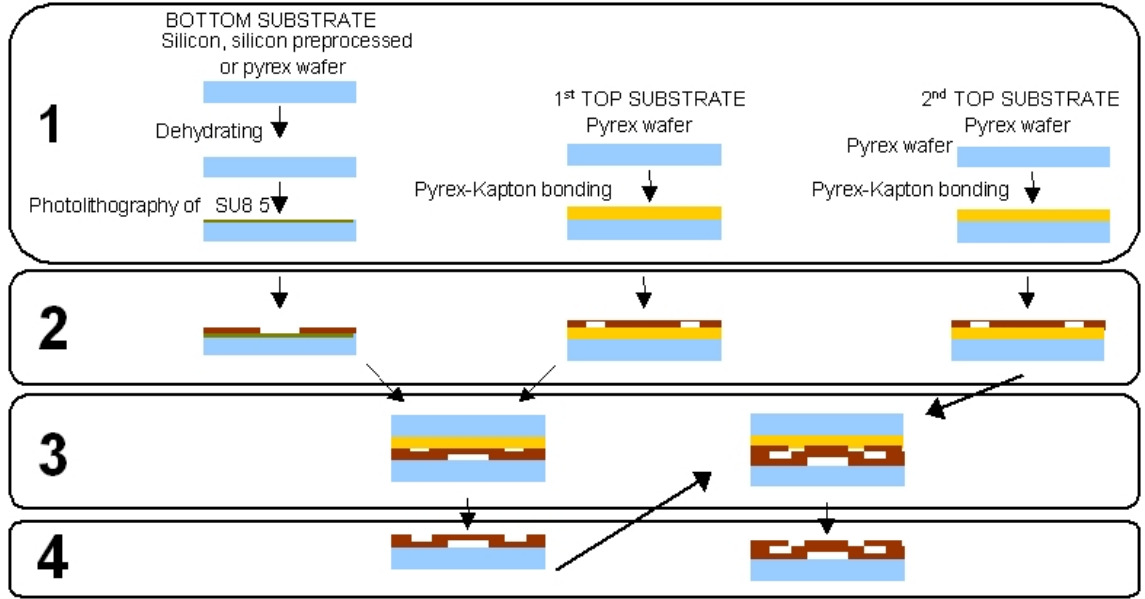


Figure B.1: Fabrication process - physical run steps with wafer cross-section.

**Top substrate:** The two top substrates were made of a 125 $\mu$ m Kapton film (Goodfellow, UK) bonded on a Pyrex wafer. Kapton was used to create a temporary substrate during SU-8 photolithography, thus the use of a sacrificial layer was not required. The poor adhesion between SU-8 and the polyimide film allows Kapton to be manually released after the bonding process. However, a 125 $\mu$ m film was too flexible to perform a correct alignment between two SU-8 layers, and a thicker film will not be transparent enough. Therefore the film was first bonded on a Pyrex wafer, in order to obtain a rigid and transparent substrate. A thin photoresist film, S1818, was spun on the Pyrex wafer at 4000rpm for 30s and used as an adhesive layer between Pyrex and Kapton. A single Pyrex-Kapton substrate was obtained by bonding together the S1818-Pyrex substrate with the Kapton film. First the two layers were put into contact under vacuum at a pressure of 0.1Pa in a substrate bonder, then a pressure of 100 kPa was applied and the system was heated at a temperature of 100  $^{\circ}$ C for 20 min. Finally, a rigid Pyrex-Kapton substrate was achieved.

## B.0.2 Photolithography

Since the top and bottom substrates were prepared, two photolithography processes were carried out using photoplotter masks. The two substrates were photopatterned in few simple

steps:

1. dynamic spin coating from 20 to 60  $\mu\text{m}$  SU-8 at 5000rpm.
2. soft baking with vacuum contact for 30 min. Progressive vacuum ramps were used to bring the heater from room temperature (RT) to 92°C, to avoid microcracking. Heater was then turned off and brought to 35°C.
3. UV exposure. The bottom substrate was exposed to 140 mJ/cm<sup>2</sup> with cross channel mask to define the cross channels. The first top substrate was exposed to 180 mJ/cm<sup>2</sup> with mix channel masks to define the two outlets on the main channel. The second top substrate was exposed to 140 mJ/cm<sup>2</sup> with cover channel masks to define the vertical channels and the junction to the fluidic outlet.
4. post baking with vacuum contact for 4 min. Progressive vacuum ramps were used to bring the heater from room temperature (RT) to 92°C, to avoid microcracking. Heater was then turned off and brought to 35°C.
5. developing in PGMEA bath for 5 min, rinsing the top of the wafer in IPA and dry spinning twice.

In order to reach a final thickness of the SU-8 stack of 200 $\mu\text{m}$ , steps 1 and 2 were repeated four times.

### **B.0.3 Bonding**

Once SU-8 was photopatterned on both substrates, top and bottom layers were placed into contact at 0.1Pa and bonded together in vacuum at 100°C with a pressure of 200kPa for 20 min. The temperature was always kept under the glass transition temperature of the partially polymerised SU-8. After the bonding process the two SU-8 layers were irreversibly joined together.

### **B.0.4 Kapton releasing**

Once both photolithography and bonding of the SU-8 layers was performed, Pyrex and Kapton had to be removed. The final wafer was first rinsed in an IPA ultrasonic bath for 10 min. The Pyrex layer was then removed by the use of a razor blade, and the Kapton film simply peeled off from the SU-8. The poor adhesion between the two materials let the final device to be undamaged after the peeling phase. Once the Kapton film was manually detached, the microfluidic inlets and outlets were open to the external world, which avoided drilling or etching procedures on the cover layer.

During the fabrication of the final specimens, a reference scale with a mark every 100 $\mu$ m was fabricated on the side of the main channel for a length of 14mm. A picture of the final chip, 25 x 15 mm in size, is shown in Fig. 2.13.

# Appendix C

## Videos

This appendix provides a description of the digital videos on the CD located inside the back cover of this thesis. The CD contains thirteen videos.

**Video I** Video I is a recording of the magnetic stirrer in function. The two metal bars are shown rotating around the syringe and the magnetic bar keeps the cells in motion into the syringe .

**Video II and Video III** Video II and Video III show the Alexa Fluor 555 two dimensionally hydrodynamic focused for the full length of the LSD and SSD, respectively.

**Video IV and Video V** Videos III and IV show the flow behaviour under shock and under the influence of an extremely high flow rate at the intersection with channel D into LSD.

**Video VI** Video V is a recording of the flow behaviour under shock at the outlet E.

**Video VII and Video III** Video VII and Video VIII, respectively, show the particles and the streaks highlighting the trajectory of the particles focused in single file into SSD, as seen in Fig. 5.13 (a) and (b).

**Video IX** Video IX is a recording of the particles focused into LSD, as shown in Fig. 5.13 (c).

**Video X and Video XI** Video X and Video XI show particles focused into LSD, correspondent to Fig. 5.13 (c) and (d), respectively.

**Video XII** Video XII is a video of Human B-cell precursor leukaemia focused into LSD at a low flow rate ratio. It is interesting to observe the two semi-detached cells flowing together but with two distinct spin axes.

**Video XIII** Video XIII is a video of Human B-cell precursor leukaemia focused into LSD at a high flow rate ratio. This video shows the smallest focused area achieved with cells in the device.

# Appendix D

## PUBLISHED WORK

### Journals

- **Chiavaroli S.**, Newport D., Woulfe B., “An optical cell counting technique with vertical hydrodynamic focusing”, *Biomicrofluidics* **4**, 024110, 2010
- Barrot Lattes C., Newport D., **Chiavaroli S.**, Morini G.L., Baldas L., Colin S., “3D reconstruction of velocity profiles in rectangular microchannels”, *Heat and Technology* **26**(1), 153-159, 2008

### Conference papers

- **Chiavaroli S.**, Newport D., Woulfe B., “New optical counting technique with 3D-Hydrodynamic focusing for leukemia cells”, *Proc. of 1st European Conference on Microfluidics*, Bologna, December 10-12, 2008
- **Chiavaroli S.**, Newport D., Woulfe B., “Efficient micro-device cell sorter with fluorescence imaging for leukemia diagnosis”, *Proc. of 3rd International Workshop on Approaches to Single-Cell Analysis*, Zurich, September 11-12, 2008
- **Chiavaroli S.**, Newport D., Morini G.L., Barrot Lattes C., Baldas L., Colin S., “Influence of concentration and number of image pairs in microPIV experiments”, *Proc.*

#### APPENDIX D. PUBLISHED WORK

---

of 5th ASME-JSME Fluids Engineering Conference, San Diego, July 30-August 2, 2007

- Barrot Lattes C., Newport D., **Chiavaroli S.**, Morini G.L., Baldas L., Colin S., “Improving micro-PIV data in 3-D geometries”, Proc. of  $\mu$ Flu’06, Toulouse, December 11-14, 2006